Imperial College London

Super Resolution Array Imaging of Embedded Defects Within Safety-Critical Components

by

Joshua Benjamin Elliott

A thesis submitted in fulfilment of the requirements for the degree of

Doctor of Engineering

Department of Mechanical Engineering
Imperial College London
London SW7 2AZ

August 2020

Declaration of Originality

The content of this thesis is my own work under the supervision from Professor Michael Lowe and Dr. Peter Huthwaite. Where I have made use of the work of others, I have made this clear and provided appropriate references.

Joshua B. Elliott
07/08/2020

Copyright

The copyright of this thesis rests with the author and is made available under a Creative Commons Attribution Non-Commercial No Derivatives licence. Researchers are free to copy, distribute or transmit the thesis on the condition that they attribute it, that they do not use it for commercial purposes and that they do not alter, transform or build upon it. For any reuse or redistribution, researchers must make clear to others the licence terms of this work.

Abstract

There is a constant drive within the nuclear power industry to improve upon the characterization capabilities of ultrasonic Non-Destructive Evaluation (NDE) inspection techniques in order to improve safety and reduce costs, with particular emphasis placed on the ability to characterize small defects. The usage of ultrasonic phased array technologies have led to significant advancements in NDT performance relative to conventional monolithic transducers and they have also led to the development of several advanced imaging algorithms. A group of these called Super Resolution (SR) algorithms have been shown to demonstrate a capability to resolve scatterers separated by less than the diffraction limit when deployed in representative NDE inspections.

In this thesis, the Factorisation Method (FM) and the Time Reversal Multiple Signal Classification (TR-MUSIC) algorithms were investigated in the imaging of embedded defects. The performance of these SR techniques in accurately characterising smooth embedded planar defects of varying size and orientations was investigated via two-dimensional (2D) Finite Element (FE) simulations and the results were experimentally validated. These studies were extended to consider more realistic three-dimensional (3D) smooth embedded planar defects in experimental trials and rough embedded planar defects, the latter being explored using 2D FE Monte Carlo simulations. The SR algorithms were also benchmarked against the conventional array Total Focusing Method, which is recognised to be a high performing and robust imaging technique.

The SR algorithms were also applied to the imaging of 2D and 3D volumetric defects in order to determine if direct, image-based sizing could be achieved with these ultrasonic methods. The final and most challenging inspection case considered within this thesis was the inspection of embedded defects within austenitic stainless steel welds. These materials exhibit spatially-varying anisotropic coarse grained microstructures which can lead to significant ultrasonic signal attenuation and beam bending effects that make their NDE inspection difficult.

Acknowledgements

I would firstly like to thank my academic supervisors Professor Mike Lowe and Dr. Peter Huthwaite and industrial supervisor Dr. David Duxbury for their technical and practical guidance throughout this project. Without their extensive knowledge and guidance, this work would not have been possible.

I would also like to my colleagues throughout the four years of the project, both at Imperial College London and Rolls-Royce Submarines in Derby. They include and are not limited to Richard Phillips, Mike Laws, Xiaotang Gu, Fan Shi and the rest of my EngD cohort. They not only provided additional support whenever I had questions, but they also immensely helped to make our working environment a fun and open place to be part of.

Additional thanks are also required for Keith Newton and Chris Scruby, who went above and beyond to help me prepare in my successful application for the Industrial Fellowship Award from the Royal Commission for the Exhibition of 1851. I am also grateful to Professor Steve Dixon for introducing me to the field of NDE and the EngD scheme initially.

Furthermore, I need to acknowledge EPSRC, RCNDE, Rolls-Royce Submarines and the Royal Commission for the Exhibition of 1851 for funding this work.

Finally but most importantly, I express my sincerest gratitude and appreciation to my wife Maya, my mum and my grandparents for their continual love and support over the years. I would not be where I am now without them and I am forever grateful and blessed to have them in my life.

Contents

1 Introduction **29**
1.1 Ultrasonic Non-Destructive Evaluation 29
1.2 Industrial Motivations 34
1.3 Outline of Thesis 38

2 Background Theory **41**
2.1 Introduction 41
2.2 Governing Equations 41
2.3 Scattering Operators 46
2.4 The Challenge of Inverse Scattering 48
2.5 Born Approximation 48
2.6 Total Focusing Method 50
2.7 Multiple Scattering 54
2.8 Super Resolution Algorithms 55
2.8.1 Factorisation Method 56
2.8.2 TR-MUSIC 57
2.8.3 Practical Implementation of the SR Algorithms 58

3 SR Imaging of Simulated Embedded Smooth Planar Defects **65**
3.1 Introduction 65
3.2 Modelling Approach 66
3.3 Imaging Sizing Methodology 71
3.4 SR Imaging Performance for Varying Defect Size 72
3.5 The Effect of Defect Misorientation on SR Imaging Performance 79
3.6 The Effect of Incoherent Noise on SR Imaging Performance . 86
3.7 Conclusions 95

4 Experimental SR Imaging of 2D Embedded Smooth Planar Defects **99**
4.1 Introduction 99
4.2 Experimental Set-Up 99
4.3 Wire Eroded Test Piece Array Imaging Results 100
4.4 Conclusions 111

5 Experimental SR Imaging of 3D Embedded Smooth Planar Defects **113**
5.1 Introduction 113
5.2 Experimental Set-Up 113
5.3 SR Image Generation from FMC Scan Data 115
5.4 Spark Eroded Test Piece Array Imaging Results 118
5.5 Conclusions 125

6 SR Imaging of Simulated Embedded Rough Planar Defects **127**

6.1 Introduction . . . 127
6.2 Background Theory of Defect Roughness . . . 127
6.3 Rough Defect Inspection Cases . . . 128
6.4 Results and Discussions . . . 130
6.4.1 Smooth Defects . . . 130
6.4.2 Rough defects . . . 132
6.5 Conclusions . . . 140

7 SR Imaging of Embedded Volumetric Defects 143
7.1 Introduction . . . 143
7.2 Simulated SDH Array Imaging . . . 145
7.3 Experimental Validation . . . 147
7.4 Conclusions . . . 151

8 SR Imaging Within Scattering Austenitic Stainless Steels 153
8.1 Introduction . . . 153
8.2 Methodology . . . 155
8.3 SR Imaging Results & Discussion . . . 159
8.3.1 Longitudinally Orientated Defects . . . 159
8.3.2 Through-Wall Orientated Defects . . . 168
8.4 Conclusions . . . 172

9 Conclusions 175
9.1 Thesis Review & Main Achievements . . . 175
9.2 Guidance for SR Algorithm Deployment & Future Work . . . 179
9.2.1 Multistatic Response Matrix Construction . . . 179
9.2.2 Noise . . . 180
9.2.3 Viewing Angle . . . 181

List of Figures

1.1 Illustration of the converse piezoelectric effect mechanism. The application of an external electric field, E, to a piezoelectric crystal can lead to its expansion and contraction from its original shape (dashed blue outline). It is this effect which is used to mechanically drive piezoelectric transducer crystals in the generation of ultrasound. This effect is reversible and consequently mechanical forces applied to a piezoelectric crystal leads to the generation of a voltage across it; this effect is used on reception of ultrasound to record a voltage time history, or A-Scan. 30
1.2 a) Schematic of an example ultrasonic NDE scan of a component containing an embedded defect, b) an example A-Scan that may be measured by the transducer when placed over the defect, c) an example B-Scan that may be generated from the various scan points along the component surface. 31
1.3 Illustration of how delay laws of varying magnitude (red) can be applied to the elements of a linear ultrasonic array (blue) to generate: a) a plane 0° wave when equal or no delay laws are applied, b) an angled plane wave when delay laws of linearly increasing magnitude are applied sequentially across the array elements, c) a focused beam where the delay laws are used to direct the energy of the array to a single point within the component. 32
1.4 Common array geometries: a) 1D linear array, b) 2D matrix array, c) annular array. 33
1.5 The array element excitation procedure for Full Matrix Capture data acquisition with a linear array. 34
1.6 The schematic for the operation of NSOM. The arrows represent the wave paths through space between the source, receiver and surface of interest. The three main modes of NSOM are shown; a) illumination mode, b) collection mode, and c) apertureless mode. 36
1.7 The schematic for general inspection cases considered in this thesis. It considers the linear array inspection of a thick-walled stainless steel component contained embedded planar defects of size on the order of $\lambda/2$ at depths greater than 10λ. These components may or may not contain a weld and the defects considered can have varying orientations. 37

2.1 The concept of wave scattering of an initial wave, ϕ_i, by an object D with boundary ∂D, resulting in a scattered wave, ϕ_s. The object D has a refractive index of n. 43

2.2 An illustration of the far-field scattering problem. a) a far-field incident from an infinite distance (figure not to scale) $\phi_i^\infty(\hat{\mathbf{r}})$ illuminating the scatterer D with boundary ∂D, b) the incident wave on scatterer D generates a new scattered wave field $\phi_s^\infty(\hat{\mathbf{r}})$ measured in the far-field. 45
2.3 a) The far-field operators, F, maps an incident far-field wave field to a scattered far-field for a scatterer and the inverse F^{-1} reverses this mapping. b) The complete far-field scattering operator, M, maps the scatterer (represented by $\mathcal{O}$ or $\tilde{\mathcal{O}}$ in the spatial frequency domain) to the complete scattering amplitude f and therefore F. The imaging operator M^{-1} is used to reverse this mapping. 47
2.4 A schematic of the Ewald limiting circle in the spatial frequency domain. 49
2.5 The configuration of the TFM algorithm. 51
2.6 a) The energy of the oscillating particles in the transducer being forced by the ultrasonic waves can be described by a simple oscillating mass on a spring. b) The total energy of the mass is conserved between elastic potential energy and kinetic energy, with both forms of energy being $\pi/2$ out of phase with each other. 52
2.7 An example of a simulated FMC A-Scan featuring a defect response. The real time-domain signal recorded by the array is shown in blue, the Hilbert transform of this signal is shown in orange and the instantaneous amplitude of the analytic signal is shown in yellow. 52
2.8 Examples of TFM images of a point scatterer using simulated FMC data from a 2 MHz 64-element array when a) the analytic signal is used as part of the algorithm, and b) when only the unprocessed time-domain signal obtained by the array is used. It can be seen that image b) exhibits a periodic variation in amplitude of $\lambda/2$ which is not indicative of the nature of the imaged point scatterer. 53
2.9 A simplified scattering scenario comprising of two scatterers. a) Paths of the incident and scattered waves under the Born approximation; only single scattering is permitted and there is no interaction between the scatterers. b) Paths of the incident and scattered fields considering multiple scattering; interaction between the scattered fields and scatterers occurs which is a key mechanism for retrieving far-field sub-wavelength information. 55

2.10 An illustration of time-domain windowing of FMC data to isolate the defect response. a) An example of a raw FMC A-Scan corresponding to the pulse-echo signal from the centre element of a 64-element 2 MHz array, featuring initial pulse ringing, the defect signal and geometric reflections. b) The TFM image generated using raw FMC data which includes low amplitude artefacts at the transducer locations (Y=70 mm), the defect indication in the centre of the image as well as a backwall response. c) An example of time-domain windowing applied to the A-Scan in a) to isolate the defect response. d) The TFM image of the windowed FMC data containing only the defect indication. 60
2.11 The impact of using different centre frequencies on single frequency FM imaging where a 5-cycle 2 MHz toneburst was used to inspect a 6 mm embedded planar defect, shown in white. The images produced used single a centre frequency of a) 1.8 MHz, b) 2.0 MHz, c) 2.2 MHz. d) is a MF-FM image centred on 2 MHz where nine frequencies were evenly sampled between 1.6 MHz – 2.4 MHz. These images were produced from the simulated FMC inspection of a planar embedded defect with a 64-element located at a distance of 42 mm, centrally positioned above the defect. The set-up is illustrated in Fig. 1.7. 62
2.12 Flowchart detailing the implementation of the TFM, MF-FM and MF-TR-MUSIC algorithms on ultrasonic array FMC datasets. Detailed description of the implementation steps are found within the main text. 63
2.13 The conventions used to define the x-, y- and z-axes and defect parameters in this thesis. a) 3D view of a linear array (blue, orientated in the $\hat{x}$-axis) inspection of an embedded planar defect (green), with the image generated in the $x-y$ plane (orange). b) $x-y$ plane projection of a) where defect width and TWH are defined. c) $y-z$ plane projection of a) where defect length is defined. 64

3.1 FE inspection setup for the array imaging of 2D embedded planar defects. The origin position of the models is located at the centre of the defect. 66
3.2 Comparison between the directivity function of the FE longitudinal wave point sources employed in this thesis, Ψ_{FE}, and an analytical far-field directivity pattern for a 2D array element, Ψ_{M-P}. Values of $\lambda = 3$ mm, $a = 1.2$ mm, $c_L = 5894\,\text{ms}^{-1}$ and $c_S = 3150\,\text{ms}^{-1}$ were used to calculate Ψ_{M-P}. These directivity functions have been normalised. In the RHS figure, the red line corresponds to angles of $\pm 48.8°$ which is the maximum angular difference between the position of the end array elements and the centrally located defects at a depth of 42 mm. 68

3.3 An illustration of the difference in viewing angle achieved by two different sized linear arrays, with the wider 64-element array achieving a larger viewing angle (θ°_{64}) than the 32-element array (θ°_{32}). 70
3.4 Visualisation of the process to generate 2D smooth embedded defects. First a smooth flat defect profile is calculated (a). The crack is then opened by a small amount, varying along its width, by displacing the top surface upwards by the half-cycle sinusoidal profile function shown in the solid red line at the top of (a) and similarly moving the bottom surface down by the dashed red at the bottom of (a). The resulting open 2D smooth defect is shown in (b). 70
3.5 a) An example of the application of the 6 dB box-fitting algorithm to a TFM image of a planar defect. From the parallelogram defined by the algorithm, the defect width as well as the defect inclination, θ, is able to be determined. b) An example of tip sizing where the defect width and inclination are defined by the straight line between the two tip maxima. 72
3.6 MF-FM, MF-TR-MUSIC, TFM and array B-Scan images from the 2D FE simulated inspection of (1, 1.5, 3, 6 and 10) mm 0° smooth planar embedded defects. The active aperture size for the B-Scan images was 16.5 mm for defects smaller than 6 mm and 15 mm otherwise. All images are plotted in a decibel scale, with all TFM and B-Scan images plotted between 0 and -6 dB. The set-up shown in Fig. 3.1 was used, featuring a 64-element 2 MHz array centred above the defects at a distance of 42 mm. 74
3.7 Illustration of how a 0° B-Scan is generated by a contact linear ultrasound array. A group of elements are fired in a pulse-echo configuration, known as the aperture, and this aperture is electronically scanned across the array to generate a B-Scan image. 75
3.8 Defect sizing results from the 2D FE simulated 2 MHz 64-element array inspection using the MF-FM, MF-TR-MUSIC, TFM and array B-Scan algorithms. 76
3.9 Defect sizing results from the 2D FE simulated 2 MHz 32-element array inspection using the MF-FM, MF-TR-MUSIC, TFM and array B-Scan algorithms. 77
3.10 SR indication trend using a simulated 1 MHz, 2 MHz and 4 MHz 64-element ultrasonic arrays. 79
3.11 Defect images produced from the 2D FE simulated 2 MHz 64-element array inspection of 1.5 mm planar defects of various orientations. The MF-FM, MF-TR-MUSIC and TFM algorithms were used. All images are plotted in a decibel scale, with all TFM images plotted between 0 and -6 dB. The set-up shown in Fig. 3.1 was used, with the array centred above the defects at a distance of 42 mm. 81
3.12 Defect sizing results from the 2D FE simulated 2 MHz 64-element array inspection of 1.5 mm planar defects of various orientations. 82

3.13 Defect orientation estimation results from the 2D FE simulated 2 MHz 64-element array inspection of 1.5 mm planar defects of various orientations. 82
3.14 Defect TWH estimation results from the 2D FE simulated 2 MHz 64-element array inspection of 1.5 mm planar defects of various orientations. 83
3.15 Defect sizing results from the 2D FE simulated 2 MHz 32-element array inspection of 1.5 mm planar defects of various orientations 84
3.16 Defect orientation estimation results from the 2D FE simulated 2 MHz 32-element array inspection of 1.5 mm planar defects of various orientations. 85
3.17 Defect TWH estimation results from the 2D FE simulated 2 MHz 32-element array inspection of 1.5 mm planar defects of various orientations. 85
3.18 MF-FM and MF-TR-MUSIC images of a 1.5 mm 90° planar 2D defect when inspected by a 2 MHz 32-element array. . . . 86
3.19 Example A-Scans from the simulated FMC data from the 2 MHz 64-element array inspection of an embedded 3 mm smooth planar defect with varying levels of added GWN. The time-windowing that was applied prior to SR imaging is shown. The eigenvalue amplitude for each corresponding FMC data set is plotted adjacent to the A-Scans. 88
3.20 MF-FM, MF-TR-MUSIC, TFM and array B-Scan images generated from the simulated 2 MHz 64-element array inspection of an embedded planar 1.5 mm defect, where varying levels of GWN were added to achieve different SNRs. All images are plotted in a decibel scale, with all TFM and B-Scan images plotted between 0 and -6 dB and all MF-FM and MF-TR-MUSIC images plotted between 0 and -10 dB. The set-up shown in Fig. 3.1 was used, with array centred above the defects at a distance of 42 mm. 89
3.21 MF-FM, MF-TR-MUSIC, TFM and array B-Scan images generated from the simulated 2 MHz 64-element array inspection of an embedded planar 3 mm defect, where varying levels of GWN were added to achieve different SNRs. All images are plotted in a decibel scale, with all TFM and B-Scan images plotted between 0 and -6 dB and all MF-FM and MF-TR-MUSIC images plotted between 0 and -10 dB. The set-up shown in Fig. 3.1 was used, with array centred above the defects at a distance of 42 mm. 90
3.22 MF-FM, MF-TR-MUSIC, TFM and array B-Scan images generated from the simulated 2 MHz 64-element array inspection of an embedded planar 6 mm defect, where varying levels of GWN were added to achieve different SNRs. All images are plotted in a decibel scale, with all TFM and B-Scan images plotted between 0 and -6 dB. The set-up shown in Fig. 3.1 was used, with array centred above the defects at a distance of 42 mm. 91

3.23 The sizing performance of the array imaging algorithms when inspecting a 1.5 mm embedded planar defect with decreasing SNR. 92
3.24 The sizing performance of the array imaging algorithms when inspecting a 3 mm embedded planar defect with decreasing SNR. 92
3.25 The sizing performance of the array imaging algorithms when inspecting a 6 mm embedded planar defect with decreasing SNR. 93
3.26 The imaging SNR methodology for the case of GWN added to noise-free FE FMC data such that the A-Scan SNR was 1 dB. Each image plotted in an absolute amplitude scale. . . 95

4.1 a) 3D illustration of the experimental set-up for array FMC data collection on the WE test pieces, showing the series of pseudo-2D WE slots within the test block with the array positioned on the test piece centreline (dashed red), directly centred above WE defects. b) The cross-sectional view ($x - y$ axes) of the experimental set-up, where the WE defect widths (X) ranged from 1.5 mm - 6 mm and the inclinations (θ) ranged from 0°-20°. c) The plan-view of the set-up ($x - z$ axes) showing the positions of the array above the defects where a single FMC dataset was collected for each location. Figure not to scale. 101
4.2 Array algorithm images for the 1.5 mm wire eroded defects using a 2 MHz 64-element probe. All images were normalised to the maximum pixel value within each image and are plotted in the decibel scale. All MF-FM and MF-TR-MUSIC are plotted between 0 and -10 dB. All TFM and B-Scan images are plotted between 0 and -6 dB. A 15 mm active aperture was used to generate the B-Scan images. The set-up shown in Fig. 4.1 was used, with the array centred above the defects at a distance of 40 mm. 102
4.3 Array algorithm images for the 3 mm wire eroded defects using a 2 MHz 64-element probe. All images were normalised to the maximum pixel value within each image and are plotted in the decibel scale. All MF-FM and MF-TR-MUSIC are plotted between 0 and -10 dB, except the MF-TR-MUSIC 10° image is between 0 and -12 dB. All TFM and B-Scan images are plotted between 0 and -6 dB. A 15 mm active aperture was used to generate the B-Scan images. The set-up shown in Fig. 4.1 was used, with the array centred above the defects at a distance of 40 mm. 103

4.4 Array algorithm images for the 6 mm wire eroded defects using a 2 MHz 64-element probe. All images were normalised to the maximum pixel value within each image and are plotted in the decibel scale. All MF-FM and MF-TR-MUSIC are plotted between 0 and -10 dB, except the MF-FM 0° image is between 0 and -15 dB. All TFM and B-Scan images are plotted between 0 and -6 dB. A 15 mm active aperture was used to generate the B-Scan images. The set-up shown in Fig. 4.1 was used, with the array centred above the defects at a distance of 40 mm. 104
4.5 The imaging SNR methodology for the 1.5 mm 0° WE defect using a 2 MHz 64-element array. Each image plotted in an absolute amplitude scale. The set-up shown in Fig. 4.1 was used, with the array centred above the defects at a distance of 40 mm. 107
4.6 Array algorithm images for the 1.5 mm wire eroded defects using a 1 MHz 32-element probe. All images were normalised to the maximum pixel value within each image and are plotted in the decibel scale. All images are plotted between 0 dB and -6 dB, except for the 10° and 20° MF-FM and MF-TR-MUSIC images which were between 0 dB and -10 dB. A 15 mm active aperture was used to generate the B-Scan images. The set-up shown in Fig. 4.1 was used, with the array centred above the defects at a distance of 40 mm. 108
4.7 Array algorithm images for the 3 mm wire eroded defects using a 1 MHz 32-element probe. All images were normalised to the maximum pixel value within each image and are plotted in the decibel scale. All images are plotted between 0 dB and -6 dB, except for the 20° MF-FM image which was between 0 dB and -8 dB. A 15 mm active aperture was used to generate the B-Scan images. The set-up shown in Fig. 4.1 was used, with the array centred above the defects at a distance of 40 mm. 109
4.8 Array algorithm images for the 6 mm wire eroded defects using a 1 MHz 32-element probe. All images were normalised to the maximum pixel value within each image and are plotted in the decibel scale. All TFM and B-Scan images are plotted between 0 and -6 dB. A 15 mm active aperture was used to generate the B-Scan images. The set-up shown in Fig. 4.1 was used, with the array centred above the defects at a distance of 40 mm. 110

5.1 a) 3D illustration of the experimental set-up for FMC array scanning of the spark eroded ellipse test pieces, showing the series of elliptical notches within the test blocks and the series of scan lines (dashed red). One scan line was used for each notch, with the linear array centred on each notch. b) The cross-sectional view ($x - y$ axes) of the experimental set-up, where the notch defect widths (X) ranged from 1 mm - 3 mm and their inclinations (θ) ranged from 0°- 20°. c) The plan-view of the set-up ($x - z$ axes), where the defect lengths (Z) varied between 1 mm - 3 mm. 114
5.2 An illustration of the experimental set-up used when collecting scanned FMC datasets from a test piece. The ultrasonic array (light blue) is manipulated across the test piece surface with the XY scanner, which can move the probe in either the primary scan axis or the secondary scan axis. Both the primary and secondary scan axes are perpendicular to each other. The XY scanner is controlled with a separate motor control unit and the ultrasonic array is controlled via a MicroPulse FMC signal generator. Both the motor control unit and the MicroPulse FMC are interfaced with a stand-alone computer which controls all the equipment. 115
5.3 Imaging methodology to generate a SR B-Scan ($x - y$) image of an embedded planar defect. The first step is to apply the TFM algorithm to the FMC scan data and estimate the (x, y, z) position of the defect. The z-extent of the defect from the C-Scan is estimated (a). The z-extent is used to truncate the SR data (b) to produce a reduced set of data which contains significant defect indications (c). (d) SR B-Scan ($x - y$) images are generated for each scan increment FMC dataset and the resultant images are summed to produce a single defect image which is used for characterisation. The set-up shown in Fig. 5.1 was used, featuring a 64-element 2 MHz array scanned centrally above the defects at a distance of 40 mm. All images are plotted on a decibel scale. 119
5.4 Array algorithm images for the (1x3) mm spark eroded elliptical defects using a 2 MHz 64-element array. All images were self-normalised to their peak amplitude value and are plotted in the decibel scale. All TFM and B-Scan images are plotted between 0 and -6 dB. A 15 mm active aperture was used to generate the 0° and 10° B-Scan images and a 16.5 mm active aperture was used to generate the 20° B-Scan images. The set-up shown in Fig. 5.1 was used, featuring a 64-element 2 MHz array scanned centrally above the defects at a distance of 40 mm. 120

5.5 Array algorithm images for the (3x1) mm spark eroded elliptical defects using a 2 MHz 64-element array. All images were self-normalised to their peak amplitude value and are plotted in the decibel scale. All TFM and B-Scan images are plotted between 0 and -6 dB. A 15 mm active aperture was used to generate all the B-Scan images. The set-up shown in Fig. 5.1 was used, featuring a 64-element 2 MHz array scanned centrally above the defects at a distance of 40 mm. . 121
5.6 The imaging SNR methodology for the (1x3) mm 0° SE case. Each image plotted in an absolute amplitude scale. The set-up shown in Fig. 5.1 was used, featuring a 64-element 2 MHz array scanned centrally above the defects at a distance of 40 mm. 124

6.1 Visualisation of the process to generate the 2D rough embedded defects. First a smooth defect profile is calculated (a), then roughness is applied to this profile following Gaussian statistics (b). The crack is then opened by a small amount, varying along its length, by displacing the top surface upwards by the half-cycle sinusoidal profile function shown in the solid red line at the top of (b) and similarly moving the bottom surface down by the dashed red at the bottom of (b). The resulting open 2D rough defect is shown in (c). 129
6.2 Images from the MF-FM, MF-TR-MUSIC and TFM algorithms for the smooth defect cases. Images a), b) and c) correspond to 1.5 mm 0° defects; d), e), and f) correspond to 1.5 mm 45° defects; g), h) and i) correspond to 3 mm 0° defects; j), k) and l) correspond to 3 mm 45° defects. All the images are plotted on a decibel scale normalised to the maximum image amplitude from the defect response. Images (a)-(f) are 4 mm x 4 mm in size, images (g)-(l) are 6 mm x 6 mm in size. The set-up shown in Fig. 3.1 was used, featuring a 64-element 2 MHz array centred above the defects at a distance of 42 mm. . . . 131
6.3 Representative images from the MF-FM, MF-TR-MUSIC and TFM algorithms for 1.5 mm rough defects. Images a), b) and c) correspond to $\sigma = 10$ μm 0° rough defects; d), e), and f) correspond to $\sigma = 100$ μm 0° rough defects; g), h) and i) correspond to $\sigma = 10$ μm 45° rough defects; j), k) and l) correspond to $\sigma = 100$ μm 45° rough defects. All the images are plotted on a decibel scale normalised to the maximum image amplitude from the defect response. The set-up shown in Fig. 3.1 was used, featuring a 64-element 2 MHz array centred above the defects at a distance of 42 mm. 133
6.4 The mean estimated defect width and inclination angle values calculated from the 100 realisations for the 1.5 mm 0° 10 μm (left plot) and 1.5 mm 0° 100 μm (right plot) rough defects. The error bars correspond to the standard deviation of the width and angle results. 134

6.5 The mean estimated defect width and inclination angle values calculated from the 100 realisations for the 1.5 mm 45° 10 μm (left plot) and 1.5 mm 45° 100 μm (right plot) rough defects. The error bars correspond to the standard deviation of the width and angle results. 135
6.6 Representative images from the MF-FM, MF-TR-MUSIC and TFM algorithms for 3 mm rough defects. Images a), b) and c) correspond to $\sigma = 10$ μm 0° rough defects; d), e), and f) correspond to $\sigma = 100$ μm 0° rough defects; g), h) and i) correspond to $\sigma = 10$ μm 45° rough defects; j), k), l) correspond to $\sigma = 100$ μm 45° rough defects. All the images are plotted on a decibel scale normalised to the maximum image amplitude from the defect response. The set-up shown in Fig. 3.1 was used, featuring a 64-element 2 MHz array centred above the defects at a distance of 42 mm. 136
6.7 The mean estimated defect width and inclination angle values calculated from the 100 realisations for the 3 mm 0° 10 μm (left plot) and 3 mm 0° 100 μm (right plot) rough defects. The error bars correspond to the standard deviation of the width and angle results. 137
6.8 The mean estimated defect width and inclination angle values calculated from the 100 realisations for the 3 mm 45° 10 μm (left plot) and 3 mm 45° 100 μm (right plot) rough defects. The error bars correspond to the standard deviation of the width and angle results. 138

7.1 The MF-FM, MF-TR-MUSIC, TFM and array B-Scan images from FE simulated SDHs of varying diameters. All the images are plotted on a decibel scale normalised to their own maximum image amplitude from the defect response. The set-up shown in Fig. 3.1 was used, featuring a 64-element 2 MHz array centred above the defects at a distance of 42 mm. 146
7.2 The SR algorithm diameter sizing results from the 2D FE simulated SDHs. 147
7.3 The MF-FM, MF-TR-MUSIC and TFM algorithm images produced from experimentally collected FMC data from SDHs of different diameters using a 2 MHz 64-element linear phased array. All the images are plotted on a decibel scale normalised to the maximum image amplitude from the defect response. The array in each case was centred directly above the defects at the distances listed in Table 7.1. 148
7.4 Experimental SDH sizing results using the SR algorithms. . 149
7.5 The TFM and MF-TR-MUSIC images produced from experimentally collected FMC data from a 2 mm diameter pore. All the images are plotted on a decibel scale normalised to the maximum image amplitude from the defect response. The 2 MHz 64-element array in each case was centred directly above the defects at the distances listed in Table 7.1. 150

8.1 Schematic for the austenitic stainless steel welded test pieces containing various embedded defects. a) is the cross-sectional view of the test pieces and b) is a plan view of the test pieces. A 2 MHz 64-element linear array and a 1 MHz 32-element linear array were scanned along the weld centreline in the $\hat{z}$ direction. Figure not to scale. 155
8.2 Schematic for the defects in the narrow gap austenitic stainless steel welded test pieces. The figures are a) cross-sectional view of the LOILF defects, b) plan view of the LOILF defects, c) cross-sectional view of the LOSWF defects, d) plan view of the LOSWF defects, e) cross-sectional view of the LOIRF defects, and f) plan view of the LOIRF defects. All defects were elliptical and planar. 156
8.3 Variation of the backwall echo amplitude of one of the austenitic stainless steel test pieces used within this chapter. Each element of a 2 MHz 64-element array was used in isolation as a 0° pulse-echo compression wave transducer to measure the backwall response across the width of the austenitic stainless steel weld in a defect free region. Overlain on the plot is a scaled profile of the narrow gap weld profile showing that the region of significant signal attenuation occurs within the boundaries of the weld region. 158
8.4 Defect #1 array images in the $x-y$ plane. All the images are plotted on a decibel scale normalised to the maximum image amplitude from the defect response. All TFM and B-Scan images are plotted between 0 and -6 dB. A 9 mm aperture was used to generate the 2 MHz B-Scan image and an 18 mm aperture was used to generate the 1 MHz B-Scan image. The array in each case was located above the defects. 160
8.5 Defect #2 array images in the $x-y$ plane. All the images are plotted on a decibel scale normalised to the maximum image amplitude from the defect response. All TFM and B-Scan images are plotted between 0 and -6 dB. A 7.5 mm aperture was used to generate the 2 MHz B-Scan image and a 18 mm aperture was used to generate the 1 MHz B-Scan image. The array in each case was centred directly above the defects. The array in each case was located above the defects. 162
8.6 Defect #3 array images in the $x-y$ plane. All the images are plotted on a decibel scale normalised to the maximum image amplitude from the defect response. All TFM and B-Scan images are plotted between 0 and -6 dB. A 21 mm aperture was used to generate the 2 MHz B-Scan image and a 27 mm aperture was used to generate the 1 MHz B-Scan image. The array in each case was centred above the defects. 164
8.7 Defect #4 array images in the $x-y$ plane. All the images are plotted on a decibel scale normalised to the maximum image amplitude from the defect response. All TFM and B-Scan images are plotted between 0 and -6 dB. A 24 mm aperture was used to generate the 2 MHz B-Scan image and a 27 mm aperture was used to generate the 1 MHz B-Scan image. The array in each case was centred above the defects. 166

8.8 The imaging SNR methodology for Defect #1 within the austenitic stainless steel test pieces in the $x - y$ plane. Each image is plotted in an absolute amplitude scale with the array positioned directly above the defect indication. 167
8.9 a) MF-TR-MUSIC image of Defect #9 (LOIRF), b) MF-TR-MUSIC image of Defect #7 (LOSWF), c) eigenvalues of F at 2 MHz when imaging Defect #9 with the MF-TR-MUSIC algorithm, d) eigenvalues of F at 2 MHz when imaging Defect #1 (LOILF) with the MF-TR-MUSIC algorithm. The array was positioned directly above the defect indication and all images were in the $x - y$ plane. 169
8.10 Defect #5 TFM array images; the first column corresponds to images in the $x-y$ plane and the second column corresponds to images in the $y - z$ plane. All the images are plotted on a decibel scale normalised to the maximum image amplitude from the defect response. The array was positioned directly above the defect indication. 170
8.11 Defect #7 TFM array images using the 2 MHz 64-element array. The left image corresponds to images in the $x - y$ plane and the right image corresponds to images in the $y - z$ plane. All the images are plotted on a decibel scale normalised to the maximum image amplitude from the defect response. The array was positioned directly above the defect indication. 171
8.12 Defect #11 TFM array images; the first column corresponds to images in the $x - y$ plane and the second column corresponds to images in the $y - z$ plane. All the images are plotted on a decibel scale normalised to the maximum image amplitude from the defect response. The array was positioned directly above the defect indication. 172
8.13 Defect #12 TFM array images; the first column corresponds to images in the $x - y$ plane and the second image corresponds to images in the $y - z$ plane. All the images are plotted on a decibel scale normalised to the maximum image amplitude from the defect response. The array was positioned directly above the defect indication. 173

9.1 TFM, MF-TR-MUSIC and MF-FM images of a series of FE simulated 1.5 mm defects at a depth of 42 mm from a 64-element 2 MHz array located above the defects. The defects were offset from the array centreline by 5 mm (top row images), 15 mm (middle row images) and 25 mm (bottom row images). The same 2D FE modelling approach that was used in Section 3.2 was applied to these simulations. 182
9.2 The schematic for the dual array inspection of an embedded planar defect (black) FE model. An example weld profile is shown by the magenta dashed lines, with the locations of the array elements denoted by the red circles. An FMC dataset would be collected from both the individual 32-element arrays to obtain 64x64 A-Scans. From this FMC dataset, the TFM, MF-FM and MF-TR-MUSIC algorithms were applied and the resultant images were obtained. 184

List of Tables

3.1 The 2D smooth planar defect sizes modelled with FE. 73
3.2 Sizing performance of the algorithms for the 2 MHz 64-element array configuration. 77
3.3 Sizing performance of the algorithms for the 2 MHz 32-element array configuration. 78
3.4 The imaging SNR of the TFM and array B-Scan algorithms when varying levels of GWN were implemented. 96

4.1 Properties of the IMASONIC arrays used through the experimental trials within this thesis. 100
4.2 Planar defect parameters within the wire eroded test pieces. Manufacturing tolerances are also provided. 100
4.3 2 MHz 64-element array imaging algorithm sizing results for wire erosion test pieces. 105
4.4 The imaging SNR of the TFM and array B-Scan algorithms from the 2 MHz experimental images generated from the WE defects. 106
4.5 1 MHz 32-element array imaging algorithm sizing results for wire erosion test pieces. 111

5.1 The elliptical defects parameters located within the spark eroded test pieces. Manufacturing tolerances are also provided. Defect width is defined in the $\hat{x}$-axis and defect length is defined in the $\hat{z}$-axis, as shown in Fig. 5.1. 116
5.2 The 2 MHz 64-element array MF-FM sizing results for the spark eroded test pieces. No sizing results are presented for the defects with 1 mm widths due to the algorithm only generating single indications meaning tip indication based sizing could not be conducted. 122
5.3 The 2 MHz 64-element array MF-TR-MUSIC sizing results for the spark eroded test pieces. 122
5.4 The 2 MHz 64-element array TFM sizing results for the spark eroded test pieces. 122
5.5 The 2 MHz 64-element array B-Scan sizing results for the spark eroded test pieces. 123
5.6 The imaging SNR of the TFM and array B-Scan algorithms from the 2 MHz experimental images generated from the SE defects. 124

6.1 The rough defect cases investigated in this study, each with their corresponding parameters. A 0° inclination angle was defined to be parallel to the ultrasonic array. 129

6.2 The characterisation results for all smooth defect equivalent cases when applying all algorithms. 130
6.3 The average characterisation results for all rough defect classes when applying the MF-FM algorithm. Std means standard deviation. 138
6.4 The average characterisation results for all rough defect classes when applying the MF-TR-MUSIC algorithm. Std means standard deviation. 139
6.5 The average characterisation results for all rough defect classes when applying the TFM algorithm. Std means standard deviation. 139

7.1 Summary of the experimental volumetric defects imaged with the array algorithms. 148
7.2 Experimental sizing results for 2 mm diameter pore within ferritic steel component. 150

8.1 The embedded planar defect parameters within the narrow gap austenitic stainless steel welded test pieces. 157
8.2 The MF-TR-MUSIC width sizing results for LOILF defects within austenitic stainless steel weld test pieces using the 2 MHz and 1 MHz arrays. 161
8.3 The TFM sizing results for LOILF defects within austenitic stainless steel weld test pieces using the 2 MHz and 1 MHz arrays. 163
8.4 The array B-Scan sizing results for LOILF defects within austenitic stainless steel weld test pieces using the 2 MHz and 1 MHz arrays. All defect inclinations were recorded as 0°. 163
8.5 The imaging SNR of the TFM and array B-Scan algorithms from the LOILF defects when using a 2 MHz 64-element array. 165
8.6 The imaging SNR of the TFM and array B-Scan algorithms from the LOILF defects when using a 1 MHz 32-element array. 167

List of Acronyms

1D	**O**ne **D**imensional **F**or
2D	**T**wo **D**imensional **H**ere
3D	**T**hree **D**imensional **F**or
ALID	**A**bsorbing **L**ayers with **I**ncreased **D**amping
BF	**B**eam**f**orming
CPU	**C**entral **P**rocessing **U**nit
DTFM	**D**iffraction **T**otal **F**ocusing **M**ethod
FE	**F**inite **E**lement
FFT	**F**ast **F**ourier **T**ransform
FM	**F**actorisation **M**ethod
FMC	**F**ull **M**atrix **C**apture
GPU	**G**raphical **P**rocessing **U**nit
GTD	**G**eometrical **T**heory of **D**iffraction
GWN	**G**aussian **W**hite **N**oise
HSTFM	**H**alf **S**kip **T**otal **F**ocusing **M**ethod
ISO	**I**nternational **O**rganisation for **S**tandardisation
LOILF	**L**ack **O**f **I**nter-**L**ayer **F**usion
LOIRF	**L**ack **O**f **I**nter-**R**un **F**usion
LOSWF	**L**ack **O**f **S**ide-**W**all **F**usion
LSM	**L**inear **S**ampling **M**ethod
MF-FM	**M**ultiple **F**requency **F**actorisation **M**ethod
MF-TR-MUSIC	**M**ultiple **F**requency **T**ime **R**eversal **M**ultiple **Si**gnal **C**lassification
NDE	**N**on-**D**estructive **E**valuation
NSOM	**N**ear-field **S**canning **O**ptical **M**icroscopy
NSRP	**N**uclear **S**team **R**aising **P**lant
RMS	**R**oot-**M**ean-**S**quare
SAFT	**S**ynthetic **A**perture **F**ocusing **T**echnique
SDH	**S**ide **D**rilled **H**ole
SE	**S**park **E**roded
SNR	**S**ignal-to-**N**oise **R**atio
SR	**S**uper **R**esolution
SVD	**S**ingular **V**alue **D**ecomposition
TFM	**T**otal **F**ocusing **M**ethod
TOFD	**T**ime-**O**f-**F**light **D**iffraction
TR-MUSIC	**T**ime **R**eversal **M**ultiple **Si**gnal **C**lassification
TWH	**T**hrough-**W**all **H**eight
WE	**W**ire **E**roded

Chapter 1

Introduction

1.1 Ultrasonic Non-Destructive Evaluation

Non-Destructive Evaluation (NDE) is a vital tool crucial to the engineering industry where insuring component integrity, minimising production time and increasing the effectiveness of post-manufacture maintenance are paramount. NDE is so widely used because it offers the unique benefit of inspecting the internals of components for any defects such as cracks or corrosion, which pose a safety risk, and characterise their physical parameters to assess the threat they pose, all whilst causing no damage. The alternative to NDE would be to destructively inspect the component, e.g. section and analyse, but as expected the component is no longer fit for purpose after inspection. A huge range of different NDE methodologies have been developed including electromagnetic testing, visual inspection, dye penetrant testing, magnetic particle inspection, radiography and ultrasonic testing [1].

Ultrasonic testing is one of the most common modes of NDE applied within both the engineering and medical sectors [2]. This method works on the principle of exciting high frequency ultrasonic waves with transducers which are then transmitted into the specimen of interest. Most ultrasonic transducers are able to generate ultrasonic waves by means of the piezoelectric effect, which is a reversible process, first observed by Jacques and Pierre Curie in 1880 [3], where the application of an external electric field on a piezoelectric crystal results in an internal mechanical strain. The ultrasonic waves are propagated through the specimen and reflections due to defects or component geometry result in scattered waves being received back at the ultrasonic crystal. These scattered ultrasonic waves generate mechanical compressional forces on the piezoelectric crystal which in turn generate a measured voltage response over time. These time-domain voltage signal, known as A-Scans, are used to infer the state of the component.

The mechanism for the piezoelectric effect is shown in Fig. 1.1. For the purpose of embedded defect detection, any defects which represents a discontinuity of the material properties result in a reflection of the incident ultrasonic wave at that position. This defect reflection would be received earlier in time compared to later reflections of the component geometry, such as a back-wall, indicating that an unwanted discontinuity is present within the specimen.

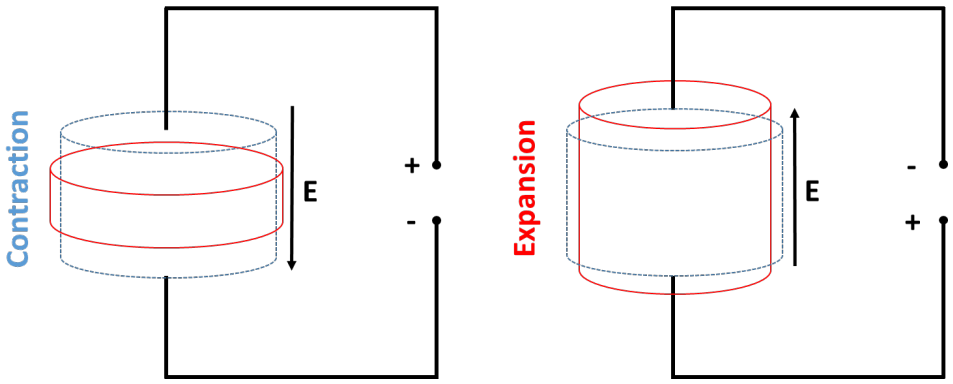


Figure 1.1: Illustration of the converse piezoelectric effect mechanism. The application of an external electric field, E, to a piezoelectric crystal can lead to its expansion and contraction from its original shape (dashed blue outline). It is this effect which is used to mechanically drive piezoelectric transducer crystals in the generation of ultrasound. This effect is reversible and consequently mechanical forces applied to a piezoelectric crystal leads to the generation of a voltage across it; this effect is used on reception of ultrasound to record a voltage time history, or A-Scan.

Conventional ultrasonic probes are used to interrogate the volume of components by typically raster scanning across the component surfaces, where the A-Scan data from each encoded probe position can be manipulated to generate a variety of images. A common way to visualise the ultrasonic data is to stack the individual A-Scans from a given raster scan line to create a two-dimensional (2D) B-Scan image [4]. An illustration of a typical ultrasonic inspection and the subsequently generated A-Scans and B-Scans is shown in Fig. 1.2. The approach of producing a B-scan can be extended to generate a C-scan [5] where individual B-Scans are stacked and usually a single parameter such as maximum amplitude is extracted from each A-Scan to create a 2D plan view image. A D-Scan is similar to a C-Scan except the imaging parameter, usually maximum amplitude, is taken across the cross-section of the component [6]. These ultrasonic imaging techniques are widely used within industry and are important tools to detect defects, characterise their morphology (e.g differentiate between planar and volumetric flaws) and estimate their size.

The advent of ultrasonic phased arrays has been a large focus of recent ultrasonic NDE research due to their potential to significantly increase inspection quality and reduce inspection times. Ultrasonic phased arrays consist of a series of individual transducer elements which can be used in isolation or combination to allow for a variety of different applications. Individual time delay laws can be applied arbitrarily to the separate elements which enables a large range of angled plane beams to be generated from a single array probe which conventionally would only be achievable by using a series of fixed angled probes. An illustration of how delay laws can be applied to a linear array configuration to manipulate the ultrasonic beam it produces is shown in Fig. 1.3. The usage of delay laws also allows focusing of the ultrasonic waves at different areas of components resulting

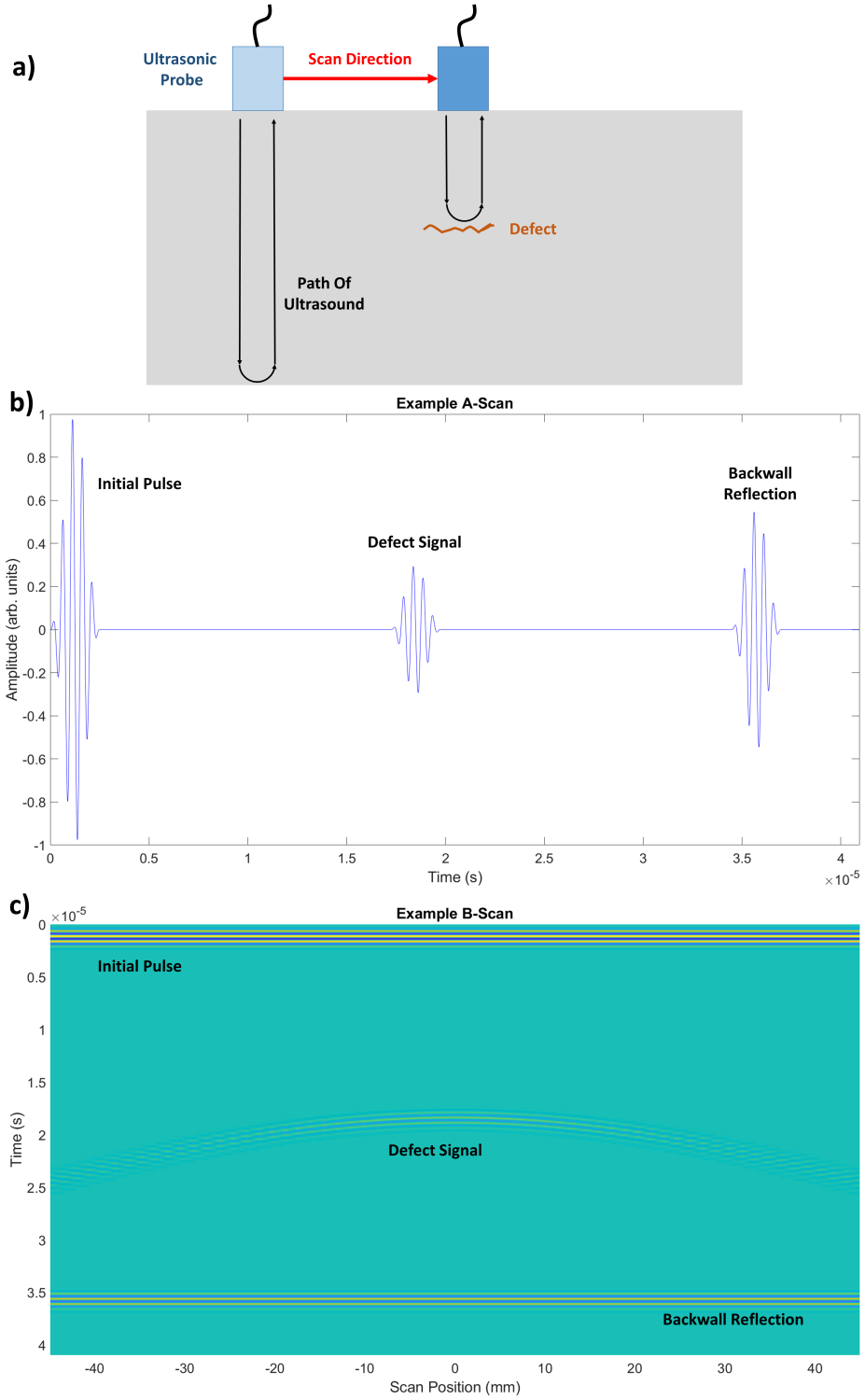


Figure 1.2: a) Schematic of an example ultrasonic NDE scan of a component containing an embedded defect, b) an example A-Scan that may be measured by the transducer when placed over the defect, c) an example B-Scan that may be generated from the various scan points along the component surface.

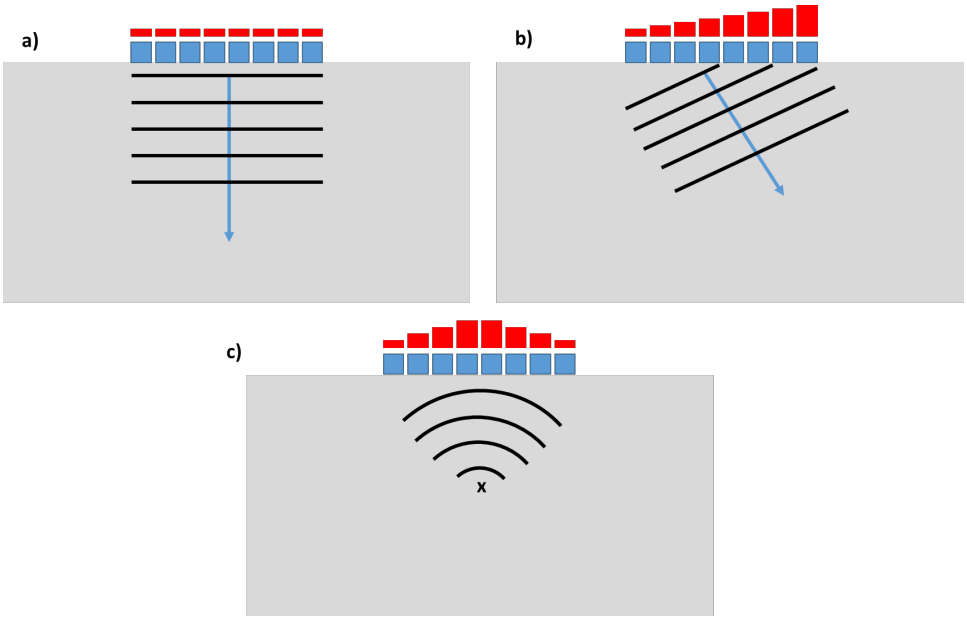


Figure 1.3: Illustration of how delay laws of varying magnitude (red) can be applied to the elements of a linear ultrasonic array (blue) to generate: a) a plane 0° wave when equal or no delay laws are applied, b) an angled plane wave when delay laws of linearly increasing magnitude are applied sequentially across the array elements, c) a focused beam where the delay laws are used to direct the energy of the array to a single point within the component.

in a greater sensitivity compared to unfocussed plane beams. A key advantage of ultrasonic arrays is the high flexibility of the probe to generate a huge variety of ultrasonic beam profiles by simply manipulating the elemental delay laws. This is in contrast to fixed-focus single crystal probes which although effectively direct ultrasound in the prescribed direction and depth, they cannot be used to inspect other parts of a component. This means a large range of fixed-focus probes are required to allow the necessary inspection coverage of components whereas a single phased array could potentially be used to achieve the same coverage requirements. Ultrasonic phased arrays can therefore be used to generate commonly used conventional imaging methods such plane, focussed and sectoral B-Scans [7, 8], and therefore C-Scans and D-Scans. This versatility in operation of phased array probes makes the technology highly attractive to industry as an alternative to conventional probe scanning as their usage could result in reduced inspection costs, by removing the need to procure the numerous single crystal probes required, as well as reducing the inspection scan time.

The most common array configuration used for NDE applications are linear one-dimensional (1D) arrays which allow imaging in a single plane, however 2D matrix arrays and annular arrays exist which allow more complex delay laws to be applied to image in multiple planes. These common array geometries are illustrated in Fig. 1.4.

The ability to focus ultrasonic waves with arrays has led to the development of several Beamforming (BF) imaging techniques. These all operate

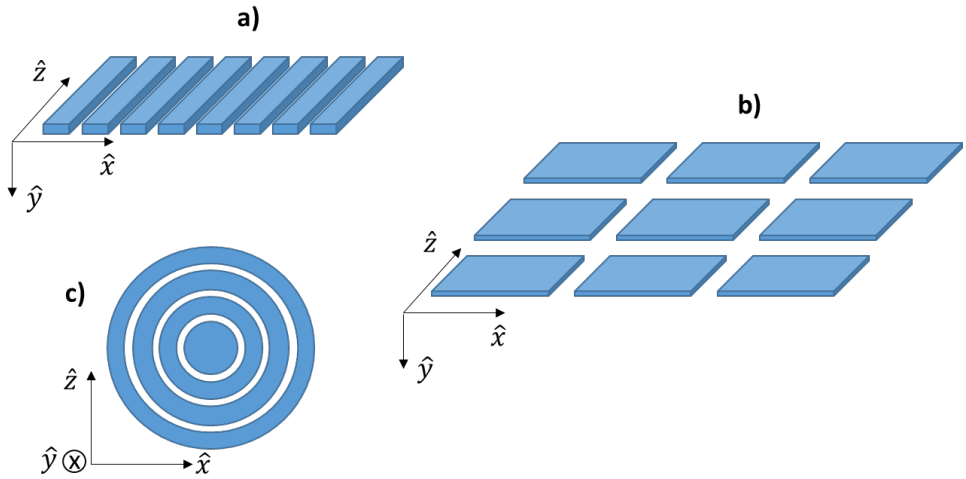


Figure 1.4: Common array geometries: a) 1D linear array, b) 2D matrix array, c) annular array.

by focusing the ultrasonic energy via delay law beam steering along a section of the component, measuring the received backscattered energy from each imaging focal point and visualising the amplitudes as a 2D image.

The method of focusing can be conducted electronically by the array during data acquisition but it can equally be conducted in post-processing through a technique called Full Matrix Capture (FMC) [8]. FMC data acquisition collects all the different send-receive combinations between each of the individual elements within the array [9, 10], as illustrated in Fig. 1.5.

The FMC data represents the maximum amount of ultrasonic information which can be collected from a given phased array, with the only assumption being that the wavefield is linear. If the wavefield exhibits non-linearity, such as in the case of the complex behaviour of ultrasonic waves interacting with partially closed cracks [11, 12], the case of individually exciting elements through FMC is not strictly equivalent to firing on multiple elements to recreate the same focussing. This is due to the fact that when firing multiple elements at once, the elastic wave amplitude at the focal point is significantly greater than that can be generated by a single array element and in cases such as partially closed cracks, the additional non-linear effects they can exhibit increase due to the increased local amplitude [13]. However in the majority of commonly encountered inspection cases, these effects can be assumed to be negligible and FMC datasets can indeed be considered to be the total information from the specific array system. As such, almost any imaging algorithm can be executed upon FMC data in post-processing. This does not only allow a large amount of flexibility in NDE data analysis and interpretation, as all conventional phased array imaging techniques could be applied to the FMC datasets, it also enabled the development of new BF imaging algorithms which offered significant benefits over the conventional methods. Several of these array BF algorithms were the Synthetic Aperture Focusing Technique (SAFT) [14] and the Total Focusing Method (TFM) [8, 15]; these can be applied to FMC datasets. These algorithms are highly robust and sensitive imaging tools among which the TFM algorithm, which will be discussed in more detail within Chapter 2, is considered by

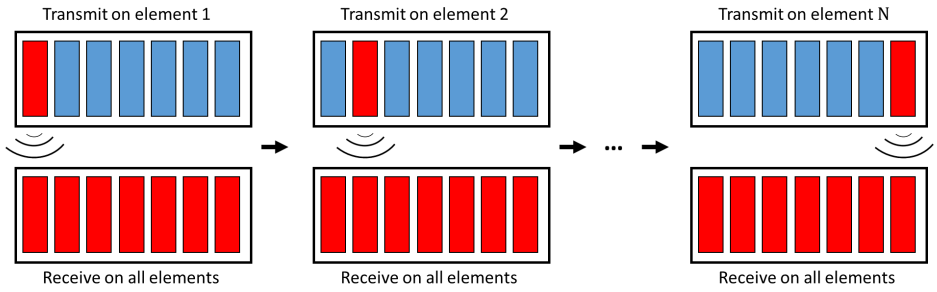


Figure 1.5: The array element excitation procedure for Full Matrix Capture data acquisition with a linear array.

many as the benchmark for array imaging within academia as it is able to provide a high defect detection and sizing capability [8, 16]. Despite the numerous improvements made with these new algorithms, they are still inherently limited in their resolution. This will be explained in further detail in the next section.

1.2 Industrial Motivations

In the verification of the structural integrity of safety-critical components in the nuclear power industry, there is a drive to detect and size increasingly smaller defects during manufacture as the requirements for critical defect sizes decrease. Above the critical defect size threshold, the component must be repaired or retired. There are multiple factors which influence this trend. One factor to drive the accurate detection and sizing of smaller defects is part of an effort to extend component life by using estimates of defect growth. If a smaller defect can reliably be sized during a manufacturer inspection or in-service inspection, conventional conservative estimates of defect growth means the component can remain in service longer before a repair/replace threshold is met. From the perspective of current in-service ageing Nuclear Steam Raising Plants (NSRPs) in the defence and power sectors, accurately characterising and sizing these smaller defects enables their lifecycles to be extended for as long as possible to maximise both the operational and financial benefits. In addition, by justifying a larger proportion of the component as defect-free of a smaller critical defect size, the subsequent lengthened component life predictions could be used to justify increased time interval between component inspections which again could save an enormous amount of expenditure. Another driving factor to develop a higher fidelity inspection capability is to bolster the component safety case which would act to provide additional confidence to industry regulators of the continued safe operation of the NSRPs.

The challenge created by this trend in performance-based NDE requirements is that the spatial resolution of ultrasonic inspections cannot be easily increased to suit the smaller defect sizes as the resolution is largely fixed by the frequency of transducers. All conventional probe and BF array techniques are naturally restricted by the diffraction limit and therefore cannot achieve a higher resolution than half the ultrasonic wavelength [17]. In an

ideal scenario, the inspection frequency would be set to the highest possible value to minimise the ultrasonic wavelength and to therefore maximise the spatial resolution which can be achieved. However, the frequency cannot be indefinitely increased as undesirable effects such as material noise also increase with ultrasonic frequency, so a compromise must be reached to balance resolution and minimise these unwanted effects. As the size of defects decreases towards the diffraction limit and the resolution of the ultrasonic inspection remains similar, the variance in response between different sized small planar defects reduces. Also, the response between small planar and volumetric flaws tend to one another. It is in this defect scale that the conventional ultrasonic NDE approaches currently employed to size and characterise defects become ineffective.

The concept of overcoming the diffraction limit and achieving a 'Super Resolution (SR)' capability has been explored in the field of optical microscopy, first suggested by Synge in 1928 [18] and experimentally observed by Ash and Nicholls in 1972 [19]. The potential of SR is based on the concept of *evanescent waves* which are able to carry subwavelength information about the structure within their vacinity. These waves however decay exponentially from their generation surface and therefore are non-propagating, which means one cannot remotely detect them in conventional measurement set-ups. Early SR microscopy methods utilised a subwavelength aperture to generate evanescent waves which would interact with the imaging target. This imaging target was located within the near field of the aperture (one wavelength) allowing sub-wavelength information to be exchanged before the evanescent waves completely decayed.

This concept was further developed through techniques such as Near-Field Scanning Optical Microscopy (NSOM) to achieve resolutions on the order of $\lambda/40$ [20, 21, 22] and better. NSOM can be operated in several modes to try and extract the subwavelength information contained within evanescent waves [23]: illumination mode, collection mode and apertureless technique. These modes are illustrated in Fig. 1.6. Illumination mode NSOM works as previously described where a subwavelength aperture is located within the near-field of the inspecting surface which allows for surface interrogation with evanescent waves. The interaction of the evanescent waves with the sample surface leads to a degree of mode conversion into propagating waves (containing the subwavelength SR information) which are able to be detected in the far-field. Collection mode NSOM is the reciprocal process where a far-field source is used to interrogate the sample surface with propagating waves, part of which are mode converted into evanescent waves, and a near-field located receiving aperture is able to receive them. Apertureless NSOM uses both a far-field source and receiver. This method, however, relies on a subwavelength tip being placed in the near-field of the sample surface allowing scattered evanescent waves to be mode converted into propagating waves which can then be measured in the far-field. All SR optical microscopic methods therefore rely on some part of the imaging system to be located within the near-field of the scatterer of interest to be able to extract the subwavelength information from the evanescent waves.

The challenge of achieving a SR capability in ultrasonic NDE is that in the

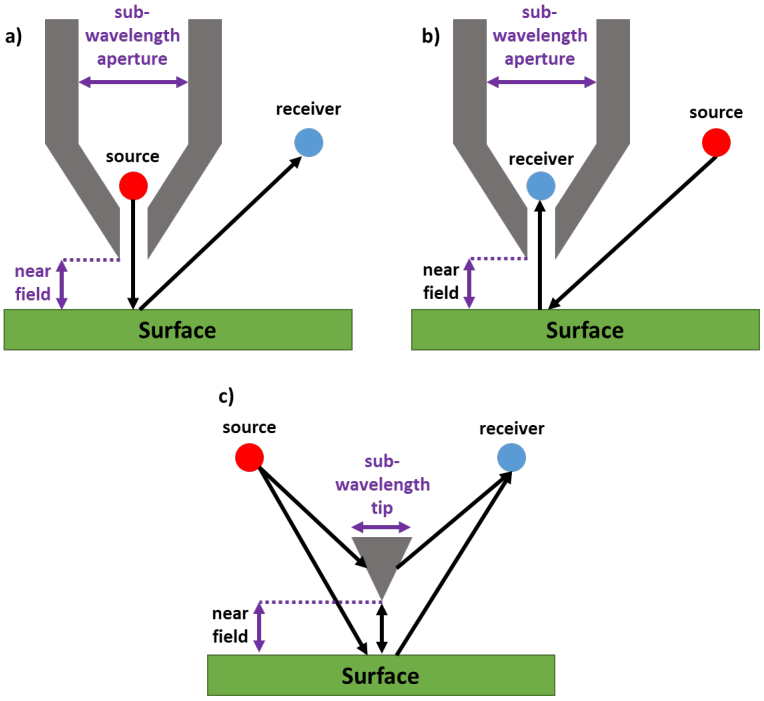


Figure 1.6: The schematic for the operation of NSOM. The arrows represent the wave paths through space between the source, receiver and surface of interest. The three main modes of NSOM are shown; a) illumination mode, b) collection mode, and c) apertureless mode.

vast majority of cases, no part of the inspection system is able to be positioned within the near-field of the scatterers of interest, completely restricting the system to far-field measurements only. If the inspection system cannot be placed within the near-field to directly measure the evanescent waves, the alternative option is for the evanescent waves to be scattered and mode converted to propagating waves to then be received by the system (similar to apertureless NSOM described above). This mechanism would therefore rely on multiple scattering. Conventional imaging algorithms however are under the constraints of the Born approximation [24, 25], which is a single scattering framework. The Born approximation therefore does not allow the wave scattering interaction between scatterers or self-interaction necessary for evanescent waves to be mode converted into propagating waves in order for subwavelength information to be measured in the far-field.

Several approaches to analysing FMC data have been developed over recent years and they have demonstrated a capability to achieve a resolution beyond the diffraction limit. A group of these algorithms, called sampling methods, are non-iterative methods to tackle the inverse scattering problem in an attempt to approximate the profile of a scattering defect [26, 27, 28, 29]. These methods are reliant on the effects of multiple scattering [30, 31] to unlock a resolution capability unreachable for the BF techniques, which are valid under the Born approximation. Two such algorithms are the Factorisation Method (FM) and the Time Reversal Multiple Signal Classification (TR-MUSIC) algorithm. Each works by determining whether an imaging

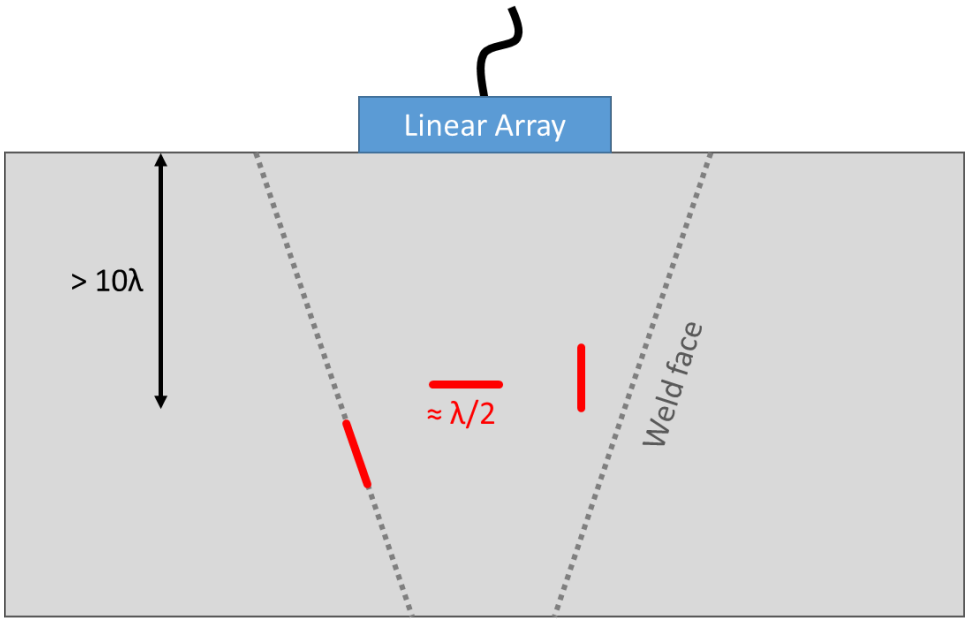


Figure 1.7: The schematic for general inspection cases considered in this thesis. It considers the linear array inspection of a thick-walled stainless steel component contained embedded planar defects of size on the order of $\lambda/2$ at depths greater than 10λ. These components may or may not contain a weld and the defects considered can have varying orientations.

pixel point corresponds to a location within the boundary of the scatterer by comparing the scattered field to a specified criterion. The SR capability of these algorithms has been demonstrated in NDE scenarios previously for a limited set of simple defects [30, 32] and more recently with some examples of their use in conjunction with limited aperture linear arrays [33, 34, 35, 36]. It has been shown that these SR algorithms can be more sensitive to a range of factors, such as signal noise and array configuration, compared to conventional array imaging methods such as TFM [37]. This means that some of the commonly encountered industry inspection geometries and challenges may potentially restrict the wider application of SR.

The general inspection scenario considered within this thesis is that of thick-walled, large diameter stainless steel pipework common to NSRPs. In this work, these geometries were simplified to that of flat-plates due to the slowly varying curvature of these component profiles. Planar embedded defect sizes on the order of the diffraction limit (half the ultrasonic wavelength) are considered of varying orientations and positions within the components to mimic the various expected manufacturing flaws commonly encountered within the industry. These specific morphologies will be discussed in more detail within subsequent chapters of this thesis. A schematic of this inspection case is illustrated in Fig. 1.7 showing a linear phased array inspecting a flat plate geometry component, containing a variety of embedded planar defect orientations.

The current approach to NDE inspections of this type is to apply a multitude of specialised single and dual crystal ultrasonic probes, with varying

incidence angle, focal depths and often ultrasonic frequency. This is to ensure that as close to complete component coverage is obtained and that the maximum opportunity for defect detection and sizing is fulfilled. However, this approach can have several disadvantages including the high cost of the probe inventory required, the often large number of scans necessary due to the numerous probes specified and redundancy in data between the various scans. Some of these problems are slowly being alleviated by moving towards phased array inspection techniques, where single arrays are capable of replicating the various inspection angles and focusing specified by the conventional probe techniques. Both the conventional probe and phased array techniques, however, are still fundamentally limited in resolution by the diffraction limit, which often is a highly optimistic capability in itself, meaning that the very smallest of defects are still a significant challenge to NDE inspections.

The aim of this thesis is to develop ultrasonic array imaging technologies for these inspection scenarios that meet the increasingly demanding NDE requirements to characterise smaller embedded planar defect sizes. As a means to achieve this, the SR array imaging algorithms are utilised and applied in post-processing to FMC datasets collected with linear phased arrays. Defect sizing and characterisation methodologies were developed for these techniques and their imaging performance will be compared against BF algorithms.

1.3 Outline of Thesis

In this thesis, the sizing and characterisation performance of advanced ultrasonic array imaging algorithms are investigated for the case of embedded defects.

In Chapter 2, the forward and inverse scattering problems are explained. The forward scattering problem consists of determining the scattered wave field from an object, given information about its structure and the initial incident wave field. This scenario is mathematically well-posed and several analytical solutions exist for specific cases. The inverse scattering, or imaging problem, aims to find the scattering object's structure given knowledge of the scattered and incident wave fields. This problem is mathematically ill-posed and therefore difficult to find a solution. Several approaches exist to attempt to solve the inverse scattering problem, from which so-called Super Resolution (SR) imaging algorithms have been developed. These SR methods alongside classical BF techniques are discussed as well as the origin for the capability of the SR methods to break the diffraction limit of $\lambda/2$.

Chapter 3 considers the practical NDE performance of the Multiple Frequency Factorisation Method (MF-FM) and Multiple Frequency Time Reversal Multiple Signal Classification (MF-TR-MUSIC) algorithms and compares them to the conventional TFM and 0° array B-Scan algorithms for the inspection of planar embedded defects. Two-dimensional (2D) Finite Element (FE) simulations were used to consider the effect of varying planar defect width and orientation on the accuracy of SR imaging performance up to defects as small as $\lambda/3$. Within this Chapter, a non-dimensional trend was

observed between the SR image indication patterns and the defect width relative to the ultrasonic wavelength. This may be used as a fast additional tool to gauge information about embedded scatterers without undertaking in-depth image analysis. The impact of incoherent noise on SR imaging is also investigated as it is known that these inverse methods can be sensitive to factors such as noise compared to classical imaging techniques.

Experimental validation of the simulation results are considered in Chapters 4 & 5. Within Chapter 4, pseudo-2D embedded planar defects are experimentally imaged using two different frequency arrays to validate the observed excellent simulated sizing and orientation estimation capability detailed in Chapter 3. The non-dimensional trend between the defect indication pattern and defect size is also experimentally validated for two inspection frequencies and multiple defect sizes. The experimental trials are extended to consider three-dimensional (3D) embedded planar elliptical flaws in Chapter 5 where a new methodology to process scanned FMC datasets with the SR algorithms is introduced. It is found that sub-diffraction limit resolutions are achievable with the MF-TR-MUSIC algorithms for the 3D planar elliptical defects and that the methods could be applied to realistic defect morphologies.

Within Chapter 6, the impact of defect roughness on SR imaging is considered for the first time. Common defect growth mechanisms within the nuclear industry are known to produce defects with significant surface roughness and it is understood that roughness can have a major impact on ultrasonic defect detection and characterisation. A 2D FE Monte Carlo study was conducted and it considered varying defect parameters including size, orientation and roughness parameters. It was found that the SR algorithms were able to retain the majority of their sizing performance for sub-wavelength defects even when typical industrially observed roughnesses were applied. Both the MF-FM and MF-TR-MUSIC algorithms were able to outperform the TFM for these sub-wavelength rough defect cases.

The applicability of the SR algorithms to size embedded volumetric defects is considered in Chapter 7. Traditional, radiographic NDE techniques were used within industry to size volumetric defects due to the inability of conventional ultrasonic methods to estimate volumetric defect profiles. Radiographic methods are more time consuming and expensive to apply in practice compared to ultrasonic methods so developing a way to reduce the requirement for them would add significant benefit to many industrial NDE scenarios. Within this Chapter, both FE numerical studies and experimental trials are conducted on side-drill hole geometries and it was found that the MF-FM and MF-TR-MUSIC could be used to directly size these volumetric defects. The MF-TR-MUSIC algorithm was also used to size a realistic 3D volumetric pore within a ferritic steel test piece.

The final investigatory aspect of this thesis considers the applicability of the SR algorithms for defect characterisation within austenitic stainless steel welded components in Chapter 8. Austenitic stainless steels are common manufacturing materials within the nuclear sector because of their highly desirable material properties. However when austenitic stainless steels are welded they can exhibit an anisotropic and coarse grained structure that can significantly hinder the quality of ultrasonic inspections. Therefore,

their NDE poses a significant challenge to the nuclear industry. The inspection performance of the SR and TFM algorithms were assessed when used to detect and size embedded defects within narrow gap welded austenitic stainless steel test pieces.

The conclusions and main contributions of this thesis are summarised in Chapter 9.

Chapter 2

Background Theory

2.1 Introduction

In this chapter, the theoretical background for the acoustic scattering problem is discussed as well as the mathematical framework for the imaging algorithms explored in this thesis. Information about the scatterer is encoded within the measured scattered field from ultrasonic inspection and the process of imaging attempts to decode this information to reconstruct its profile. This Chapter will first consider the *forward scattering problem* where a scatterer's profile is used to estimate the resultant total scattered wave field, as well as the *inverse scattering problem* where information about the measured wave field is used to reconstruct the scatterer structure.

The forward scattering operation maps the properties of the scatterers within the system to the total wave field, comprised of both the incident and scattered fields. In the case of no scatterer being present, the measured total field would exactly equal the incident field. In the case of scatterers, the measured total field would comprise of the sum of both the incident field and the scattered field component. The forward scattering problem is well-posed [38], meaning that there exists a unique and stable solution for mapping scatterers to the total wave field [39] and in many cases, an exact analytical solution exists. The inverse scattering problem, also known as the imaging problem, attempts to map the measured total wave field back to the scatterers. This problem is ill-posed [39] and non-linear meaning that most solutions to the problem are only approximate and their results can vary significantly.

The mathematical basis of the TFM method is introduced in this chapter and its inherent resolution limit is explained. Following this the SR algorithms considered in this thesis are introduced, which are linear sampling methods aimed to solve the *inverse scattering problem*, and their capability to go beyond the conventional diffraction limit is explained.

2.2 Governing Equations

In this Section, the governing equations for acoustic wave scattering are described which form the basis of the forward scattering problem. The acoustic wave description can be used to describe the propagation of longitudinal waves and this framework is used for simplicity due to the significant additional complexity introduced by considering the full elastic problem and

the fact that the main concepts can be demonstrated using the acoustic solution [40, 41].

To begin the description of the behaviour of acoustic waves, one must start with the wave equation in homogeneous media [40]:

$$\nabla^2\Phi = \frac{1}{c^2}\frac{\partial\Phi}{\partial t^2}, \tag{2.1}$$

where ∇^2 is the Laplace operator, c is the sound speed and Φ is the wave potential, which is a function of both space, $\mathbf{r}$, and time, t.

Eq. (2.1) can be solved by assuming that the wave potential is separable into two independent functions of space and time, $\phi(\mathbf{r})$ and $T(t)$, as:

$$\Phi(\mathbf{r}, t) = \phi(\mathbf{r})T(t). \tag{2.2}$$

One can substitute Eq. (2.2) into Eq. (2.1) leading to the expression:

$$\frac{\nabla^2\phi}{\phi} = \frac{1}{c^2T}\frac{\partial T^2}{\partial t^2}. \tag{2.3}$$

As the Left-Hand Side (LHS) is only dependent on $\mathbf{r}$, and the Right-Hand Side (RHS) is dependent only on t, both sides must be equal to a constant. For convenience, this constant is set to $-k^2$, where k is the wavenumber ($k = \frac{2\pi f}{c}$ where f is the wave frequency). By considering the LHS of Eq. (2.3), the homogeneous Helmholtz equation can be immediately found:

$$(\nabla^2 + k^2)\phi(\mathbf{r}) = 0. \tag{2.4}$$

The simplest solution to the Helmholtz equation is that of a plane wave:

$$\phi(\mathbf{r}) = Ae^{i(k\mathbf{r}-wt)} + Be^{i(k\mathbf{r}+\omega t)}, \tag{2.5}$$

where ω is the angular frequency ($\omega = 2\pi f$) and A and B are complex amplitudes associated with the outwardly (1^{st} term on RHS) and inwardly (2^{nd} term on RHS) propagating solutions.

As the homogeneous Helmholtz equation considers only constant material properties, no scattering can occur and therefore this approach cannot be used to model practical ultrasonic NDE. In realistic inspection scenarios, materials are not mathematically ideal and often inhomogeneities are normally present. The forward scattering problem attempts to map these inhomogeneities to the scattered field. The inhomogeneous Helmholtz equation can be used to describe scattering of monochromatic waves from wave-penetrable inhomogeneities:

$$(\nabla^2 + k_0^2)\phi(\mathbf{r}, \omega) = -\mathcal{O}(\mathbf{r}, \omega)\phi(\mathbf{r}, \omega), \tag{2.6}$$

where k_0 is the wavenumber in the background homogeneous medium and $\mathcal{O}(\mathbf{r}, \omega)$ is called the object function and characterises the inhomogeneities interaction with the wave field. The object function describes a scatterer

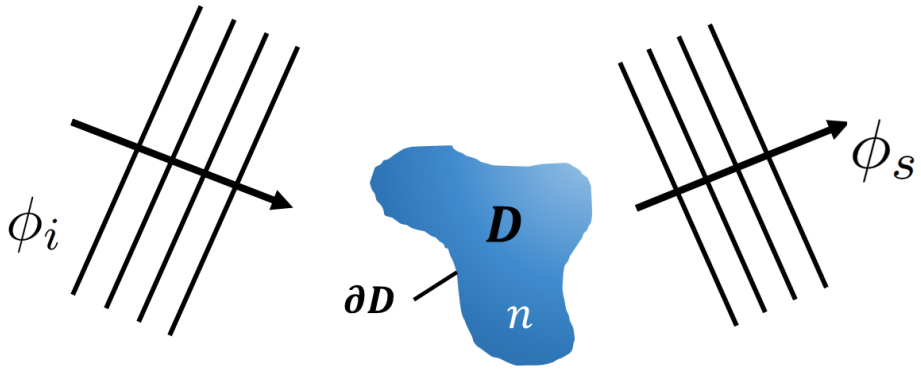


Figure 2.1: The concept of wave scattering of an initial wave, ϕ_i, by an object D with boundary ∂D, resulting in a scattered wave, ϕ_s. The object D has a refractive index of n.

with support D with a wavenumber of k. $\mathcal{O}$ is defined within D to be [41]:

$$\mathcal{O}(\mathbf{r},\omega) = k_0^2\left[\rho(\mathbf{r})\kappa(\mathbf{r})c_0^2 - 1\right] = k_0^2\left[n^2(\mathbf{r}) - 1\right], \tag{2.7}$$

where c_0 is the wave speed in the background medium, ρ, κ and n are the inhomogeneity density, compressibility and refractive index respectively.

The total wave field can be decomposed into the incident field, ϕ_i, and scattered field, ϕ_s, as follows:

$$\phi = \phi_i + \phi_s, \tag{2.8}$$

and as the incident field satisfies Eq. (2.4), Eq. (2.6) can be rewritten as:

$$(\nabla^2 + k_0^2)\phi_s(\mathbf{r},\omega) = -\mathcal{O}(\mathbf{r},\omega)\phi(\mathbf{r},\omega), \tag{2.9}$$

where ϕ_s is the scattered wave. The concept of this wave scattering is illustrated in Fig. 2.1.

In order to solve Eq. (2.6), Green's function, G, is introduced [40]. It is applied when considering inhomogeneous differential equations, such as the inhomogeneous Helmholtz equation. Green's function is defined as the impulse response to such equations, meaning when operated on by any linear differential operator, it returns the Dirac delta function, δ. Green's function is a solution to the Helmholtz equation of the form:

$$(\nabla^2 + k^2)G(\mathbf{r},\mathbf{r}_0) = \delta(\mathbf{r} - \mathbf{r}_0). \tag{2.10}$$

The analytical solutions to Eq. (2.10) in 2D and 3D are given by [40]:

$$G_{2D}(\mathbf{r},\mathbf{r}_0) = -\frac{i}{4}H_0^1(kr), \tag{2.11}$$

$$G_{3D}(\mathbf{r},\mathbf{r}_0) = \frac{e^{ikr}}{4\pi r}, \tag{2.12}$$

where H_0^1 is the zeroth order Hankel function of the first kind and $r = |\mathbf{r} - \mathbf{r}_0|$ is the distance from the source to measurement location. These both

correspond to point sources with unit amplitude. Hankel functions are solutions to 2D Bessel differential equations and are a re-writing of the wave equation in polar coordinates. They are expressed as [42]:

$$H_\alpha^1(x) = J_\alpha(x) + iY_\alpha(x), \tag{2.13}$$

$$H_\alpha^2(x) = J_\alpha(x) - iY_\alpha(x), \tag{2.14}$$

where H_α^1 is the Hankel function of order α of the first kind, corresponding to an outwardly propagating wave, and H_α^2 is the Hankel function of order α of the second kind, corresponding to an inwardly propagating wave. J_α and Y_α are Bessel functions of the first and second kind of order α respectively.

In practice, one cannot excite and measure the wave fields at every point in space, but rather at a set of discrete points in the far-field of the scatterer (i.e. phased array element locations). Eq. (2.11) can be simplified when considering the 2D far field limit ($r \to \infty$) as it converges to the asymptotic form [42]:

$$G_\infty(\hat{\mathbf{r}}, \mathbf{r}_0) = -\frac{e^{i(kr+\frac{\pi}{4})}}{\sqrt{8\pi kr}}. \tag{2.15}$$

It should be noted that while this is an asymptotic approximation, it is a very good approximation when used at least one wavelength from the source.

Eq. (2.10) is a very important relation because when realising a scattering source can be modelled as a sum of Dirac delta functions, the solution is also a sum of Green's functions. This exploits the linearity of the Helmholtz equation. This concept is expressed mathematically through the convolution of G with a source term and can equally be applied to the scatterer's object function returning the solution to Eq. (2.6) [43]:

$$\phi_s(\mathbf{r}, \omega) = \int_V G(\mathbf{r}, \mathbf{r}')\mathcal{O}(\mathbf{r}', \omega)\phi(\mathbf{r}', \omega)d\mathbf{r}', \tag{2.16}$$

where $\mathbf{r'}$ is a position within the inhomogeneity and V is the inhomogeneity volume.

Thus one can arrive at the expression for the total wave field:

$$\phi(\mathbf{r}, \omega) = \phi_i(\mathbf{r}, \omega) - k_0^2 \int_V G(\mathbf{r}, \mathbf{r}')\mathcal{O}(\mathbf{r}', \omega)\phi(\mathbf{r}', \omega)d\mathbf{r}', \tag{2.17}$$

where ϕ_i is the incident wave field. This is known as the Lippmann-Schwinger equation and states that the scattered field can be constructed from the superposition of infinitely small point sources distributed across the inhomogeneity volume V [44].

By ignoring the time dependence and writing G as a plane wave of the form $e^{ik_0\hat{\mathbf{r}_0}\cdot\mathbf{r}}$, where $\hat{\mathbf{r}_0}$ is the plane wave propagation direction, taking the far-field limit ($r \to \infty$) and applying the asymptotic relation in Eq. (2.15),

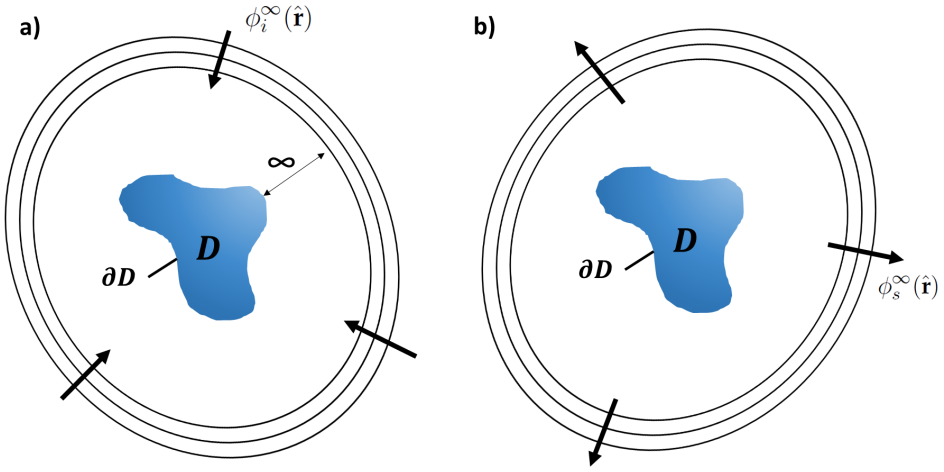


Figure 2.2: An illustration of the far-field scattering problem. a) a far-field incident from an infinite distance (figure not to scale) $\phi_i^\infty(\hat{\mathbf{r}})$ illuminating the scatterer D with boundary ∂D, b) the incident wave on scatterer D generates a new scattered wave field $\phi_s^\infty(\hat{\mathbf{r}})$ measured in the far-field.

Eq. (2.17) in 2D can be reduced to:

$$\phi(\mathbf{r}, k_0\hat{\mathbf{r}_0}) = e^{ik_0\hat{\mathbf{r}_0}\cdot\mathbf{r}} + \Pi f(k_0\hat{\mathbf{r}}, k_0\hat{\mathbf{r}_0})\frac{e^{ik_0 r}}{\sqrt{r}}, \text{where } \Pi = \frac{k_0^2 e^{i(\frac{\pi}{4}+k_0)}}{\sqrt{8\pi k_0}}, \tag{2.18}$$

and where $f(k_0\hat{\mathbf{r}}, k_0\hat{\mathbf{r}_0})$, termed the scattering amplitude, is given by:

$$f(k_0\hat{\mathbf{r}}, k_0\hat{\mathbf{r}_0}) = \int_D \mathcal{O}(\mathbf{r}')\phi(\mathbf{r}', \hat{\mathbf{r}_0})e^{-ik_0\hat{\mathbf{r}}\cdot\mathbf{r}'}d\mathbf{r}', \tag{2.19}$$

where D is the 2D closed surface of the scatterer. The scattering amplitude corresponds to the complex amplitude of a scattering wave in direction $\hat{\mathbf{r}}$ as a result of an incident wave in direction $\mathbf{r}_0$

Therefore the far-field scattered wave field, ϕ_s^∞, which is the only component of the scattered field which can be measured in practical NDE, can be written as:

$$\phi_s^\infty(\hat{\mathbf{r}}, k_0) = -k_0^2 \int_D \mathcal{O}(\mathbf{r}')\phi(\mathbf{r}', \hat{\mathbf{r}_0})G_\infty(\mathbf{r}, \mathbf{r}')d\mathbf{r}'. \tag{2.20}$$

In a similar way, the incident near-field locally around D, $\phi_i(\mathbf{r})$, can be calculated from the far-field incident wave, $\phi_i^\infty(\hat{\mathbf{r}'})$, as:

$$\phi_i(\mathbf{r}) = \int_S \phi_i^\infty(\hat{\mathbf{r}'})G_\infty(\hat{\mathbf{r}'}, \mathbf{r})d\hat{\mathbf{r}'}. \tag{2.21}$$

where the 2D integration is conducted over all angles on the unit circle S encompassing the scatterer profile D.

Eqs. (2.21) & (2.20) represent the mapping of the incident far-field to the incident near-field local to the scatterer and the total field around the scatterer to the scattered far-field. In fact, the far-field incident wave can be

mapped to the far-field scattered wave by the far-field scattering operator, F, by [30, 45]:

$$\phi_s^\infty(\hat{\mathbf{r}}) = F\phi_i^\infty(\hat{\mathbf{r}}). \tag{2.22}$$

This represents the far-field scattering problem where $\phi_s^\infty(\hat{\mathbf{r}})$ is attempted to be determined given knowledge of $\phi_i^\infty(\hat{\mathbf{r}})$; this is visually illustrated in Fig. 2.2.

As a result of the linear nature of F, the far-field scattered field can be reconstructed from a linear summation of the scattering of incident plane waves representing the far-field incident wave field. This means that the scattering amplitude $f(\hat{\mathbf{r}}, \hat{\mathbf{r}}_0)$ defined in Eq. (2.19) can be used to describe the LHS of Eq. (2.22) resulting in [30]:

$$F\phi_i^\infty(\hat{\mathbf{r}}) = \int_S \phi_i^\infty(\hat{\mathbf{r}'}) f(\hat{\mathbf{r}'}, \mathbf{r}) d\hat{\mathbf{r}'}. \tag{2.23}$$

The scattering amplitude f can be measured experimentally for a given scattering problem by measuring the resultant scattered wave fields by the transmission of plane waves in all directions, thus allowing F to be calculated.

2.3 Scattering Operators

As discussed previously, various aspects of the scattering problem can be mapped to each other with certain operators. This Section will expand the concept of this mapping in more detail in relation to the *inverse scattering problem* and it will describe how this can be used to form the basis of the super-resolving Factorisation Method (FM). To begin, the far-field operator F has been shown to map ϕ_i^∞ to ϕ_s^∞. For a single scattering instance, the scattering amplitude f is only dependent on the object function $\mathcal{O}(\mathbf{r})$. Therefore a mapping exists between $\mathcal{O}(\mathbf{r})$ and $f(\hat{\mathbf{r}'}, \mathbf{r})$:

$$f(\hat{\mathbf{r}'}, \mathbf{r}) = M\mathcal{O}(\mathbf{r}), \tag{2.24}$$

where M is termed the complete far-field scattering operator. The inverse of the complete far-field scattering operator, M^{-1}, also known as the imaging operator, maps F to the Fourier transform of the object function, $\tilde{\mathcal{O}}$. These mappings are shown in Fig. 2.3. Calculating the form of M^{-1} is the *inverse scattering problem* and it is often an extremely difficult problem to solve. This is because of the non-linear nature of M^{-1}, meaning determining its form is ill-posed [45]. Also in practice, it is not possible to measure the wave field everywhere leading only a sub-set of the information of f to be known. As a result, is it generally impossible to determine M^{-1} exactly meaning exactly calculating $\mathcal{O}(\mathbf{r})$ is also impossible.

The far-field scattering operator F is of significant importance to the derivation of the FM imaging algorithm and is the subject of this Section. The FM is one of the main SR array imaging techniques considered within this thesis and its planar defect sizing and characterisation capabilities will be assessed within subsequent Chapters. It is therefore paramount that its derivation is fully understood prior to its practical application. To better

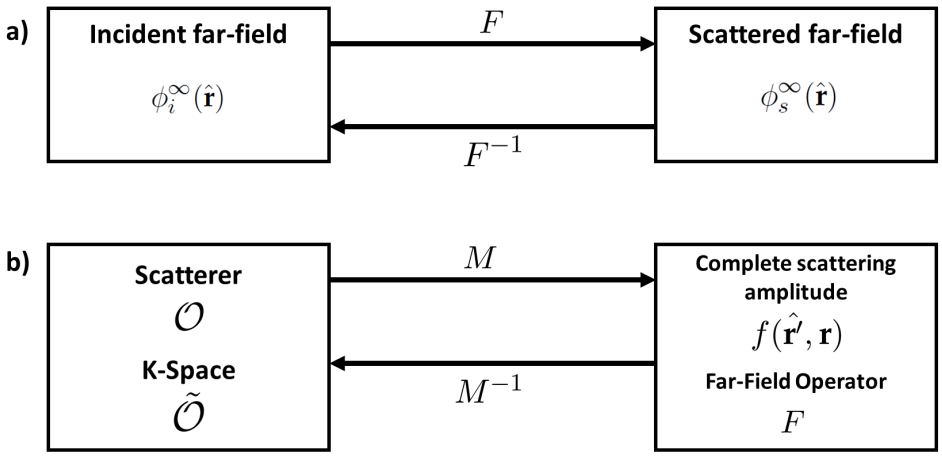


Figure 2.3: a) The far-field operators, F, maps an incident far-field wave field to a scattered far-field for a scatterer and the inverse F^{-1} reverses this mapping. b) The complete far-field scattering operator, M, maps the scatterer (represented by $\mathcal{O}$ or $\tilde{\mathcal{O}}$ in the spatial frequency domain) to the complete scattering amplitude f and therefore F. The imaging operator M^{-1} is used to reverse this mapping.

understand the mathematical basis for the FM, it is convenient to decompose F into three separate sub-operators [46].

The first sub-operator H, called the Herglotz operator, maps the far-field incident wave field to the incident field on a section of the scatterer boundary ∂D (equivalent to Eq. (2.21)) [46]:

$$H\phi_i^\infty(\hat{\mathbf{r}}) = \phi_i(\mathbf{r}') \quad \mathbf{r}' \in \partial D. \tag{2.25}$$

The second sub-operator S maps the interaction of the incident field on ∂D to the local scattered field, assuming a continuous distribution of point sources, g, on D:

$$S\phi_i(\mathbf{r}') = g(\mathbf{r}') \quad \mathbf{r}' \in \partial D. \tag{2.26}$$

The third and final sub-operator H^* propagates this local scattered field to the actual far-field measurements:

$$H^* g(\mathbf{r}') = \phi_s^\infty(\hat{\mathbf{r}}) \quad \mathbf{r}' \in \partial D, \tag{2.27}$$

where H^* is the adjoint of H and can be calculated by:

$$\phi_s^\infty(\hat{\mathbf{r}}) = \int_{\partial D} g(\mathbf{r}') G_\infty(\mathbf{r}, \hat{\mathbf{r}}') \quad \mathbf{r}' \in \partial D. \tag{2.28}$$

Using these sub-operators, the far-field scattered wave field can be written as:

$$\phi_s^\infty = F\phi_i^\infty = H^* S H \phi_i^\infty, \tag{2.29}$$

and it can then be easily seen that the operator F can be factorised as:

$$F = H^* S H. \tag{2.30}$$

This factorisation forms the basis of the FM imaging algorithm which is introduced in Section 2.8.1. The next Section discusses proposed solutions to the inverse scattering problem using classical imaging methods as well as recently developed SR methods, including the FM.

2.4 The Challenge of Inverse Scattering

The inverse scattering problem, also known as the imaging problem, aims to determine the exact nature of M^{-1} in an attempt to calculate $\mathcal{O}(\mathbf{r})$ given knowledge of the scattering amplitude $f(\hat{\mathbf{r}}', \mathbf{r})$. As discussed in Section 2.3, it is often impossible to do this exactly as one can only practically measure a sub-set of $f(\hat{\mathbf{r}}', \mathbf{r})$ due to finite sampling. Other experimental factors such as material and sensor noise can lead to significant artefacts in the reconstruction of $\mathcal{O}(\mathbf{r})$ because M^{-1} is ill-posed.

Implicit iterative methods to estimate the form of the object function, $\hat{\mathcal{O}}(\mathbf{r})$, can be utilised when an explicit formulation cannot be reached by minimising:

$$\hat{\mathcal{O}}(\mathbf{r}) = \text{argmin}_{\hat{\mathcal{O}}(\mathbf{r})} \left|\left| M(\hat{\mathcal{O}}(\mathbf{r}) - f(\hat{\mathbf{r}}', \mathbf{r})) \right|\right|. \tag{2.31}$$

There exist successful iterative methods using this technique [47] however these methods are often slow to calculate due to the search space of $\hat{\mathcal{O}}(\mathbf{r})$ being large and containing multiple local minima. As a result of these difficulties, many imaging methodologies have been developed which aim to simply the problem such as by using linear approximations of M to reach a solution. A widely applied methodology to address these challenges is the Born approximation, which will be discussed in detail within the following Section.

2.5 Born Approximation

A common simplification used to linearise the scattering problem is known as the Born approximation. The Born approximation is a single scattering framework, i.e. where the interaction of an already scattered wave with the object (multiple scattering) is ignored. It assumes that any inhomogeneities present result in only weak scattering:

$$\phi_s \ll \phi_i, \tag{2.32}$$

thus the total change of phase of the incident field, due to sound speed variations in the inhomogeneity, is less than π [25]. This is because if the perturbed wave which passes through the inhomogeneity is phased shifted by π, it will destructively interfere with the unperturbed wave field. The Born approximation means Eq. (2.20) can be approximated to:

$$\phi_s^{\infty,B}(\hat{\mathbf{r}}) \approx -k_0^2 \int_V G_\infty(\hat{\mathbf{r}}, \mathbf{r}') \mathcal{O}(\mathbf{r}') \phi_i(\mathbf{r}') d\mathbf{r}', \tag{2.33}$$

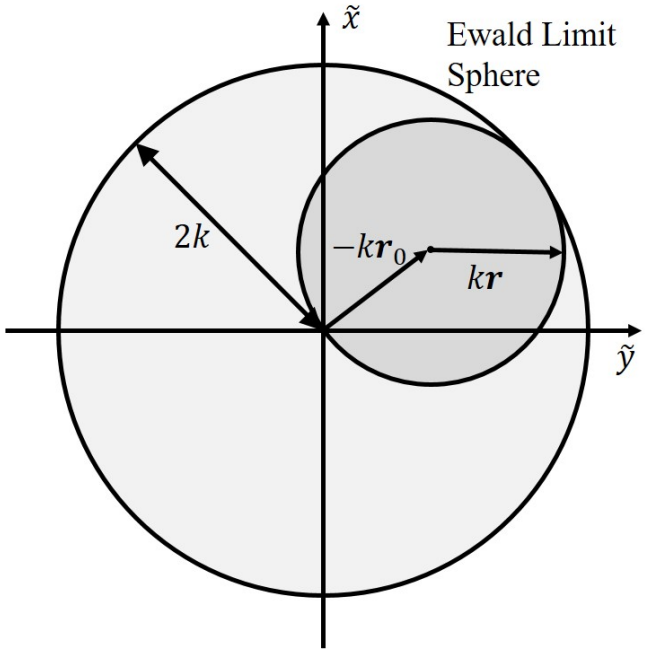


Figure 2.4: A schematic of the Ewald limiting circle in the spatial frequency domain.

where $\phi_s^{\infty,B}$ denotes the Born approximated scattered wave field.

Mathematically, the Born approximation can be applied when the following validity condition is met [30]:

$$\sup_{r<l} |\mathcal{O}(\mathbf{r})| < \mathcal{C}\frac{\lambda}{l}, \tag{2.34}$$

where l is the characteristic size of the inhomogeneity and $\mathcal{C}$ is a constant with different proposed values.

From Eq. (2.33) it is clear that when under the Born approximation, the far-field scattered wave field is linear in $\mathcal{O}(\mathbf{r})$ and therefore the Born approximation of M, M_{Born}, is also linear. This allows for the Born approximated imaging operator, M_{Born}^{-1}, to be explicitly calculated non-iteratively which is also linear and well-posed [48]. Due to the simplistic nature of these simplified operators, their explicit form can be calculated quickly allowing one to approximate the nature of $\mathcal{O}(\mathbf{r})$.

A limitation of the Born approximation is that it exhibits an intrinsic resolution limit. This can be understood by considering an incident plane wave with direction vector $\hat{\mathbf{r}_0}$; the scattering amplitude in Eq. (2.19) can be written as:

$$f(\hat{\mathbf{r}}, \hat{\mathbf{r}}_0) = \int_D \mathcal{O}(\mathbf{r}') e^{ik_0 \hat{\mathbf{r}_0} \cdot \mathbf{r}'} e^{-ik_0 \hat{\mathbf{r}} \cdot \mathbf{r}'} d\mathbf{r}' = \int_D \mathcal{O}(\mathbf{r}') e^{-ik_0 (\hat{\mathbf{r}} - \hat{\mathbf{r}}_0) \cdot \mathbf{r}'} d\mathbf{r}'. \tag{2.35}$$

The RHS of Eq. (2.35) is equal to the spatial Fourier transform of the object function:

$$f(\hat{\mathbf{r}}, \hat{\mathbf{r}}_0) = \tilde{\mathcal{O}}\left(k_0(\hat{\mathbf{r}}_0 - \hat{\mathbf{r}})\right) \tag{2.36}$$

By varying the incident direction $\hat{\mathbf{r}}_0$ and the scattered wave direction $\hat{\mathbf{r}}$ across all possible angles, all values in spatial frequency k-space within the geometry shown in Fig.2.4 can be measured [30]. Therefore, the Born approximation can only measure scattered waves with a wavenumber within this Ewald limiting circle of radius $2k$, which corresponds to a minimum spatial resolution of $\frac{\lambda}{2}$. Under this approximation, no information about features from a scattering object can be accounted for within the far-field scattered wave field and leads to the classical diffraction limit [30].

2.6 Total Focusing Method

The Total Focusing Method (TFM) is a type of BF algorithm and one of the most widely researched ultrasonic array algorithms aimed at determining the location of point scatterers [8, 15]. In this thesis, TFM will been applied to FMC datasets in post-processing by simulating the focusing of the beam at predetermined nodes within a grid placed within the region of interest, as shown in Fig. 2.5. This is achieved by considering the times of flight from the transmitting transducer element to the grid point and back to the receiving element, and then calculating the image intensity. Referring to Fig. 2.5, the times of flight from transducer i to the grid point P, T_{iP}, and from transducer j to P, T_{Pj}, are expressed as:

$$T_{iP} = \frac{\sqrt{(x_i - x)^2 + (y_i - y)^2}}{c}, \tag{2.37}$$

$$T_{Pj} = \frac{\sqrt{(x_j - x)^2 + (y_j - y)^2}}{c}, \tag{2.38}$$

where c is the wave speed. From this, the intensity of the TFM image, $I_{TFM}(P)$, for every grid point $P(x, y)$ produced by an array of N elements is given by [49]:

$$\begin{aligned} I_{TFM}(P) &= \sum_{i,j=1}^{N} H(S_{ij})(T_{iP} + T_{Pj}) \\ &= \sum_{i,j=1}^{N} H(S_{ij}) \frac{1}{c} \left(\sqrt{(x_i - x)^2 + y^2} + \sqrt{(x_j - x)^2 + y^2} \right). \end{aligned} \tag{2.39}$$

where S_{ij} is the collected time-domain FMC signal in matrix form where transducer i is the transmitter and transducer j is the receiver, H is the analytic time-domain signal of the FMC data and $y_{i/j} = 0$.

The analytic time-domain signal, H, is a complex-valued signal with no negative frequency components. The analytic signal is reached by applying the Hilbert transform to the FMC data, S_{ij}, as follows [50]:

$$H(t) = S(t) + iS^h(t), \tag{2.40}$$

where $S^h(t)$ is the Hilbert transform of $S(t)$. The concept of the analytic signal can be thought of as measure of the total energy of the particles being displaced within the transducer when interacting with the ultrasound. This is illustrated in Fig. 2.6a) by considering the particles as simple masses

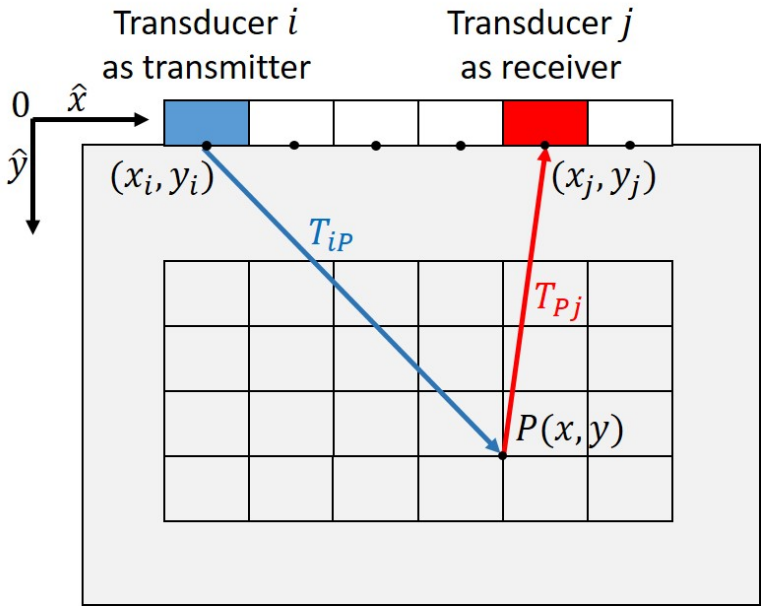


Figure 2.5: The configuration of the TFM algorithm.

on a spring which have been set into motion by the ultrasonic wave. The transducer itself only measures the displacement of the particles and therefore only information related to their elastic potential energy is obtained. This means that where the displacement is measured zero, or equivalently when the amplitude of the measured A-Scan is zero, no information about the energy of the wave is obtained. This means that if only the information in $S(t)$ is used, the TFM algorithm would output an imaging amplitude of zero at these points which we know to be incorrect. By applying the principle of energy conservation, however, the total energy of the system must be conserved. At the points when the displacement is zero (and therefore the elastic potential energy is zero), the particles are actually travelling at their highest velocity. This means that all of their energy is in the form of kinetic energy, with the kinetic energy always being $\pi/2$ out of phase with the potential energy as shown in Fig. 2.6b). The Hilbert transform of $S(t)$, $S^h(t)$, can be thought of as a measure of the kinetic energy of the particles and one must use information from both $S(t)$ and $S^h(t)$ to measure the total energy of the system. This is done by calculating the *instantaneous amplitude* of the analytic signal defined as [50]:

$$\sqrt{(S)^2 + (S^h)^2}. \tag{2.41}$$

An example of a simulated FMC A-Scan featuring a defect response is shown in Fig. 2.7. The real time-domain signal recorded by the array is seen to be $\pi/2$ out of phase with its Hilbert transformed signal. The instantaneous amplitude as mentioned can be thought of as the total energy of the system and from Fig. 2.7 it can be seen to act as an 'envelope' function of the recorded array A-Scan.

The importance of using the analytic signal within Eq. (2.39) as opposed

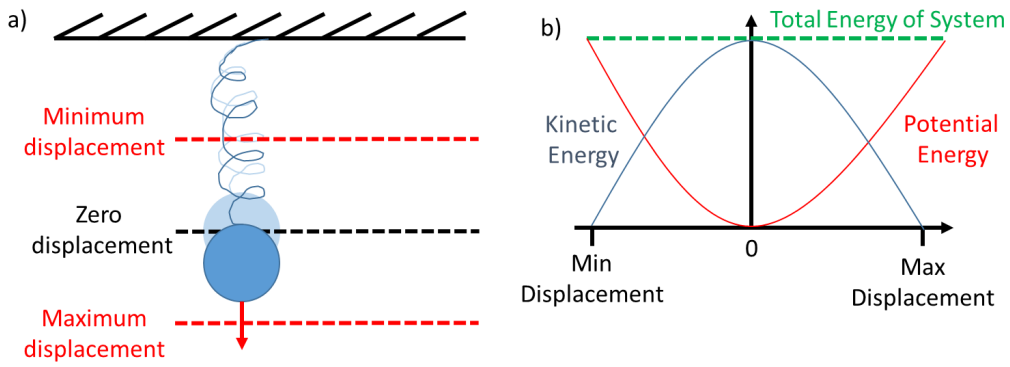


Figure 2.6: a) The energy of the oscillating particles in the transducer being forced by the ultrasonic waves can be described by a simple oscillating mass on a spring. b) The total energy of the mass is conserved between elastic potential energy and kinetic energy, with both forms of energy being $\pi/2$ out of phase with each other.

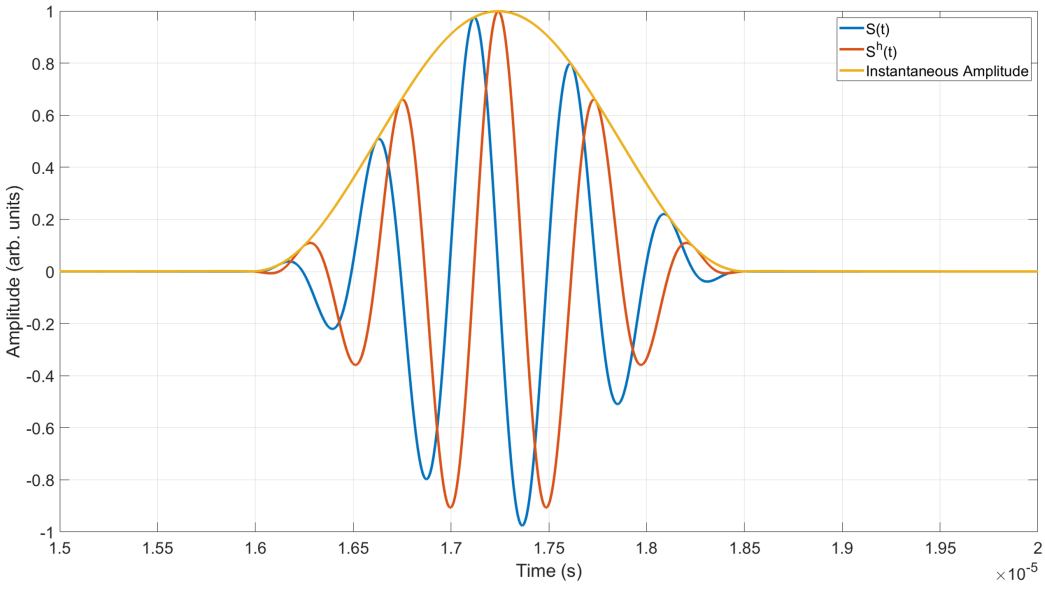


Figure 2.7: An example of a simulated FMC A-Scan featuring a defect response. The real time-domain signal recorded by the array is shown in blue, the Hilbert transform of this signal is shown in orange and the instantaneous amplitude of the analytic signal is shown in yellow.

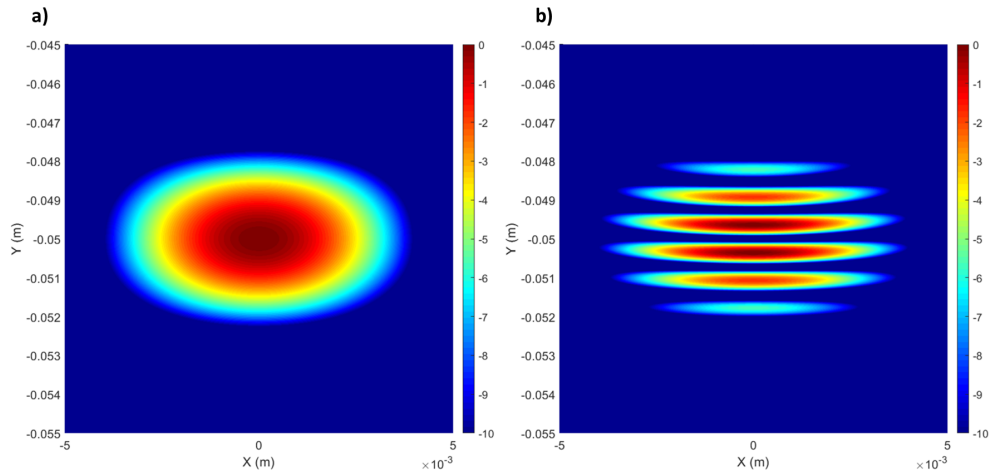


Figure 2.8: Examples of TFM images of a point scatterer using simulated FMC data from a 2 MHz 64-element array when a) the analytic signal is used as part of the algorithm, and b) when only the unprocessed time-domain signal obtained by the array is used. It can be seen that image b) exhibits a periodic variation in amplitude of $\lambda/2$ which is not indicative of the nature of the imaged point scatterer.

to the unprocessed array A-Scan data is shown in Fig. 2.8. Both TFM images presented are of a point scatterer located at (0, -50) mm, with Fig. 2.8a) generated using the full analytic signal, $H(t)$, and Fig. 2.8b) only using the unprocessed array A-Scan data $S(t)$. Fig. 2.8a) provides the uniform amplitude profile expected from such a defect whereas Fig. 2.8b) exhibits a variation in amplitude with periodicity $\lambda/2$. This image profile is not indicative of the true nature of the imaged point scatterer but is a manifestation of only considering part of the information contained within the signal data (the oscillating amplitude of the real measured A-Scans). It is therefore paramount that the analytic signal is used with the TFM algorithm such that accurate defect characterisation can be conducted without unwanted artefacts being present within the images.

Another formulation of the TFM but in the frequency domain begins by replacing the incident field in Eq. (2.33) by its equivalent Green's function:

$$\phi_s(\mathbf{r},\omega) = \int_V G(\mathbf{r},\mathbf{r}')\mathcal{O}(\mathbf{r}',\omega)G(\mathbf{r}',\hat{\mathbf{r}}_0)d\mathbf{r}'. \tag{2.42}$$

By considering a point scatterer, Eq. (2.42) can be simplified to:

$$\phi_s(\mathbf{r},\omega) = G(\mathbf{r},\mathbf{r}')qG(\mathbf{r}',\hat{\mathbf{r}}_0), \tag{2.43}$$

where q is the scattering potential at the point scatterer location $\mathbf{r}'$. By rearranging in terms of q and considering the multiple pairs of transmitters

and receivers, $I(P)$ can be expressed as:

$$\begin{aligned} I_{TFM}(P) &= \int_{\mathcal{S}} \int_{\mathcal{S}} \frac{\phi_s(\mathbf{r},\omega)}{\exp(ik|\mathbf{r}'-\hat{\mathbf{r}}_0|)(\exp(ik|\hat{\mathbf{r}}-\mathbf{r}'|))} d\mathbf{r} d\hat{\mathbf{r}}_0 \\ &= \sum_{\omega} \sum_{i,j=1}^{N} \phi_{ij}^{s}(\omega) \exp\left[ikc(T_{iP}+T_{Pj})\right]. \end{aligned} \tag{2.44}$$

where the term $\exp(ik|\hat{\mathbf{r}}-\mathbf{r}'|)$ is known as the steering function. The steering function is similar to Green's function but only considers phase shifts. The steering function will be discussed in later Sections during the derivations of the SR algorithms.

TFM has been shown to achieve a better resolution than other array imaging methods such as focussed B-scans [8] and the imaging area of TFM can be much larger than other scanning methodologies as it utilises FMC data which is not limited to a single beam direction.

2.7 Multiple Scattering

In Section 2.2, the far-field scattering amplitude was derived in Eq. (2.19). The Born approximation described in Section 2.5 can be applied to this equation which replaces the total field by a plane wave incident field given by Eq. (2.35). This equation, as described previously, is simply the Fourier transform of the object function at the spatial frequency $k_0(\hat{\mathbf{r}}_0-\hat{\mathbf{r}})$, $\tilde{\mathcal{O}}(k_0(\hat{\mathbf{r}}_0-\hat{\mathbf{r}}))$.

To return back to full generality to include both the Born approximation and not losing the scattered wave ϕ_s, the full far-field scattering amplitude can be written as:

$$f(k_0\hat{\mathbf{r}}, k_0\hat{\mathbf{r}}_0) = \tilde{\mathcal{O}}(k_0(\hat{\mathbf{r}}-\hat{\mathbf{r}}_0)) + \int_D \mathcal{O}(\mathbf{r}')\phi_s(\mathbf{r}')e^{-ik_0\hat{\mathbf{r}}\cdot\mathbf{r}'}d^2r'. \tag{2.45}$$

This equation is the Born approximated scattering amplitude but now with an additional integral term, corresponding to multiple scattering events. The Born approximation view of scattering as well as the generalised multiple scattering view are visually represented in Fig. 2.9. The significance of the integral term in Eq. (2.45) become more apparent if the equation is reformulated following the derivation by Simonetti [30]. The transition amplitude is now introduced, K, defined as [51]:

$$K(\alpha\hat{\mathbf{u}}, k_0\hat{\mathbf{r}}_0) = \int_D \mathcal{O}(\mathbf{r}')\phi(\mathbf{r}')e^{-i\alpha\hat{\mathbf{u}}\cdot\mathbf{r}'}d^2r', \tag{2.46}$$

where α is an arbitrary constant and $\hat{\mathbf{u}}$ is an arbitrary unit vector. It is clear that when $\alpha\hat{\mathbf{u}} = k_0\hat{\mathbf{r}}$, $K(k_0\hat{\mathbf{r}}, k_0\hat{\mathbf{r}}_0) = f(k_0\hat{\mathbf{r}}, k_0\hat{\mathbf{r}_0})$. By introducing the eigenfunction expansion of Green's function [52]:

$$G(\mathbf{r},\mathbf{r}') = -\frac{1}{8\pi^3}\int_{-\infty}^{\infty} \frac{\exp^{i\alpha\hat{\mathbf{u}}\cdot(\mathbf{r}-\mathbf{r}')}}{k_0^2-\alpha^2+i\epsilon}, \tag{2.47}$$

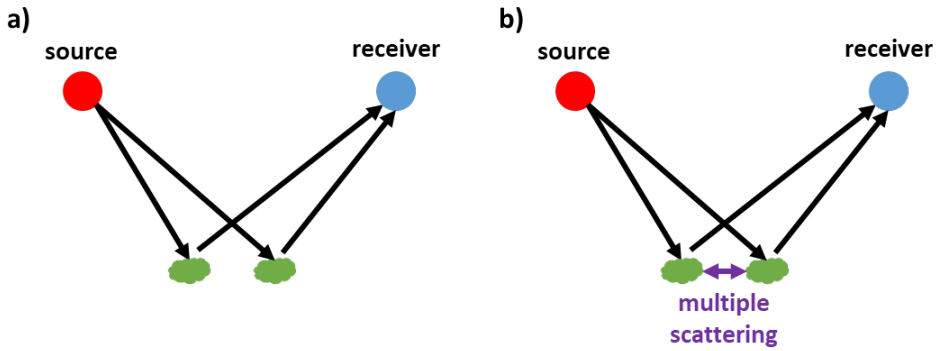


Figure 2.9: A simplified scattering scenario comprising of two scatterers. a) Paths of the incident and scattered waves under the Born approximation; only single scattering is permitted and there is no interaction between the scatterers. b) Paths of the incident and scattered fields considering multiple scattering; interaction between the scattered fields and scatterers occurs which is a key mechanism for retrieving far-field sub-wavelength information.

where ϵ is an infinitesimally small value included to remove the singularities when $k_0^2 = \alpha^2$, and after some manipulation, Eq. (2.46) can be written as:

$$K(k_0\hat{\mathbf{r}}, k_0\hat{\mathbf{r}_0}) = \tilde{\mathcal{O}}(k_0(\hat{\mathbf{r}} - \hat{\mathbf{r}}_0)) + \frac{k_0^2}{8\pi^3} \int_{-\infty}^{+\infty} \frac{\tilde{\mathcal{O}}(k_0\hat{\mathbf{r}} - \alpha\hat{\mathbf{u}}) K(\alpha\hat{\mathbf{u}}, k_0\hat{\mathbf{r}_0})}{k_0^2 - \alpha^2 + i\epsilon} d^2\alpha, \quad (2.48)$$

or equivalently Eq. (2.45) can be written as:

$$f(k_0\hat{\mathbf{r}}, k_0\hat{\mathbf{r}_0}) = \tilde{\mathcal{O}}(k_0(\hat{\mathbf{r}} - \hat{\mathbf{r}}_0)) + \frac{k_0^2}{8\pi^3} \int_{-\infty}^{+\infty} \frac{\tilde{\mathcal{O}}(k_0\hat{\mathbf{r}} - \alpha\hat{\mathbf{u}}) f(\alpha\hat{\mathbf{u}}, k_0\hat{\mathbf{r}_0})}{k_0^2 - \alpha^2 + i\epsilon} d^2\alpha. \quad (2.49)$$

This is Eq. (2.45) but now entirely described within the k-space domain. As can be seen it contains two components; the Born approximated view, $\tilde{\mathcal{O}}$, and an integral term. The Born approximate term considers spatial frequencies constrained by the Ewald limiting circle as described in Section 2.5. The integral term however considers spatial frequencies over the entire k-space, including spatial frequencies greater than $2k_0$, corresponding to physical separations less than $\frac{\lambda}{2}$. Thus these larger spatial frequencies do indeed affect the far-field scattering amplitude so the potential exists for the Born approximated resolution limit to be overcome [53] and for super resolution to be achieved.

2.8 Super Resolution Algorithms

Within this Section the derivations for the Super Resolution (SR) array imaging algorithms utilised within this thesis will be outlined, namely the Factorisation Method (FM) and the TR-MUSIC algorithms. Both of these techniques rely upon higher spatial frequency information being accounted for

within the far-field scattered wave field, physically captured by the effects of multiple scattering.

2.8.1 Factorisation Method

The FM is a well-established SR algorithm which is actually based on the Linear Sampling Method (LSM) developed by Colton and Kirsch [54] and it is therefore convenient to first derive the LSM. LSM is a monochromatic sampling method that was the first non-iterative inverse imaging algorithm developed to reconstruct the boundary of a scatterer, D, that required no prior knowledge of the geometry or properties of the scatterer [54, 55]. Both the LSM and FM operate by computing a spatially varying imaging function based on the far-field operator F. This imaging function tends to infinity on the boundary of the scatterer and zero elsewhere meaning an image of the scatterer profile can be plotted.

The LSM and the FM both use the concept of the far-field operator F [46] which maps a far-field incident wave field to the resultant far-field scattered wave field. The LSM uses the assumption that the scattered wave field is only generated from the scatterer's boundary D and not outside of it, meaning:

$$F\phi_i^\infty(\hat{\mathbf{r}}) = g_z(\hat{\mathbf{r}}, z), \tag{2.50}$$

where z is a sampling point in space and g_z is known as the steering function. g_z has the form:

$$g_z(\hat{\mathbf{r}}, z) = e^{-ik_0\hat{\mathbf{r}}\cdot z} \tag{2.51}$$

and it is essentially the far-field Green's function for a point source located at the sampling position z. One can attempt to directly calculate the inverse of F in order to determine $|\phi_i^\infty(\hat{\mathbf{r}})|$, which tends to infinity when not on the scatterer D, therefore can be used to plot an image of D using $1/\left|\phi_i^\infty(\hat{\mathbf{r}})\right|^2$. An alternative method is to apply Tikhonov-Morozov regularisation to the linear equation produced under the LSM to determine the structure of D [56, 57]. However, this approach will not be considered further.

The LSM was modified by Kirsch [58] to develop the FM which considered the following equation:

$$(F^*F)^{\frac{1}{4}}\phi_i^\infty(\hat{\mathbf{r}}) = g_z(\hat{\mathbf{r}}, z), \tag{2.52}$$

where F^*F is the time-reversal operator T introduced by Prada, 1996 [59]. T is defined by the decomposition of F using Singular Value Decomposition (SVD) to determine the following singular system [60]:

$$F\xi_j = \mu_j\nu_j, \tag{2.53}$$

$$F^*\nu_j = \mu_j\xi_j, \tag{2.54}$$

where j indexes the singular system ξ_j, ν_j and μ_j. The normal equations for the above systems are:

$$F^*F\xi_j = \mu_j^2\xi_j, \tag{2.55}$$

$$FF^*\nu_j = \mu_j^2\nu_j, \tag{2.56}$$

where the T matrix is defined by,

$$T \equiv F^* F. \tag{2.57}$$

Following the derivation by Kirsch [61], it can be shown that for lossless media, where $\mathcal{O}(\mathbf{r})$ is real, Eq. (2.52) only has a solution when the sampling point z lies exactly on D. This can be evaluated by considering the fact that F is normal in this case and by utilising Picard's theorem, Eq. (2.52) is solvable if and only if [30]:

$$\sum_{n=1}^{\infty} \frac{1}{|\mu_n|} |\langle g_{\mathbf{z}} | \nu_{\mathbf{z}}^n \rangle|^2 < \infty, \tag{2.58}$$

where μ_n and $\nu_{\mathbf{z}}$ are eigenvalues and eigenfunctions of F respectively and $\langle | \rangle$ refers to the Dirac brak-ket notation [62]. In the FM, the steering function is used to probe the grid within the region of interest and if a point $\mathbf{z}$ lies within D, then the value of Eq. (2.58) is bounded, otherwise it is unbounded (i.e. ∞). Thus the reciprocal of Eq. (2.58) is taken to give the FM pseudospectrum, $I_{FM}(\mathbf{z})$, as [30]:

$$I_{FM}(\mathbf{z}) = \left(\sum_{n=1}^{\infty} \frac{1}{|\mu_n|} |\langle g_{\mathbf{z}} | \nu_{\mathbf{z}}^n \rangle|^2 \right)^{-1} \text{ is } \begin{cases} > 0 & \text{if } \mathbf{z} \text{ on } D \\ = 0 & \text{if } \mathbf{z} \text{ not part of } D. \end{cases} \tag{2.59}$$

If no noise is present, Eq. (2.59) reconstructs D with unlimited resolution however with noise present, SR images are still possible to produce [30].

2.8.2 TR-MUSIC

As well as the LSM and FM, there exist several other methodologies to solve the imaging problem. One such technique is the time-reversal method which has been demonstrated to achieve very high resolutions [63, 59]. Time-reversal methods in general are based on the reciprocity of the wave equation in most circumstances, i.e. the solution to the wave equation is *time-invariant* and therefore both $\phi(t)$ and $\phi(-t)$ are solutions. This concept is shown by Eq. (2.5) which contains both outwardly and inwardly propagating waves. The time-reversal method can therefore be used to take waves in their *'final state'*, after being scattered by an object and received by an array, and reverse their propagation and focus them back to the scattering object. These techniques can allow for the detection of point scatterers within a medium or can be used to approximate the profile of extended scatterers.

The time-reversal method, however, can only be applied when the scatterers being imaged are said to be *well-resolved* [60]. In well-resolved cases, the number of scatterers, M, is less than the number of elements in the inspecting phased array N and the singular system of $(e_j, \nu_j, \sigma > 0)$ can be mapped in a *one-to-one manner* to the M scatterers. It can be derived that the singular vectors ν_j with non-zero singular values $\sigma_j > 0$ are given by:

$$\nu_j = \frac{g_r(X_j)}{||g_r(X_j)||}, \tag{2.60}$$

where $j = 1, 2, ..., M$ and the singular values are related to the scatterer strengths via [60]:

$$\sigma_j = k_0^2 |\tau_j| ||g_r(X_j)|| ||g_t(X_j)||. \tag{2.61}$$

The time reversal method can only be used in such well-resolved cases.

There exist several modified versions of the time reversal method to try to overcome its inherent shortcomings, particularly its limitation in its applicability to only well-resolved targets. By employing a MUltiple-SIgnal-Classification (MUSIC) type algorithm, which can be more suited in dealing with non-well-resolved targets as well as extended targets, in conjunction with time reversal, a more robust SR algorithm is formed, often termed Time Reversal MUltiple-SIgnal-Classification (TR-MUSIC) [64, 65].

For a medium with M scatterers, which is less than the number of transducers N, the time reversal matrix in Eq. (2.57) has M eigenvectors with non-zero eigenvalues with (N-M) eigenvectors with zero eigenvalues [64]. The (N-M) eigenvectors with zero eigenvalues are often termed to be part of the *noise* subspace. Due to the orthogonality of these eigenvectors with the Green's steering vectors, $g_{\mathbf{z}}$, an image pseudospectrum for the TR-MUSIC method can be formulated, $I_{TR-MUSIC}$, and is given by [64]:

$$I_{TR-MUSIC}(\mathbf{z}) = \frac{1}{\sum_{j=M+1}^{N} |\langle g_{\mathbf{z}} | \nu_j \rangle|^2}. \tag{2.62}$$

For both *well-resolved* and *non-well resolved* scatterers, this algorithm produces distinct peaks at the scatterer locations. This is because the denominator represents the wavefield at a point $\mathbf{z}$ due to an incident field due to ν_j, vanishes whenever $\mathbf{z}$ corresponds to a scatterer location.

The forms of the pseudospectrums of the FM and TR-MUSIC algorithms are very similar and for the case of imaging point scatterers, it has been shown that the FM and TR-MUSIC algorithm are actually equivalent [46, 66].

2.8.3 Practical Implementation of the SR Algorithms

In this thesis, the FM and TR-MUSIC algorithms were applied in the frequency-domain to the array FMC datasets whereas the TFM algorithm was applied to the time-domain FMC datasets.

Throughout this thesis, ultrasonic linear array inspections were both numerically modelled and experimentally conducted to acquire the FMC datasets. For a given linear array with N number of elements, an N x N sized matrix of A-Scans corresponding to the FMC dataset were collected. The Fast Fourier Transform (FFT) of each A-Scan in the time-domain FMC datasets at the central frequency of the array, ω, was carried out [58] and the complex value of the FFT result at the frequency corresponding to ω was used to populate $F(\omega)$, which is also often called the multistatic response matrix.

From the $F(\omega)$ matrix, SVD was conducted to generate the required set of singular eigenvalues, μ_i, and their corresponding eigenvectors, ν_i, where $i = 1, 2, ..., N$. In this thesis where the FM has been utilised, all eigenvectors generated from the SVD of the $F(\omega)$ matrix were considered whereas in the application of the TR-MUSIC algorithm, the eigenvectors were separated

into two separate subspaces; the *signal* subspace and the *noise* subspace. In an idealised noise free scenario, there would exist a set of non-zero eigenvalues whose corresponding eigenvectors belong to the *signal* subspace and the remaining eigenvectors would belong to the *noise* subspace. In practice, there exists a finite level of noise in the inspection system so a non-zero threshold value must be used to determine the point of separation between these two subspaces and the separation point varies depending on the particular inspection case. The typical threshold values used in this thesis were between 30-50 dB less than the maximum eigenvalue calculated, based on observing a step function-like separation in amplitude between the signal and noise subspace eigenvalues. Although there have been some cases presented within the literature of also separating eigenvalues in the application of the FM [35], the majority utilise the full eigenvalue range thus the results presented in this thesis aimed to investigate the most common implementation of these algorithms.

Post-SVD of the $F(\omega)$ matrix, the steering vector, g_z, to propagate the eigenvectors to different positions, $\mathbf{z}$, in the imaging grid was taken as:

$$g_z(\mathbf{z}) = [G_\infty(\mathbf{R}_1, \mathbf{z}), G_\infty(\mathbf{R}_2, \mathbf{z}), ..., G_\infty(\mathbf{R}_N, \mathbf{z})], \tag{2.63}$$

where $\mathbf{R}_N$ corresponds to the N array element locations and G correspond to the Green's function of the propagation medium.

As strictly only the far-field scattered wave field should be processed by the SR imaging algorithms, an additional step was applied to the time-domain FMC datasets prior to determining $F(\omega)$. This was achieved by windowing the time traces with a Hann window at the appropriate temporal location corresponding to the expected scattered signal for the wave-mode of interest. For simulated cases considered in this thesis, knowing where to implement the window was trivial. In experimental inspection cases where the exact defect location is not strictly known, it is suggested that TFM imaging is applied to gauge the approximate defect location before subsequently using this information to conduct the windowing prior to applying the SR methods. This step helps to avoid major reflection features from component/model geometric boundaries, mode converted reflections and probe ringing being processed by the SR algorithms as they would lead to the corruption of $F(\omega)$ and inclusion of artefacts of the subsequent images. An illustration of this process is shown in Fig. 2.10. In this thesis, only direct contact phased array imaging was considered and therefore longitudinal waves were used as the inspection mode.

By utilising only a single frequency ω in the SR format described previously, the resultant algorithms are highly sensitive to signal noise and information encoded in other frequencies is discarded. There is therefore potential for improved reconstructions by incorporating frequencies from across the ultrasonic pulse-width into the algorithm. As a result, broadband implementations of the SR algorithms were used for the entirety of this thesis. The monochromatic SR algorithms given by Eqs. (2.59) & (2.62) were modified

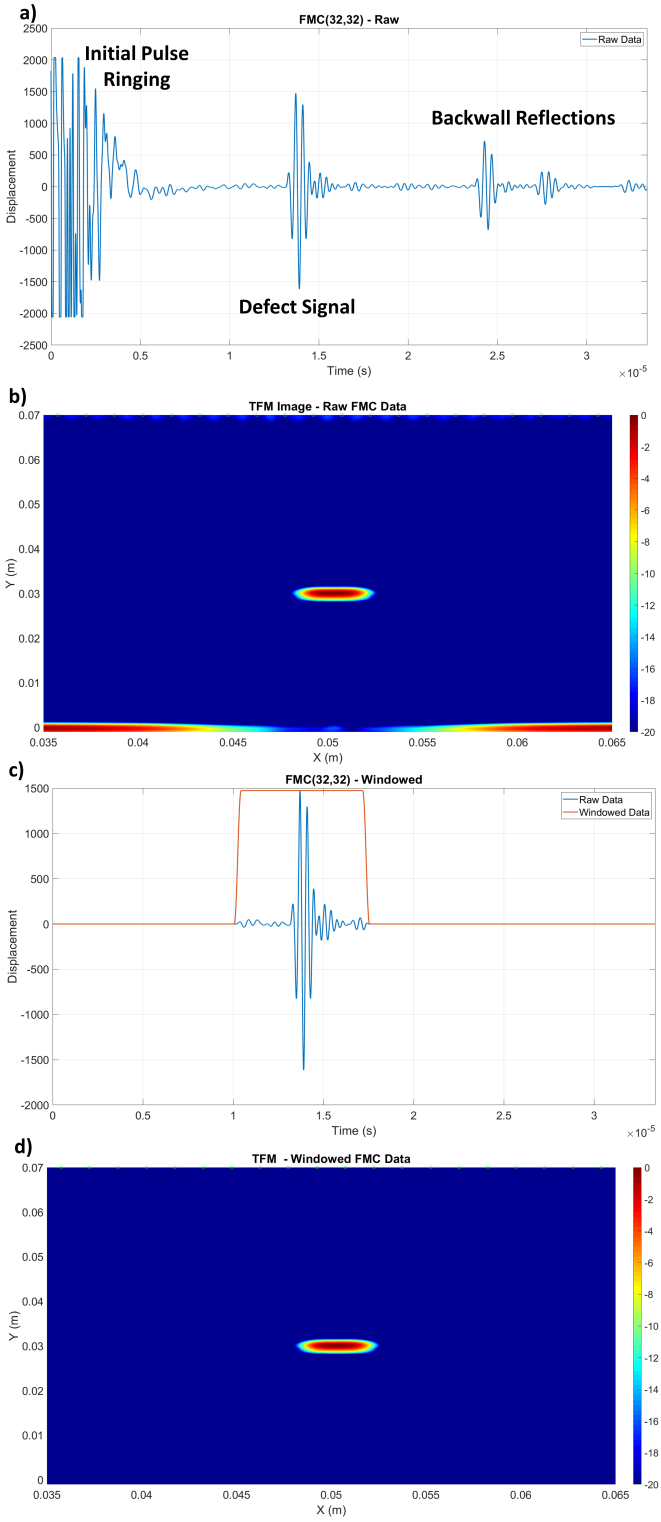


Figure 2.10: An illustration of time-domain windowing of FMC data to isolate the defect response. a) An example of a raw FMC A-Scan corresponding to the pulse-echo signal from the centre element of a 64-element 2 MHz array, featuring initial pulse ringing, the defect signal and geometric reflections. b) The TFM image generated using raw FMC data which includes low amplitude artefacts at the transducer locations (Y=70 mm), the defect indication in the centre of the image as well as a backwall response. c) An example of time-domain windowing applied to the A-Scan in a) to isolate the defect response. d) The TFM image of the windowed FMC data containing only the defect indication.

to utilise F matrix data over a range of frequencies. The resultant Multiple Frequency Factorisation Method (MF-FM) and Multiple Frequency TR-MUSIC (MF-TR-MUSIC) algorithms were implemented [65]:

$$I_{MF-TRM}(\mathbf{r}) = \frac{1}{\sum_{\omega} \sum_{j=M+1}^{N} |\langle g(\mathbf{r},\omega)|\nu_j(\omega)\rangle|^2}, \tag{2.64}$$

$$I_{MF-FM}(\mathbf{r}) = \frac{1}{\sum_{\omega} \sum_{j=1}^{N} \frac{1}{|\mu_j|} |\langle g(\mathbf{r},\omega)|\nu_j(\omega)\rangle|^2}. \tag{2.65}$$

In addition, by using a range of frequencies, the imaging performance became less reliant on accurately selecting a single specific frequency value corresponding to the centre frequency of the ultrasonic signal, which allowed easier automation of applying the SR methods to the FMC datasets. Due to the finite pulse lengths used in practical NDE, there is an inherent spread in frequency of the ultrasonic waves and it has been found that even slight variations in centre frequency can have a significant impact on the resultant SR image. This is shown in Fig. 2.11 where there are major variations between the different FM images, whereas when the MF-FM was applied, a more accurate image for sizing is generated. It was also found that the multiple frequency SR algorithms demonstrated higher robustness to factors such as noise and defect roughness, and therefore they were chosen to be used.

In this thesis, the frequency selection range used to populate $F(\omega)$ during the implementation for the SR algorithms was set to be approximately the full width at half maximum of the bandwidth profile of the ultrasonic toneburst. For the commonly utilised 2 MHz waveforms applied this thesis, this corresponded to a half-spread of 0.4 MHz about the 2 MHz centre frequency. A total of nine equally spaced frequency values were sampled across this frequency range when implementing the MF-FM and MF-TR-MUSIC methods, with an odd number ensuring the centre frequency was considered. All SR images and results discussed subsequently in this thesis refer to the application of the MF-FM and MF-TR-MUSIC algorithms.

The steps detailed above which discuss the practical implementation of the MF-FM, MF-TR-MUSIC and TFM imaging algorithms upon ultrasonic phased array FMC datasets are visually illustrated in Fig. 2.12.

Throughout this thesis, the defect sizing performance of the SR and TFM linear array algorithms are assessed for various inspection scenarios. To make these comparisons, several performance metrics were used. These are the algorithm's estimation of planar defect width (2D and 3D defects), defect length (3D defects only), defect orientation angle (2D and 3D defects) and through-wall height (TWH) (2D and 3D defects). Imaging Signal-To-Noise Ratio (SNR) was also considered.

The following conventions have been used to define the x-, y- and z-axes within this thesis. The x-axis is defined to be the direction along the linear array considered within an inspection case. The y-axis is defined to be the direction directly under the array into the component being inspected. The z-axis is defined to be in the direction perpendicular to the $x-y$ plane.

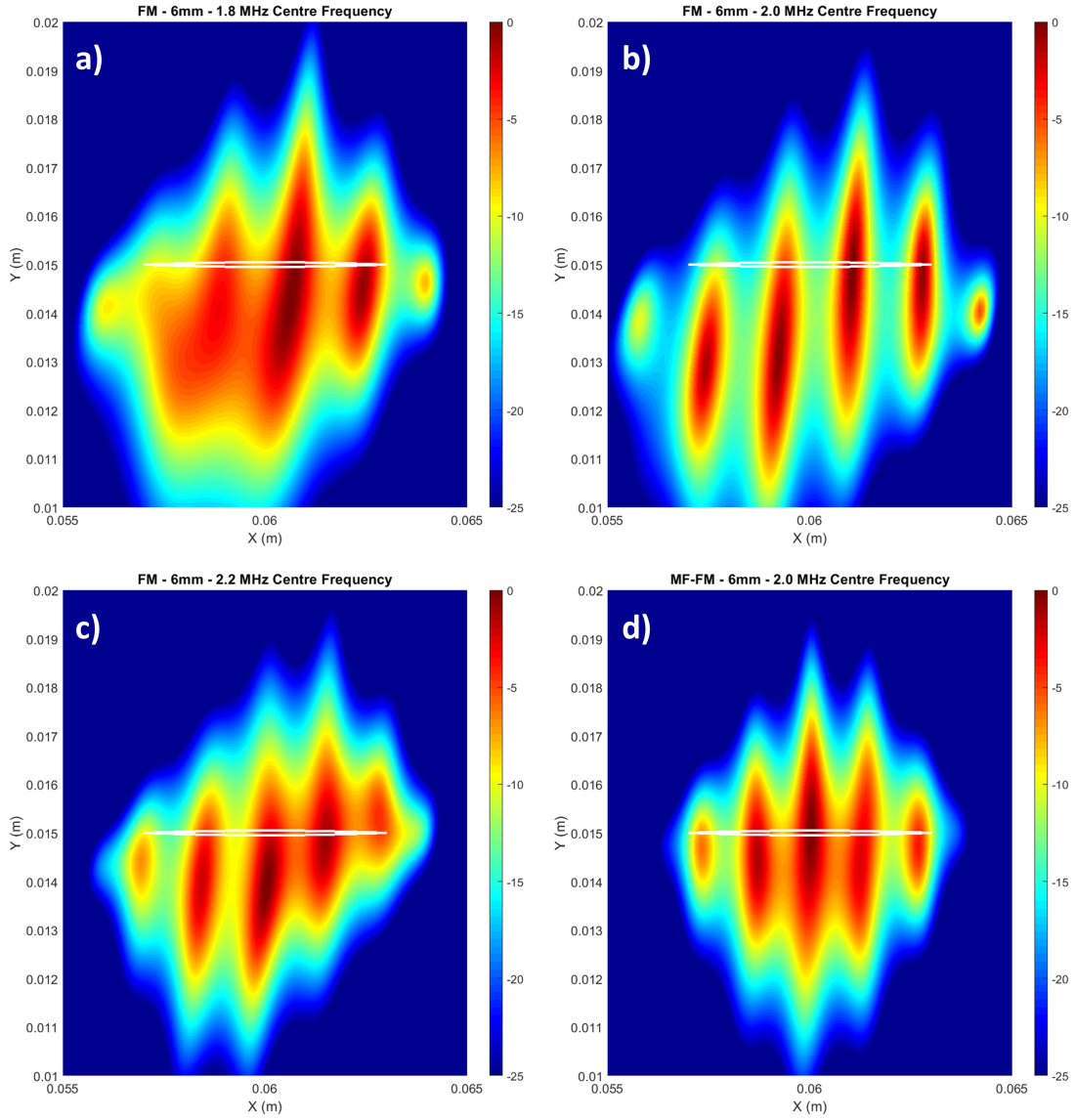


Figure 2.11: The impact of using different centre frequencies on single frequency FM imaging where a 5-cycle 2 MHz toneburst was used to inspect a 6 mm embedded planar defect, shown in white. The images produced used single a centre frequency of a) 1.8 MHz, b) 2.0 MHz, c) 2.2 MHz. d) is a MF-FM image centred on 2 MHz where nine frequencies were evenly sampled between 1.6 MHz – 2.4 MHz. These images were produced from the simulated FMC inspection of a planar embedded defect with a 64-element located at a distance of 42 mm, centrally positioned above the defect. The set-up is illustrated in Fig. 1.7.

These conventions are illustrated in Fig. 2.13. Defect width and length correspond to the minor and major dimensions of the defect, and orientation describes the rotation of the defect plane relative to the component coordinate system. In the examples included in the following Chapters, the majority of defects considered are representative of longitudinal weld defects (major defect axis aligned with the welding direction). Defect width therefore lies in the through thickness plane, or xy-plane, direct TWH aligns

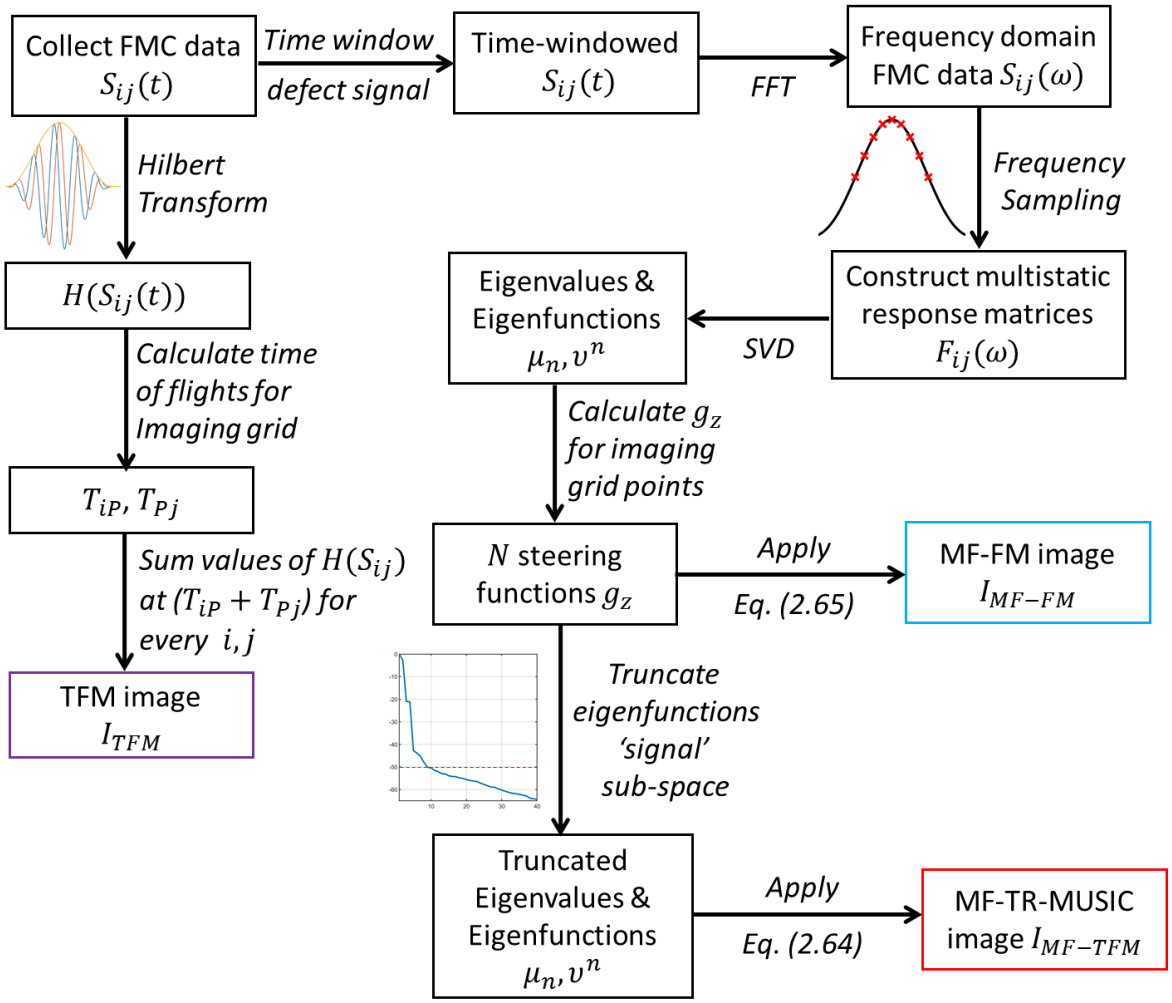


Figure 2.12: Flowchart detailing the implementation of the TFM, MF-FM and MF-TR-MUSIC algorithms on ultrasonic array FMC datasets. Detailed description of the implementation steps are found within the main text.

with the y-axis, and defect length aligns with the z-axis.

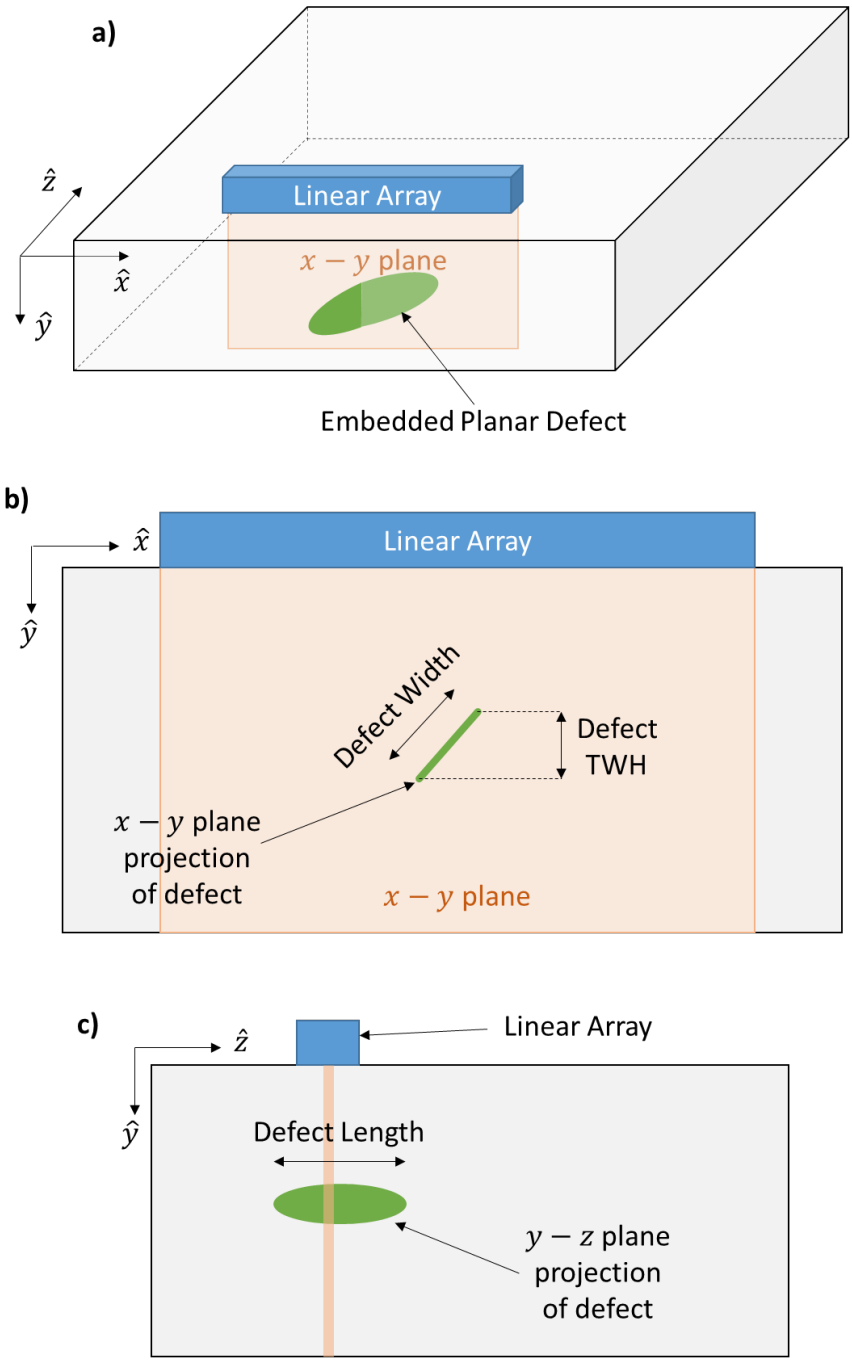


Figure 2.13: The conventions used to define the x-, y- and z-axes and defect parameters in this thesis. a) 3D view of a linear array (blue, orientated in the $\hat{x}$-axis) inspection of an embedded planar defect (green), with the image generated in the $x-y$ plane (orange). b) $x-y$ plane projection of a) where defect width and TWH are defined. c) $y-z$ plane projection of a) where defect length is defined.

Chapter 3

SR Imaging of Simulated Embedded Smooth Planar Defects

3.1 Introduction

In the assessment of the structural integrity of safety-critical components in the nuclear power industry, there is a drive to detect and size increasingly smaller defects particularly during manufacture. This is partly due to progressively more stringent inspection procedure requirements of critical defect sizes in an attempt to not only bolster the component safety case but also with the aim of extending component life. If a smaller defect can reliably be sized during a manufacturer inspection or in-service inspection, conventional conservative estimates of defect growth means the component can remain in service longer before a repair/replace threshold is met. With the ageing nature of current NSRPs in the defense and power sectors, there is a strong drive to accurately characterise and size these small defects. SR phased array imaging methods have been recently developed which may unlock the capability to size sub-wavelength defects and overcome some of the inspection challenges facing industry today.

This Chapter discusses the use of two-dimensional (2D) Finite Element (FE) modelling techniques to simulate the linear ultrasonic array inspection of embedded smooth planar defects within isotropic stainless steel components, a common material used within the nuclear sector. Simulated FMC datasets were collected from defects of varying parameters such as size and orientation, as well as varying inspection parameters such as the inspection frequency, size of the array and levels of incoherent noise in the obtained signals.

Understanding the capabilities of these SR methods, namely the MF-FM and MF-TR-MUSIC algorithms, in these simple inspection cases (i.e. fully embedded, smooth, 2D approximation) allows for a baseline understanding of the behaviour of these algorithms to be established before more complex modelling and experimental investigations can be conducted. As will be seen, the sizing capabilities of the SR algorithms against varying embedded planar defect width and orientation has been quantitatively determined for the first time. The impact of random noise on these defect morphologies has also been established. In addition, a new non-dimensional

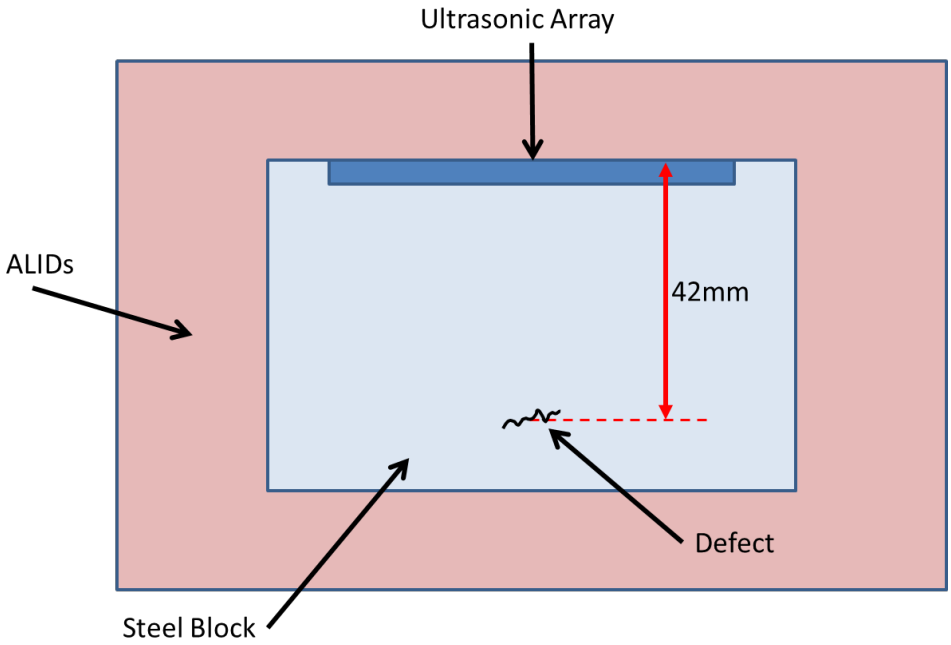


Figure 3.1: FE inspection setup for the array imaging of 2D embedded planar defects. The origin position of the models is located at the centre of the defect.

trend between the indication pattern of the SR algorithms and planar defect size was observed which suggests that sizing estimates may be achievable by simply observing the image patterns generated.

3.2 Modelling Approach

To model an array inspection of 2D planar defects, full FE simulations were run using the GPU-based solver Pogo [67], which allowed significantly faster simulation run times compared to conventional CPU-based FE solvers.

The inspection schematic used for the FE models is shown in Fig. 3.1. In all the cases, a steel block was simulated with dimensions of 100 mm x 50 mm, a Young's modulus of 200 GPa, Poisson's ratio of 0.3, density of 7750 kgm^{-3} and a longitudinal wave velocity of 5894 ms^{-1}. As a simplification, material attenuation was not considered.

The ultrasonic array was modelled using a series of pure longitudinal wave point sources at the array element positions, which were separated by half the ultrasonic longitudinal wave wavelength corresponding to the centre frequency. For example at 2 MHz in stainless steel, $(\lambda/2)$ corresponds to 1.5 mm. This separation is typical of ultrasonic arrays. A 5-cycle Hann windowed toneburst was used to generate the ultrasonic pulse at the required centre frequency. On the reception of the ultrasonic signal, only the component of displacement normal to the array length was recorded. To model the longitudinal wave point sources, the closest four nodes within the FE mesh located about the excitation positions, corresponding to the phased array element centre points, were excited uniformly radially away from

those locations. This ensured that symmetric radially emanating longitudinal waves were generated, with a shear-wave component close to zero.

The directivity of the point sources used in the FE models, $\Psi_{FE}(\theta)$, can be considered as the product of the transmission directivity function, $\Psi^T_{FE}(\theta)$, and the reception directivity function, $\Psi^R_{FE}(\theta)$:

$$\Psi_{FE}(\theta) = \Psi^T_{FE}(\theta)\Psi^R_{FE}(\theta) = \Psi^R_{FE}(\theta) = \cos(\theta), \tag{3.1}$$

where $\Psi^T_{FE} = 1$ as it is uni-directional due to its point source nature. A real array element's directivity can be analytically modelled in the far-field as the directivity of a strip source of finite width on a surface of a semi-infinite solid, $\Psi_{M-P}(\theta)$, using the outputs from Miller and Pursey [68] and Wooh and Shi [69]:

$$\Psi_{M-P}(\theta) = \text{sinc}\left(\frac{\pi a \sin(\theta)}{\lambda}\right) \frac{\left((c_L/c_S)^2 - 2\sin^2(\theta)\right)\cos(\theta)}{F_0(\sin(\theta))}, \tag{3.2}$$

where a is the array element width, c_L is the bulk longitudinal wave velocity, c_S is the bulk shear wave velocity, and F_0 is defined by:

$$F_0(\tau) = \left(2\tau^2 - \left(\frac{c_L}{c_S}\right)^2\right)^2 - 4\tau^2(\tau^2-1)^{\frac{1}{2}}\left(\tau^2 - \left(\frac{c_L}{c_S}\right)^2\right)^{\frac{1}{2}}. \tag{3.3}$$

The directivity profiles of Ψ_{FE} and Ψ_{M-P} are compared in Fig. 3.2 using representative input values of $\lambda = 3$ mm, $a = 1.2$ mm, $c_L = 5894$ ms^{-1} and $c_S = 3150$ ms^{-1}. It can be seen that Ψ_{FE} slightly overestimates the directivity profile compared to $\Psi_{M-P}(\theta)$ with a maximum deviation of 8.6% at $\pm 45.8°$. The maximum angular offset of the defects in the FE simulations from the end of the 2 MHz 64-element arrays considered was $\pm 48.8°$ corresponding to an overestimation in wave field amplitude of 8.5%. The highly simplistic modelling approach utilised in this thesis of exciting only single point sources to represent the array elements was considered to be a reasonable approximation for a realistic linear array based on the similarity between the directivity profiles. Experimental validation conducted in later Chapters will be used to validate this approach.

Different excitation approaches were used for the transmission and reception of the ultrasound in the models in an attempt to more accurately represent the operation of realistic phased arrays whilst retaining some of idealised behaviour. The benefit of using pure longitudinal wave point sources during excitation means that a negligible amount of shear waves are generated within the model; acting to simply analysis by reducing the number of mode converted signals with the simulated datasets. The downside of this source model is that they are not realistic in terms of their directivity. By only loading FE nodes in the direction perpendicular to the array length, a much more realistic directivity is achieved as shown in Fig. 3.2, however the downside is that both longitudinal and shear waves are generated. By combining these approaches by exciting pure longitudinal waves and enforcing directivity on reception, models with high wave mode purity can be obtained whilst edging towards a more realistic scenario in terms of directivity. This approach is of course no longer reciprocal, hence why the full

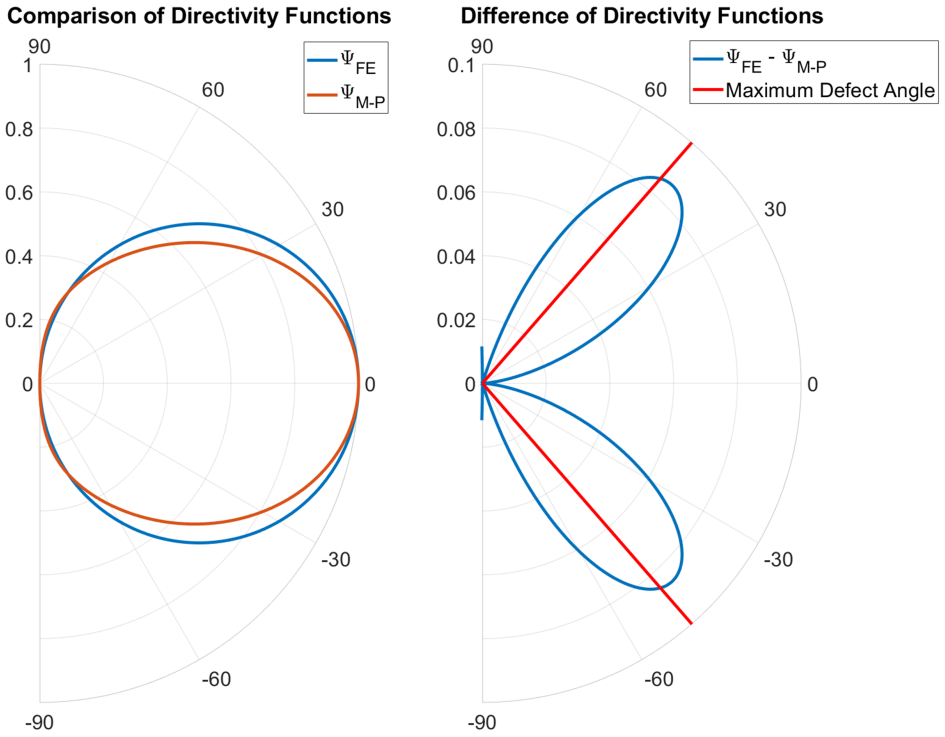


Figure 3.2: Comparison between the directivity function of the FE longitudinal wave point sources employed in this thesis, Ψ_{FE}, and an analytical far-field directivity pattern for a 2D array element, Ψ_{M-P}. Values of $\lambda = 3$ mm, $a = 1.2$ mm, $c_L = 5894$ ms^{-1} and $c_S = 3150$ ms^{-1} were used to calculate Ψ_{M-P}. These directivity functions have been normalised. In the RHS figure, the red line corresponds to angles of $\pm 48.8°$ which is the maximum angular difference between the position of the end array elements and the centrally located defects at a depth of 42 mm.

FMC datasets have been simulated instead of depending on reciprocity to generate FMC data from half-matrix capture approaches. It is expected that the non-reciprocal nature of the simulation will have minimal effect on the imaging algorithms applied.

The steel block region in the FE models was surrounded by the regions of Absorbing Layers with Increased Damping (ALIDs) [70, 71]. These layers were used to absorb unwanted reflections from model boundaries to help ensure that only the defect scattered signal was recorded by the array and subsequently processed by the imaging algorithms. This represented the idealised scenario of a noise-free inspection with no unwanted reflections from component geometry or defect mode conversions.

The FE element size, d, was set to 50 μm which corresponds to $(\lambda/d) = 60$. It was set to this value to best conform to the defect surfaces, particularly for the rough defects considered in later Chapters, so as to capture as much of the complex scattering as possible. Previous work has shown this level of refinement to be sufficient for these types of surfaces [72, 73]. The ALIDs

were set to be 180 FE elements thick (3λ). The FE meshes consisted of triangular elements and were structured everywhere, except in the local region of the defect where they were set to be unstructured to allow for optimal conformity to the defect profile. Triangular elements were selected for optimal defect conformity. The built-in mesher within the FE modelling package Abaqus FEA [74] was used to construct the meshes, with the `CPE3` element type.

A case with no defect was modelled for each array configuration to capture any small unwanted reflection from the ALIDs, and this recorded FMC dataset was subtracted from all subsequent defect simulations using the same array configuration.

The defects were centred symmetrically under the array to maximize the viewing angle on the defects to enhance the SR imaging capability, at a depth of 42 mm (14λ) from the array. The simulated work presented in this thesis considered idealised cases where the ultrasonic array viewing angle has been maximized for a particular inspection scenario and the imaging algorithms were applied to the noise-free FE simulation data. It should be noted that both viewing angle and noise can have significant effects on the performance of SR imaging.

The impact of viewing angle on imaging has been previously studied by Hutt [37]. The concept of viewing angle is illustrated in Fig. 3.3. Hutt considered the imaging capability of the TFM and FM algorithms and demonstrated how as the aperture of a circular array decreased (equivalent to the definition of viewing angle used in this thesis), the accuracy of defect profile reconstruction through imaging worsened. The performance of the TFM algorithm was observed to decrease more rapidly with a reducing viewing angle than the FM. This was because as the aperture decreases, the number of large singular eigenvalues decreased implying that the significance of the smaller singular values becomes more prominent. As the TFM algorithm is reliant on the information carried by the largest eigenvalues [37], the imaging reconstructions from them degrade rapidly as the aperture decreases. The FM utilised all eigenvalues and therefore is less impacted by a reduction in viewing angle. It is noted that even though a larger linear array may have a geometrically larger viewing angle, the effect of increasing the number of elements indefinitely has an increasingly smaller effect on the received information from the scatterer due to the inherent directivity of the elements which do not equally emit ultrasound energy in all angular directions (predominantly focussed down from the array).

To simulate defect opening, the profile of flat smooth defects were opened apart symmetrically by displacing the top and bottom surfaces by a half-cycle sinusoidal function. The maximum opening was twice the FE element size (100 μm) at the centre of the defect and no opening at the defect tips. This process to generate the 2D open smooth cracks is shown graphically in Fig. 3.4. Open defects were used instead of defects with no thickness to increase the realism of the modelling. It is noted that there was no significant difference in ultrasonic response and images between the gaped and un-gaped planar defects, which is expected due to negligible profile change relative to the ultrasonic wavelength.

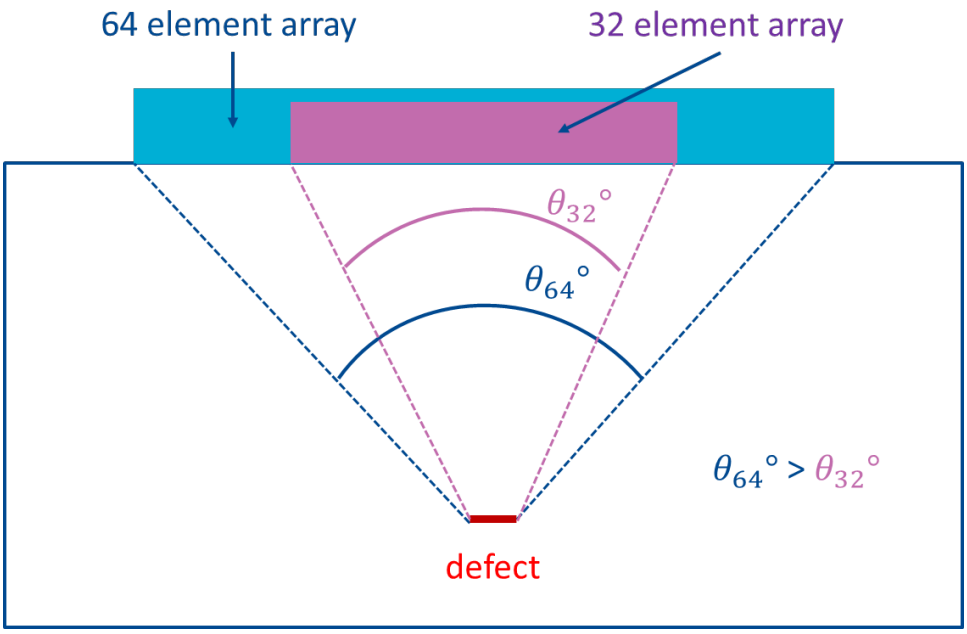


Figure 3.3: An illustration of the difference in viewing angle achieved by two different sized linear arrays, with the wider 64-element array achieving a larger viewing angle (θ°_{64}) than the 32-element array (θ°_{32}).

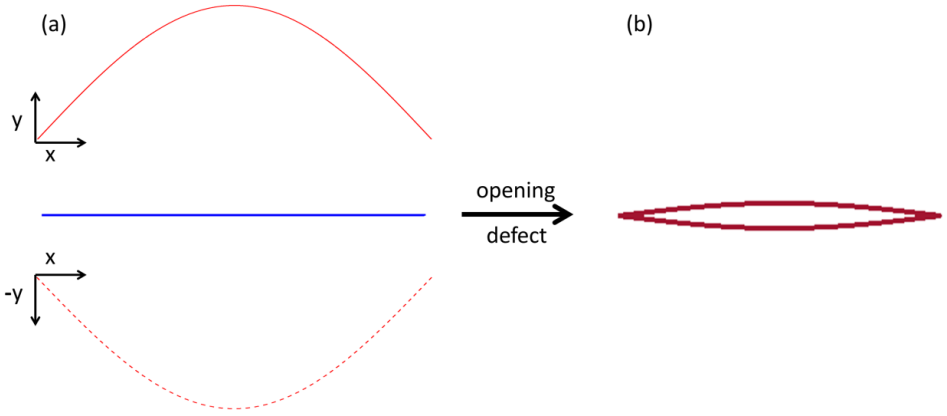


Figure 3.4: Visualisation of the process to generate 2D smooth embedded defects. First a smooth flat defect profile is calculated (a). The crack is then opened by a small amount, varying along its width, by displacing the top surface upwards by the half-cycle sinusoidal profile function shown in the solid red line at the top of (a) and similarly moving the bottom surface down by the dashed red at the bottom of (a). The resulting open 2D smooth defect is shown in (b).

3.3 Imaging Sizing Methodology

When conventionally inspecting planar embedded defects with a single crystal pulse-echo probe in a specular or near-specular incidence configuration, a Pattern 2 type response would be expected to be obtained as defined by the British NDE standard BS EN ISO 16827 [75]). For this type of defect response, when the ultrasonic beam is moved over the defect the received signal rises smoothly to a plateau and it is maintained with minor variations across the planar defect face. This happens until the beam moves off the defect, where the signal falls smoothly down to background noise level. For this type of response, the 6 dB drop method would be used to estimate the defect size. The 6 dB drop method is employed by moving the ultrasonic probe across the defect and the width of the measured amplitude profile is related to the flaw size. In this case, the width between the indication centre (maximum amplitude) and to where the signal level drops to half of this peak amplitude (-6 dB) is estimated to be half the size of the defect [76, 75]. The method works well for well-defined flaws whose size is larger than the beam width and that are at normal or near-normal incidence.

When using TFM, a 6 dB box-fitting algorithm was applied to the images to provide an estimate of the size and orientation of the defect. This sizing algorithm fits a parallelogram box to the TFM images with the constraint that the box must contain all image pixels within a -6 dB range of the maximum indication pixel value. The algorithm finds the optimal orientation of the box such that all the pixels above -6 dB are included whilst minimizing the number of pixels which are below this threshold. The defect width was attributed to the width of the pair of parallelogram sides orientated in the direction closest to the known defect orientation. The slant angle of this same pair of sides was the measured defect inclination. An illustration of the application of the 6 dB box-fitting algorithm is shown in Fig. 3.5a). When using TFM and other conventional ultrasonic techniques to image embedded planar defects which have a misorientation angle far from the normal, tip diffraction signals are often used for sizing. This is done by locating the central positions of the tip indications within the image, and assuming the defect is a straight line between these points. This line is used to estimate the defect width and orientation. An illustration of the application of tip sizing is shown in Fig. 3.5b).

When using the SR algorithms to characterise defect indications, it is important to understand the imaging patterns they produce for embedded flaws. Both algorithms essentially work by determining the likelihood that a point scatterer exists at the imaging grid points, based on the scattered field information. When imaging small planar defects, strong indications are often produced from the tips of the defects as the diffraction effects from these locations correspond most closely to that of point scatterers. It is from these tip locations that the defect width and orientation can be estimated. This sizing methodology is often not possible with TFM images of small defects and amplitude based methods must be applied. For volumetric defects, such as large pores and side drilled holes, similar indications are produced from the SR algorithms as when applied to planar defects. However, as the defect size approaches zero and becomes more point-like, only single indications are produced by the algorithms and no direct sizing information

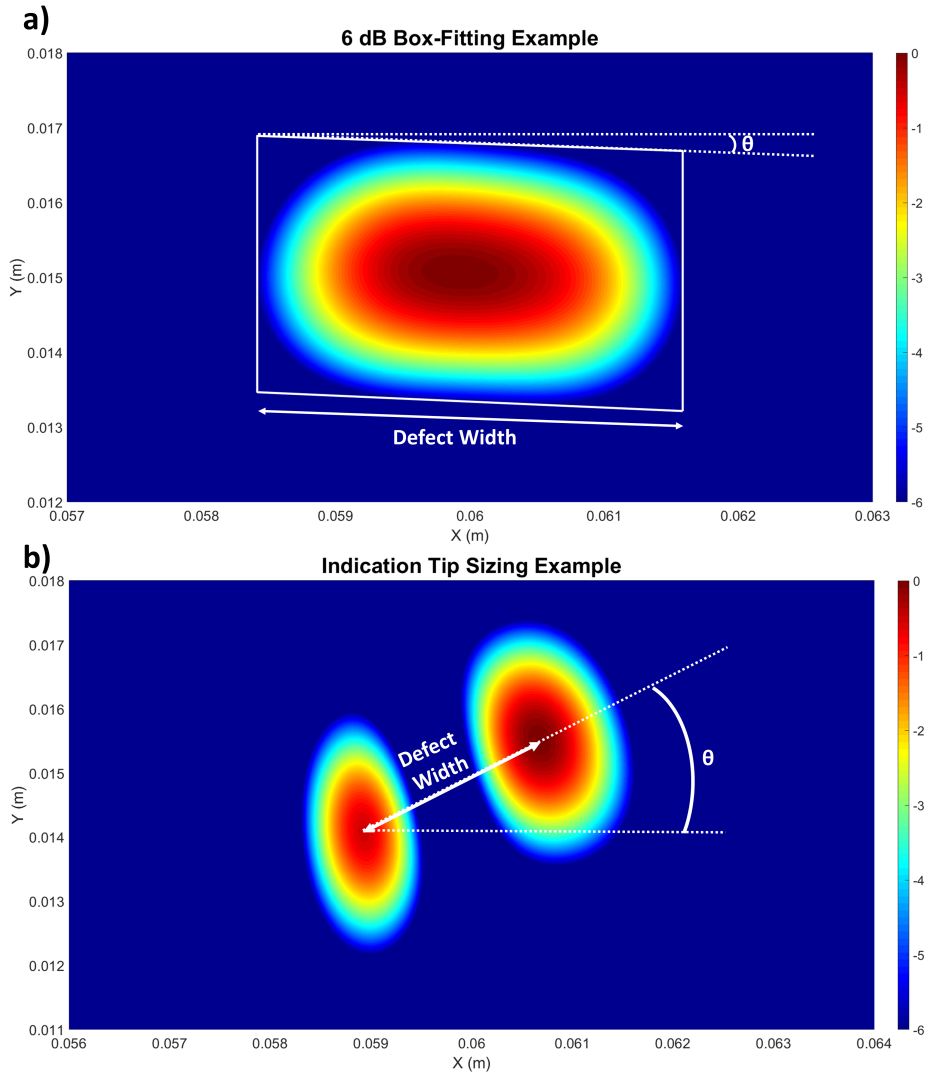


Figure 3.5: a) An example of the application of the 6 dB box-fitting algorithm to a TFM image of a planar defect. From the parallelogram defined by the algorithm, the defect width as well as the defect inclination, θ, is able to be determined. b) An example of tip sizing where the defect width and inclination are defined by the straight line between the two tip maxima.

can be gained. In these cases, one could infer that the defect size is smaller than the smallest defect size that can be reliably characterised.

3.4 SR Imaging Performance for Varying Defect Size

This Section investigates the sizing capability of the advanced array imaging algorithms when inspecting smooth, planar defects of varying width. 2D FE simulations were performed, using the set-up described in Section 3.2, to obtain modelled FMC datasets upon which the TFM and SR algorithms were applied. The defects were orientated parallel to the array and were

Table 3.1: The 2D smooth planar defect sizes modelled with FE.

Defect Size (mm)	Defect Size (λ)
1	0.33
1.5	0.5
3	1
4	1.33
5	1.66
6	2
10	3.33

centrally located underneath it to maximise the viewing angle to ensure maximum performance could be achieved.

Two array configurations were considered: a 2 MHz 64-element array and a 2 MHz 32-element array. Each array was identical apart from the difference in number of elements, resulting in arrays different in length by a factor of two. This resulted in the 32-element array having a reduced viewing angle on the defect as well as a reduction in the total information collected and analysed for imaging. The reduced viewing angle should theoretically result in a poorer reconstruction of the defect through imaging and a potential drop in sizing performance. The variance in performance is quantified below.

A total of seven different sized smooth planar defects were simulated, with their widths listed in Table 3.1. The images generated by the MF-FM, MF-TR-MUSIC and TFM algorithms when imaging these defects with the 2 MHz 64 element array configuration are shown in Fig. 3.6.

In addition, the array data was used to generate a 0° B-Scan image. This is the array equivalent to a 0° pulse-echo B-Scan where conventionally, a monolithic transducer with a fixed aperture is scanned along the component and an image is generated from the pulse-echo data. The array B-Scan is similar to the conventional transducer B-Scan but a group of adjacent elements, known as the aperture, are fired in a pulse-echo configuration to mimic a fixed aperture transducer. This array aperture is then electronically rastered along the array with a scan increment equal to the array element pitch. A schematic for 0° B-Scan array imaging is shown in Fig. 3.7. In these simulations the element pitch, and therefore the B-Scan increment, was 1.5 mm which resulted in an inherent lateral resolution of 0.75 mm within the images. Array B-Scan images were generated alongside the other algorithms for the different sized defects and are also shown in Fig. 3.6. For each B-Scan imaging case, the aperture size was optimised to output the most accurate defect size so that the best possible array B-Scan performance can be compared.

For each algorithm, the image pixel size was set to 50 μm.

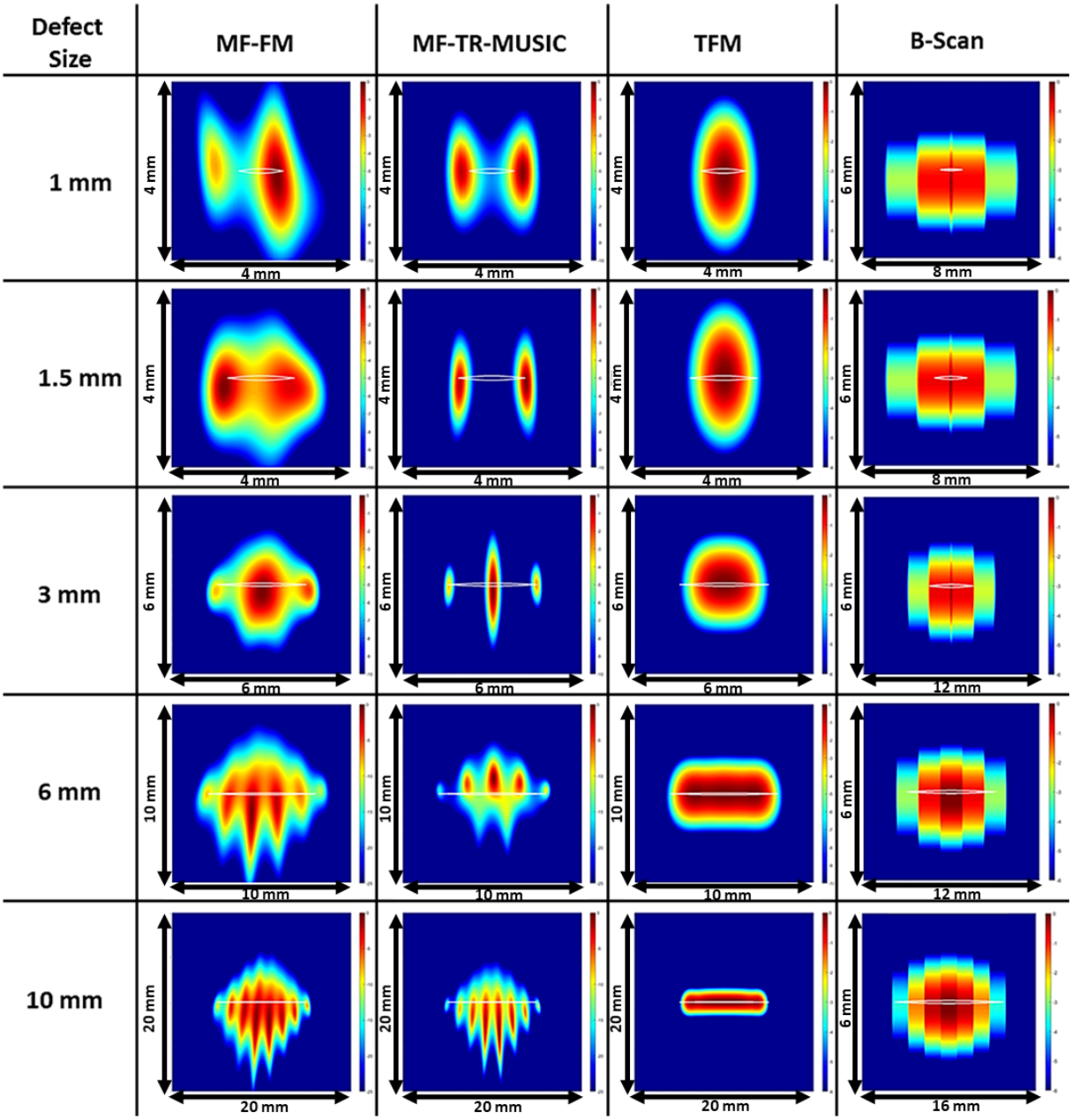


Figure 3.6: MF-FM, MF-TR-MUSIC, TFM and array B-Scan images from the 2D FE simulated inspection of (1, 1.5, 3, 6 and 10) mm 0° smooth planar embedded defects. The active aperture size for the B-Scan images was 16.5 mm for defects smaller than 6 mm and 15 mm otherwise. All images are plotted in a decibel scale, with all TFM and B-Scan images plotted between 0 and -6 dB. The set-up shown in Fig. 3.1 was used, featuring a 64-element 2 MHz array centred above the defects at a distance of 42 mm.

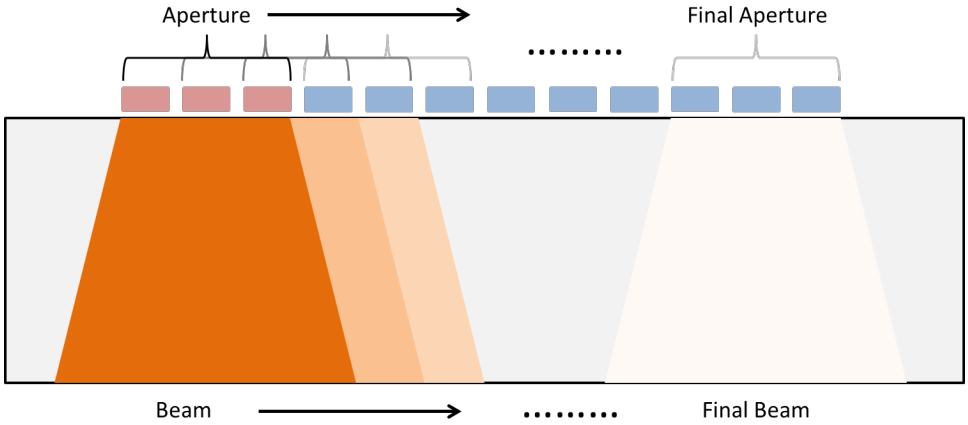


Figure 3.7: Illustration of how a 0° B-Scan is generated by a contact linear ultrasound array. A group of elements are fired in a pulse-echo configuration, known as the aperture, and this aperture is electronically scanned across the array to generate a B-Scan image.

As discussed in Section 3.3, the SR images produce indications from the tips of the defects. When imaging the planar flaws at or below the diffraction limit (1.5 mm) in Fig. 3.6, the only indications generated by the SR algorithms are located at tips of the defects. As discussed previously, an assumption of the SR algorithms is that they are based on the imaging of idealised point scatterers which act to generate pure diffractive scattered wavefields. As the tips of the planar defects most closely resemble point scatterers, combined with the small planar surface naturally leading to a minimal specular scattered component, it is expected that the only indications generated by the SR algorithms are from the tips of the flaws.

However, as can be seen in Fig. 3.6 when imaging defects larger than the diffraction limit, multiple indications are generated across the planar face of the defects as well from the defect tip positions. Despite the assumption of the background theory of the SR algorithms being based on point scatterers, it has been shown that these methods can be used to reconstruct the profile of extended defects well [37], as opposed to the discontinuous, clustered indication patterns shown in Fig. 3.6. In the cases where good reconstruction of extended defects has been shown in previous studies, it is noted that either full or near-full angular coverage has been obtained, as demonstrated by Hutt (2012) [37] who simulated the 2D inspection of an embedded kite-shaped flaw with a circular array. It was shown that an accurate, continuous representation of the flaw profile was obtained when the viewing angle of the circular array was 120° or greater. This is expected as an assumption of the SR algorithms is that full angular coverage of defects is obtained. When the viewing angle was dropped to 80°, although the general size of the defect was clear within the image, the reconstructed defect profile started to become discontinuous and similar in nature to Fig. 3.6. The model utilised within [37] also employed uni-directional point source transducer elements which would lead to unrealistic idealised sensitivities. The model used within this thesis was that of a linear array with realistic element directivity functions meaning that although viewing angles of

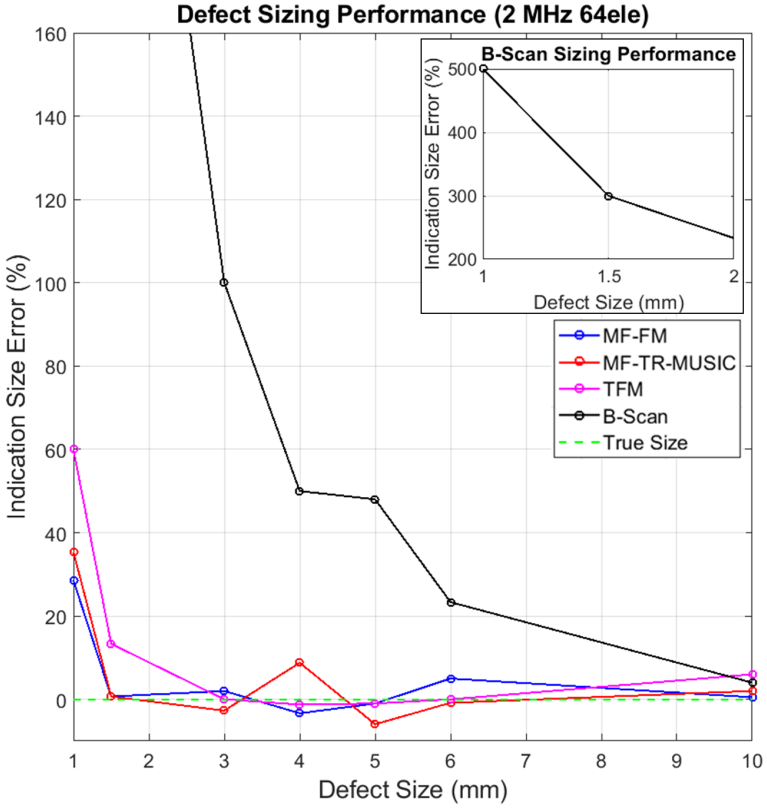


Figure 3.8: Defect sizing results from the 2D FE simulated 2 MHz 64-element array inspection using the MF-FM, MF-TR-MUSIC, TFM and array B-Scan algorithms.

98° and 59° are achieved with the 64-element and 32-element 2 MHz array configurations, the sensitivities of the elements worsened the further they were located away from the flaw. This leads to effective viewing angles of the linear arrays being lower than their absolute value. It is therefore expected that the ability of the SR algorithms to reconstruct the profile of the extended flaws considered within this Section are diminished and that only parts of the defect profiles can be reconstructed in this challenging limited view inspection.

Despite these complex indication patterns generated by the SR algorithms, they are still able to consistently generate image indications from the tips of the defects and therefore these were used to width size them. The 6 dB drop sizing method was used to size the TFM and B-Scan images. The width sizing results from the algorithms for the 2 MHz 64-element and 32-element configurations are plotted in Fig. 3.8 and Fig. 3.9 respectively. The results are also listed in Table 3.2 and Table 3.3.

Considering the results from the 2 MHz 64-element array configuration, it can be seen that for all defects below 10 mm (3.33 λ), the MF-FM, MF-TR-MUSIC and TFM significantly outperform the array 0° B-Scan. The B-Scan method returns a minimum size of the defects of 6 mm, indicating that in this configuration, the technique is beam width limited to this value and is therefore incapable of accurately sizing smaller defects. For the defects 3 mm (1 λ) wide and above, the TFM and SR algorithms were very similar

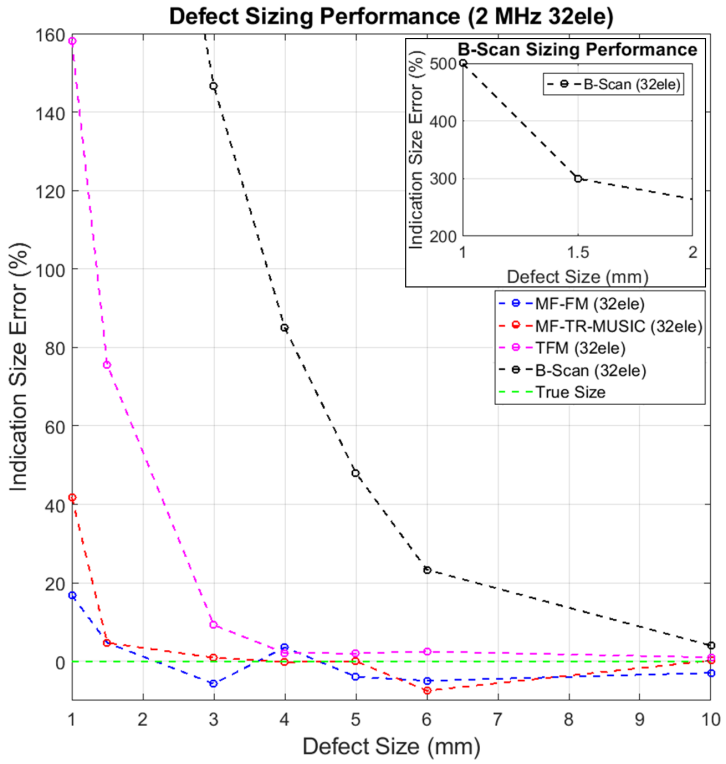


Figure 3.9: Defect sizing results from the 2D FE simulated 2 MHz 32-element array inspection using the MF-FM, MF-TR-MUSIC, TFM and array B-Scan algorithms.

Table 3.2: Sizing performance of the algorithms for the 2 MHz 64-element array configuration.

Defect Size (mm)	**MF-FM (mm)**	**MF-TR-MUSIC (mm)**	**TFM (mm)**	**B-Scan (mm)**
1	1.29 ± 0.04	1.35 ± 0.04	1.60 ± 0.04	6 ± 1
1.5	1.51 ± 0.04	1.51 ± 0.04	1.70 ± 0.04	6 ± 1
3	3.06 ± 0.04	2.92 ± 0.04	3.00 ± 0.04	6 ± 1
4	3.87 ± 0.04	4.35 ± 0.04	3.95 ± 0.04	6 ± 1
5	4.95 ± 0.04	4.70 ± 0.04	4.95 ± 0.04	7 ± 1
6	6.30 ± 0.04	5.95 ± 0.04	6.00 ± 0.04	7 ± 1
10	10.05 ± 0.04	10.20 ± 0.04	10.60 ± 0.04	10 ± 1

with all estimating the defect size accurately to less than 10% error. The TFM algorithm was the most accurate within this range, with a maximum sizing error of 6%.

It is below a defect size of 3 mm where the performance of the TFM and SR algorithms diverge. The TFM algorithm becomes beam width limited and it struggles to accurately size defects at or below the diffraction limit ($\lambda/2$). The performance of the algorithm is still significantly better than the B-Scan equivalent with only an overestimating sizing error of 13% and 60%

Table 3.3: Sizing performance of the algorithms for the 2 MHz 32-element array configuration.

Defect Size (mm)	**MF-FM (mm)**	**MF-TR-MUSIC (mm)**	**TFM (mm)**	**B-Scan (mm)**
1	1.17 ± 0.04	1.42 ± 0.04	2.58 ± 0.04	6 ± 1
1.5	1.57 ± 0.04	1.57 ± 0.04	2.63 ± 0.04	6 ± 1
3	2.83 ± 0.04	3.03 ± 0.04	3.28 ± 0.04	7 ± 1
4	4.147 ± 0.04	3.99 ± 0.04	4.08 ± 0.04	7 ± 1
5	4.80 ± 0.04	5.00 ± 0.04	5.10 ± 0.04	7 ± 1
6	5.70 ± 0.04	5.55 ± 0.04	6.15 ± 0.04	7 ± 1
10	9.70 ± 0.04	10.02 ± 0.04	10.10 ± 0.04	10 ± 1

for the 1.5 mm and 1 mm defect cases respectively. Both of the SR methods are able to outperform TFM at these defect scales, being able to accurately size defects at the diffraction limit (1.5 mm) and return more accurate sizing results for the ($\lambda/3$) size defects ($\approx$ 30% overestimation error).

Comparing the 64-element configuration results to the 32-element configuration results, the B-Scan results are almost identical. This is expected as the number of elements used within each aperture between the 64-element and 32-element was the same and as the defects were centred under the array, the aperture was able to be adequately rastered across it. The TFM algorithm for defects above 3 mm also produced similar results to the 64-element configuration; however there was a significant performance reduction for smaller defects. This was due to the beam width size increasing for the smaller array size as expected due to a reduced ability of the array to generate a smaller focal spot. The SR algorithms performance remained very similar across both array configuration set-ups indicating that for defects of this orientation, a 32-element array size was sufficient to collect FMC data sufficient to generate accurate SR images.

A key feature that is apparent within the SR images shown in Fig. 3.6 is that as the defect size being imaged increases, the number of indications produced by the algorithms also increases. To determine whether this trend is present at other inspection frequencies, several other array configurations were simulated at different frequencies featuring a range of defect sizes scaled to the ultrasonic wavelength. As well as the 2 MHz 64-element array that was already modelled, a 1 MHz 64-element array and a 4 MHz 64-element array was modelled. For each array, the element pitch was maintained at $\lambda/2$. The number of indications generated by the different array configurations for varying defect size is shown in Fig. 3.10. As can be seen from the graph, there is a general linear trend between the planar defect size measured in wavelengths and the number of indications produced by the SR algorithms.

It is observed that generally, the number of indications is equal to the number of nodes present within a waveform of length specified by the defect

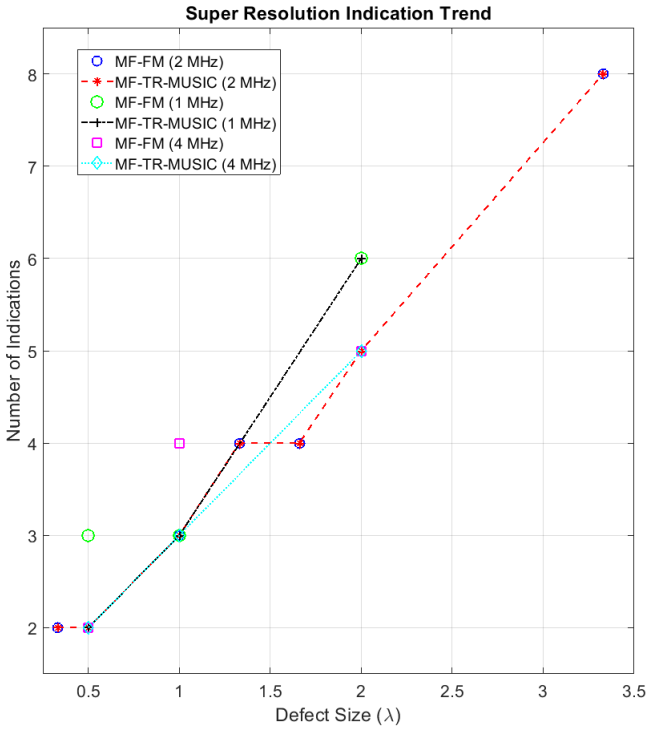


Figure 3.10: SR indication trend using a simulated 1 MHz, 2 MHz and 4 MHz 64-element ultrasonic arrays.

size measured in wavelengths. For example, a half wavelength sized defect is expected to have two indications, a wavelength sized defect is expected to have three indications and two wavelength sized defect is expected to have five indications. It is currently not known the mechanism which leads to the multiple indication patterns generated by the SR algorithms however this empirical trend may potentially be used as guidance for defect sizing using the SR imaging techniques.

It is noted that although the number of array elements is held constant as the inspection frequency is varied, the viewing angle of each array is different due to the element pitch being fixed at half the ultrasonic wavelength. The fixed pitch resulted in array sizes of 192 mm, 96 mm and 48 mm for the 1 MHz, 2 MHz and 4 MHz configurations respectively. This may account for some of the slight variation between the different inspection frequencies. The trends presented here are only for a single range value of 42 mm from the arrays to the defect depth position. It is expected that it will not hold for all range values, with a worsening imaging performance occurring as the range continues to increase (as the apparent array viewing angle decreases) and it is anticipated that the SR algorithms would begin to underestimate the defect size (fewer indications for a given defect).

3.5 The Effect of Defect Misorientation on SR Imaging Performance

Another defect parameter which can have a significant impact on defect characterisation is that of defect misorientation. This is because it is widely

recognised that the presence of defect misorientation reduces the amplitude of a specularly reflected ultrasonic signal in comparison to the reflected signal that would have otherwise returned from the defect if it had be aligned perpendicular to the incident beam. The greater the defect misorientation angle, the greater the reduction of the signal amplitude. For highly misorientated defects, it is often not possible to apply amplitude based sizing techniques and sizing becomes reliant on defect tip detection. For sub-wavelength sized defects, the resolution restrictions of conventional ultrasonic NDE techniques means it is not always possible to obtain accurate sizing of these misorientated defects.

2D FE simulations were run to simulate the 2 MHz array inspection of 1.5 mm defects of varying tilt. The same model set-up as described in Section 3.2 was used.

The 1.5 mm ($\lambda/2$) defect case was selected as this represents a challenging defect inspection and one which may potentially benefit from the SR array algorithms. The tilt of the defects was varied from 0°, defined to be parallel to the array (maximum specular response), to 90° which was perpendicular to the array, in 10° increments.

The SR sizing methodology described in Section 3.3 was employed in all cases. The 6 dB drop sizing method was used for the TFM algorithm when clear tip responses could not be resolved.

The simulations were run in both 64-element and 32-element array configuration to investigate any performance differentials between the set-ups. A selection of the array images for the 2 MHz 64-element configuration are shown in Fig. 3.11.

As well as FE simulations to model the array inspection of the defects, 2D Time-Of-Flight Diffraction (TOFD) simulations were run for the equivalent defects using CIVA [77]. The CIVA models consisted of two 5 MHz 60° longitudinal wave probes separated by 145 mm. This separation value was selected such that the included angle between the beams incident on the defect was close to 120°, as recommended by the ISO TOFD inspection standard [78] to maximise the diffracted compression waves from the defect tips [79]. The TOFD probes were scanned across the 2D defect in the simulation and the set-up parameters and Through-Wall Height (TWH) sizing procedures were in line with the ISO TOFD inspection standard [78]. The TOFD sizing method is only able to be used to estimate the TWH of a defect, not its true width and tilt. In practical NDE inspections, TWH is often the most important defect parameter in terms of sizing due to the extremely high influence it has on the structural integrity of NSRP components. CIVA uses the Geometrical Theory of Diffraction (GTD) [80] when modelling defect edges in the TOFD configuration and the approximation is generally valid when considering off-specular incident angles and in-direct forward transmission paths.

The defect sizing results, orientation estimation results and TWH sizing results for the 2 MHz 64-element array configuration are shown in Fig. 3.12, Fig. 3.13 and Fig. 3.14.

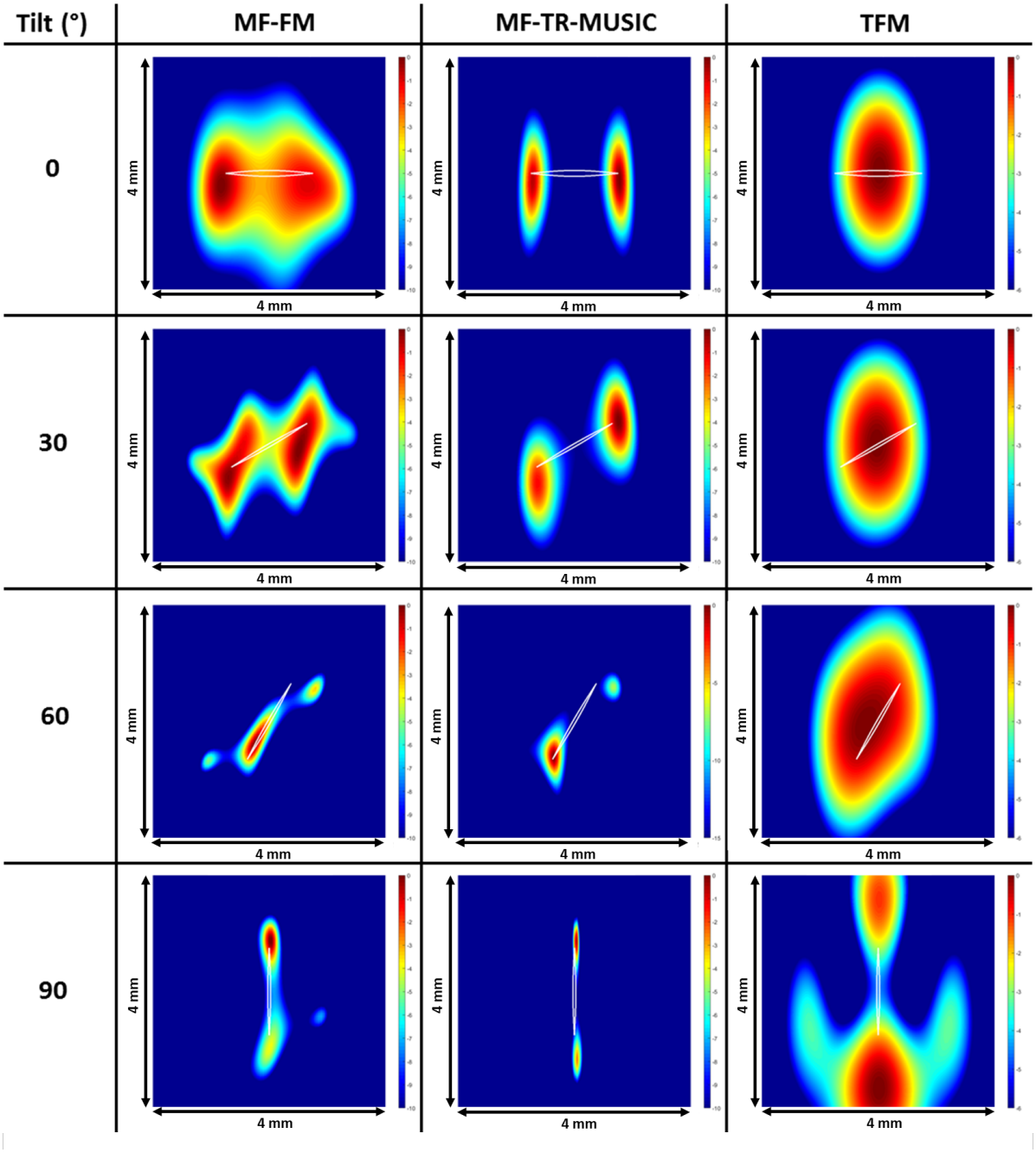


Figure 3.11: Defect images produced from the 2D FE simulated 2 MHz 64-element array inspection of 1.5 mm planar defects of various orientations. The MF-FM, MF-TR-MUSIC and TFM algorithms were used. All images are plotted in a decibel scale, with all TFM images plotted between 0 and -6 dB. The set-up shown in Fig. 3.1 was used, with the array centred above the defects at a distance of 42 mm.

Considering the sizing results shown in Fig. 3.12, it can be seen that the TFM provides a reasonably accurate sizing result for the 0° and 10° cases where it overestimates the defect size by around 13%. The performance progressively worsens gradually to around 33% overestimation at 50° inclination. The performance then sharply drops as the inclination increases

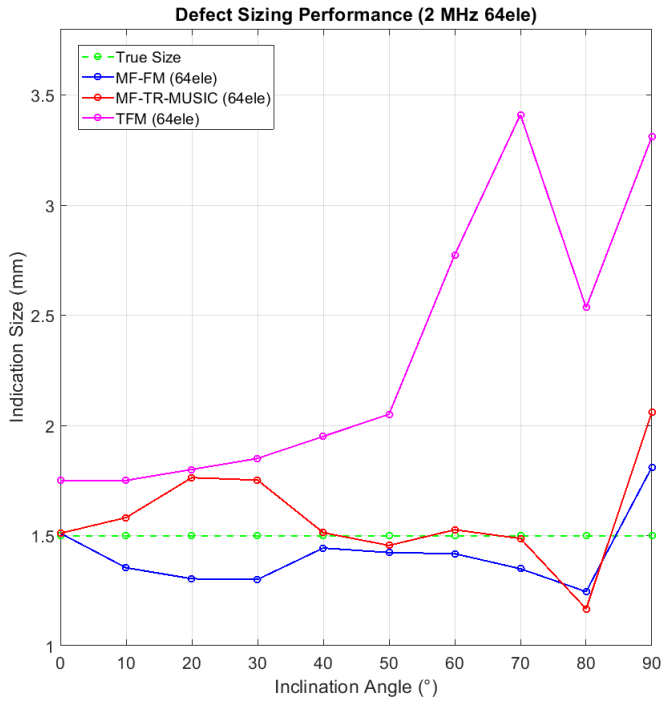


Figure 3.12: Defect sizing results from the 2D FE simulated 2 MHz 64-element array inspection of 1.5 mm planar defects of various orientations.

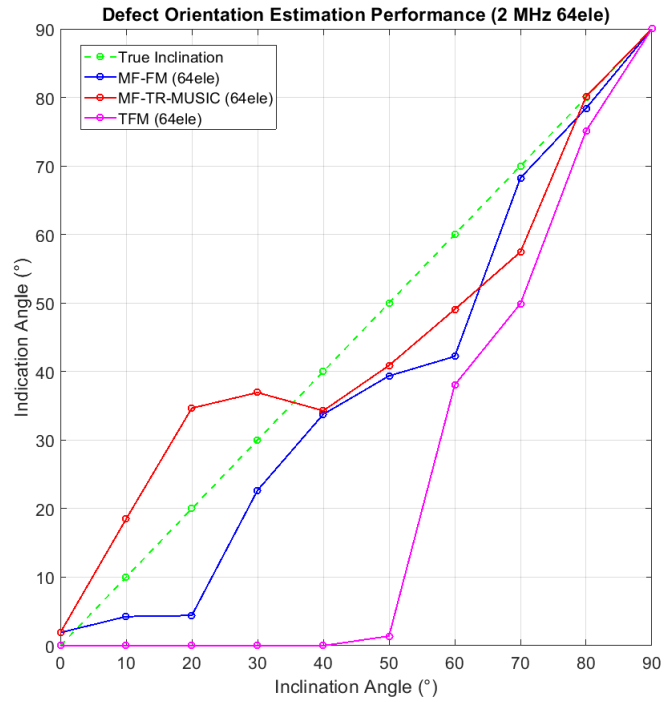


Figure 3.13: Defect orientation estimation results from the 2D FE simulated 2 MHz 64-element array inspection of 1.5 mm planar defects of various orientations.

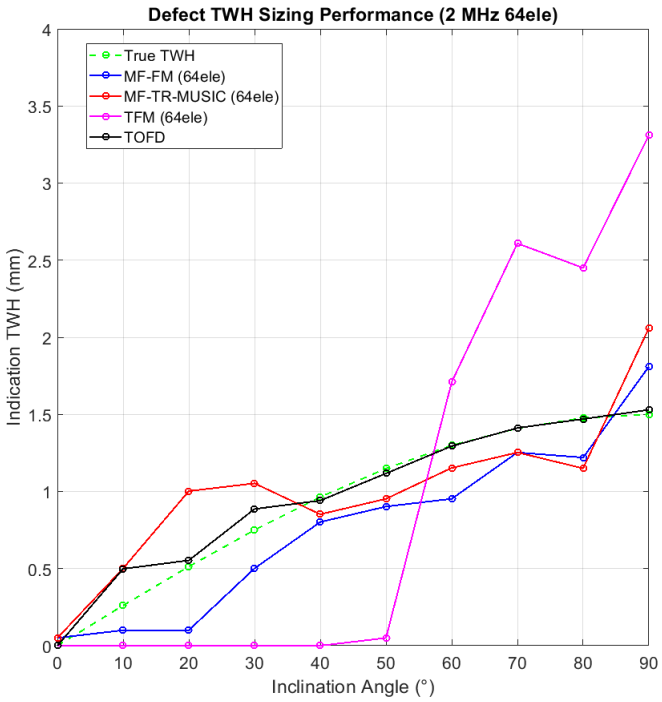


Figure 3.14: Defect TWH estimation results from the 2D FE simulated 2 MHz 64-element array inspection of 1.5 mm planar defects of various orientations.

to 70° with a maximum sizing error of around 120%. This is due to the applicability of the 6 dB drop sizing method becoming increasingly invalid as the specularly reflected component of the scattered ultrasound decreases as misorientation increases. For the 80° and 90° cases, tip indications could be resolved with TFM which accounts for some performance being regained however it still consistently overestimates the defect size by over 70%.

From Fig. 3.13 and Fig. 3.14, it is clear that the TFM algorithm also fails to accurately estimate the defect TWH across the entire inclination range and only at high inclination angles can it accurately estimate the defect misorientation. The lack of performance of TFM for this sub-wavelength case is expected due to inspection being carried out at the diffraction limit.

From Fig. 3.12, it can be seen that the SR algorithms achieve a much better performance than TFM in terms of sizing and maintain accuracy across the entire defect inclination range. This is due to the techniques being able to generate defect tip indications for all misorientation angles, as shown in Fig. 3.11. Fig. 3.13 and Fig. 3.14 also show that both the MF-FM and MF-TR-MUSIC algorithms can effectively estimate the defect orientation and therefore the defect TWH.

Also from Fig. 3.14, it can be seen that the simulated TOFD results are extremely accurate at and above 20°. For defects in the range 0°-10°, the use of TOFD becomes challenging due to the difficulty in resolving between individual peak signals from the separate tips. Although TOFD provided the most accurate TWH sizing results, the clear disadvantage of the method is

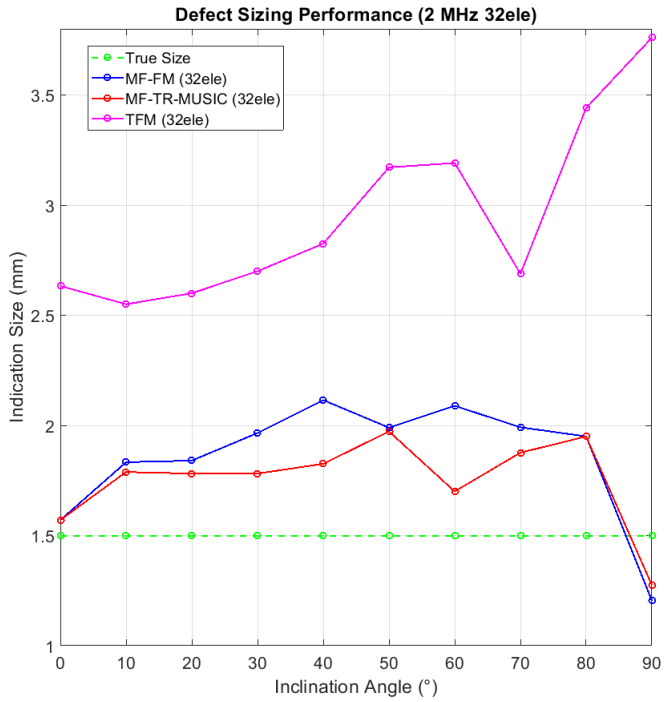


Figure 3.15: Defect sizing results from the 2D FE simulated 2 MHz 32-element array inspection of 1.5 mm planar defects of various orientations

a lack of information of the defect width and orientation, which the array algorithms could provide. Also in practice, several separate TOFD scans would be needed to effectively analyse different depth ranges in a component, whereas a single FMC array scan has the potential to generate a more informative description of embedded planar defects regardless of depth.

It is worth noting that at the higher defect inclinations, indications located at the sides of the defect appear, particularly within the TFM images. These have been attributed to Rayleigh surface waves that are generated on the defect when incident with the ultrasonic beam. These surface waves travel along the defect and then are mode converted to diffracted compression waves at the defect tips at slightly later times, thus producing indications away from the defect location.

The defect width sizing results, orientation estimation results and TWH sizing results for the 2 MHz 32-element array configuration are shown in Fig. 3.15, Fig. 3.16 and Fig. 3.17 respectively.

The 32-element TFM sizing results show similar trends to the 64-element case, however the results at lower inclination angles ($< 60°$) show significantly poorer sizing accuracy as they overestimate the defect width by around 70%. This is in agreement with the results presented in Section 3.4. The 32-element TFM results for defect orientation estimation and TWH sizing are also similar to the 64-element case.

For the defects at or less than 80° inclination, the 32-element SR algorithms

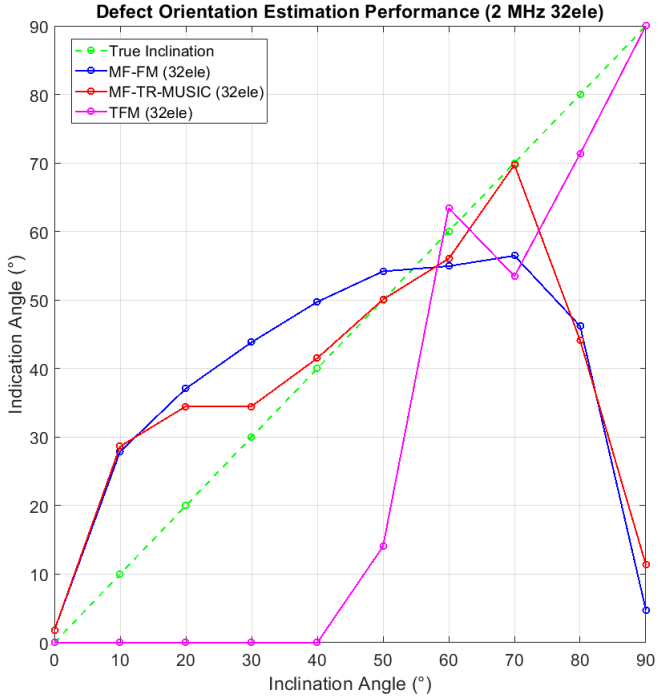


Figure 3.16: Defect orientation estimation results from the 2D FE simulated 2 MHz 32-element array inspection of 1.5 mm planar defects of various orientations.

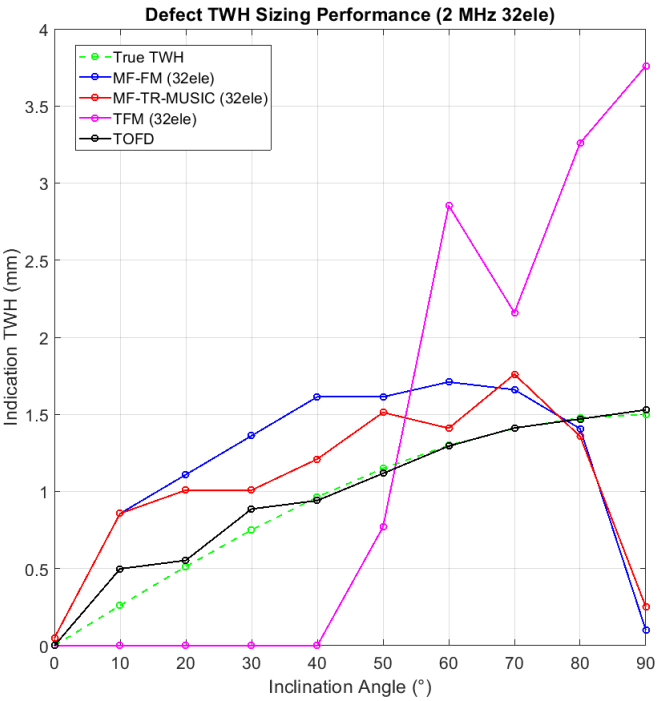


Figure 3.17: Defect TWH estimation results from the 2D FE simulated 2 MHz 32-element array inspection of 1.5 mm planar defects of various orientations.

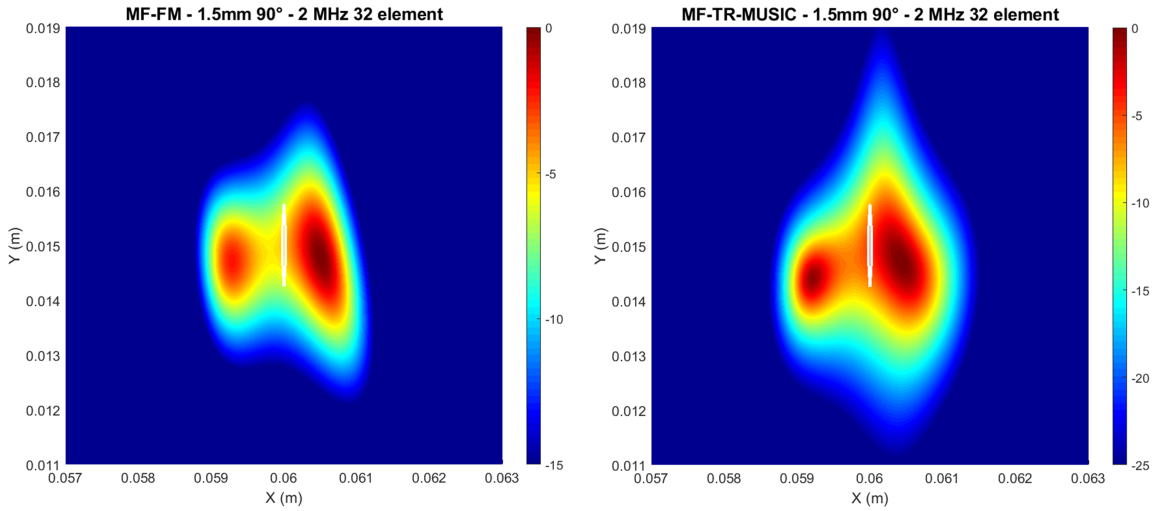


Figure 3.18: MF-FM and MF-TR-MUSIC images of a 1.5 mm 90° planar 2D defect when inspected by a 2 MHz 32-element array.

largely produce results similar to the 64-element case with a slight performance reduction of around 10%. The biggest difference in performance between the array configurations comes when imaging the fully inclined 90° tilted defects. In this case, as shown in Fig. 3.18, the SR algorithms fail to reconstruct the true profile of the defect and produce images representative to a 0° equivalent flaw. This results in an extremely poor estimation of the defect orientation and TWH, as illustrated by the sharp drop off in accuracy in Fig. 3.16 and Fig. 3.17.

3.6 The Effect of Incoherent Noise on SR Imaging Performance

In the FE simulated results considered in Sections 3.4 and 3.5, the FMC data obtained were almost perfectly '*clean*' signals with no unwanted reflections from model boundaries leaving only the initial pulse and defect scattered signals in the A-Scans. This is an idealised scenario as in practical inspections, there are a variety of sources of signal noise which act to reduce the Signal-To-Noise (SNR) of the collected data.

There are two broad classes of signal noise: incoherent noise and coherent noise [81]. Incoherent noise is a type of random noise which is uncorrelated over time and thus can be averaged out to reduce its effect. Coherent noise is correlated over time and thus cannot be averaged out over time, therefore posing a major problem for some inspections. An example of coherent noise is material grain noise caused by sub-structures within the component leading to local scattering and path deviation. Components with austenitic stainless steel welds can often exhibit spatially-varying anisotropic, large grained structures and can therefore lead to significant amounts of coherent noise within the collected ultrasonic data. The SR algorithms in particular have been shown to degrade in imaging performance when significant levels of signal noise are present [34, 37].

Fan *et al.* [34] investigated the impact of noise on the TFM and TR-MUSIC algorithm through both simulation and experimentation. The simulation studies, which added varying levels of random Gaussian White Noise (GWN) to the noise-free simulation data, found that when the SNR was greater than 20 dB, the TR-MUSIC algorithm outperformed TFM when imaging two separated point reflectors in terms of resolution and 6 dB image area size. When the SNR was less than 5 dB however, the TR-MUSIC algorithm was particularly poor as the resolution capability dropped sharply, as did the 6 dB image area size (which featured large elongated indications) and the abundance of unwanted imaging artefacts. SNR was defined as:

$$\text{SNR} = 20\log_{10}\left(\frac{A_{peak}}{A_{Noise}}\right), \tag{3.4}$$

where A_{peak} is the amplitude of the maximum defect scattered signal within the FMC dataset and A_{Noise} is the Root-Mean-Squared (RMS) amplitude of the random GWN added.

The experimental findings reported in [34] compared the imaging performance of TFM and the TR-MUSIC algorithms when inspecting two closely separated 0.5 mm Side Drilled Holes (SDHs) in steel and copper samples. The low material noise steel samples were imaged effectively by both algorithms however in the copper sample, which exhibited significantly more material noise, the TFM algorithm showed far better noise robustness than the TR-MUSIC method.

Hutt [37] investigated the impact of random GWN to the simulated circular array imaging of an arbitrary kite-shaped reflector on the TFM and FM algorithms. GWN was also added to noise-free simulated data in this study to investigate the impact of incoherent noise on imaging performance. It was found that the FM was far more sensitive to noise than the TFM method. The TFM algorithm mainly uses the information carried by the largest singular eigenvalues that are not significantly affected by noise, which partly explains its robustness to noise. The FM attempts to use the information from all the eigenvalues, including ones with small singular values that are significantly impacted by noise. This leads to the higher sensitivity of the FM algorithms to noise.

In this Section, the effect of incoherent noise on array imaging is investigated by adding GWN into the noise-free FMC simulated data generated in Section 3.4. GWN was added to the datasets to achieve four different levels of SNR: 40 dB, 20 dB, 10 dB and 1 dB. The same definition of SNR as described in Eq. (3.4) was used. The noise-free FMC data collected via a 2 MHz 64-element array for the 1.5 mm, 3 mm and 6 mm planar smooth defects from Section 3.4 was used to add the varying levels of GWN. Example A-Scans from the 3 mm defect cases with varying SNRs are shown in Fig. 3.19. Fig. 3.19 also demonstrates the time windowing that was applied when generating the SR images.

As well as the visible change in SNR in the A-Scans, Fig. 3.19 also shows the variation in eigenvalue amplitude (as generated post-SVD of the FMC data) as the SNR increases. As expected, the number of significant eigenvalues, corresponding to the *signal* subspace as discussed in Section 2.8.2, decreases

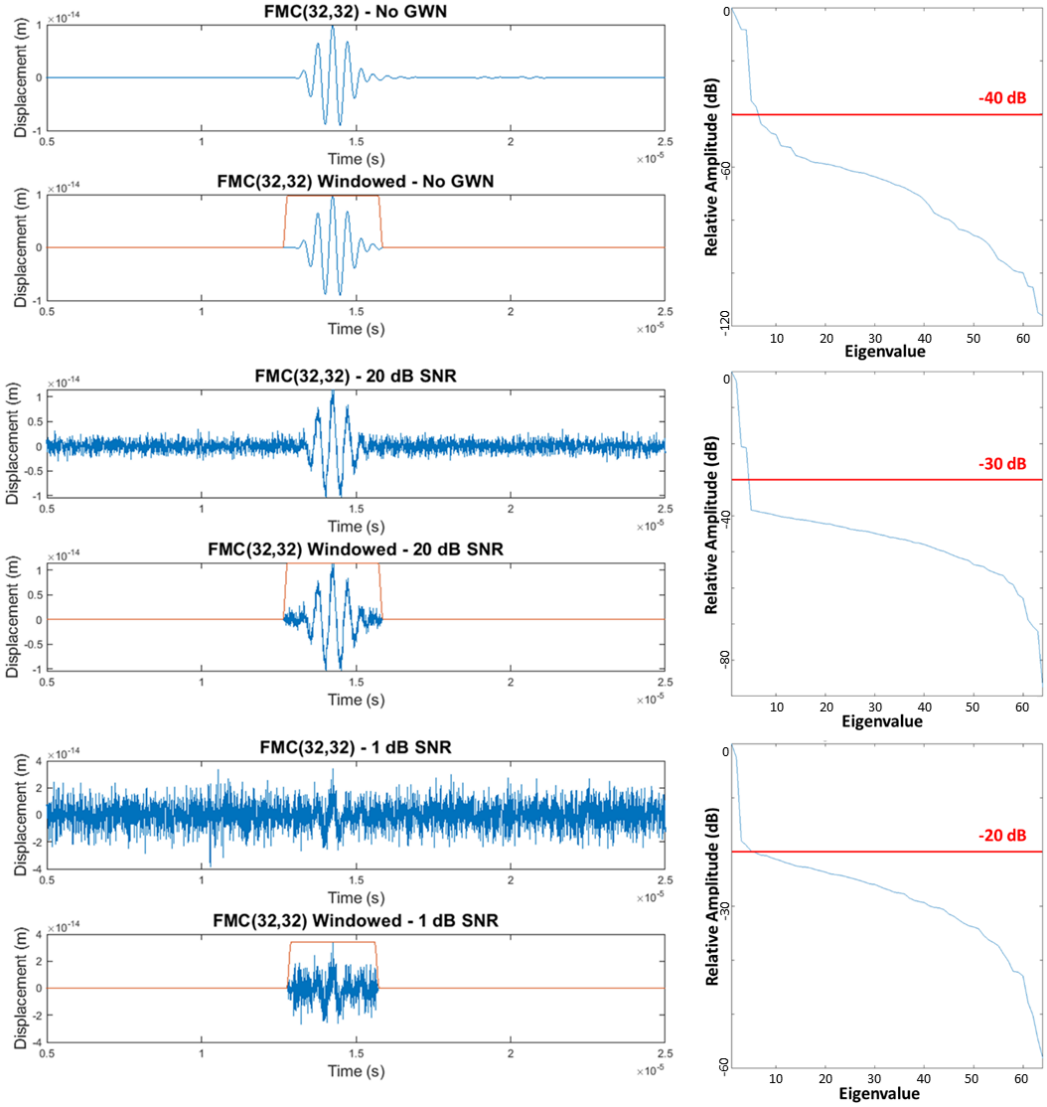


Figure 3.19: Example A-Scans from the simulated FMC data from the 2 MHz 64-element array inspection of an embedded 3 mm smooth planar defect with varying levels of added GWN. The time-windowing that was applied prior to SR imaging is shown. The eigenvalue amplitude for each corresponding FMC data set is plotted adjacent to the A-Scans.

as the noise increases. This results in requiring a lower eigenvalue cut-off when conducting TR-MUSIC imaging.

The images produced by the MF-FM, MF-TR-MUSIC, TFM and array B-Scan algorithms are shown in Fig. 3.20, Fig. 3.21 and Fig. 3.22 when varying levels of GWN was applied to the simulated noise-free FMC datasets from the 1.5 mm, 3 mm and 6 mm defects.

The sizing performance of all the algorithms against increasing SNR for the different defect sizes are shown in Fig. 3.23, Fig. 3.24 and Fig. 3.25.

First considering the B-Scan images and results, it can be seen that as the SNR decreases there are increasing levels of imaging noise in comparison

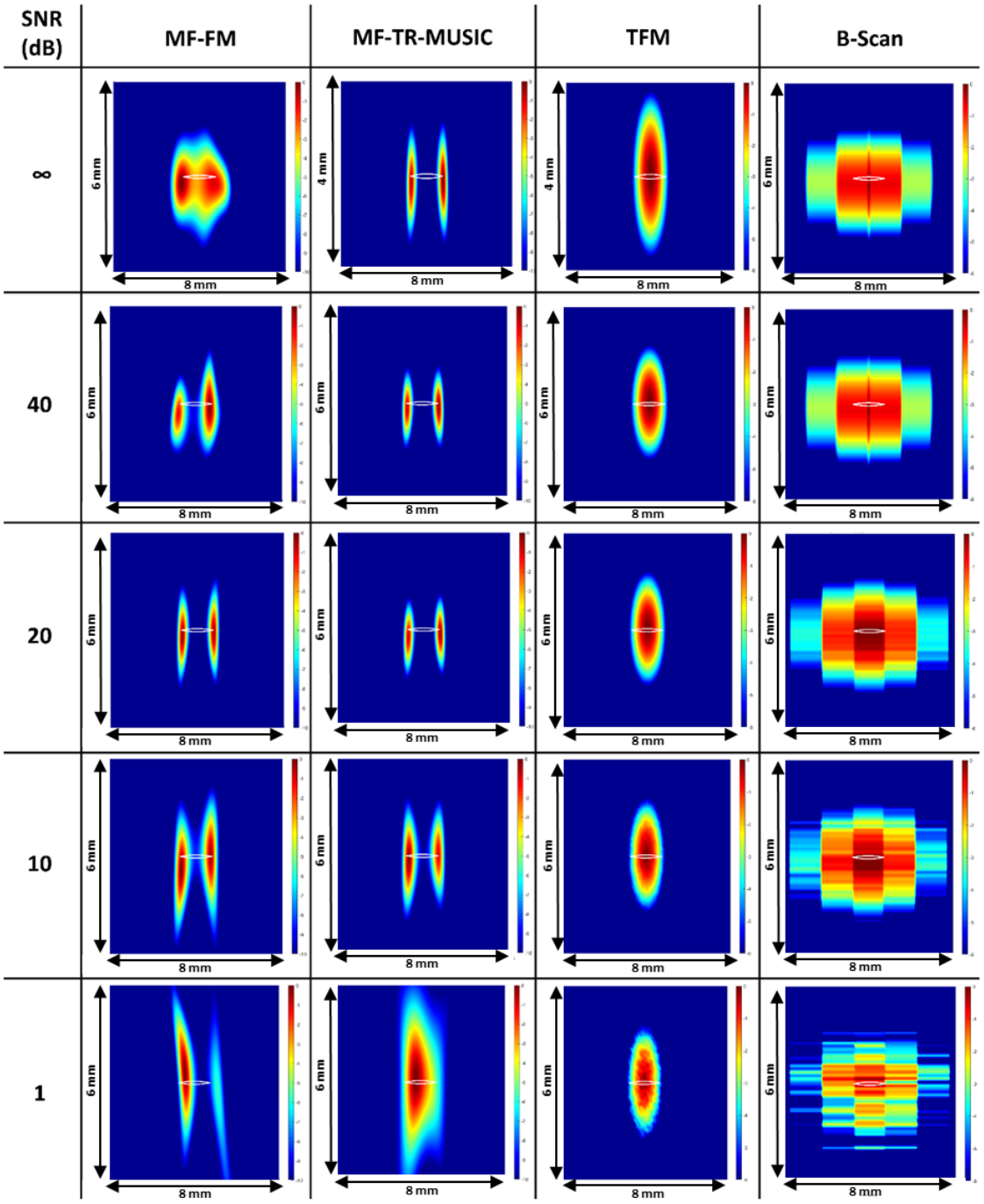


Figure 3.20: MF-FM, MF-TR-MUSIC, TFM and array B-Scan images generated from the simulated 2 MHz 64-element array inspection of an embedded planar 1.5 mm defect, where varying levels of GWN were added to achieve different SNRs. All images are plotted in a decibel scale, with all TFM and B-Scan images plotted between 0 and -6 dB and all MF-FM and MF-TR-MUSIC images plotted between 0 and -10 dB. The set-up shown in Fig. 3.1 was used, with array centred above the defects at a distance of 42 mm.

to the noise-free image. The sizing performance generally remains stable

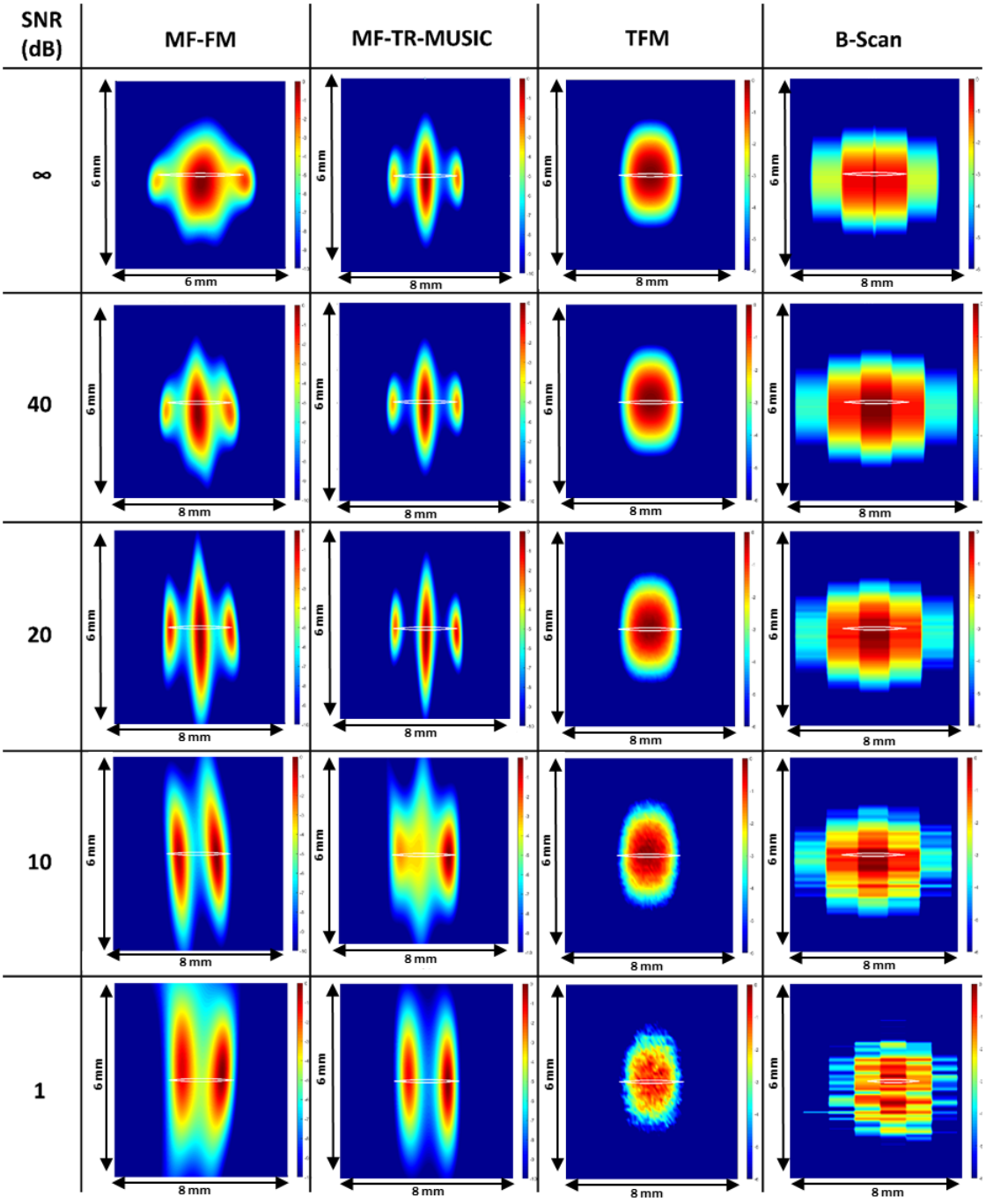


Figure 3.21: MF-FM, MF-TR-MUSIC, TFM and array B-Scan images generated from the simulated 2 MHz 64-element array inspection of an embedded planar 3 mm defect, where varying levels of GWN were added to achieve different SNRs. All images are plotted in a decibel scale, with all TFM and B-Scan images plotted between 0 and -6 dB and all MF-FM and MF-TR-MUSIC images plotted between 0 and -10 dB. The set-up shown in Fig. 3.1 was used, with array centred above the defects at a distance of 42 mm.

however, it is only when the SNR reduces below 10 dB that a relative performance drop is observed. The drop in performance is seen as a step change

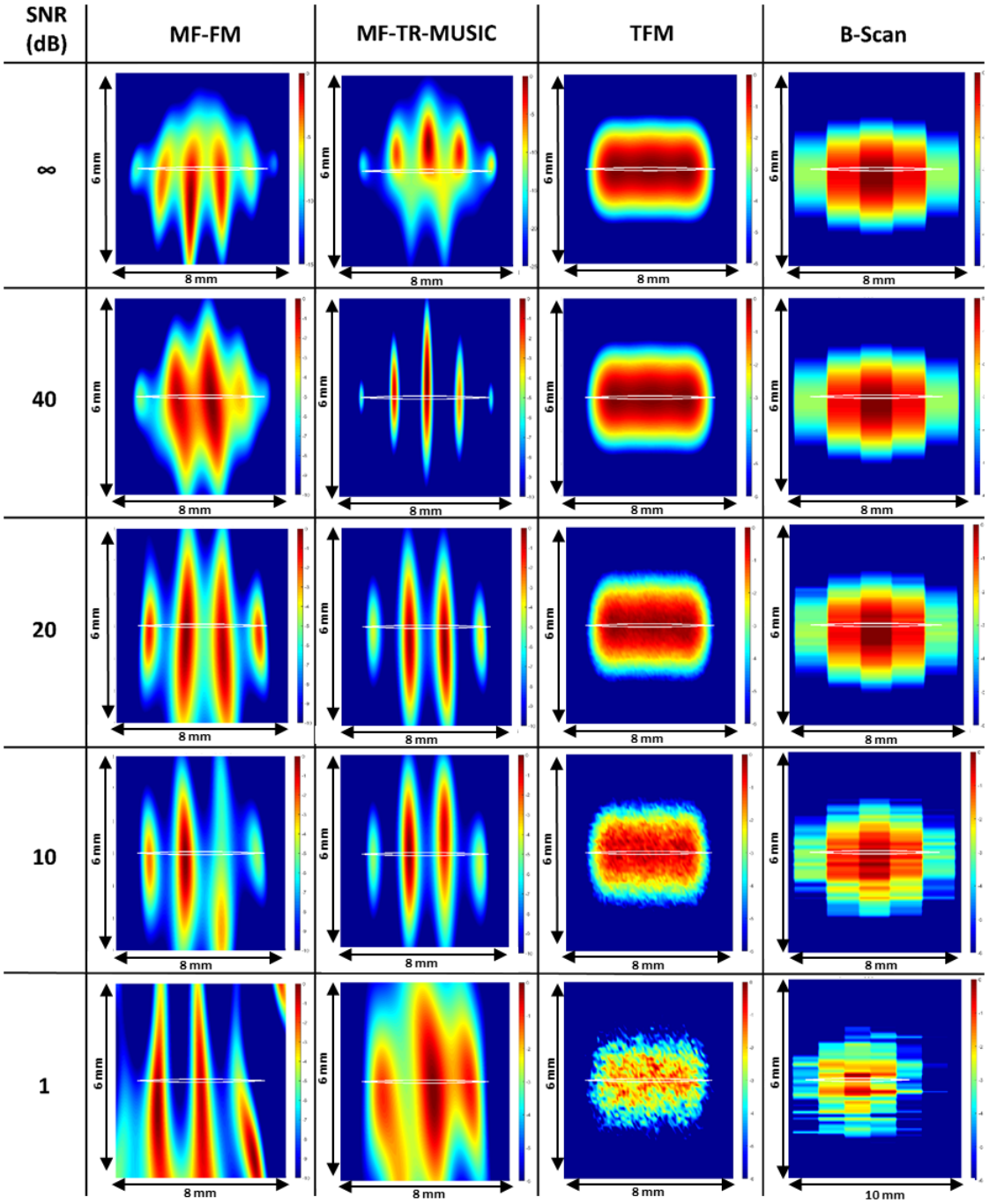


Figure 3.22: MF-FM, MF-TR-MUSIC, TFM and array B-Scan images generated from the simulated 2 MHz 64-element array inspection of an embedded planar 6 mm defect, where varying levels of GWN were added to achieve different SNRs. All images are plotted in a decibel scale, with all TFM and B-Scan images plotted between 0 and -6 dB. The set-up shown in Fig. 3.1 was used, with array centred above the defects at a distance of 42 mm.

in an estimation of the defect size, which is equal to the electronic scanning increment (1.5 mm). This is the inherent resolution of the array B-Scanning technique.

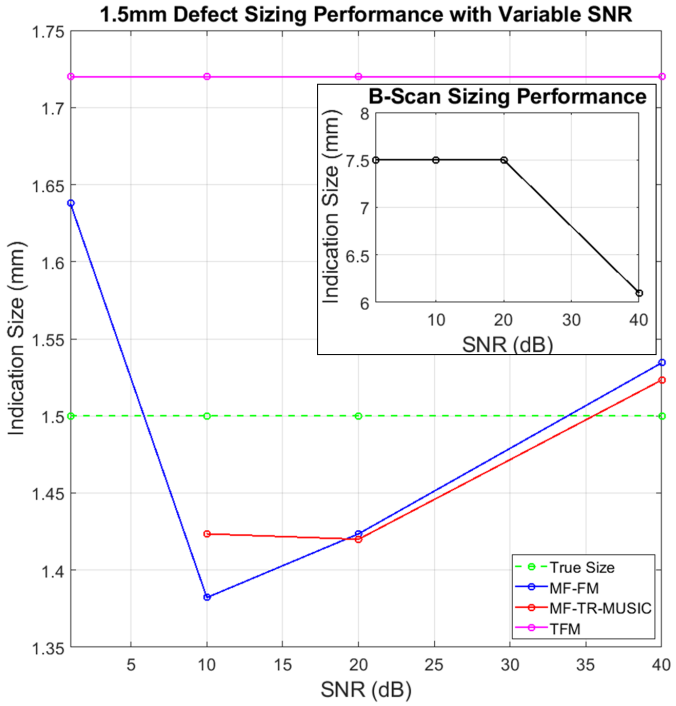


Figure 3.23: The sizing performance of the array imaging algorithms when inspecting a 1.5 mm embedded planar defect with decreasing SNR.

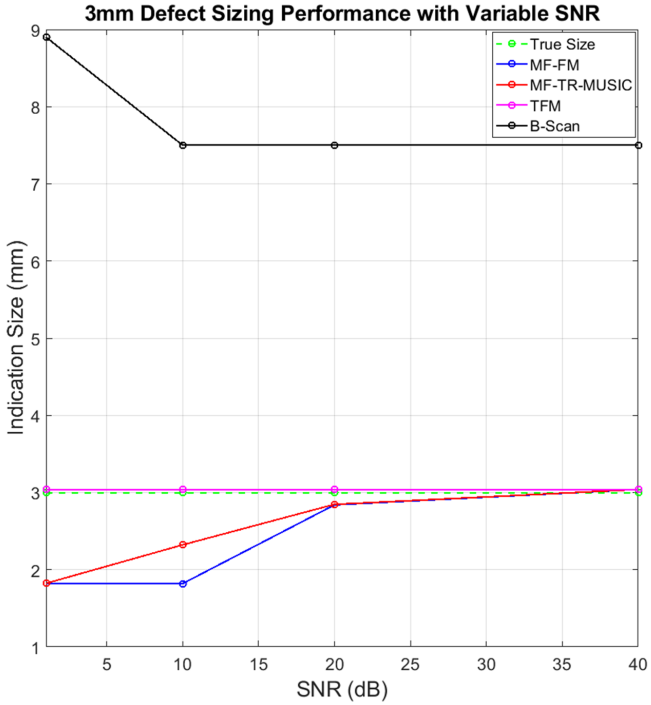


Figure 3.24: The sizing performance of the array imaging algorithms when inspecting a 3 mm embedded planar defect with decreasing SNR.

A similar visual degradation of the TFM images is observed as SNR decreases. However it is observed that the sizing performance is generally

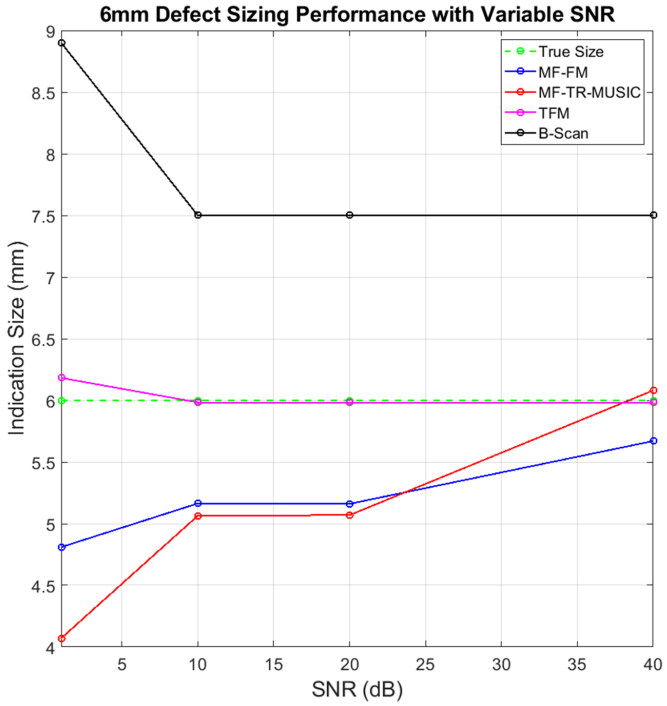


Figure 3.25: The sizing performance of the array imaging algorithms when inspecting a 6 mm embedded planar defect with decreasing SNR.

stable across the entire SNR range investigated, demonstrating excellent robustness to incoherent noise. This performance is expected due to TFM essentially averaging the time-domain signals as part of the summation process in the algorithm (see Eq. (2.39)), leading to a reduction in the effects of incoherent noise.

Observing the SR images presented in Fig. 3.20, Fig. 3.21 and Fig. 3.22, the SR methods were able to generate representative images for the defects for almost all GWN levels thus sizing was achievable. The only case where sizing was not possible was using the MF-TR-MUSIC algorithm to size the 1.5 mm defect at a SNR of 1 dB. In this instance, only a single indication was produced and no tip responses could be resolved.

One prominent trend across both SR algorithms when imaging the 3 mm and 6 mm defects was that as the SNR decreased, the number of indications produced by the algorithms also decreased. This is apparent in Fig. 3.21 where at 10 dB SNR, the MF-FM went from generating three indications to only two indications. At 1 dB SNR, both SR algorithms also only produced two indications. In Fig. 3.22, at 20 dB SNR both of algorithms went from generating five indications at higher SNRs to only four indications. At 1 dB in the same figure, the number of indications dropped once again to three indications which were noticeably distorted. This reduction in the number of indications is accompanied by a decrease in sizing performance, specifically an underestimation in defect size. As was described in Section 3.4, there is a roughly linear trend between the number of SR indications and defect size. Thus if the increase in noise results in a reduction in image indications, it is expected that it would provide an underestimating estimation

of the defect size. These effects however only begin to have a significant impact on the sizing performance at or below around 10 dB SNR, which is general classified as a substantial amount of signal noise in current ultrasonic NDE.

Another change that was observed in the SR images as noise increased was that the indications became progressively elongated in the direction perpendicular to the defect width. This is evident in all figures and is consistent with observations made by Fan *et al.* (2014) [34]. There seemed to be far less impact that incoherent noise had when imaging the 1.5 mm defects as it was only at the highest noise level of 1 dB SNR that the defect tips could not be resolved by the MF-TR-MUSIC. This imaging stability is reflected in the sizing performance in Fig. 3.23 where the SR algorithms were consistently more accurate than TFM across the entire noise range. It is worth noting that the TFM algorithm itself was generally quite accurate in only overestimating the defect width by around 0.2 mm (≈15% error). For the larger defect sizing results in Fig. 3.24 and Fig. 3.25, the TFM remained consistently accurate across the entire SNR range, outperforming all the other algorithms. The SR algorithms progressively undersized the defects as the SNR decreased. The drop in sizing accuracy coincided when the number of indications reduced.

To quantify the imaging robustness to noise, the imaging SNR of the TFM and array B-Scan algorithms, SNR_{TFM} and SNR_{BScan}, were estimated from Fig. 3.20, Fig. 3.21 and Fig. 3.22. The methodology consists of measuring imaging equivalents to A_{noise} and A_{peak} as described in Eq. (3.4). The value of A_{noise} was estimated by considering a region of the image before the defect indication and calculating the RMS of the imaging amplitude values within that region. For the images generated using a 2 MHz array, a 7.5 mm wide square box region was used. For the 1 MHz array images generated in later Chapters, a 10 mm wide square box region was used. An example of the imaging noise sampling box is shown in Fig. 3.26 as the red box in all images. The value of A_{peak} was taken to be the maximum amplitude value from the defect indication. The values of A_{noise} and A_{peak} were then inputted into Eq. (3.4) to estimate the imaging SNR for each separate image. When scanned FMC data was considered for defect characterisation in later Sections, the scan step which featured the highest value defect indication amplitude was used to estimate A_{noise} and A_{peak}.

The imaging SNR of the TFM and B-Scan algorithms compared against the SNR of the GWN added to the noise-free FE FMC data is shown in Table 3.4. It can be seen that both of the algorithms achieve an SNR far greater than the SNR value of GWN that was added to the FE datasets. TFM demonstrated a higher level of robustness to incoherent noise compared to the array B-Scan algorithm, with the relative difference in SNR increasing as the defect size decreased. This is explained due to the inherent averaging of the time-domain data which occurs during the TFM imaging process.

It is worth noting that an assumption that has been made is that the implemented noise is only incoherent in time. When considering realistic arrays, spatial coherence is also important as, for example, electrical noise may not be independent between different array element channels so it may have a

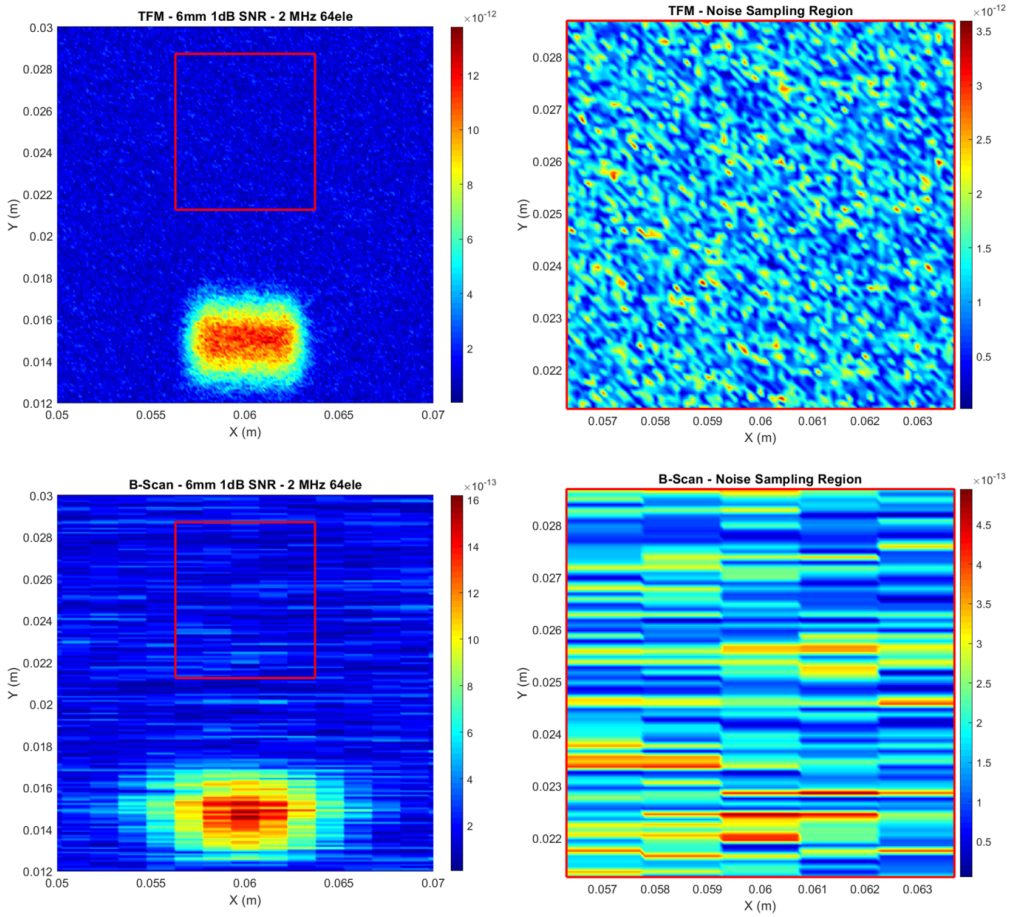


Figure 3.26: The imaging SNR methodology for the case of GWN added to noise-free FE FMC data such that the A-Scan SNR was 1 dB. Each image plotted in an absolute amplitude scale.

more complex impact on imaging. These results also only considered incoherent noise and not coherent noise. The effect of coherent noise can only easily be considered through experimental testing in components known to exhibit significant material noise. In addition, this work only considered optimal defect positioning (directly centred under the array) and in the ideal orientation (parallel to the array), so the effects of noise are likely be more severe for more challenging inspection set-ups.

3.7 Conclusions

The findings reported within this Section demonstrate an initial feasibility study into the potential applicability of advanced array algorithms to ultrasonic NDE.

2D FE modelling techniques were used to simulate the array inspection of smooth embedded planar defects within stainless steel. From the simulated FMC datasets calculated, images using the array 0° B-Scan, TFM, MF-FM and MF-TR-MUSIC algorithms were generated to study their suitability for NDE defect characterisation.

Table 3.4: The imaging SNR of the TFM and array B-Scan algorithms when varying levels of GWN were implemented.

Defect Width (mm)	**SNR**$_{GWN}$	**SNR**$_{TFM}$	**SNR**$_{BScan}$
1.5	40	67.4	57.4
1.5	20	48.4	36.3
1.5	10	38.5	26.7
1.5	1	29.8	18.7
3	40	63.5	56.8
3	20	43.7	36.5
3	10	33.9	27.7
3	1	25.3	18.3
6	40	57.8	56.1
6	20	38.0	36.2
6	10	28.5	26.3
6	1	20.7	18.0

In Section 3.4, it was found that the MF-FM, MF-TR-MUSIC and TFM algorithms were able to accurately size planar defects below the diffraction limit ($\lambda/2$), and they consistently outperformed the array B-Scan imaging method. It was also found that for defects at or below the diffraction limit, the performance of the TFM algorithm expectedly plateaued as it became limited by beam width constraints. The SR algorithms however were able to overcome this barrier and more accurately size sub-wavelength defects than the other methods demonstrating their super resolution capabilities. A key finding within this Section was an observed non-dimensional trend between the number of image indications generated for embedded planar defects with the SR algorithms and the defect size measured in wavelengths. This may have the potential to act as visual sizing guidance to aid defect analysis.

In Section 3.5, it was found that the SR algorithms were able to effectively image sub-wavelength defects at a range of misorientations and accurately estimate the defect width and TWH. At large angles of misorientation, the 32-element array configuration was found to drop-off in performance more in comparison to the 64-element array results. The TFM was found to be ineffective to characterise the defects, as expected due to the defect size being at the diffraction limit.

In Section 3.6, the effect of incoherent noise on array imaging was investigated. The TFM algorithm showed excellent robustness in its sizing performance for all levels of GWN applied as well as in image quality demonstrated by the high values of SNR$_{TFM}$ measured. The SR algorithms also showed robustness to incoherent noise for SNRs above 10 dB. When sizing the 3 mm (λ) and 6 mm (2λ) sized defects below 20 dB SNR, there was observed to be a reduction in the F matrix eigenvalues which corresponded

to the *signal* subspace. This led to the algorithms producing images corresponding to those which would be expected of smaller defects in a noise-free scenario resulting in defect under-sizing at high levels of noise. When imaging the 1.5 mm defects ($\lambda/2$), significant robustness was demonstrated to 10 dB SNR for the SR algorithms. The results in Section 3.6 suggest that when significant levels of incoherent noise is present within array data, this may need to be accounted and corrected for when applying the SR algorithms to size embedded planar defects.

Chapter 4

Experimental SR Imaging of 2D Embedded Smooth Planar Defects

4.1 Introduction

This Chapter aims to experimentally validate the 2D FE simulated array imaging results presented within Chapter 3 by considering representative experimental embedded planar defects using Wire Eroded (WE) test pieces, which are described in more detail in the next Section. The SR algorithms' performance in terms of sizing and orientation estimation was considered as well as verifying the novel non-dimensional trend between defect size and the SR image indication pattern observed through simulation. The latter will be carried out using both a 2 MHz and 1 MHz array on a range of defect sizes, which would also provide information on the effect of reduced sampling of the far-field scattered wavefield. This simplified experimental set-up allowed for an assessment of the upper limit of SR imaging performance to be established before other factors such as finite defect length would act to hinder its NDE capability.

4.2 Experimental Set-Up

To experimentally validate the 2D FE studies conducted previously, WE test pieces were manufactured that contained defects that extended across the entire test piece width meaning the defects were a good practical approximation to the 2D FE models. These WE test pieces featured planar defects 1.5 mm, 3 mm and 6 mm wide with each defect size at 0°, 10° and 20° of tilt. A schematic of the test pieces is shown in Fig. 4.1 and the defect parameters are listed in Table 4.2. The defect tolerances listed in Table 4.2 were provided by the test piece manufacturer. The test pieces were manufactured from 304 stainless steel.

Two ultrasonic phased arrays were used in direct contact with the test pieces to collect FMC data. These were a 2 MHz 64-element linear phased array (IMASONIC, 96 mm active aperture size) and a 1 MHz 32-element linear phased array (IMASONIC, 96 mm active aperture size). The full array properties are detailed within Table 4.1. A data collection sampling frequency of 100 MHz was used for both the 2 MHz and 1 MHz array configurations

Table 4.1: Properties of the IMASONIC arrays used through the experimental trials within this thesis.

Frequency (MHz)	Number of Elements	Element Pitch (mm)	Active Aperture (mm)	Element Width (mm)
2	64	1.5	95.75	15
1	32	2.95	93.9	22

Table 4.2: Planar defect parameters within the wire eroded test pieces. Manufacturing tolerances are also provided.

Defect Width (mm)	Inclination Angle (°)
1.5 ± 0.2	0.00 ± 0.25
1.5 ± 0.2	10.00 ± 0.25
1.5 ± 0.2	20.00 ± 0.25
3.0 ± 0.2	0.00 ± 0.25
3.0 ± 0.2	10.00 ± 0.25
3.0 ± 0.2	20.00 ± 0.25
6.0 ± 0.2	0.00 ± 0.25
6.0 ± 0.2	10.00 ± 0.25
6.0 ± 0.2	20.00 ± 0.25

using a MicroPulse FMC. The arrays were placed directly above each defect to maximise the array viewing angle, as conducted in Chapter 3, with the arrays central to the test piece width to minimise edge effects of the block faces. Although an extra parameter of 3D beam width has been introduced, this experiment represents the closest approximation to the 2D FE simulations conducted previously.

4.3 Wire Eroded Test Piece Array Imaging Results

The array 0° B-Scan, TFM, MF-FM and MF-TR-MUSIC algorithms were applied to the collected FMC from the WE test pieces. A pixel size of 50 μm was used for all images in this Section.

First considering the results from the 2 MHz 64-element array, the images produced from the corresponding FMC datasets are shown in Fig. 4.2, Fig. 4.3 and Fig. 4.4. From these images, it is clear that the same indication profiles are produced as the simulated images presented in Section 3.4. The SR algorithms again generated a series of discrete indications along the defect width, with the number of indications related to the defect size in accordance with Fig. 3.10. The TFM and array B-Scan algorithms produced extended indications corresponding to the specular reflections from the planar defect faces.

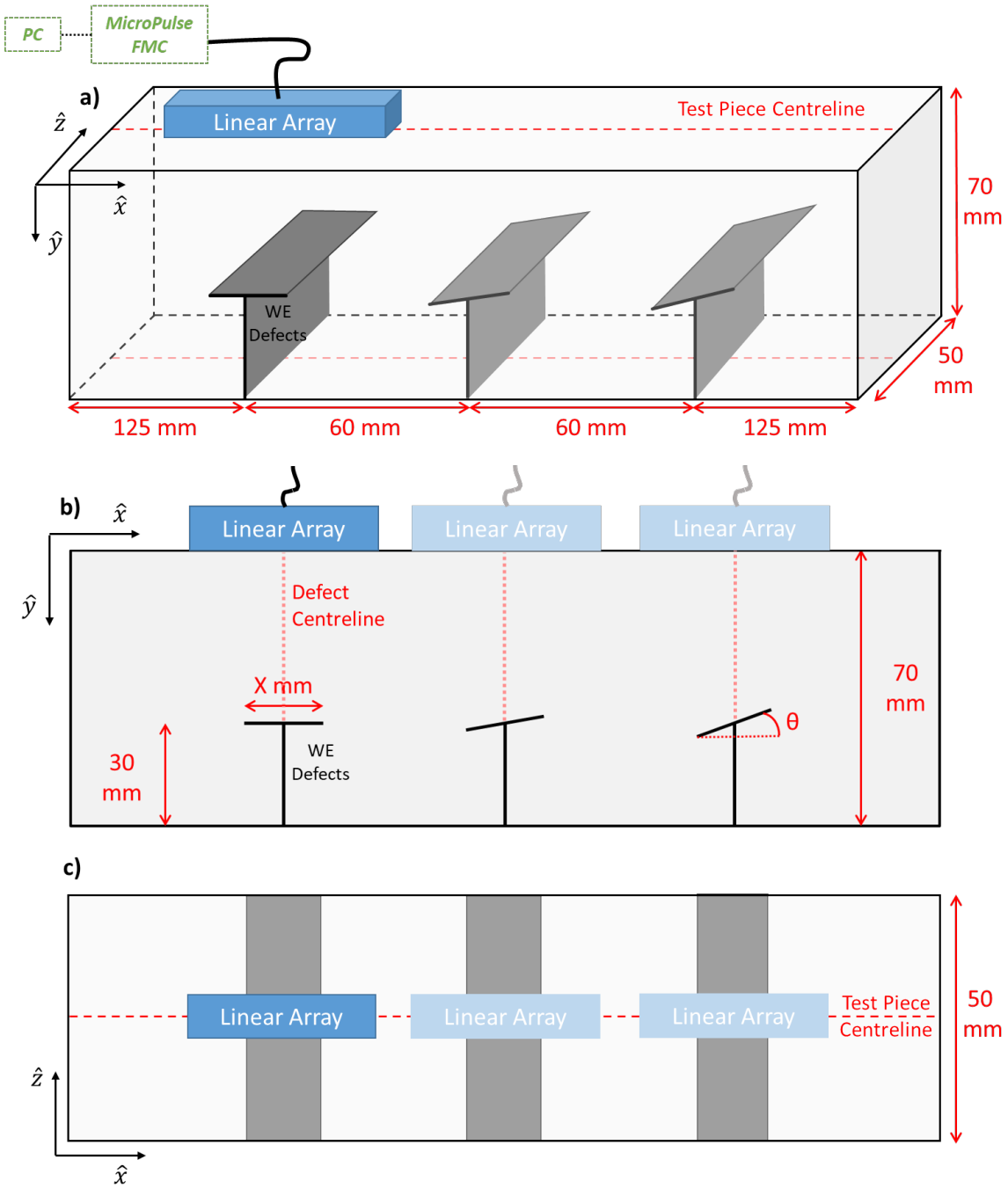


Figure 4.1: a) 3D illustration of the experimental set-up for array FMC data collection on the WE test pieces, showing the series of pseudo-2D WE slots within the test block with the array positioned on the test piece centreline (dashed red), directly centred above WE defects. b) The cross-sectional view ($x-y$ axes) of the experimental set-up, where the WE defect widths (X) ranged from 1.5 mm - 6 mm and the inclinations (θ) ranged from 0°-20°. c) The plan-view of the set-up ($x-z$ axes) showing the positions of the array above the defects where a single FMC dataset was collected for each location. Figure not to scale.

For the 1.5 mm ($\lambda/2$) defects, two indications are generated by the SR algorithms, for the 3 mm (λ) defects three indications are generated and for

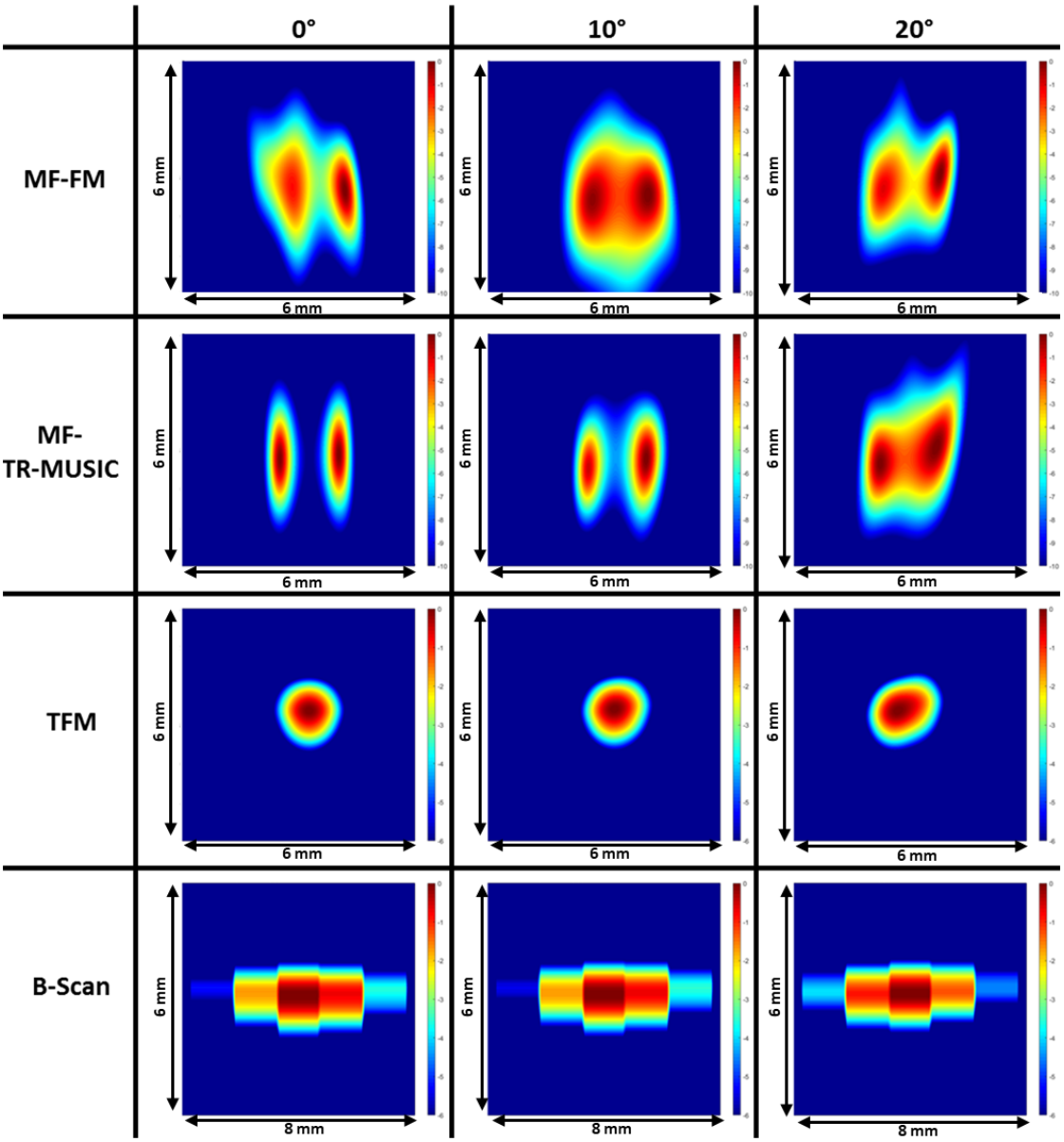


Figure 4.2: Array algorithm images for the 1.5 mm wire eroded defects using a 2 MHz 64-element probe. All images were normalised to the maximum pixel value within each image and are plotted in the decibel scale. All MF-FM and MF-TR-MUSIC are plotted between 0 and -10 dB. All TFM and B-Scan images are plotted between 0 and -6 dB. A 15 mm active aperture was used to generate the B-Scan images. The set-up shown in Fig. 4.1 was used, with the array centred above the defects at a distance of 40 mm.

the 6 mm (2λ) defects five indications are generated. The trend observed here between number of image indications and defect width in wavelength matches the trend established in the simulation studies. It is also observed that the number of indications from the SR algorithms remains consistent even as the defects are tilted from 0° to 20°. It is observed that for the 6 mm 20° WE defects, the central indications on the SR images have started to

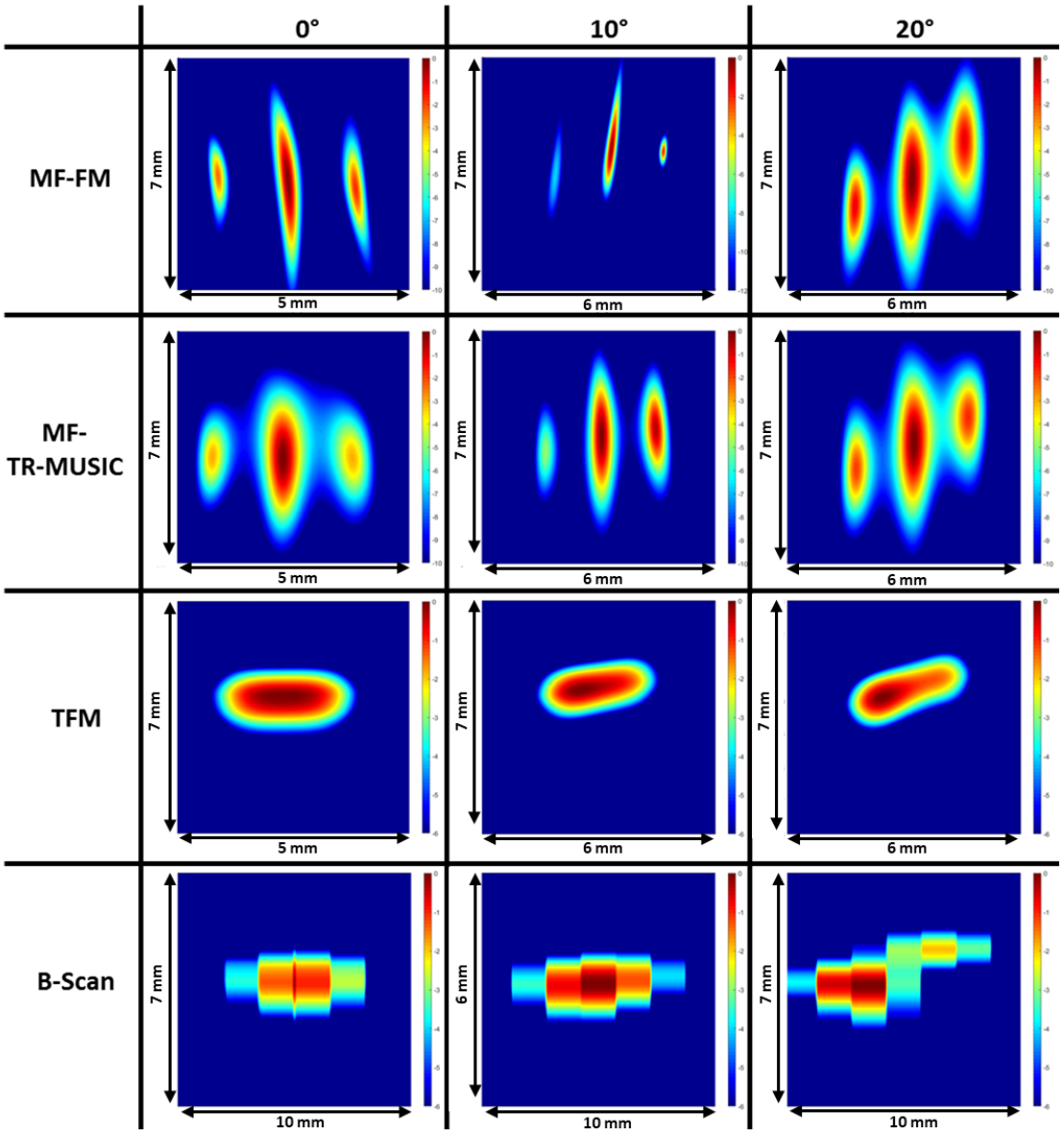


Figure 4.3: Array algorithm images for the 3 mm wire eroded defects using a 2 MHz 64-element probe. All images were normalised to the maximum pixel value within each image and are plotted in the decibel scale. All MF-FM and MF-TR-MUSIC are plotted between 0 and -10 dB, except the MF-TR-MUSIC 10° image is between 0 and -12 dB. All TFM and B-Scan images are plotted between 0 and -6 dB. A 15 mm active aperture was used to generate the B-Scan images. The set-up shown in Fig. 4.1 was used, with the array centred above the defects at a distance of 40 mm.

become slightly distorted. However importantly, the positions of the defect tip indications were located at the expected positions which enabled accurate sizing to be carried out.

From the images, the same SR sizing methodologies used in Section 3.3 were applied to algorithms to estimate the defect size and tilt angle. The

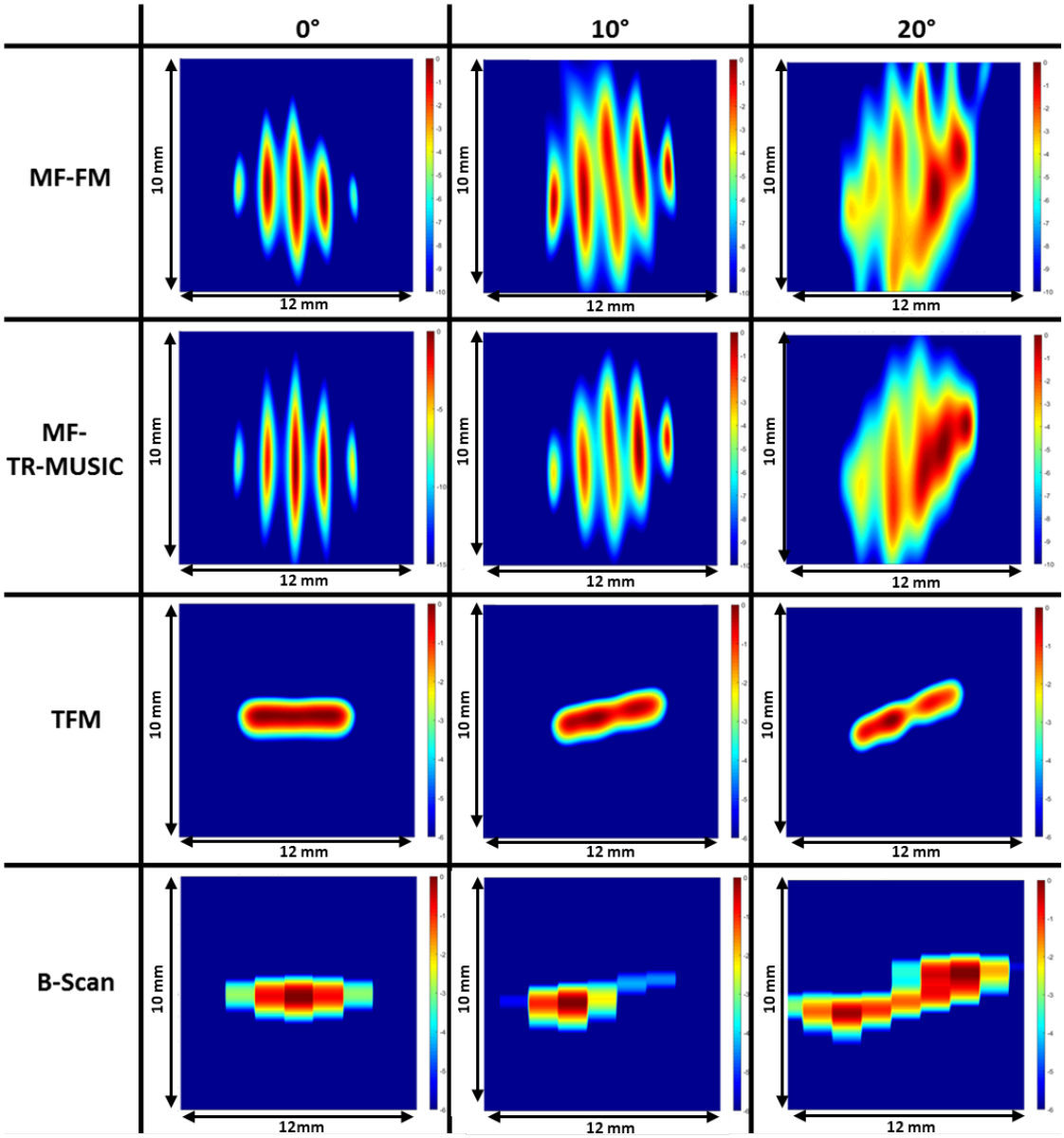


Figure 4.4: Array algorithm images for the 6 mm wire eroded defects using a 2 MHz 64-element probe. All images were normalised to the maximum pixel value within each image and are plotted in the decibel scale. All MF-FM and MF-TR-MUSIC are plotted between 0 and -10 dB, except the MF-FM 0° image is between 0 and -15 dB. All TFM and B-Scan images are plotted between 0 and -6 dB. A 15 mm active aperture was used to generate the B-Scan images. The set-up shown in Fig. 4.1 was used, with the array centred above the defects at a distance of 40 mm.

6 dB drop sizing method was applied to the TFM and B-Scan images unless clear tip responses could be distinguished for the higher defect tilts, in which case the tip responses were used to size the defects. Tips were used to size the 3 mm 20° and the 6 mm 20° B-Scan images.

The characterisation results from all the algorithms are listed in Table 4.3. The errors for the sizing for the SR and TFM algorithms are based on the

Table 4.3: 2 MHz 64-element array imaging algorithm sizing results for wire erosion test pieces.

Actual Parameters		**MF-FM**		**MF-TR-MUSIC**		**TFM**		**B-Scan**	
Size (mm)	Tilt (°)	Size (mm)	Tilt (°)	Size (mm)	Tilt (°)	Size (mm)	Tilt (°)	Size (mm)	Tilt (°)
1.5	0	1.36 ± 0.05	2 ± 2	1.51 ± 0.05	4 ± 2	1.81 ± 0.05	0 ± 2	7.4 ± 1.5	0 ± 2
1.5	10	1.42 ± 0.05	6 ± 2	1.52 ± 0.05	8 ± 2	1.84 ± 0.05	8 ± 2	7.4 ± 1.5	0 ± 2
1.5	20	1.51 ± 0.05	15 ± 2	1.53 ± 0.05	17 ± 2	2.06 ± 0.05	18 ± 2	7.4 ± 1.5	1 ± 2
3	0	3.01 ± 0.05	8 ± 1	3.03 ± 0.05	0 ± 1	3.18 ± 0.05	0 ± 1	6.1 ± 1.5	0 ± 1
3	10	2.87 ± 0.05	15 ± 1	2.96 ± 0.05	14 ± 1	3.23 ± 0.05	10 ± 1	7.4 ± 1.5	2 ± 1
3	20	3.42 ± 0.05	36 ± 1	3.27 ± 0.05	28 ± 1	3.40 ± 0.05	21 ± 1	3.2 ± 1.5	20 ± 1
6	0	5.97 ± 0.05	4.3 ± 0.5	5.80 ± 0.05	1.9 ± 0.5	6.15 ± 0.05	0.5 ± 0.5	7.6 ± 1.5	0.0 ± 0.5
6	10	6.02 ± 0.05	13.5 ± 0.5	5.98 ± 0.05	14.0 ± 0.5	6.19 ± 0.05	9.8 ± 0.5	9.0 ± 1.5	6.4 ± 0.5
6	20	6.09 ± 0.05	24.3 ± 0.5	5.99 ± 0.05	26.8 ± 0.5	6.33 ± 0.05	19.9 ± 0.5	6.2 ± 1.5	15.8 ± 0.5

imaging pixel size of 50 μm and using standard error propagation. The error for the B-Scan images are based on the inherent image resolution of 1.5 mm in the x-axis direction related to the electronic scan increment.

First considering the 1.5 mm characterisation results using the 2 MHz 64-element array listed in Table 4.3, the TFM and SR algorithms significantly outperform the array B-Scan algorithm. The B-Scan results demonstrate a similar beam width limited performance as found in Section 3.4, severely overestimating the defect size by around 400% and providing no estimation of the defect tilt. The TFM algorithm achieved far more accurate characterisation results. The width sizing results were very similar to the simulated results, with the method overestimating the defect size by around 25%. TFM was also able to effectively estimate the defect tilt which would allow TWH sizing to be undertaken. Both of the SR algorithms were able to achieve almost perfectly accurate width sizing for all defect orientations and they were also able to estimate the defect tilts with reasonable accuracy, again facilitating TWH sizing. Considering both the width sizing and orientation estimation accuracy, the MF-TR-MUSIC algorithm generally performed slight better than the MF-FM. Both SR algorithms performed better than the conventional array algorithms.

Considering the 3 mm characterisation results using the 2 MHz 64-element array listed in Table 4.3, similar performance is observed from the algorithms. The B-Scan algorithm again significantly oversized the defects for the 0° and 10° case. However for the 20° case, the defect tips could be resolved and therefore accurate length and orientation estimations were achieved. The TFM algorithm again produced accurate sizing results as well as being able to effectively estimate the defect tilt which would allow TWH sizing to be undertaken. The sizing performance progressively worsened as tilt increased due to the applicability of amplitude-based sizing becoming increasingly invalid as the defect moved away from the specular orientation. The SR algorithms were able to achieve accurate sizing for all defect orientations as well as to provide good estimations of the defect tilts. Considering both the sizing and orientation estimation accuracy,

Table 4.4: The imaging SNR of the TFM and array B-Scan algorithms from the 2 MHz experimental images generated from the WE defects.

Defect Width (mm)	**SNR**$_{GWN}$	**SNR**$_{TFM}$	**SNR**$_{BScan}$
1.5	0	46.4	38.0
1.5	10	44.2	37.2
1.5	20	44.2	33.5
3	0	53.4	43.3
3	10	48.5	39.8
3	20	52.1	30.4
6	0	51.7	50.7
6	10	59.9	42.3
6	20	49.7	32.4

the MF-TR-MUSIC algorithm again performed better than the MF-FM. The performance of both SR algorithms was once again superior to those of the conventional array algorithms.

Considering the 6 mm characterisation results using the 2 MHz 64-element array listed in Table 4.3, the same trends are generally observed once again. The B-Scan algorithm oversized the defect length significantly for the 0° and 10° cases but was able to accurately characterise the 6 mm 20° defect, due to tip indications being resolvable. TFM achieved accurate sizing and tilt estimation, with the maximum width sizing error of around 5%. Both SR algorithms performed equally accurately in terms of producing successful width and tilt estimations.

Using the methodology described in Section 3.6, the imaging SNR of the TFM and array B-Scan algorithms were estimated from the 2 MHz 64-element array images and are listed in Table 4.4. A representative example experimental SNR case for the WE test pieces (1.5 mm 0° defect) is shown in Fig. 4.5. The imaging SNR of both of the algorithms considered in Table 4.4 are high, which is expected from the easily inspectable material from which the test pieces were manufactured from. As shown in Section 3.6, the TFM algorithm was able to achieve a higher image SNR compared to the array B-Scan algorithm.

Now considering the results from the 1 MHz 32-element array, the images produced are shown in Fig. 4.6, Fig. 4.7 and Fig. 4.8 for the 1.5 mm ($\lambda/4$), 3 mm ($\lambda/2$) and 6 mm (λ) WE defects respectively.

The characterisation results from all the algorithms are listed in Table 4.5. The errors for the sizing for the SR and TFM algorithms are based on the imaging pixel size of 50 μm and using standard error propagation. The error for the B-Scan images are based on the inherent image resolution of 3 mm related to the electronic scan increment.

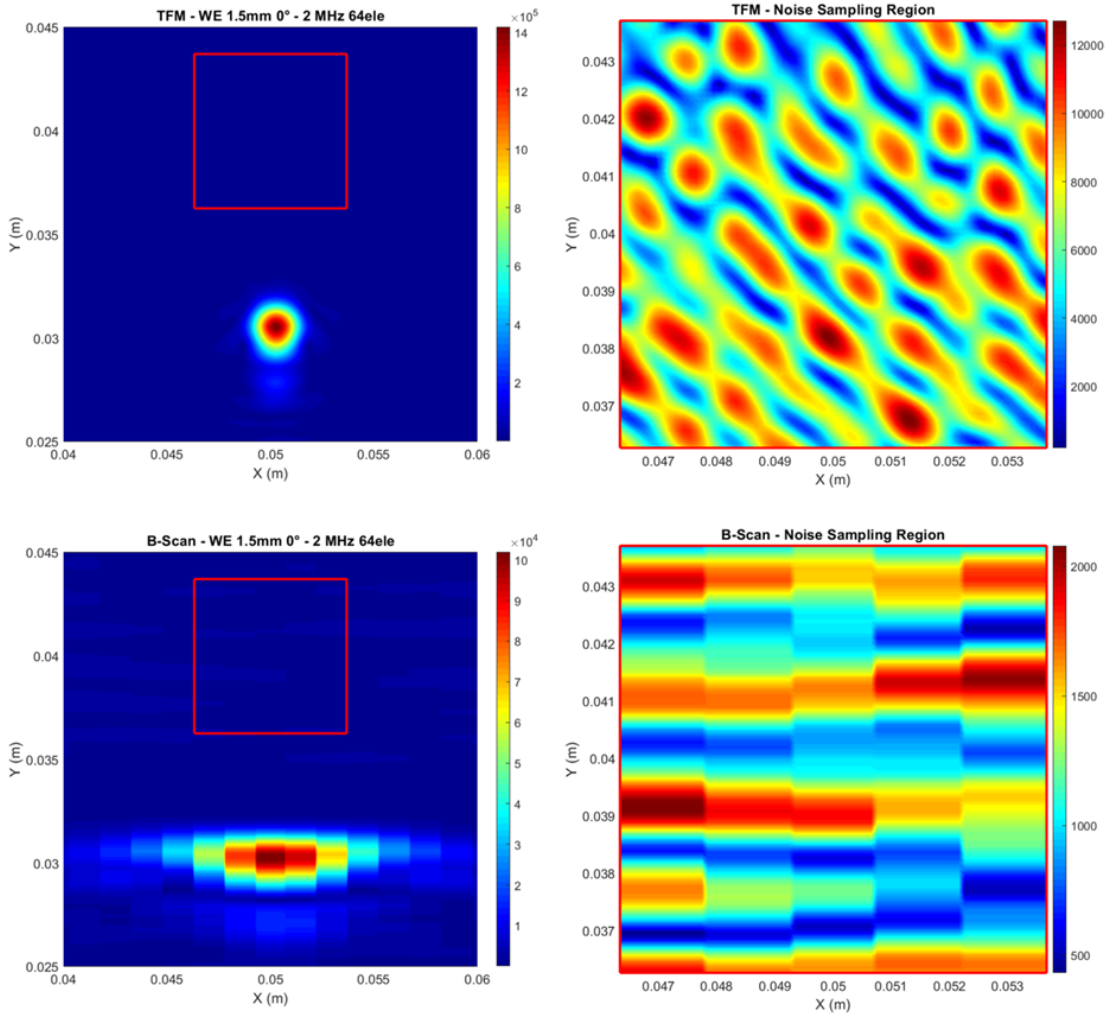


Figure 4.5: The imaging SNR methodology for the 1.5 mm 0° WE defect using a 2 MHz 64-element array. Each image plotted in an absolute amplitude scale. The set-up shown in Fig. 4.1 was used, with the array centred above the defects at a distance of 40 mm.

From the images shown in Fig. 4.6 for the 1.5 mm ($\lambda/4$) WE defect using the 1 MHz array, it can be seen that both SR algorithms are only able to generate a single indication for the defect and are not able to resolve the defect tips. This means that the SR sizing approach described in Section 3.3 cannot be applied here and this is reflected in Table 4.5 where both SR algorithms are unable to estimate the defect size direction. The only sizing information that could be inferred from the case of a single indication being generated is that the defect size must be smaller than the diffraction limit ($\lambda/2 = 3$ mm) which has been shown to produce two indications. TFM seems to produce similar indications for all tilt angles for the 1.5 mm defects, however there is a slight visual change in the inclination of the image indications suggesting that some tilt estimation may be achievable. From Table 4.5, the TFM algorithms are shown to overestimate the defect size by over 100% as it returns values just above the diffraction limit (3 mm) which is the maximum theoretical resolution limit of the algorithm. The results also show that some

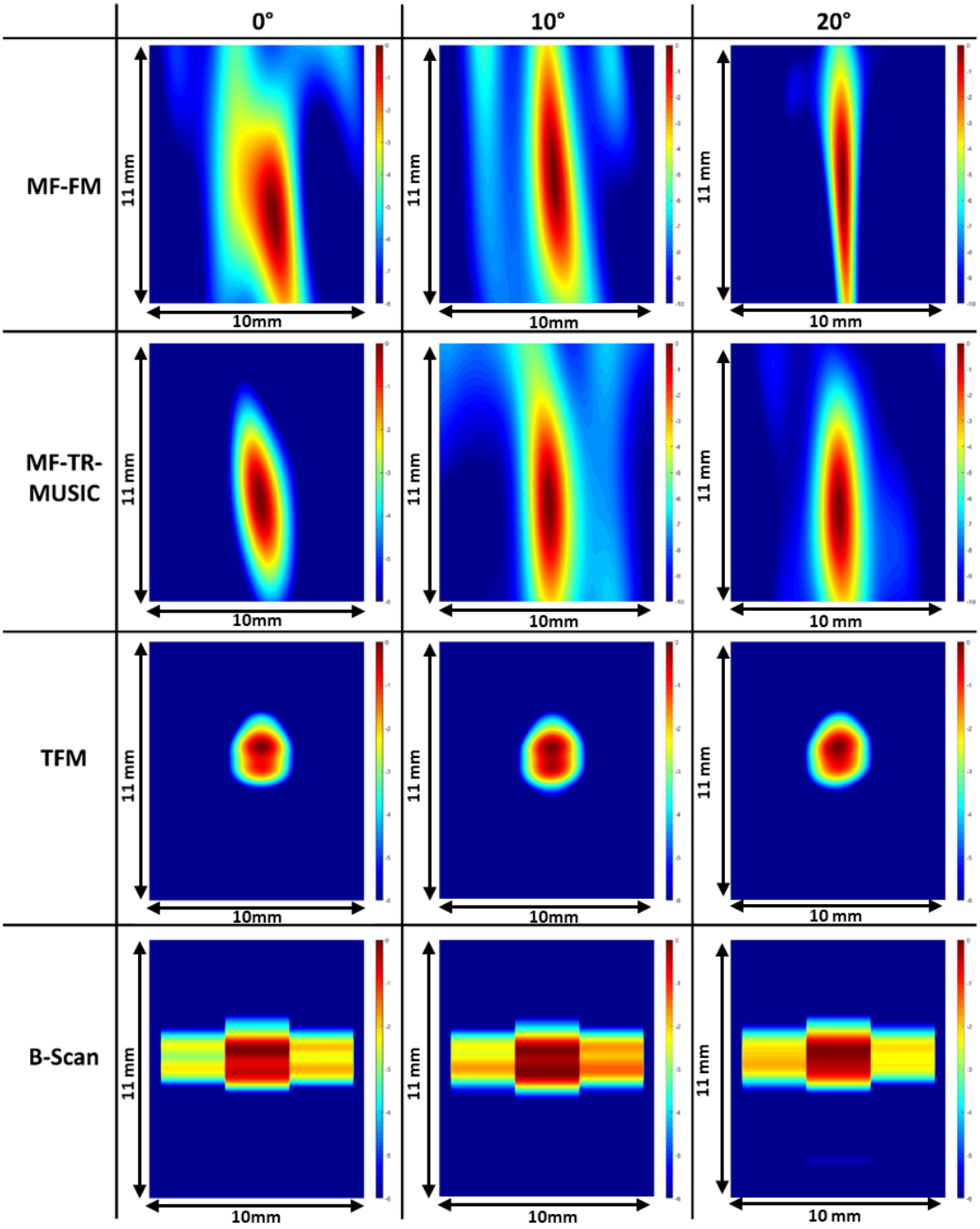


Figure 4.6: Array algorithm images for the 1.5 mm wire eroded defects using a 1 MHz 32-element probe. All images were normalised to the maximum pixel value within each image and are plotted in the decibel scale. All images are plotted between 0 dB and -6 dB, except for the 10° and 20° MF-FM and MF-TR-MUSIC images which were between 0 dB and -10 dB. A 15 mm active aperture was used to generate the B-Scan images. The set-up shown in Fig. 4.1 was used, with the array centred above the defects at a distance of 40 mm.

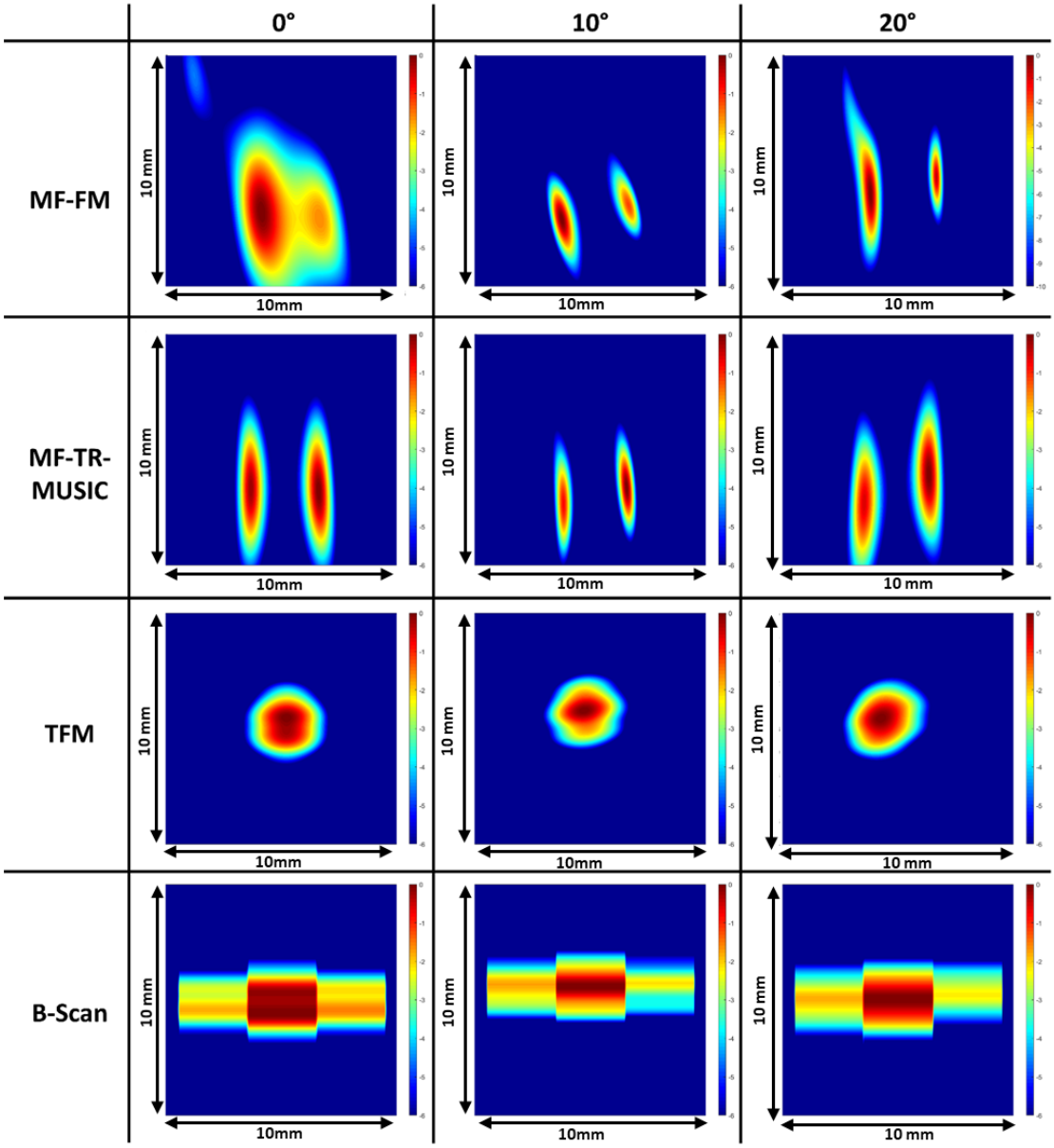


Figure 4.7: Array algorithm images for the 3 mm wire eroded defects using a 1 MHz 32-element probe. All images were normalised to the maximum pixel value within each image and are plotted in the decibel scale. All images are plotted between 0 dB and -6 dB, except for the 20° MF-FM image which was between 0 dB and -8 dB. A 15 mm active aperture was used to generate the B-Scan images. The set-up shown in Fig. 4.1 was used, with the array centred above the defects at a distance of 40 mm.

estimation of the defect tilt can be extracted, although the tilt estimates are significantly underestimated. The B-Scan array algorithm severally overestimates the defect size (by 500%) and cannot estimate the defect tilt, indicating that the method is considerably beam width limited.

From the 3 mm ($\lambda/2$) defect images shown in Fig. 4.7, the SR algorithms are now able to generate indications from the tips of the defects which enabled

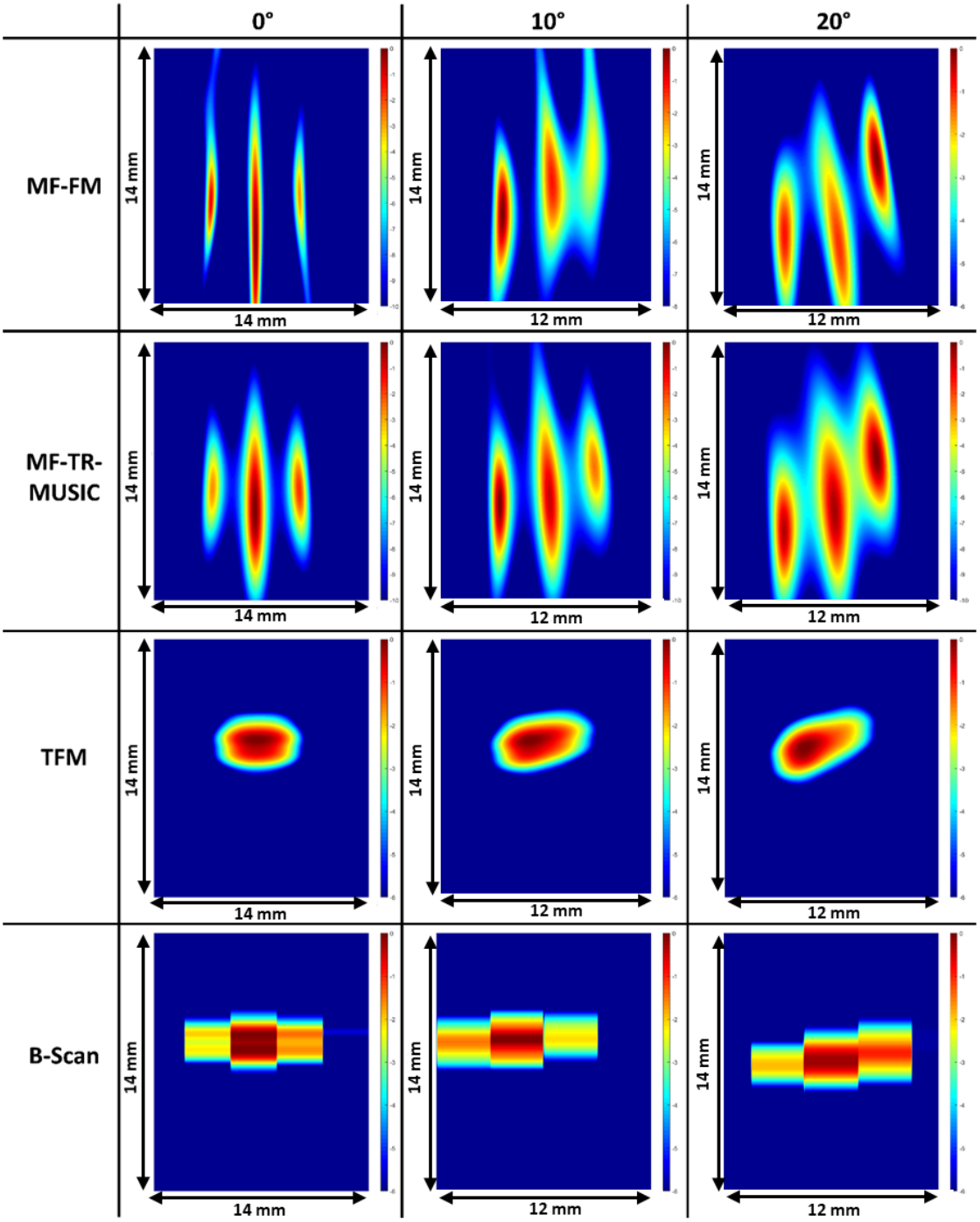


Figure 4.8: Array algorithm images for the 6 mm wire eroded defects using a 1 MHz 32-element probe. All images were normalised to the maximum pixel value within each image and are plotted in the decibel scale. All TFM and B-Scan images are plotted between 0 and -6 dB. A 15 mm active aperture was used to generate the B-Scan images. The set-up shown in Fig. 4.1 was used, with the array centred above the defects at a distance of 40 mm.

accurate sizing estimations to be carried out. The characterisation results in Table 4.5 show a similar trend to Table 4.3 where the SR methods are able

Table 4.5: 1 MHz 32-element array imaging algorithm sizing results for wire erosion test pieces.

Actual Parameters		**MF-FM**		**MF-TR-MUSIC**		**TFM**		**B-Scan**	
Size (mm)	Tilt (°)	Size (mm)	Tilt (°)	Size (mm)	Tilt (°)	Size (mm)	Tilt (°)	Size (mm)	Tilt (°)
1.5	0	-	-	-	-	3.15 ± 0.05	0 ± 2	9 ± 3	0 ± 2
1.5	10	-	-	-	-	3.21 ± 0.05	4 ± 2	9 ± 3	0 ± 2
1.5	20	-	-	-	-	3.24 ± 0.05	9 ± 2	9 ± 3	0 ± 2
3	0	2.51 ± 0.05	5 ± 1	2.95 ± 0.05	2 ± 1	3.65 ± 0.05	0 ± 1	9 ± 3	0 ± 1
3	10	2.96 ± 0.05	12 ± 1	2.83 ± 0.05	13 ± 1	3.69 ± 0.05	21 ± 1	9 ± 3	0 ± 1
3	20	2.95 ± 0.05	15 ± 1	3.09 ± 0.05	23 ± 1	3.91 ± 0.05	21 ± 1	9 ± 3	0 ± 1
6	0	5.78 ± 0.05	2.5 ± 0.5	5.67 ± 0.05	1.0 ± 0.5	6.08 ± 0.05	0.5 ± 0.5	12 ± 3	0.0 ± 0.5
6	10	5.98 ± 0.05	32.4 ± 0.5	5.69 ± 0.05	21.2 ± 0.5	6.03 ± 0.05	9.5 ± 0.5	9 ± 3	0.2 ± 0.5
6	20	6.52 ± 0.05	38.6 ± 0.5	6.57 ± 0.05	37.7 ± 0.5	6.20 ± 0.05	17.9 ± 0.5	12 ± 3	1.4 ± 0.5

to most accurately estimate the defect size and inclination angle compared to TFM and the B-Scan algorithms. In the majority of 1 MHz cases, the MF-TR-MUSIC was the most accurate method. TFM overestimated the defect size by around 25% but is able to accurately estimate the defect inclination. As with the 1.5 mm defects, the B-Scan algorithm severely overestimates the defect size and cannot estimate the defect tilt. This is expected due to the method being beam width limited in this configuration.

For the 6 mm (λ) defect results in Table 4.5, TFM is seen to produce the most accurate characterisation results in terms of both length sizing and orientation estimation. The SR algorithms, although not hugely inaccurate, cannot match this performance. This drop-off in performance relative to Table 4.3 (for the λ sized case at 2 MHz) is likely due to the reduction in information contained within the FMC data. Although both arrays achieve the same viewing angle, the 1 MHz array has half the elements of the 2 MHz array and therefore contains 3072 fewer A-Scans from which the defect profile is reconstructed. The B-Scan again performs the worst out of all the considered algorithms.

A key trend that is observed when considering the images from both the 2 MHz and 1 MHz SR array images are the consistency in the number of indications produced for a given defect size measured in terms of wavelength. All SR images from the $\lambda/2$ sized defects returned two indications and all the λ sized defects returned three indications. These results represent experimental validation of the SR imaging trend shown in Fig. 3.10.

4.4 Conclusions

In this Chapter, experimental validation of the simulated results in Chapter 3 was conducted on pseudo-2D wire eroded test pieces containing planar defects of varying size and orientation. It was found that the SR algorithms could accurately size the WE defects up to sizes of half the ultrasonic wavelength as well as effectively estimate the tilt angle, albeit only up to

the maximum defect inclination of 20°. The TFM algorithms were not able to match their performance at this length scale but it produced accurate characterisation results for the λ and 2λ sized defects. The array 0° B-Scan algorithm was found to be the least accurate array imaging algorithm used as it considerably overestimated the defect widths.

Importantly, the non-dimensional SR imaging trend for planar defects observed in the simulated results in Section 3.4 was experimentally validated over the WE defect size range considered, adding confidence that this trend could be used in estimating planar defect size using only knowledge of the ultrasonic wavelength. This trend was also valid for defect orientations up to the maximum tilt of 20° considered.

It is noted however that these results, as in for Section 3.4, are for a single range value of around 40 mm between the array and defects. It is expected that it will not hold for all range values, with a worsening imaging performance occurring as the range continues to increase (as the apparent array viewing angle decreases). Also the results in this Section utilised arrays of different frequencies but with a consistent active aperture size of 96 mm. It is anticipated that active aperture size, and therefore viewing angle, is a key parameter for SR imaging and therefore deviations from this trend may occur as the active aperture size begins to differ significantly. Further investigation into the complex relationship between active aperture size, defect range and viewing angle is required to fully understand the imaging behaviour beyond the parameter space considered.

Chapter 5

Experimental SR Imaging of 3D Embedded Smooth Planar Defects

5.1 Introduction

In this Chapter, the experimental studies conducted in Chapter 4 were extended to consider three-dimensional (3D) embedded planar defects, which are more representative of commonly encountered NDE inspection flaws than the pseudo-2D wire eroded defects considered previously. This was done by using test pieces containing Spark Eroded (SE) inclined ellipses and applying an FMC scanning array technique.

As will be discussed, using all FMC datasets collected from the full scan paths in conjunction with the SR algorithms generates images far more difficult to interpret than those produced by conventional imaging methods. This is because the SR algorithms are capable of generating images featuring high amplitude erroneous indications from datasets which do not even include significant defect responses within the time trace data. This would inevitably lead to confusion during data interpretation. To tackle this problem, an imaging methodology was established to process the scanned FMC datasets acquired on the 3D targets in order to effectively apply the SR algorithms for defect sizing characterisation. This method utilised information gained from the TFM algorithm to allow appropriate time-domain windowing of signals prior to SR imaging to enable accurate defect width sizing. This step is vital if the method is to be used in practical NDE scenarios where prior knowledge of the temporal location of defects is not available.

Using this method, the sizing performance of the SR algorithms were assessed for the 3D flaws and compared to the simplified 2D cases previously considered in this thesis. This validation is a crucial step to determine their applicability for realistic defect morphologies present within practical NDE inspections.

5.2 Experimental Set-Up

The SE test pieces were manufactured containing 3D elliptical planar targets from 304 stainless steel. These SE test pieces featured different sized

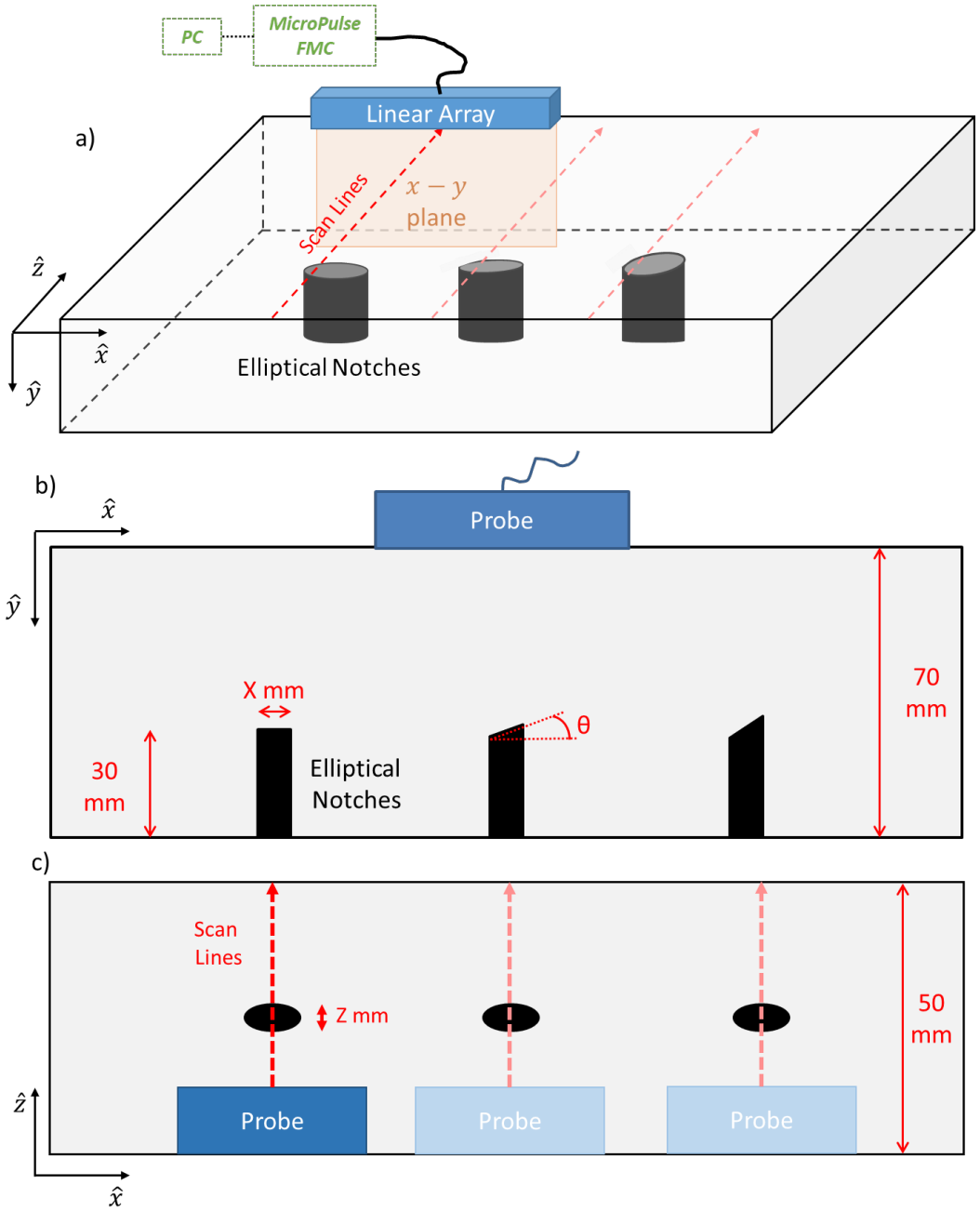


Figure 5.1: a) 3D illustration of the experimental set-up for FMC array scanning of the spark eroded ellipse test pieces, showing the series of elliptical notches within the test blocks and the series of scan lines (dashed red). One scan line was used for each notch, with the linear array centred on each notch. b) The cross-sectional view ($x-y$ axes) of the experimental set-up, where the notch defect widths (X) ranged from 1 mm - 3 mm and their inclinations (θ) ranged from 0°- 20°. c) The plan-view of the set-up ($x-z$ axes), where the defect lengths (Z) varied between 1 mm - 3 mm.

defects at various inclination angles. A schematic of the SE test pieces is shown in Fig. 5.1 and the defect parameters are listed in Table 5.1. The defect tolerances listed in Table 5.1 were provided by the test piece manufacturer.

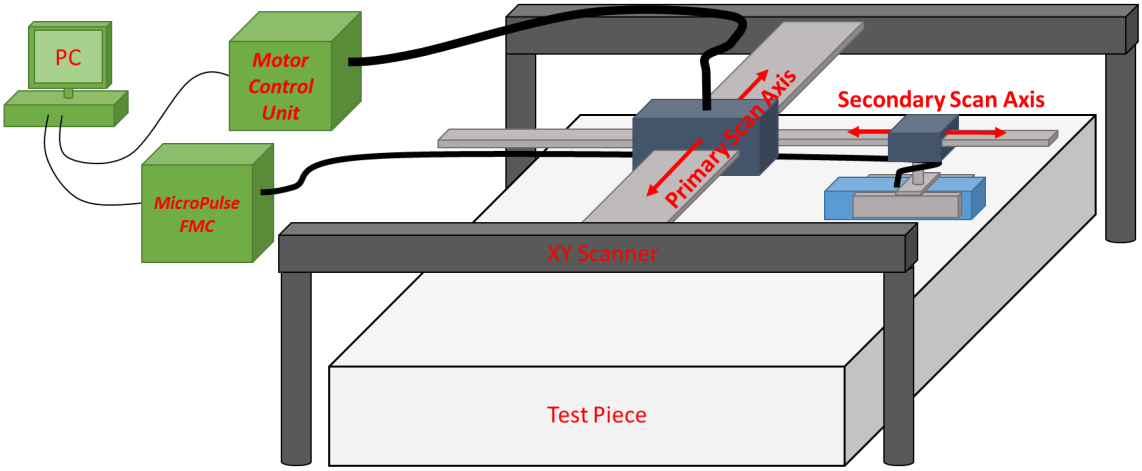


Figure 5.2: An illustration of the experimental set-up used when collecting scanned FMC datasets from a test piece. The ultrasonic array (light blue) is manipulated across the test piece surface with the XY scanner, which can move the probe in either the primary scan axis or the secondary scan axis. Both the primary and secondary scan axes are perpendicular to each other. The XY scanner is controlled with a separate motor control unit and the ultrasonic array is controlled via a MicroPulse FMC signal generator. Both the motor control unit and the MicroPulse FMC are interfaced with a stand-alone computer which controls all the equipment.

A 2 MHz 64-element linear phased array (IMASONIC, 96 mm active aperture) was used in direct contact to collect FMC data from the test pieces. The full array properties are detailed within Table 4.1. A sampling frequency of 25 MHz was used for data collection. The array was placed directly above each defect to maximise the array viewing angle, as conducted in Chapter 4.

The defects were then scanned across the test piece surface along the block width, with the primary aim of sizing the defect width which was parallel to the array ($\hat{x}$-axis). The secondary aim was to size the defect length, which is defined in the $\hat{z}$-axis and parallel to the scan direction. From this, a series of FMC datasets were obtained from which the array imaging algorithms were applied. A 1 mm scan increment was used, which was the limitation of the XY scanner and manipulator file available. An illustration of the experimental set-up used to acquire FMC scan data is shown in Fig. 5.2.

5.3 SR Image Generation from FMC Scan Data

Unlike the FMC datasets acquired in Chapters 3 & 4, this study represented the first time the SR algorithms were applied to a series of FMC datasets from 3D defect profiles as opposed to single shot FMC data from 2D defects.

Unlike conventional imaging algorithms, the SR algorithms behave very differently when presented with various imaging scenarios. For example, indications generated from large defects (in comparison to the wavelength) are non-intuitive and do not resemble the generally smooth varying indications generated by either the TFM or B-Scan methods. Examples of this can

Table 5.1: The elliptical defects parameters located within the spark eroded test pieces. Manufacturing tolerances are also provided. Defect width is defined in the $\hat{x}$-axis and defect length is defined in the $\hat{z}$-axis, as shown in Fig. 5.1.

Defect Width (mm)	**Defect Length (mm)**	**Inclination Angle (°)**
1.0 ± 0.1	3.0 ± 0.1	0 ± 2
1.0 ± 0.1	3.0 ± 0.1	10 ± 2
1.0 ± 0.1	3.0 ± 0.1	20 ± 2
3.0 ± 0.1	1.0 ± 0.1	0 ± 2
3.0 ± 0.1	1.0 ± 0.1	10 ± 2
3.0 ± 0.1	1.0 ± 0.1	20 ± 2

be seen in previous chapters, such as in Fig. 4.4 where although the defects are known to be smooth and planar in nature, multiple indications are generated by the SR algorithms. This is unlike the expected uniform specular responses produced by the TFM and array B-Scan algorithms.

Another difference in imaging behaviour occurs when scanning over a component which contains defects as well as large regions of defect-free material. From an imaging method such as TFM, scanning a specularly-orientated planar target, one would expect the resultant scan image to consist of a high indication response from the defect with the surrounding material having a much lower image response (due to it being defect free). A typical C-Scan from such a conventional imaging case is shown in Fig. 5.3a). TFM C-Scans, such as the image presented in Fig. 5.3a), were constructed by stacking several $x - y$ TFM images together along the z-axis to create a 3D volume of data. Then for every $x-z$ coordinate, the maximum image amplitude value along the y-axis is used to plot a $x - z$ C-Scan image. The image was then subsequently normalised to the maximum C-Scan amplitude and plotted in a decibel scale.

For the equivalent SR imaging case, this does not occur. When the array is scanned directly over the target, the familiar defect indication images are produced as have been previously shown within this thesis. However, when scanning over a defect free region the image does not consist of low amplitude responses but is in fact the opposite. Moreover, the image responses from the defect free-region can match the amplitude of the image responses from when a defect is present. This leads to the SR algorithms generating C-Scans for such a case shown in Fig. 5.3b).

SR algorithm C-Scans were generated in a similar way to the TFM C-Scans by stacking several $x - y$ SR images together along the z-axis. However, each separate $x - y$ SR image is normalised to the maximum image value present within that image and the whole image is then converted to a decibel scale. The reason each image was self-normalised was due to the highly varying maximum amplitude value obtained from the various scans, where often a defect free region may output a higher maximum image amplitude

than responses corresponding to the known defect. The final SR C-Scan image was then constructed by again finding the maximum image value along the y-axis for every $x - z$ coordinate. A suggested reason why such high image responses occur for defect-free regions of the scan is related to the theoretical background of the SR methods. They essentially determine the likelihood that point scatterers are positioned at the imaging locations so when imaging a defect, strong indications are produced at those locations. However for a defect-free region, the A-Scans collected are relatively consistent in amplitude across time, albeit almost zero amplitude, and the SR algorithms interpret this as defects being present everywhere. Therefore, images are produced with high near-uniform amplitudes.

To tackle this problem, a two-stage imaging methodology was designed which utilised the information provided from TFM to inform the SR imaging in an effort to generate representative defect reconstructions suitable for sizing. The methodology does this by using the TFM algorithm, which is known to be very effective at identifying defect locations, to highlight areas of significant defect signal intensity upon which the SR algorithms would be able to reliably image the flaw. In a sense, the method acts as a supplementary tool alongside TFM to complement its robust defect detection capability with the potentially higher sizing resolution of the SR algorithms. The methodology is illustrated in Fig. 5.3. The approach is as follows:

1. Generate TFM images from the FMC data obtained from each scan line described in Fig. 5.1a). From the images, determine a rough estimate of the (x, y, z) position of the defect as well as measure its 6 dB length (extent in the z-axis as shown in Fig. 5.1c)) in the scan direction. The position of the defect allows for appropriate time windowing of the data to be carried out so only the reflected signal from the defect is processed (as stated in Section 2.8.3). The 6 dB length of a defect estimated using this method is shown in the C-Scan image shown in Fig. 5.3a), where the z-axis extent of the defect is denoted by the dashed red lines.

2. Using this estimate of the z-axis extent of the defect length, the FMC scan data is truncated such that only FMC data from within that z-axis remains. This means only data which contain a significant defect signal will be imaged by the SR algorithms and thus generate effective images for defect width sizing in the $x - y$ plane, as shown in Fig. 5.1b)). An example of a full, untruncated SR C-Scan image using the full scan line is shown in Fig. 5.3b) and the subsequently generated truncated SR C-Scan shown in Fig. 5.3c).

3. Using these truncated scan datasets, the SR algorithms are used to generate a series of B-Scans ($x - y$ plane images) at each of the scan increments within the z-axis range defined in step 1. These individual B-Scan images are then summed along the scan direction to generate a single SR image corresponding to only the z-axis region local to the defect. An example of a summed SR B-Scan is shown in Fig. 5.3d).

It is emphasized that the SR images are summed as opposed to selecting

maximum values. This is due to the small variations which can occur between separate B-Scan $x-y$ plane images from the different scan increments. Summing results in the most prominent and consistent image features to have the greatest impact to allow for a stable defect characterisation performance. This method means that only defect sizing can only be achieved in the B-Scan dimensions ($x-y$ plane) and due to the complexity of the SR images, it is not recommended that they are used to size the defects along the scan direction (z-axis).

5.4 Spark Eroded Test Piece Array Imaging Results

The array 0° B-Scan, TFM, MF-FM and MF-TR-MUSIC algorithms were applied to the collected FMC scan data from the SE test pieces using the methodology presented in Section 5.3. The images produced are shown in Fig. 5.4 and Fig. 5.5.

The images shown in Fig. 5.4 and Fig. 5.5 are generally consistent with all previous images for 2D defects shown within this thesis. The SR algorithms generated images with two indications corresponding to the defect tips in most cases, which aligned with the expected empirical number of indications for defects of this size shown in Fig. 3.10. However when imaging the 1 mm ($\lambda/3$) width dimension of the (1x3) mm SE defects, the MF-FM was unable to resolve the defect tips and only single indications were produced, as shown in Fig. 5.4. This is similar to the experimental images shown in Fig. 4.6 where both SR methods were unable to resolve defect tips for the ($\lambda/4$) sized WE flaws. This meant that sizing using tip responses was not possible. The reason amplitude-based sizing was not conducted instead, as was carried out with the TFM and array B-Scan algorithms, was due to the fact that the amplitude of the SR images do not necessarily correspond to direct physical acoustic responses in the same way that the amplitude responses from beamforming algorithms do (see description of 6 dB drop sizing method in Section 3.3). It is therefore suggested that further studies are required to be carried out in order to determine if empirical amplitude-based sizing can be accurately and reliably conducted using the SR techniques for embedded planar defects, similar to the studies by Zhang *et al.* (2018) [36] for surface-breaking defects. Based on the trend presented in Fig. 3.10, one could infer that because only a single indication was produced by the MF-FM algorithm the defect width must be smaller than $\lambda/2$, placing an upper limit on this parameter. Both the TFM and array B-Scan algorithms produced single small indications, as is expected for these sub-wavelength sized SE flaws.

The characterisation results from the MF-FM, MF-TR-MUSIC, TFM and array 0° B-Scan images for the SE defects in Fig. 5.4 and Fig. 5.5 are listed in Table 5.2, Table 5.3, Table 5.4 and Table 5.5 respectively.

Despite the MF-FM algorithm not being able to resolve the tips of the (1x3) mm SE flaws, the MF-TR-MUSIC algorithm using the scanned FMC dataset methodology presented in Section 5.3 was able to achieve accurate width sizing of the 1 mm ($\lambda/3$) dimension of the defects. Reasonable estimations of the defect orientation was also possible with the MF-TR-MUSIC technique, except for the 0° case which overestimated the tilt by more than 25°

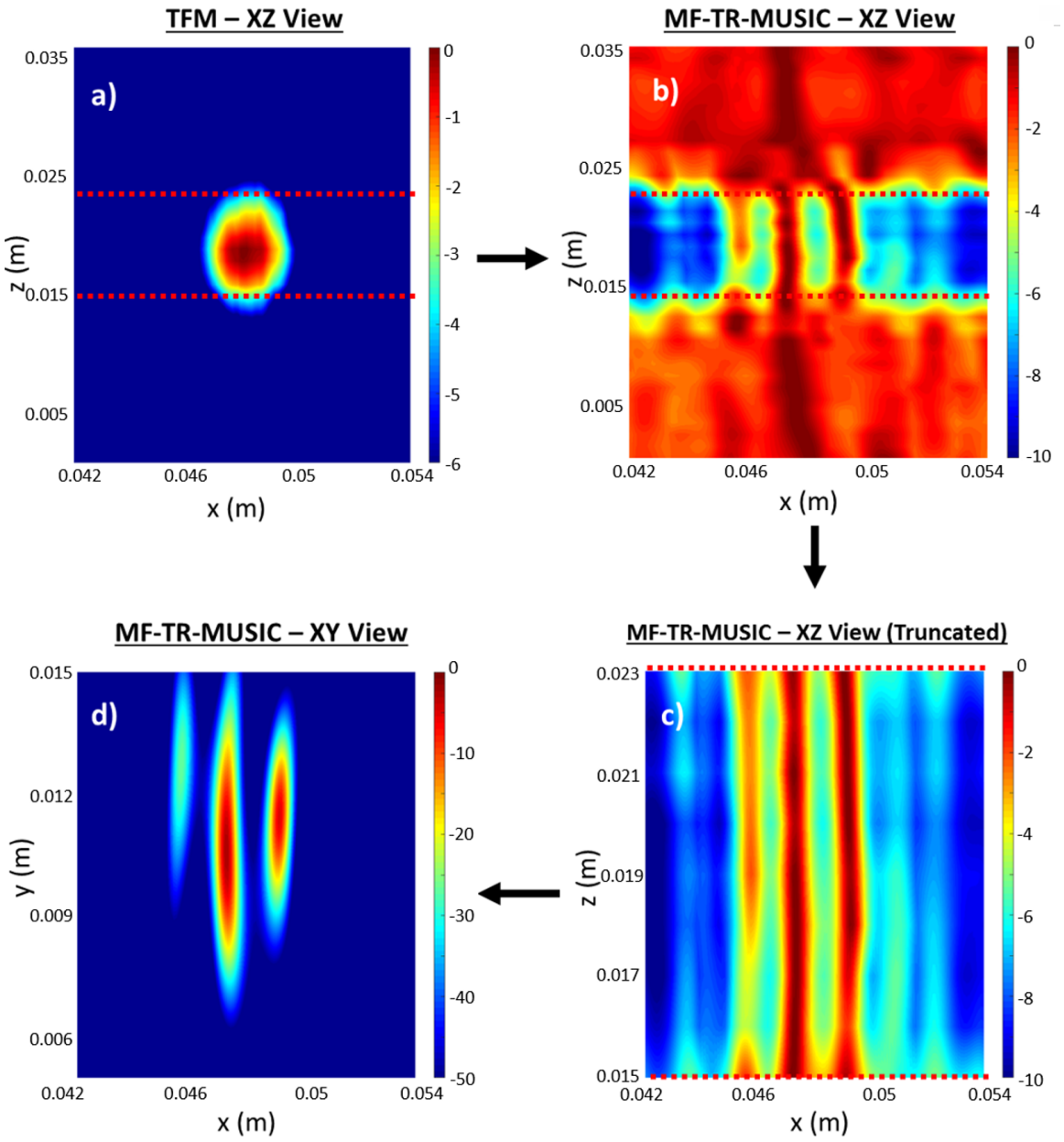


Figure 5.3: Imaging methodology to generate a SR B-Scan ($x-y$) image of an embedded planar defect. The first step is to apply the TFM algorithm to the FMC scan data and estimate the (x, y, z) position of the defect. The z-extent of the defect from the C-Scan is estimated (a). The z-extent is used to truncate the SR data (b) to produce a reduced set of data which contains significant defect indications (c). (d) SR B-Scan ($x-y$) images are generated for each scan increment FMC dataset and the resultant images are summed to produce a single defect image which is used for characterisation. The set-up shown in Fig. 5.1 was used, featuring a 64-element 2 MHz array scanned centrally above the defects at a distance of 40 mm. All images are plotted on a decibel scale.

as shown in Fig. 5.4. These results experimentally demonstrate the super

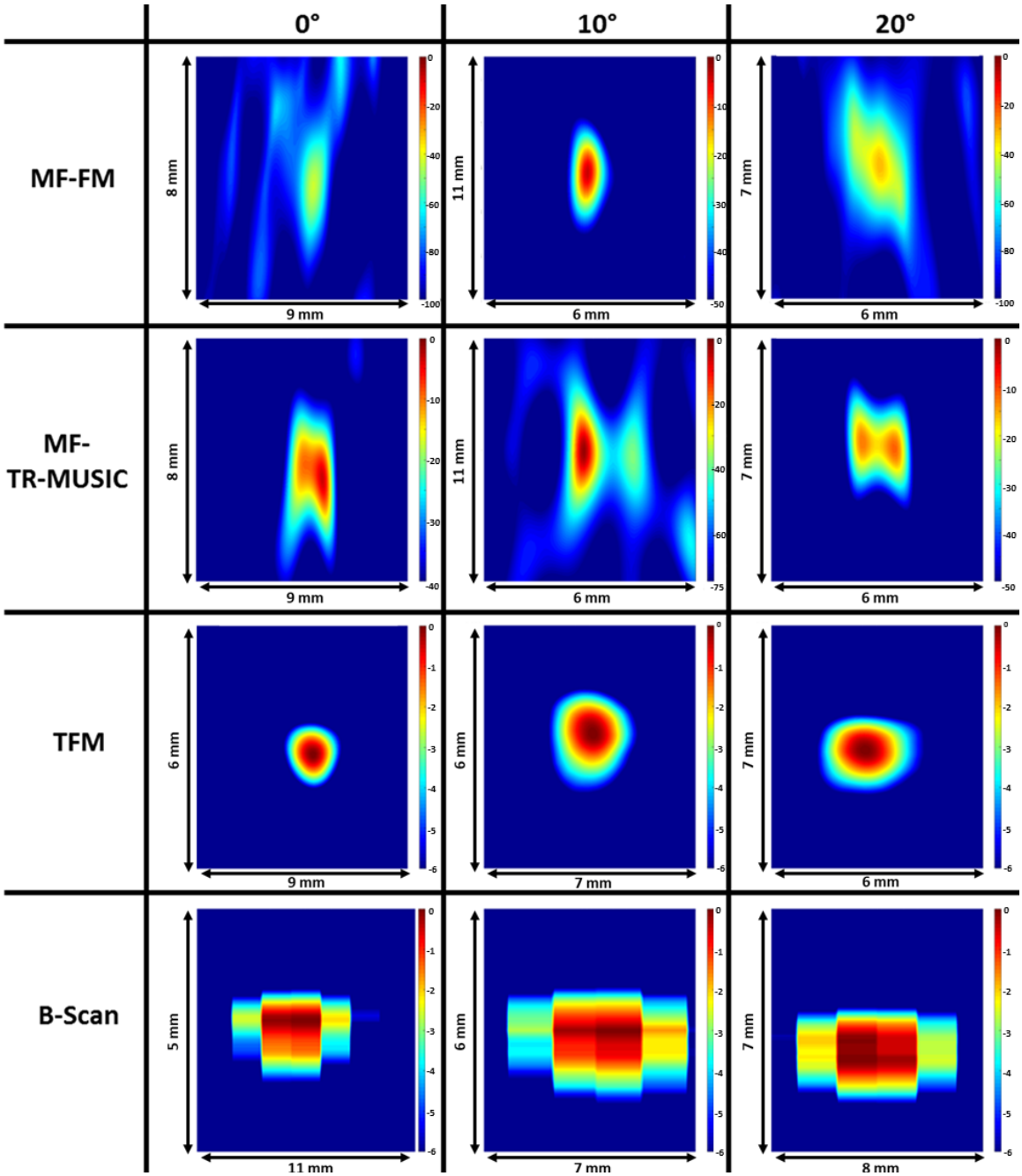


Figure 5.4: Array algorithm images for the (1x3) mm spark eroded elliptical defects using a 2 MHz 64-element array. All images were self-normalised to their peak amplitude value and are plotted in the decibel scale. All TFM and B-Scan images are plotted between 0 and -6 dB. A 15 mm active aperture was used to generate the 0° and 10° B-Scan images and a 16.5 mm active aperture was used to generate the 20° B-Scan images. The set-up shown in Fig. 5.1 was used, featuring a 64-element 2 MHz array scanned centrally above the defects at a distance of 40 mm.

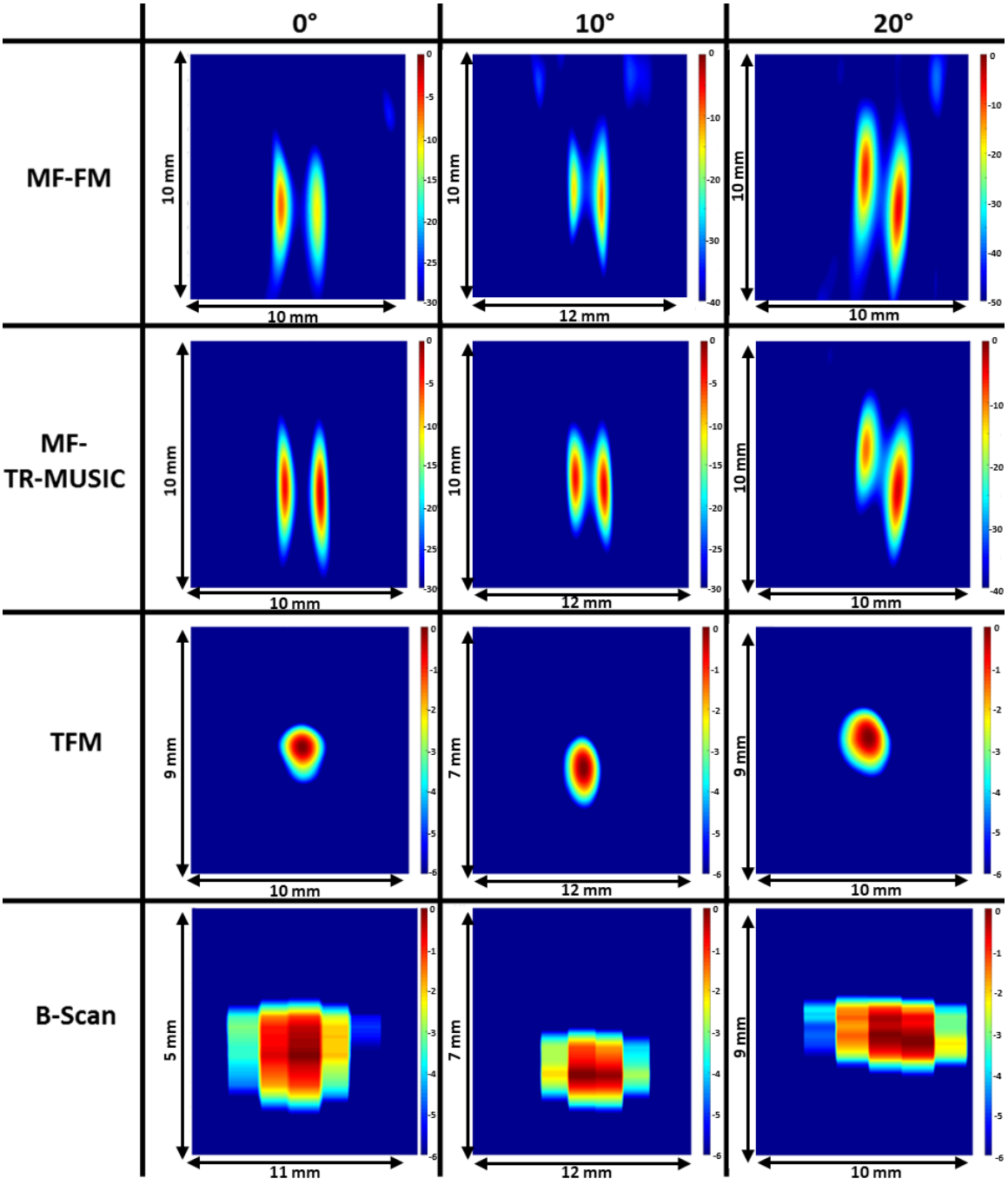


Figure 5.5: Array algorithm images for the (3x1) mm spark eroded elliptical defects using a 2 MHz 64-element array. All images were self-normalised to their peak amplitude value and are plotted in the decibel scale. All TFM and B-Scan images are plotted between 0 and -6 dB. A 15 mm active aperture was used to generate all the B-Scan images. The set-up shown in Fig. 5.1 was used, featuring a 64-element 2 MHz array scanned centrally above the defects at a distance of 40 mm.

Table 5.2: The 2 MHz 64-element array MF-FM sizing results for the spark eroded test pieces. No sizing results are presented for the defects with 1 mm widths due to the algorithm only generating single indications meaning tip indication based sizing could not be conducted.

Actual Defect Parameters			**MF-FM Sizing Results**	
Width (mm)	**Length (mm)**	**Tilt (°)**	**Width (mm)**	**Tilt (°)**
1	3	0	-	-
1	3	10	-	-
1	3	20	-	-
3	1	0	1.73 ± 0.05	10 ± 2
3	1	10	1.68 ± 0.05	18 ± 2
3	1	20	2.16 ± 0.05	44 ± 1

Table 5.3: The 2 MHz 64-element array MF-TR-MUSIC sizing results for the spark eroded test pieces.

Actual Defect Parameters			**MF-TR-MUSIC Sizing Results**	
Width (mm)	**Length (mm)**	**Tilt (°)**	**Width (mm)**	**Tilt (°)**
1	3	0	0.90 ± 0.05	26 ± 3
1	3	10	1.35 ± 0.05	13 ± 2
1	3	20	1.04 ± 0.05	11 ± 2
3	1	0	1.73 ± 0.05	10 ± 2
3	1	10	1.65 ± 0.05	14 ± 2
3	1	20	2.28 ± 0.05	48 ± 1

Table 5.4: The 2 MHz 64-element array TFM sizing results for the spark eroded test pieces.

Actual Defect Parameters			**TFM Sizing Results**		
Width (mm)	**Length (mm)**	**Tilt (°)**	**Width (mm)**	**Length (mm)**	**Tilt (°)**
1	3	0	2.43 ± 0.05	7 ± 1	0 ± 1
1	3	10	2.97 ± 0.05	8 ± 1	8 ± 1
1	3	20	2.95 ± 0.05	7 ± 1	2 ± 1
3	1	0	2.30 ± 0.05	7 ± 1	0 ± 1
3	1	10	2.20 ± 0.05	7 ± 1	3 ± 1
3	1	20	2.58 ± 0.05	8 ± 1	9 ± 1

resolution capability of the method by being able to accurately size significantly sub-wavelength sized 3D defects with realistic morphologies. The

Table 5.5: The 2 MHz 64-element array B-Scan sizing results for the spark eroded test pieces.

Actual Defect Parameters			Array B-Scan Sizing Results		
Width (mm)	**Length (mm)**	**Tilt (°)**	**Width (mm)**	**Length (mm)**	**Tilt (°)**
1	3	0	7.5 ± 1.5	7 ± 1	0 ± 1
1	3	10	6.0 ± 1.5	8 ± 1	0 ± 1
1	3	20	6.1 ± 1.5	7 ± 1	5 ± 1
3	1	0	7.5 ± 1.5	7 ± 1	0 ± 1
3	1	10	6 ± 1.5	6 ± 1	0 ± 1
3	1	20	7.5 ± 1.5	8 ± 1	9 ± 1

TFM algorithm expectedly overestimated the 1 mm defect width by producing estimations close to 3 mm. TFM was significantly more accurate however than the B-Scan algorithm which overestimated the size by over 500% for each inclination case. In terms of length sizing of the 3 mm (λ) dimension of the (1x3) mm SE flaws, the TFM and B-Scan produced identical results of at least 7 mm thus demonstrating poor resolution in the array scanning direction. As explained in Section 5.3, reliable sizing in the array scanning direction could not be achieved with the SR methods.

When width sizing the 3 mm (λ) dimension of the (3x1) mm defect images shown in Fig. 5.5, both SR and TFM algorithms undersized the defects for all orientation angles by around 30% as shown in Tables 5.2-5.4. Due to the defect having a small extent in the array scanning direction (1 mm) with a high rate of change of width profile, there is a strong likelihood that the 1 mm scan increment used was insufficient to ensure the array was exactly aligned with the major axis of the elliptical defects in order to accurately measure it. The fact that the TFM algorithm, which tends not to undersize planar flaws larger than the diffraction limit, also underestimated the width along with the SR methods suggesting that this scenario might have occurred. A different equipment set-up that would allow a finer scan increment to be implemented would be required to confirm this postulation. When length sizing the 3 mm ($\lambda/3$) dimension of (3x1) mm SE flaws, the TFM and B-Scan again produced similar oversizing results consistent with the (1x3) mm case.

Using the methodology described in Section 3.6, the imaging SNR values of the TFM and array B-Scan algorithms were estimated from the 2 MHz 64-element array images and are listed in Table 5.6. A representative example experimental SNR case for the SE test pieces ((1x3) mm 0° defect) is shown in Fig. 5.6. The imaging SNR of both of the algorithms considered in Table 5.6 are high, which is expected from the low scattering material from which the test pieces were manufactured. However as shown previously in Chapter 4, the TFM algorithm achieved a far higher imaging SNR compared to the array B-Scan algorithm by roughly a factor of two. The imaging SNR values for the SE defects were also expectedly lower than for the WE defects presented in Table 4.4 as the area of the scattering surfaces

Table 5.6: The imaging SNR of the TFM and array B-Scan algorithms from the 2 MHz experimental images generated from the SE defects.

Defect Size (mm)	Tilt Angle (°)	$\mathbf{SNR}_{TFM}$	$\mathbf{SNR}_{BScan}$
1x3	0	35.6	16.3
1x3	10	34.8	17.5
1x3	20	37.5	17.1
3x1	0	31.0	17.9
3x1	10	33.3	18.5
3x1	20	31.3	12.7

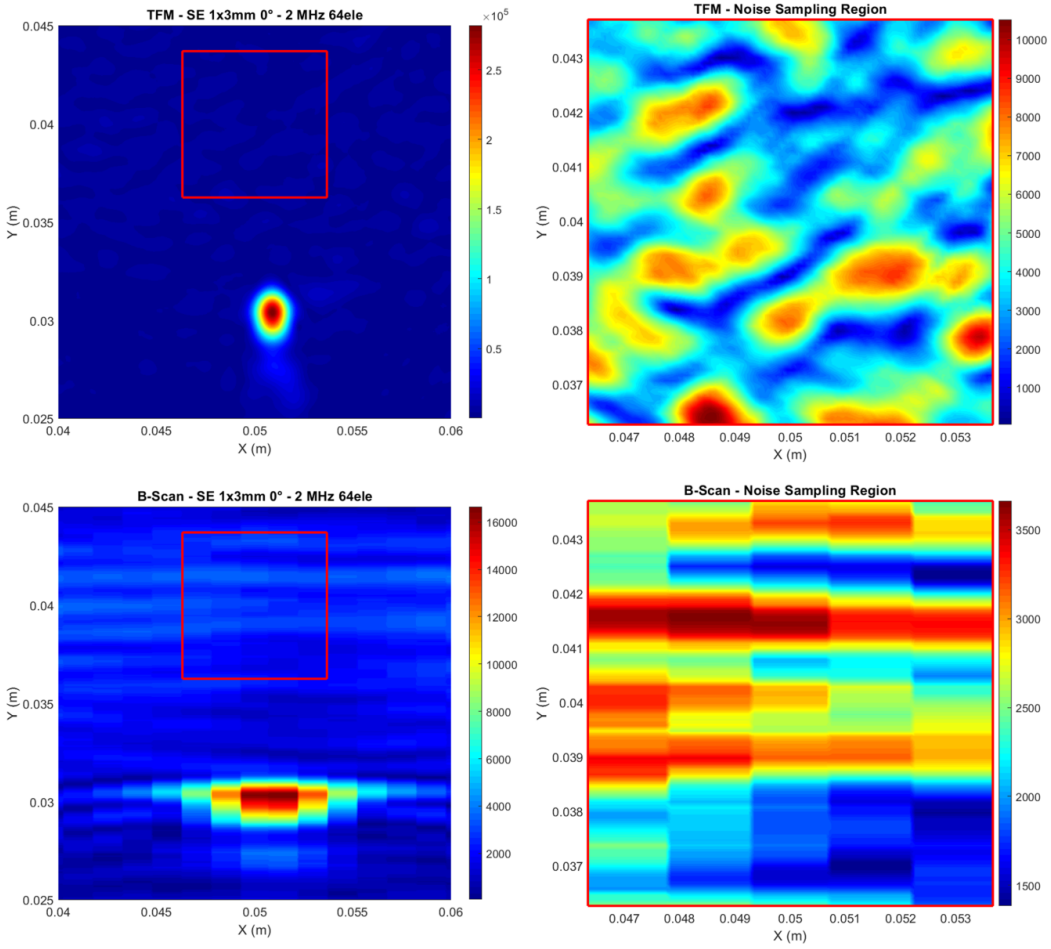


Figure 5.6: The imaging SNR methodology for the (1x3) mm 0° SE case. Each image plotted in an absolute amplitude scale. The set-up shown in Fig. 5.1 was used, featuring a 64-element 2 MHz array scanned centrally above the defects at a distance of 40 mm.

of the 3D SE flaws were far smaller than the pseudo-2D WE defects.

5.5 Conclusions

In this Chapter, the experimental performance of the array algorithms were extended beyond the 2D cases considered in Chapter 4 as 3D elliptical spark eroded defects of varying size and orientation were imaged. A methodology was presented which allowed SR imaging to be conducted from array FMC scan data. This methodology however was only used for enhanced defect sizing for flaws that were already detected by another imaging method, in this case the TFM algorithm. Due to the complex indication patterns generated by the SR algorithms, they could only be used to confidently size the defects in the $x - y$ plane, i.e. width sizing only.

It was found that by applying this imaging methodology, the MF-TR-MUSIC algorithm in particular allowed for excellent defect sizing for defects well below the diffraction limit; in this study down to $\lambda/3$. This level of performance could not be achieved by either the MF-FM, TFM or the array $0°$ B-Scan algorithms. For the $\lambda/3$ sized defects, the MF-FM method only produced a single indication which meant the tip sizing methodology could not be applied and only an upper limit of the defect width of $\lambda/2$ could be inferred. The TFM and array B-Scan algorithms became beam width limited at this size regime as expected and they could not be used to effectively size the defects.

This validation of the applicability of the SR methods for sizing 3D defects with realistic morphologies is a crucial step towards any practical implementation of the algorithms within industrial NDE inspections.

Chapter 6

SR Imaging of Simulated Embedded Rough Planar Defects

6.1 Introduction

One prominent challenge present within the nuclear industry is the inspection of rough defects. Due to the often extreme conditions components are exposed to within this sector, defect growth mechanisms such as thermal fatigue cracking [82] and stress corrosion cracking can occur which are known to produce defects with significant surface roughness [83, 84].

Ultrasonically, the extent of defect roughness can have a major impact on the scattered field emitted from them [85, 86], often hindering their detection and characterisation which can lead to a large degree of conservatism to be placed on their inspection. This inevitably is costly to industry.

Although there is a demand within industry in general to size smaller defects which may exist within the sub-wavelength regime, an issue which could potentially be addressed by the SR algorithms, these methods must first demonstrate a significant performance enhancement compared to historically preferred techniques whilst displaying robustness to various experimental factors. Defect roughness is one such factor which must be considered before these advanced algorithms can be deployed.

In this Chapter, 2D FE modelling was used to simulate the array inspection of embedded rough planar defects and to investigate the impact of varying roughness parameters on array imaging performance. The same 2D FE modelling approach that was used in Section 3.2 was applied within this Chapter.

The results presented within this Chapter represent the peer-reviewed published findings by the author J. B. Elliott *et al.* (2019) [87].

6.2 Background Theory of Defect Roughness

A statistical framework to model rough cracks, which is commonly adopted in literature [88], is that of a Gaussian distribution of the geometric features of the rough surface; this approach was also utilised in this study. Planar 2D rough defects can be modelled simply as follows.

If the crack size is aligned along the x-axis, and the height in the y-axis, the variation of crack height, h, defined as the deviation from a flat reference surface is given by:

$$y = h(x). \tag{6.1}$$

The ensemble average, $\langle\rangle$, of the height function of the crack is assumed to be [89]:

$$\langle h \rangle = 0. \tag{6.2}$$

The probability that the surface height exists between the values h and $h + dh$, where $dh > 0$, can be written as $p(h)dh$, where $p(h)$ is the probability density function. Applying Gaussian statistics, $p(h)$ can be written as [89]:

$$p(h) = \frac{1}{\sigma\sqrt{2\pi}} \exp\left(\frac{-h^2}{2\sigma^2}\right), \tag{6.3}$$

where σ is defined as the surface Root-Mean-Squared (RMS) height:

$$\sigma = \sqrt{\langle h \rangle} = \sqrt{\frac{1}{N\sum_{i=1}^{N} h_i^2}}. \tag{6.4}$$

The correlation function, $C(R)$, describes the lateral variation of the surface height by relating the height of two points along x separated by a distance R. It can be defined as [88]:

$$C(R) = \frac{\langle h(x)h(x+R)\rangle}{\sigma^2} = \exp\left(\frac{-R^2}{\lambda_0^2}\right), \tag{6.5}$$

where λ_0 is called the surface correlation length and is defined as the distance over which $C(R)$ decays by $\frac{1}{e}$.

Rough defect profiles were generated by using a moving average approach with the above Gaussian statistics, in line with previous studies [72, 90]. To simulate defect opening, an additional step was implemented which was to open apart two identical rough surfaces by symmetrically displacing the top and bottom surfaces by a half-cycle sinusoidal function. The maximum opening was twice the FE element size (0.1 mm) at the centre of the defect and no opening at the defect tips. This process to generate the 2D open rough cracks is shown graphically in Fig. 6.1. Open defects were used instead of defects with no thickness as they would more closely represent defects encountered in the nuclear sector.

Smooth defects were also created as reference imaging examples. In these cases, the defects were opened in the same way as described above but with no roughness imposed, as shown by Fig. 3.4.

6.3 Rough Defect Inspection Cases

A series of rough defect cases with different parameters were used in this study and are listed in Table 6.1. The values of σ and λ_0 were chosen in line with typical experimentally measured values from thermal fatigue and stress corrosion cracks from components within the nuclear industry [83,

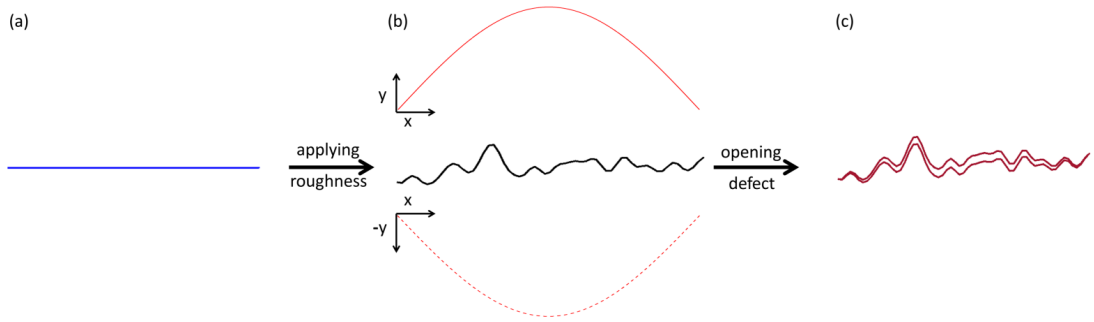


Figure 6.1: Visualisation of the process to generate the 2D rough embedded defects. First a smooth defect profile is calculated (a), then roughness is applied to this profile following Gaussian statistics (b). The crack is then opened by a small amount, varying along its length, by displacing the top surface upwards by the half-cycle sinusoidal profile function shown in the solid red line at the top of (b) and similarly moving the bottom surface down by the dashed red at the bottom of (b). The resulting open 2D rough defect is shown in (c).

Table 6.1: The rough defect cases investigated in this study, each with their corresponding parameters. A 0° inclination angle was defined to be parallel to the ultrasonic array.

Defect Size (mm)	Inclination Angle (°)	σ (μm)	λ_0 (μm)
1.5	0	10	150
1.5	45	10	150
1.5	0	100	150
1.5	45	100	150
3	0	10	150
3	45	10	150
3	0	100	150
3	45	100	150

84]. Although the defect growth mechanism and component material can lead to large variations in the resultant defect parameters, it was reported that thermal fatigue cracking produced defects with $\sigma \approx 10 - 20$ μm and $\lambda_0 \approx 100 - 200$ μm in ferritic low alloy steels and $\sigma \approx 70 - 100$ μm and $\lambda_0 \approx 100 - 200$ μm in stainless steels [83, 84]. Stress corrosion cracking defects were shown to exhibit roughly the same parameters. These types of defects were considered to be the most relevant to the potential application of array inspections utilising SR algorithms, hence rough defects with $\lambda_0 = 150$ μm and $\sigma = 10$ μm, 100 μm were considered.

For each defect width, roughness and orientation combination listed in Table 6.1, 100 different FE realisations were used when assessing the imaging algorithms' performances. To justify the total number of realisations, the

Table 6.2: The characterisation results for all smooth defect equivalent cases when applying all algorithms.

Actual			**MF-FM**		**MF-TR-MUSIC**		**TFM**	
Width (mm)	Width (λ)	Angle (°)	Width (mm)	Angle (°)	Width (mm)	Angle (°)	Width (mm)	Angle (°)
1.5	0.5	0	1.51	1.91	1.51	1.91	1.7	0
1.5	0.5	45	1.46	40.84	1.47	38.07	1.95	0.001
3	1	0	3.12	0.92	2.92	0.99	3	0
3	1	45	3.70	46.13	4.37	54.87	2.35	43.29

statistical variation of the measured width for each rough defect parameter set was calculated and the results showed good convergence with only slight variations remaining for some of the higher roughness cases. This provided a basis to legitimise any results derived from the Monte Carlo study. This number of realisations to achieve adequate convergence is also consistent with the results presented by Pettit *et al.* [72]. Defect widths of 1.5 mm ($\frac{\lambda}{2}$) and 3 mm (λ) were considered to focus the investigation on small defects at or below the ultrasonic wavelength. Defect inclinations of 0° and 45° were selected to compare the performance differential between an optimal defect orientation (0°) to a non-optimal case.

In addition, a smooth defect case was run for each combination of defect width and inclination angle shown in Table 6.1 to establish a benchmark for the different algorithms.

6.4 Results and Discussions

For each of the rough defect realisations and smooth defect cases, the TFM, MF-FM and MF-TR-MUSIC algorithms were applied to the simulated FMC datasets and the sizing methodologies described in Sec. 3.4 were implemented to estimate the defect width and orientation from the images. The pixel size in all image reconstructions was set to 50 μm.

6.4.1 Smooth Defects

It is important to assess the performance of the SR algorithms on smooth defects initially before adding further complexities to the inspection, such as defect roughness, in order to establish their baseline capabilities. The images produced for these smooth defect cases are shown in Fig. 6.2 and the associated characterisation results are detailed in Table 6.2.

First considering the 1.5 mm ($\frac{\lambda}{2}$) smooth defect results in Table 6.2, it can be seen that the MF-FM and MF-TR-MUSIC algorithms produce far more accurate results than TFM for both inclination values. There is a 1-2% error in the width sizing of the SR algorithms for both orientations, compared to the 13-30% overestimation of TFM. In terms of estimating the defect inclination,

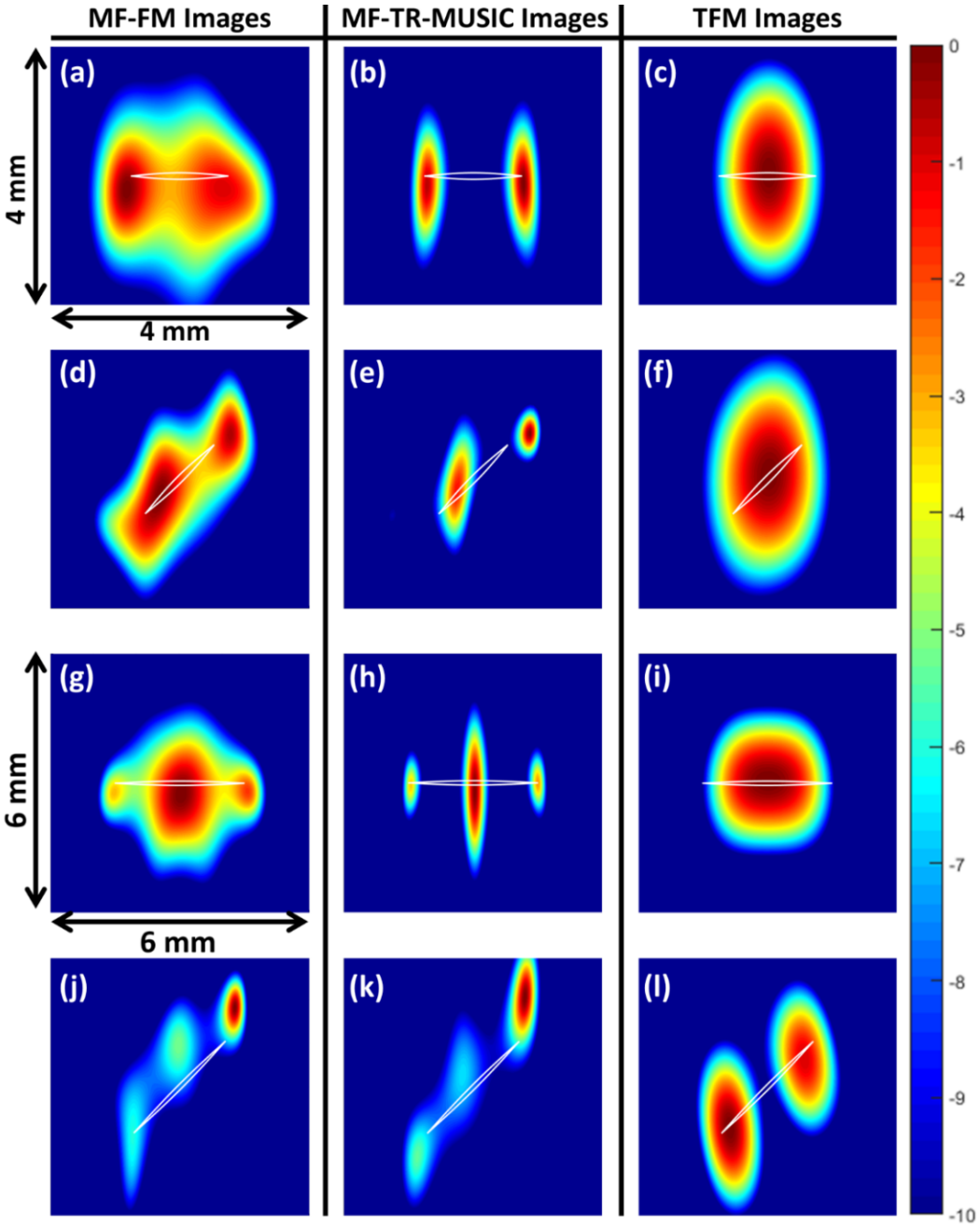


Figure 6.2: Images from the MF-FM, MF-TR-MUSIC and TFM algorithms for the smooth defect cases. Images a), b) and c) correspond to 1.5 mm 0° defects; d), e), and f) correspond to 1.5 mm 45° defects; g), h) and i) correspond to 3 mm 0° defects; j), k) and l) correspond to 3 mm 45° defects. All the images are plotted on a decibel scale normalised to the maximum image amplitude from the defect response. Images (a)-(f) are 4 mm x 4 mm in size, images (g)-(l) are 6 mm x 6 mm in size. The set-up shown in Fig. 3.1 was used, featuring a 64-element 2 MHz array centred above the defects at a distance of 42 mm.

TFM produces the same estimation of 0° for both defect orientations indicating that the technique is not viable to measure this parameter for defects

on this scale. This is visible in the images in Fig. 6.2(c) and (f) where the limited resolution of TFM results in a single blurred indication and gives no measure of orientation. The SR algorithms are not limited in this way and they estimate the defect angles successfully to within 2° and 7° in the 0° and 45° cases respectively. This in turn allows good estimation of defect through-wall heights (TWHs); this is the projection of the defect size in the component thickness direction and hence depends on angle.

Considering the 3 mm (λ) 0° smooth defect imaging results in Table 6.2, TFM now performs with excellent accuracy as it is no longer diffraction limited. The SR algorithms still perform well with around a 4% error in sizing and less than 1° error in inclination estimation. In the 3 mm 45° case however, there is a significant drop-off in performance for all the algorithms. TFM is able to resolve the tip diffraction signals, however it undersizes the width by around 20% despite accurately estimating the inclination. Both of the SR algorithms oversize the defect significantly, with the MF-FM overestimating the width by 23% and the MF-TR-MUSIC algorithm by 46%. This is visible in the images in Fig. 6.2(j) and (k) where the defect tip indications can be seen to deviate from the actual tip location considerably.

These results along with the findings from the previous Chapters demonstrate that the SR algorithms could provide an accurate sizing capability for sub-wavelength smooth defects. The SR algorithms additionally showed good defect orientation estimation performance for both 0° and 45° cases, unlike TFM which could not estimate this parameter effectively. This is a significant result as it demonstrates that through-wall sizing is achievable using the SR algorithms on ($\frac{\lambda}{2}$) sized smooth inclined planar defects. The TWH of defects is a vital parameter that must be estimated accurately in most inspections as it often can be the largest influence on the structural integrity of components. The lack of performance of TFM was attributed to the defect width being at the diffraction limit and it was shown that the SR algorithms could potentially bridge this performance gap on this size scale. For larger wavelength sized defects, the results showed there was no significant benefit of applying the SR algorithms over conventional TFM as generally TFM produced accurate characterisation results comparable or slightly better than the SR methods. This was expected as these defects were comfortably within the theoretical resolution limit of the method.

6.4.2 Rough defects

To begin the analysis beyond the smooth cases, the 1.5 mm ($\frac{\lambda}{2}$) 0° rough defect imaging results were considered. Representative images from the imaging algorithms produced for the 1.5 mm defects, with each of the orientation and roughness combinations, are shown in Fig. 6.3. In total, 100 separate FE realisations were run for each defect parameter combination shown in Fig. 6.3, from which the statistical mean and standard deviation of the defect width and inclination angle were calculated to determine the performance of each algorithm. The standard deviation was used as the statistical error for the obtained results.

Fig. 6.4 compares the sizing and orientation estimation results of all the algorithms to the true values for the 1.5 mm 0° 10 μm and 100 μm rough

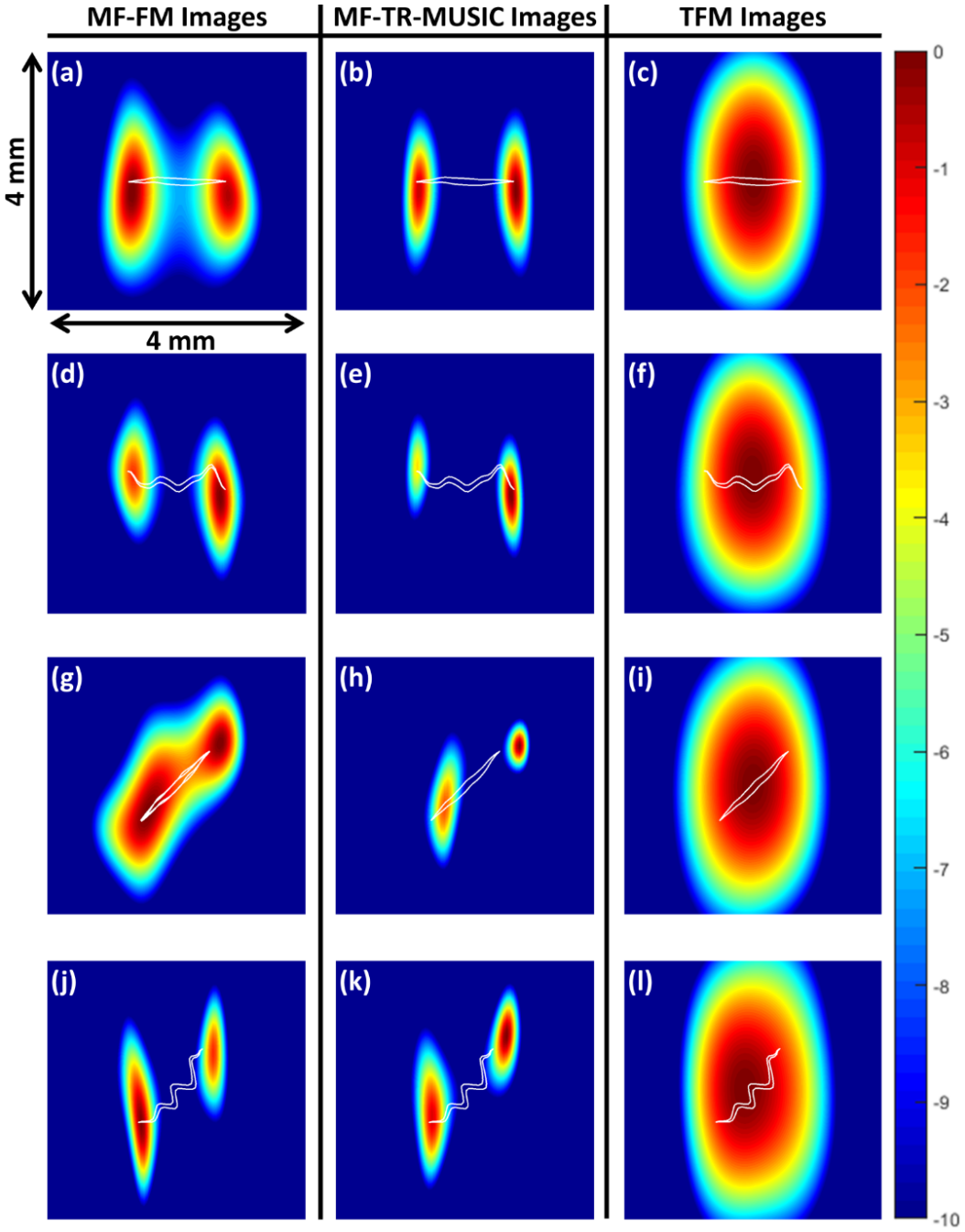


Figure 6.3: Representative images from the MF-FM, MF-TR-MUSIC and TFM algorithms for 1.5 mm rough defects. Images a), b) and c) correspond to $\sigma = 10$ μm 0° rough defects; d), e), and f) correspond to $\sigma = 100$ μm 0° rough defects; g), h) and i) correspond to $\sigma = 10$ μm 45° rough defects; j), k) and l) correspond to $\sigma = 100$ μm 45° rough defects. All the images are plotted on a decibel scale normalised to the maximum image amplitude from the defect response. The set-up shown in Fig. 3.1 was used, featuring a 64-element 2 MHz array centred above the defects at a distance of 42 mm.

defect cases. It can be seen that in the 10 μm cases, both of the SR algorithms estimate the defect width more accurately than TFM. Both of the SR

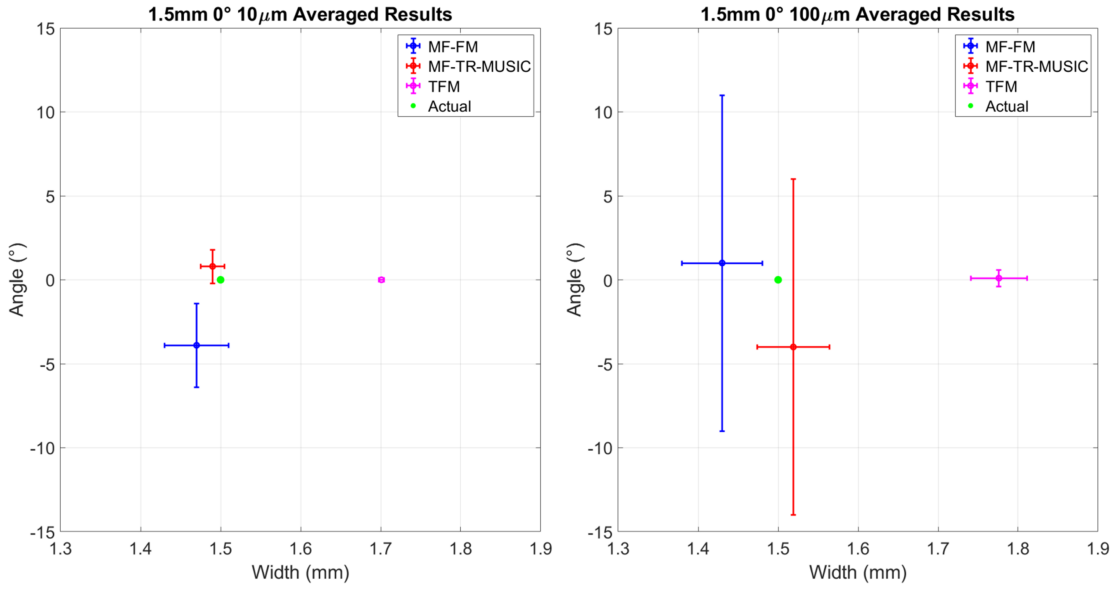


Figure 6.4: The mean estimated defect width and inclination angle values calculated from the 100 realisations for the 1.5 mm 0° 10 μm (left plot) and 1.5 mm 0° 100 μm (right plot) rough defects. The error bars correspond to the standard deviation of the width and angle results.

algorithms' mean width estimations are within one standard deviation of the true value of 1.5 mm, with MF-FM producing a result of (1.47$\pm$0.04) mm and the MF-TR-MUSIC estimating the width to be (1.490$\pm$0.015) mm. TFM overestimates the defect width, (1.701$\pm$0.004) mm, due to the blurring caused by the resolution limit. In terms of estimating the defect inclination, MF-TR-MUSIC is accurate with a small standard deviation. MF-FM has a slight negative bias in its inclination estimation and the mean value is just over one standard deviation from the true value of 0°. The value it estimates is still close to the true value and is accurate enough to have negligible influence on correctly estimating the through-wall height of the defect. TFM is accurate in its estimation of the 0° inclination, however, as has been shown from the smooth cases, this is a misleading result as it cannot estimate this parameter for small defects. Comparing these results to the smooth defect results, it is clear that the effect of low roughness was negligible on the imaging capability of the algorithms.

Now comparing the 10 μm results to the 100 μm results in Fig. 6.4, the most apparent difference is the increased standard deviation in the SR algorithms' inclination estimations, with both methods having a standard deviation of 20° compared to less than 5° previously. This was attributed to how the positions of the 100 μm rough tip ends generally exhibited significant vertical variation compared to the 10 μm cases. This is shown in Fig. 6.3 where in the images (a) and (b), the rough crack tips lie in approximately the same depth plane and therefore so do the SR indications. However in plots (d) and (e), the rough crack tips do not lie in the same depth plane and thus neither do the SR indications, inevitably outputting non-zero inclination estimations. TFM in this case again misleadingly produced inclination estimations close to the correct value of 0°, a result of its inability to estimate

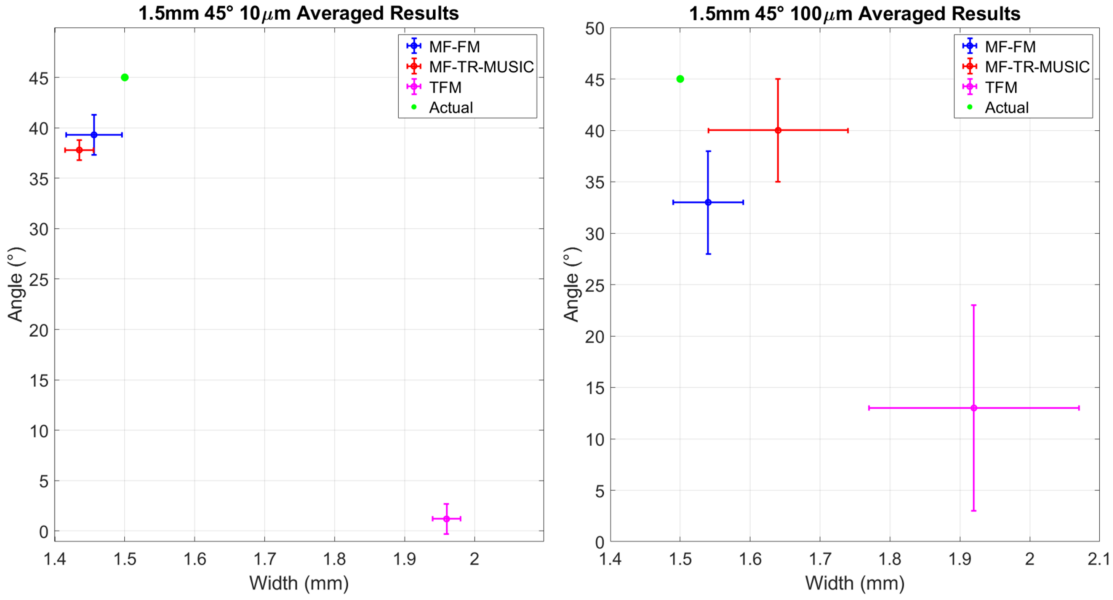


Figure 6.5: The mean estimated defect width and inclination angle values calculated from the 100 realisations for the 1.5 mm 45° 10 μm (left plot) and 1.5 mm 45° 100 μm (right plot) rough defects. The error bars correspond to the standard deviation of the width and angle results.

this parameter for the $\frac{\lambda}{2}$ sized defects. Importantly, the SR algorithms still produced more accurate width estimations compared to TFM despite the increased roughness. The estimations produced were (1.52±0.045) mm for MF-TR-MUSIC and (1.43±0.05) mm for MF-FM, which are more accurate than the (1.78±0.035) mm for TFM.

The averaged characterisation results for the 1.5 mm 45° rough defects are shown in Fig. 6.5. As can be seen in the low 10 μm roughness results, both of the SR result algorithms outperform TFM in estimating the defect width and inclination. MF-FM estimated these parameters to be (1.46±0.04) mm and (39±2)°, MF-TR-MUSIC estimated them to be (1.44±0.02) mm and (38±1)° and TFM estimated them to be (1.96±0.02) mm and (1±1.5)°. TFM again shows its limited performance when imaging sub-wavelength defects as it provides poor estimations for defect width as well as not being able to estimate the defect inclination at all. For the 1.5 mm 45° 100 μm roughness results, the same trends as for the low roughness cases are observed. Despite reduced performance with the higher roughness, both SR algorithms were significantly more accurate than TFM in estimating the defect parameters, with around 25% better width sizing accuracy and 50% better orientation estimation. MF-FM estimated the defect parameters to be (1.54±0.05) mm and (33±5)°, MF-TR-MUSIC estimated them to be (1.64±0.1) mm and (40±5)° and TFM estimated them to be (1.92±0.15) mm and (13±10)°.

Representative images from the imaging algorithms for the 3 mm (λ) defects with each of the orientation and roughness combinations are shown in Fig. 6.6. The same analysis as for the 1.5 mm rough defect results were applied and the averaged characterisation parameters from the algorithms are plotted in Fig. 6.7 and Fig. 6.8, corresponding to the 0° and 45° inclined

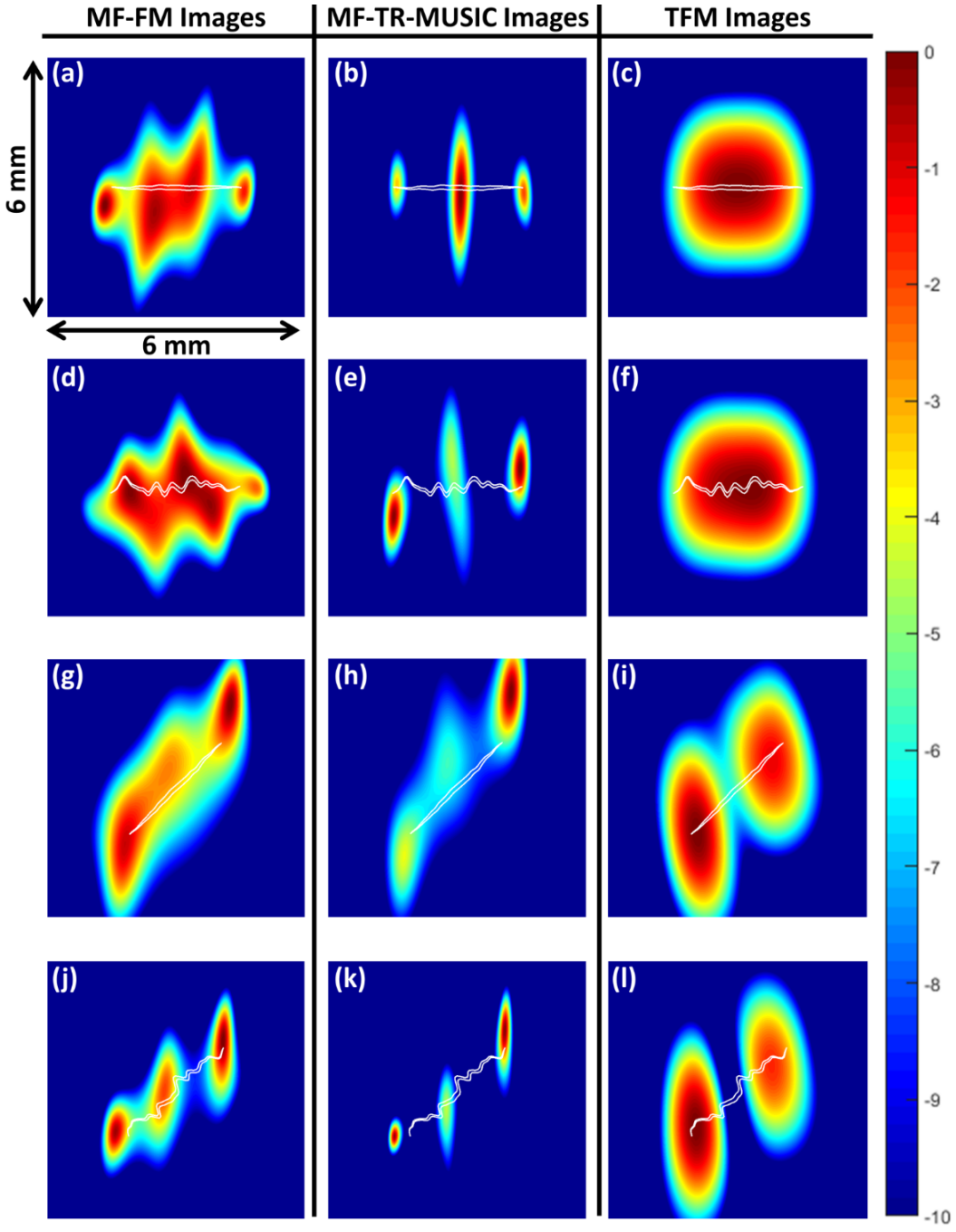


Figure 6.6: Representative images from the MF-FM, MF-TR-MUSIC and TFM algorithms for 3 mm rough defects. Images a), b) and c) correspond to $\sigma = 10$ μm 0° rough defects; d), e), and f) correspond to $\sigma = 100$ μm 0° rough defects; g), h) and i) correspond to $\sigma = 10$ μm 45° rough defects; j), k), l) correspond to $\sigma = 100$ μm 45° rough defects. All the images are plotted on a decibel scale normalised to the maximum image amplitude from the defect response. The set-up shown in Fig. 3.1 was used, featuring a 64-element 2 MHz array centred above the defects at a distance of 42 mm.

cases respectively. From the 3 mm 0° averaged results shown in Fig. 6.7, it can be seen that in both roughness cases, despite the SR algorithms being

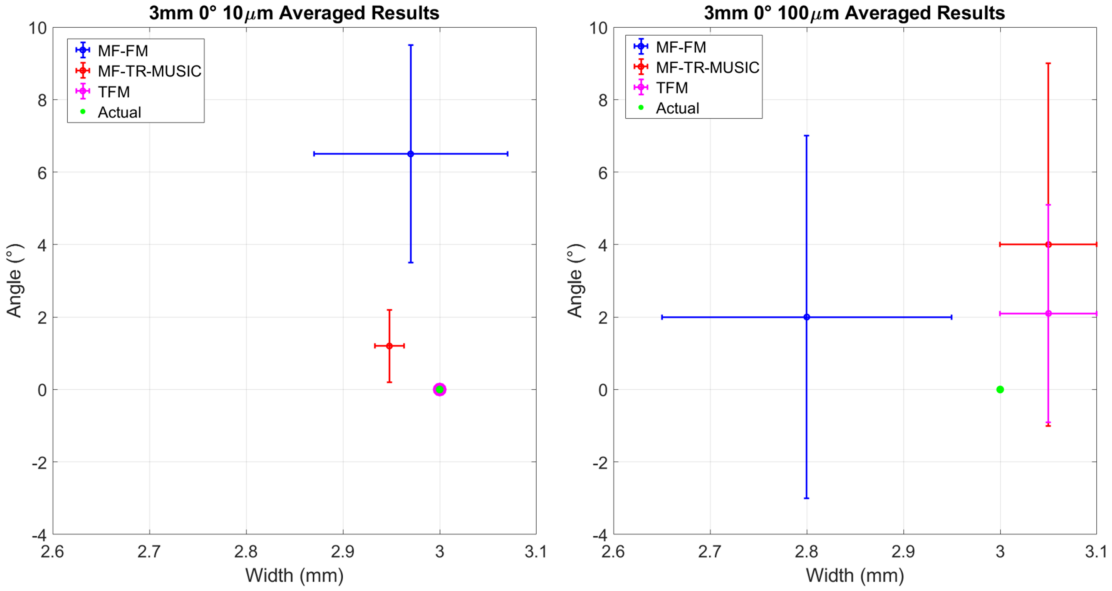


Figure 6.7: The mean estimated defect width and inclination angle values calculated from the 100 realisations for the 3 mm 0° 10 μm (left plot) and 3 mm 0° 100 μm (right plot) rough defects. The error bars correspond to the standard deviation of the width and angle results.

able to estimate the defect width and inclination relatively accurately, they are not as accurate as TFM which is now operating well within its resolution capability. This performance differential is most apparent in the 10 μm case where TFM is extremely accurate in terms of estimating the defect size and inclination.

Considering the 3 mm 45° results presented in Fig. 6.8, it is observed that there is a contrast in the performance of the SR algorithms between the different roughness cases. In the low roughness 10 μm case, the averaged results are similar to the smooth defect results presented in Table 6.2, with both SR algorithms overestimating the defect parameters significantly and TFM producing comparatively more accurate results. The difference comes when considering the higher roughness 100 μm case where the sizing accuracy of both SR algorithms increases dramatically to within 10% error, which makes them slightly better than TFM. This increase in performance can be visually seen by comparing the images shown in Fig. 6.6(g) and (h) to the images in Fig. 6.6(j) and (k), where in the rougher 100 μm defect cases, the SR algorithms produce tip indications much closer to the actual defect tip locations than in the 10 μm defect cases.

The quantitative characterisation results discussed above are summarised in Table 6.3, Table 6.4 and Table 6.5.

The rough defect imaging results have shown there is potential for the SR algorithms to size sub-wavelength planar defects accurately even when the flaws exhibit roughness parameters representative of in-service flaws in the nuclear sector. For the $\frac{\lambda}{2}$ sized rough defects, the SR algorithms demonstrated significantly better sizing capability than TFM for roughness values

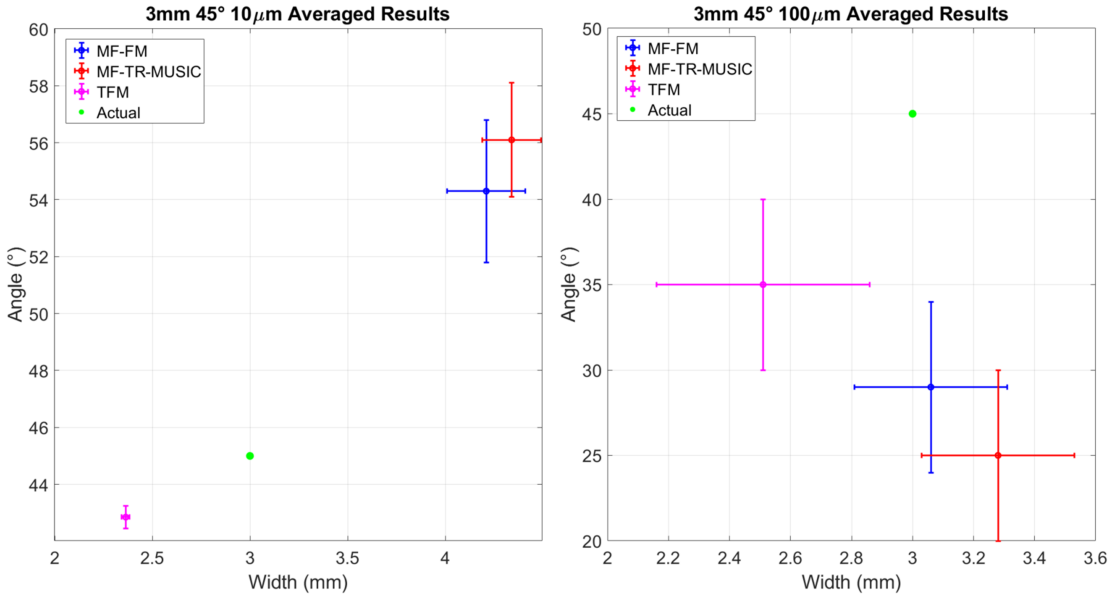


Figure 6.8: The mean estimated defect width and inclination angle values calculated from the 100 realisations for the 3 mm 45° 10 μm (left plot) and 3 mm 45° 100 μm (right plot) rough defects. The error bars correspond to the standard deviation of the width and angle results.

Table 6.3: The average characterisation results for all rough defect classes when applying the MF-FM algorithm. Std means standard deviation.

Actual			**Measured (MF-FM)**			
Size (mm)	Angle (°)	σ (μm)	Width (mm)	Width Std (mm)	Angle (°)	Angle Std (°)
1.5	0	10	1.47	0.08	-3.9	5
1.5	45	10	1.46	0.08	39.3	4
1.5	0	100	1.43	0.1	1	20
1.5	45	100	1.54	0.1	33.3	10
3	0	10	2.97	0.2	6.5	6
3	45	10	4.21	0.4	54.3	5
3	0	100	2.8	0.3	2	10
3	45	100	3.06	0.5	29	10

up to 100 μm, with averaged results similar to the smooth defect equivalent cases. The standard deviation error associated with the sizing results for the SR algorithms in these cases were very similar to those obtained from conventional TFM meaning the performance of the various methods can be directly compared to each other. The SR algorithms also maintained capability to estimate defect orientation which it demonstrated for smooth defects meaning their TWH sizing performance is also robust to the levels of roughness considered in the study.

Table 6.4: The average characterisation results for all rough defect classes when applying the MF-TR-MUSIC algorithm. Std means standard deviation.

Actual			**Measured (MF-TR-MUSIC)**			
Size (mm)	Angle (°)	σ (μm)	Width (mm)	Width Std (mm)	Angle (°)	Angle Std (°)
1.5	0	10	1.49	0.03	0.8	2
1.5	45	10	1.44	0.04	37.8	2
1.5	0	100	1.52	0.09	-4	20
1.5	45	100	1.64	0.2	40	10
3	0	10	2.95	0.03	1.2	2
3	45	10	4.34	0.3	56.1	4
3	0	100	3.05	0.1	4	10
3	45	100	3.28	0.5	25	10

Table 6.5: The average characterisation results for all rough defect classes when applying the TFM algorithm. Std means standard deviation.

Actual			**Measured (TFM)**			
Size (mm)	Angle (°)	σ (μm)	Width (mm)	Width Std (mm)	Angle (°)	Angle Std (°)
1.5	0	10	1.701	0.007	0.0002	0.0003
1.5	45	10	1.96	0.04	1.2	3
1.5	0	100	1.78	0.07	0.1	1
1.5	45	100	1.92	0.3	13	20
3	0	10	3.00	0.00	0.0003	0.0004
3	45	10	2.36	0.04	42.85	0.8
3	0	100	3.05	0.1	2.1	6
3	45	100	2.51	0.7	35	10

For the wavelength sized rough defects, similar trends to the smooth defect equivalent cases were observed where TFM produced the more accurate and precise sizing and orientation estimation results. The one exception to this trend was for the 3 mm 45° 100 μm averaged results which showed that the SR sizing performance increased dramatically from the smooth case and it outperformed TFM. It is unclear the exact origin of this result; it is suggested that it could be due to the increased scattered signal being received by the array because of the increase in magnitude of the diffuse scattered field component for the rougher inclined defects. This would usually hinder conventional TFM as it could obscure the much weaker tip diffraction

signals but it seemed to enhance the SR imaging performance. This may be because the increase in defect roughness would inevitably increase the overall amplitude of the scattered wavefield received by the array, but particularly the multiple scattered component of the wavefield. This would enhance the information contained within the lower valued eigenfunctions containing the higher spatial frequency information which the SR algorithms are reliant on, unlike TFM, leading to an increase in their ability to accurately reconstruct the defect profile.

Considering the potential practical deployment of the SR methods, it is recommended that it is used in conjunction with conventional methods for several reasons. Firstly, it is a requirement of the SR algorithms to process only the defect scattered signal so collected ultrasonic data must be appropriately windowed based on a priori knowledge of approximately where the defect is located in the component. This basic prior knowledge is suggested to be attained using simple conventional techniques or with TFM. Secondly, the SR images predominantly show strong indications from the planar defect tip locations and not a consistent surface response. This may lead to confusion in classifying the defect type from the images, i.e. whether the indications shown in Fig. 6.3 were caused by two close-by point reflectors or a single planar flaw. Further work must be conducted to try to overcome this limitation. Nevertheless, the SR algorithms have still demonstrated a superior sizing capability compared to TFM thus even when considering the worst case defect characterisation result where a small volumetric defect is classified as a small planar crack, a less pessimistic size would be obtained via the SR methods.

Due to the strict regulatory restrictions imposed upon the UK nuclear sector, advanced array imaging algorithms such as the SR methods and even TFM are not widely used as of yet. The nuclear industry currently prefers to use conventional single and dual crystal probes and scanning imaging techniques such as Time-Of-Flight Diffraction and simple B-scan plots. These methods, although tried and tested for many years, are intrinsically limited in several aspects. For new methods to be deployed in addition to the current methods or to replace them, they must be stringently validated to show reliability and robustness to in-service inspection conditions. By considering the impact of defect roughness, the results presented in this Chapter mark a step forward for validating the performance of the FM and TR-MUSIC algorithms on realistic defects.

6.5 Conclusions

In this Chapter, the MF-FM and MF-TR-MUSIC imaging algorithms were compared against the TFM method in the ultrasonic array inspection of 2D embedded rough planar defects. A Monte Carlo finite element simulation study was conducted for varying defect parameters including sizes, orientation and roughness parameters comparable to that of in-service defects from the nuclear sector generated by thermal fatigue and stress corrosion cracking mechanisms.

The results presented show that for sub-wavelength ($\lambda/2$) defects, both of the SR algorithms were able to size and estimate defect orientation accurately for the smooth case, low roughness cases of $\sigma = 10\ \mu m$ and for defects with up to $\sigma = 100\ \mu m$. The most accurate SR imaging performance was achieved for the $\lambda/2$ sized defects in either the 0° or 45° tilt orientation. This was in contrast to the poor performance of TFM in these cases which consistently oversized these defects and could not be used to estimate the defect orientation, making through-wall sizing with this method impossible.

The work in this Chapter is a step towards the application of these imaging methods in the nuclear industry and demonstrates the potential of these algorithms to deal with some of the prominent inspection challenges facing the sector today.

Chapter 7

SR Imaging of Embedded Volumetric Defects

7.1 Introduction

So far in this thesis, only embedded planar crack-like flaws have been considered. This chapter will now consider another common defect type encountered within industry which are embedded volumetric defects. Many different types of volumetric defects exist. These include gas pores and porosity, which can be initiated through manufacturing techniques such as welding, as well as foreign material inclusions, which can be common in certain types of castings and can also be initiated through welding where welding tip material can inadvertently enter the melt pool. Although volumetric defects are generally less critical to the structural integrity of components compared to cracks, they are regularly inspected for within the nuclear industry and the majority of inspection techniques place constraints on the maximum size of volumetric defects present.

The major difference between volumetric defects and crack-like flaws are in their morphology, with volumetric features generally being more spherical compared to flat planar cracks. Due to the geometrical nature of volumetric defects, they scatter sound in a very different way to planar defects. Spherical volumetric defects tend to scatter sound in a range of directions when incident with an ultrasonic beam, especially small volumetric defects such as pores which predominantly generate diffracted waves in all directions. This is unlike typical planar defects which scatter most wave energy in the specular direction from their planar faces, with lower amplitude diffraction responses occurring at the defect tips. As the size of a planar defect decreases, the tip diffraction responses become a more dominating effect.

To size planar defects, the specular reflection is used for amplitude based sizing or tip diffraction responses are used as described in Section 3.3. However, for volumetric defects there are fewer established ways to directly size them using ultrasound, with the common approach to associate the amplitude response from them to an equivalent known reflector such as a Side Drilled Hole (SDH) within a calibration test piece. A method to provide an upper limit on a defect size (planar or volumetric) when using conventional ultrasonic probe imaging is when a Pattern 1 type A-Scan response is observed [75]. This pattern corresponds to when a defect is smaller than the ultrasonic beam width and amplitude based sizing cannot be accurately applied. However, it can be inferred that the defect being inspected must

be less than or equal in extent than the beam width, which allows an upper size limit to be applied. This approach can be used for any defect morphology where the defect size is smaller than the beam width.

The only way to truly accurately determine the size of volumetric flaws in current NDE inspections is through radiographic methods. Although they are generally capable of achieving accurate volumetric defect sizing, except for the challenging inspection cases of small flaws in thick-sectioned components, it is a costly and time consuming technique that poses a radiation exposure risk to inspectors which must be considered and planned for. Ultrasonic methods are generally fast and cheap in comparison with no requirement to handle radioactive sources and therefore would be an ideal NDE mode for volumetric defect sizing.

It is noted that methodologies exist within the literature to infer the parameters of volumetric defects from their measured scattering response [91, 92]. Within these referenced studies, the measured scattering matrix from a defect with unknown parameters are essentially compared to a database of scattering matrices from different defects with known parameters and a comparison metric is used to estimate the defect's geometric properties. This is done with the aid of Principal Component Analysis (PCA) to reduce the dimensionality of the data within the scattering matrices to allow only the significant defect feature components to be extracted and compared to the pre-existing database. It is noted that these techniques are currently only considered within academia and not yet applied within industry. There are no other methods to the author's knowledge to size volumetric defects through direct imaging alone with conventional ultrasonic NDE equipment.

Tant *et al.* (2017) [35] used the MF-FM to estimate the size of SDHs using both simulated and experimental FMC data. In the simulated case, a 2.5 mm diameter SDH was modelled and the MF-FM algorithm was used to accurately estimate the diameter to be 2.8 mm. In the experimental case, a 3 mm diameter SDH was sized to within an error of 0.1 mm. It is noted that in both of these cases, a 6 dB amplitude drop sizing technique was applied to the SR algorithm which is different from the approach applied in this thesis.

In this Chapter, 2D FE modelling was used to simulate the array inspection of smooth embedded volumetric defects to investigate the nature of the imaging responses generated by the SR algorithms. It is suggested that the SR algorithms may have the potential to directly size volumetric defects from their images. The practical equivalent of the 2D defects simulated within this Section are Side Drilled Holes (SDHs). Although SDH profiles do not relate to a type of defect found within real NDE inspections, they are common within ultrasonic NDE test pieces as calibration targets and act as a simplified case for 3D equivalent defects such as pores.

Experimental validation of the 2D volumetric flaw FE results using test pieces containing SDHs was conducted as well as extending the scope to consider a fully 3D volumetric pore defect.

7.2 Simulated SDH Array Imaging

The same 2D FE modelling approach that was used in Section 3.2 was applied within this study to simulate the 2 MHz 64-element array inspection of embedded SDHs of varying diameter. As in all previous Chapters of this thesis, the defects were centrally located beneath the array to maximise the viewing angle achieved.

The SDH diameters considered in this Section were 0.75 mm ($\lambda/4$), 1 mm ($\lambda/3$), 1.5 mm ($\lambda/2$), 3 mm (λ) and 4 mm (1.25λ). The MF-FM, MF-TR-MUSIC, TFM and array 0° B-Scan imaging algorithm were applied to the simulated FMC datasets collected from these defects and the resultant images are shown in Fig. 7.1.

The TFM and B-Scan images shown in Fig. 7.1 represent the expected responses from SDHs. From the sub-wavelength SDHs, images are produced which correspond to the beam width of the respective imaging method. For larger defects, the strongest responses are produced from the region of the SDH closest to the array which is not representative of the full defect profile and amplitude-based sizing would severely underestimate the diameter. The SR algorithms however produce far different images. Both SR methods produce images which were very similar to the images from planar defects as shown in previous Chapters. Indications were generated close to the edges of the flaws and the total number of indications from the main response pattern were related to the defect size (diameter), showing the same behaviour as reported in Section 3.4. This means the same sizing methodology described in Section 3.3 can be applied to the SR images of SDHs.

The sizing results from the MF-FM and MF-TR-MUSIC algorithms are shown in Fig. 7.2. From these results, it can be seen that for the wavelength sized SDHs or smaller ($\leq$3 mm), both SR algorithms produce accurate sizing results. The results suggest that the SR sizing performance seems to plateau for defects smaller than the diffraction limit ($\lambda/2$) and indicate that above this size, the SR algorithms tend to underestimate the defect size and the magnitude of this underestimation increases as defect size increases. For example at 1.5 mm, the percentage sizing error of the algorithms is around -13%, at 3 mm it is around -17% and at 6 mm it is roughly -30%.

Within the SR images for the 6 mm diameter SDH in Fig. 7.1, indications are produced near the bottom of the defect as well as the higher amplitude main indication group. It is recommended that further work is conducted to investigate if for large SDH diameters, these additional indications could be used to produce a more accurate estimation of the SDH diameter. It is noted that these indications however are around 20-30 dB lower than the peak amplitude responses which means that they may not be as prominent within experimental inspections due to the inevitably lower SNR present within experimental data relative to clean FE data. It is also noted that real volumetric defects may not exhibit a spherical morphology but could have irregular geometries. This would inevitably influence their ultrasonic detectability, for example changing the defect reflection directivity to align with specific beam angle orientations similar to planar flaws which may either enhance or hinder imaging.

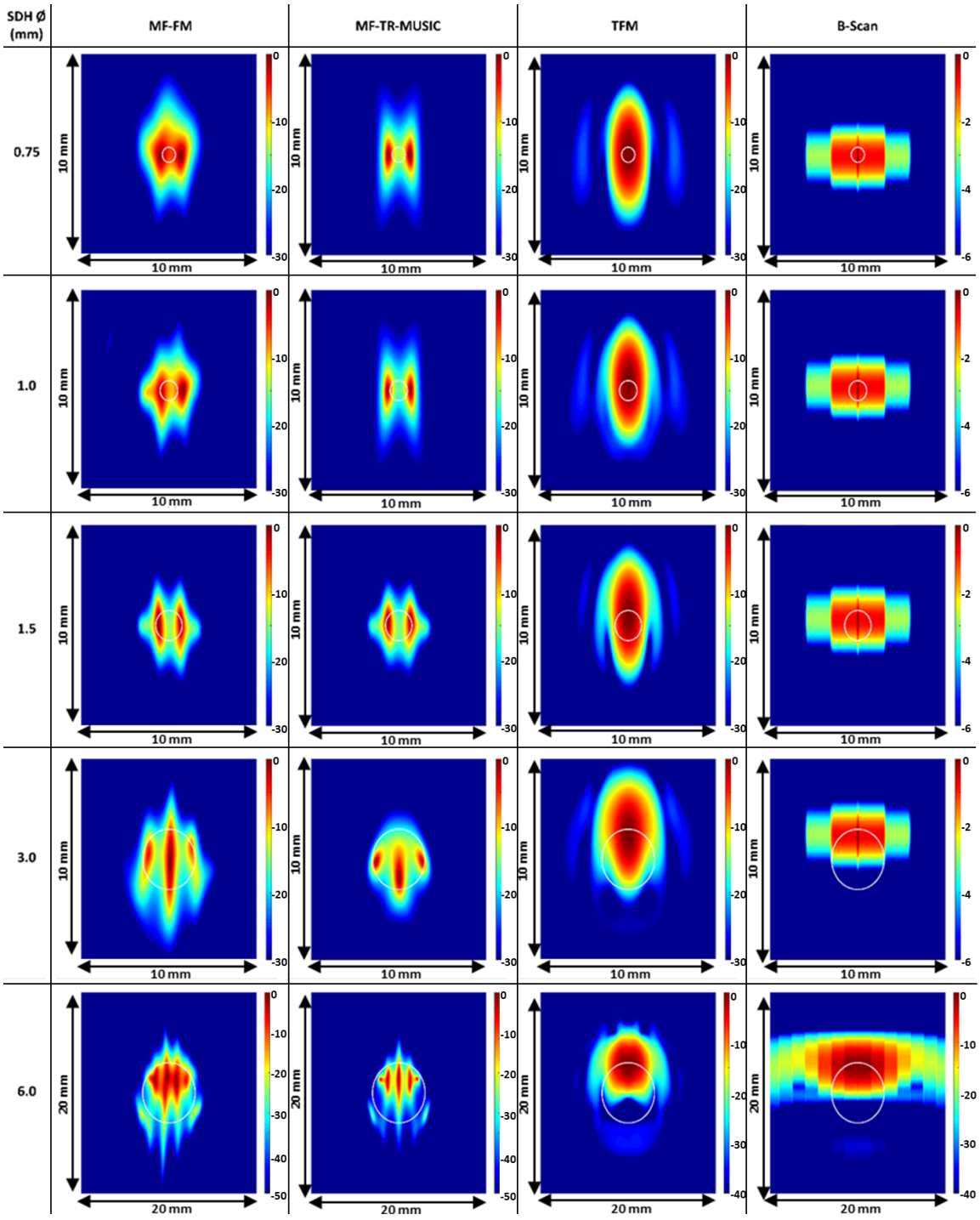


Figure 7.1: The MF-FM, MF-TR-MUSIC, TFM and array B-Scan images from FE simulated SDHs of varying diameters. All the images are plotted on a decibel scale normalised to their own maximum image amplitude from the defect response. The set-up shown in Fig. 3.1 was used, featuring a 64-element 2 MHz array centred above the defects at a distance of 42 mm.

Although the SR algorithms could potentially be used to size the volumetric defects, it is evident from the images produced in Fig. 7.1 that the algorithms are not suitable to distinguish between planar and volumetric

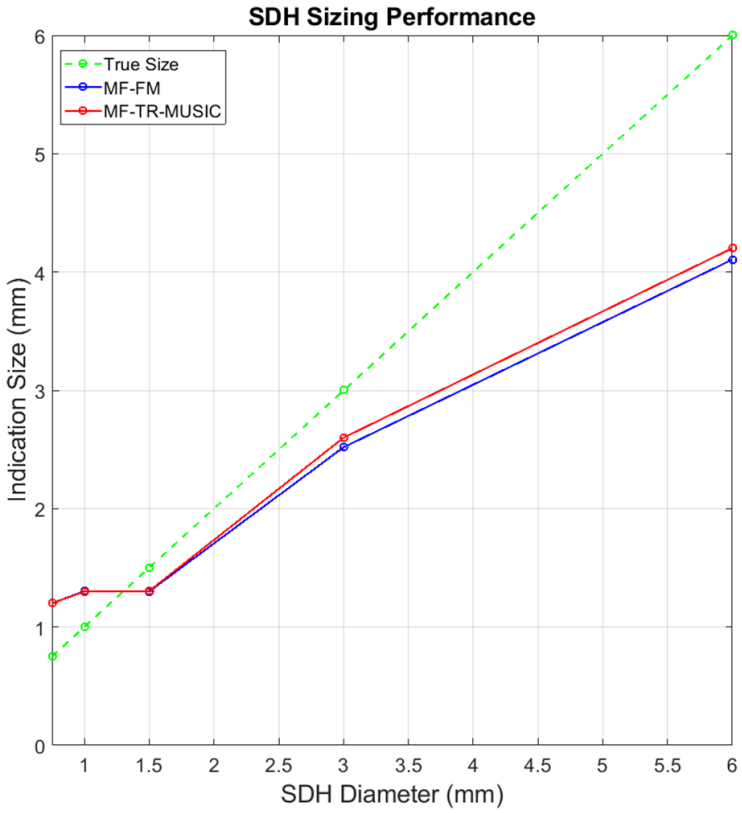


Figure 7.2: The SR algorithm diameter sizing results from the 2D FE simulated SDHs.

reflectors. This is because the algorithms produce broadly the same indication patterns for both planar and volumetric defects for the inspection configurations considered in this thesis. It is therefore recommended that additional conventional techniques are used to help classify the defect morphology as either volumetric or planar if possible, before applying SR sizing. If this is not possible, the worst case planar defect profile should be assumed for a conservative approach.

7.3 Experimental Validation

To validate the findings from Section 7.2, array imaging of experimental calibration blocks containing SDHs was conducted and to extend the findings, a test piece containing an embedded pore was inspected. In all cases, a 2 MHz 64-element linear phased array (IMASONIC, 96 mm active aperture) was used in direct contact to collect FMC data from the test pieces. The full array properties are detailed within Table 4.1. The array was placed centrally above each defect to maximise the array viewing angle. A summary of the defects and test pieces used within this Section are listed in Table 7.1.

When inspecting the SDHs, a single FMC dataset was acquired due to the defects having a significant extent out of the imaging plane of the array (as conducted in Chapter 4). A sampling frequency of 50 MHz was used for data collection.

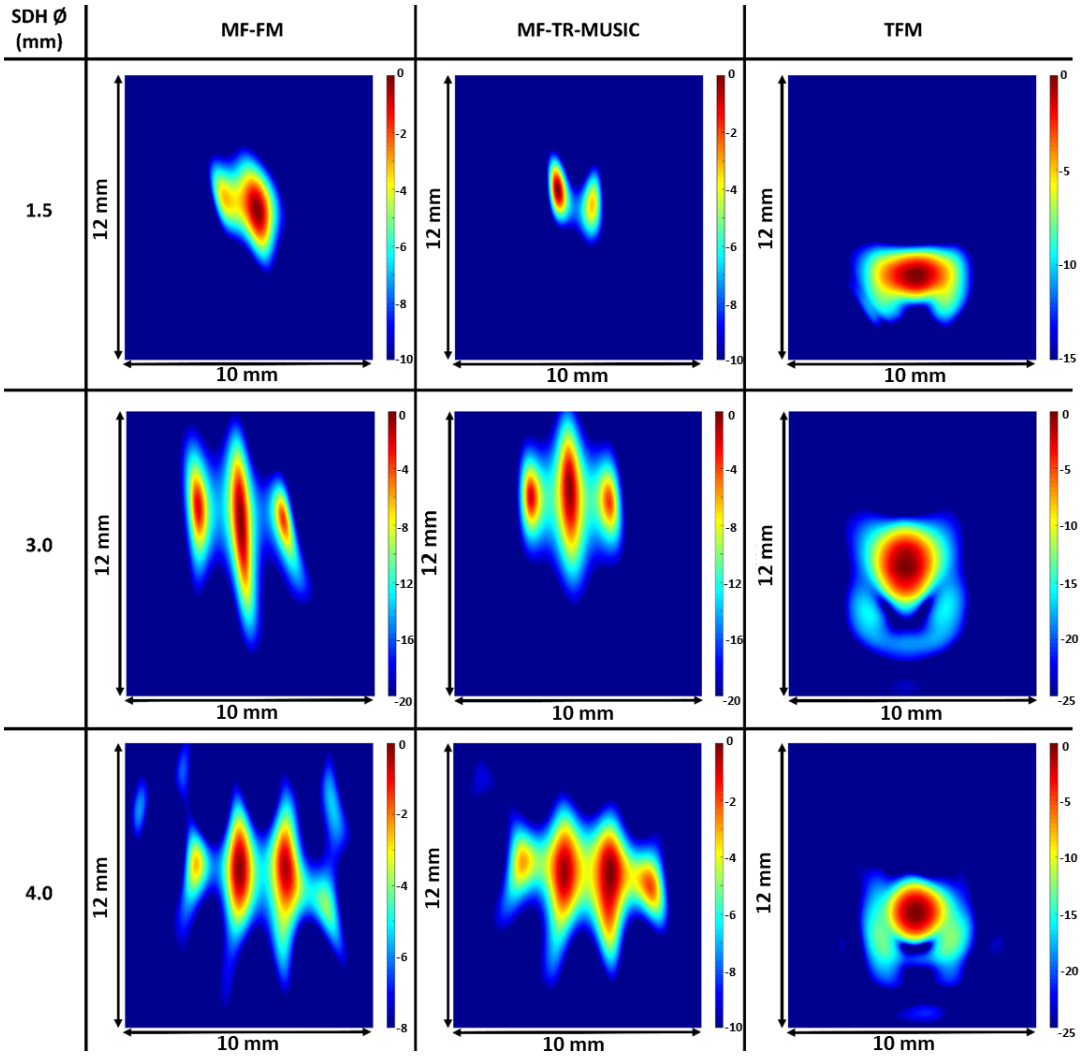


Figure 7.3: The MF-FM, MF-TR-MUSIC and TFM algorithm images produced from experimentally collected FMC data from SDHs of different diameters using a 2 MHz 64-element linear phased array. All the images are plotted on a decibel scale normalised to the maximum image amplitude from the defect response. The array in each case was centred directly above the defects at the distances listed in Table 7.1.

Table 7.1: Summary of the experimental volumetric defects imaged with the array algorithms.

Defect Type	Diameter (mm)	Depth From Inspecting Surface (mm)	Material
SDH	1.5	30	304 Steel
SDH	3	35	304 Steel
SDH	4	20	304L Steel
Pore	2	30	S275 Steel

The SDH defects listed in Table 7.1 were imaged with the MF-FM, MF-TR-MUSIC and TFM algorithms and the resultant plots shown in Fig. 7.3. The

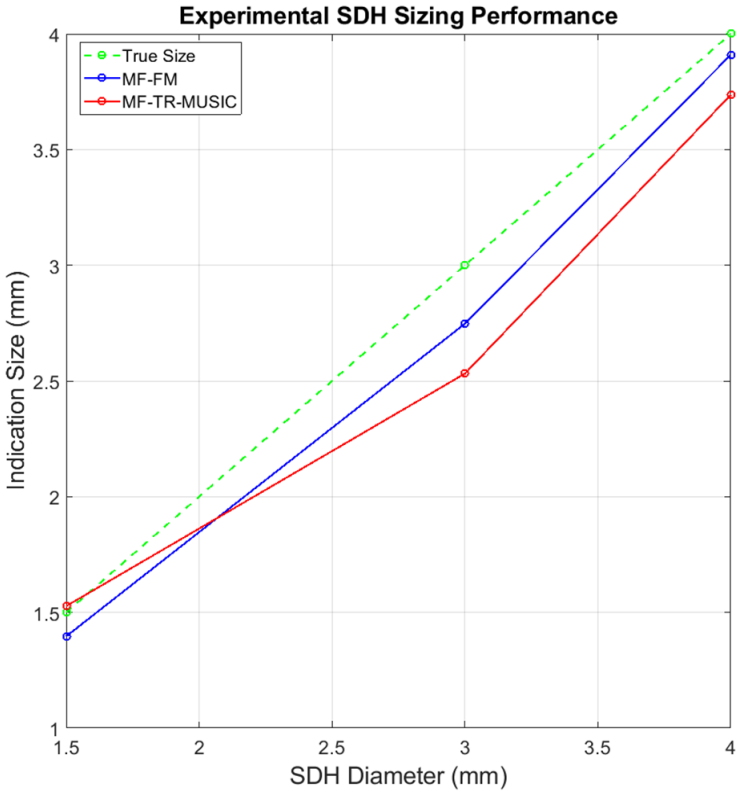


Figure 7.4: Experimental SDH sizing results using the SR algorithms.

indications produced are very similar to those reported in Section 7.2, with several distinct indications present across the defect profile which are in line with the patterns from planar defects. These indication patterns also agree with the trend established in Fig. 3.10, providing additional experimental validation of this observation for both planar and volumetric defects. From the SR images in Fig. 7.3, the diameters of the SDHs were estimated and the sizing results are plotted in Fig. 7.4. It can be seen that for all SDH diameters, the SR algorithms are able to accurately estimate the defect diameter. These experimental results show excellent agreement with the true defect diameters and demonstrate that the SR algorithms can be used to accurately size 2D volumetric flaws.

So far, only 2D SDHs have been considered when investigating SR imaging performance for volumetric defects. The most common volumetric defects that occur in actual components correspond to fully 3D pores, porosity and inclusions. To investigate the array performance for 3D volumetric defects, experimental FMC scan data was collected on a ferritic steel test piece (listed in Table 7.1) containing a single 2 mm diameter pore. A 2 MHz 64-element linear array (IMASONIC, 96 mm active aperture) was used and the TFM and SR algorithms were applied in post-processing using the methodology outlined in Section 5.3. A 25 MHz sampling frequency and a 1 mm scan increment were utilised. This scan step was the minimum increment the XY scanner and manipulator file could accurately implement. An illustration of the experimental set-up used to acquire FMC scan data is shown in Fig. 5.2.

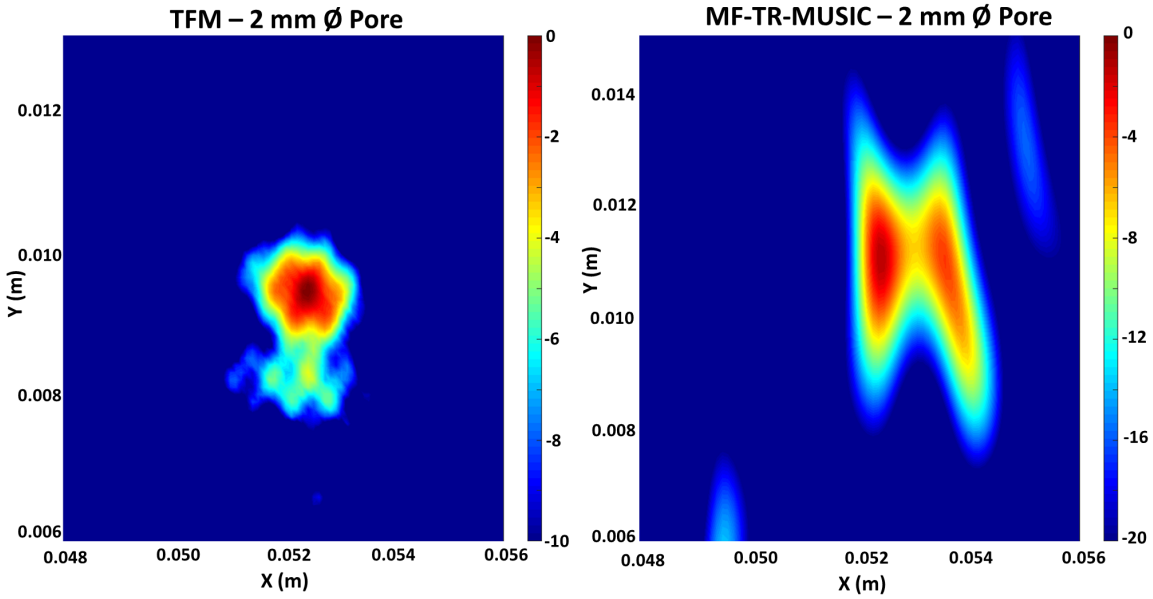


Figure 7.5: The TFM and MF-TR-MUSIC images produced from experimentally collected FMC data from a 2 mm diameter pore. All the images are plotted on a decibel scale normalised to the maximum image amplitude from the defect response. The 2 MHz 64-element array in each case was centred directly above the defects at the distances listed in Table 7.1.

Table 7.2: Experimental sizing results for 2 mm diameter pore within ferritic steel component.

Imaging Algorithm	Indication Length (mm)	Indication Width (mm)
TFM	8 ± 1	1.7 ± 0.1
MF-TR-MUSIC	-	1.4 ± 0.1

Fig. 7.5 shows the TFM and MF-TR-MUSIC images that were generated from this pore and the sizing results are listed in Table 7.2. The MF-FM image was not shown due to only a single indication being produced, such as the MF-FM images shown in Fig. 5.4, which could not be used for defect sizing. This is another example of the MF-FM having difficulty in generating images useable for direct defect characterisation in a practical NDE inspection scenario. Adding an eigenvalue truncation step to the algorithm, as occurs in the TR-MUSIC algorithm and as implemented by Tant *et al.* (2017) [35], may enhance the viability of the method by removing some of the impact of experimental noise.

From Table 7.2, it can be seen that the MF-TR-MUSIC algorithm estimates the quoted defect size fairly accurately, with it underestimating the diameter by 30%. As discussed in Section 5.4, due to the defect having a small extent in the scan direction (2 mm) with a high rate of change of width profile, there is a likelihood that the scan increment was insufficient to ensure the array was exactly aligned with the maximum pore width plane. Although

the TFM algorithm produces a 6 dB amplitude drop size of 1.7 mm, which is within 15% accuracy, it is likely simply sizing the beam width rather than the true defect size as the amplitude-based sizing methodology is invalid when applied to spherical volumetric defects. In terms of defect detection, the TFM algorithm achieved an imaging SNR of 14.6 dB in the experimental pore inspection. The TFM image also featured indications directly below the high amplitude pore indication, which is likely related to back-filled weld material used in the manufacture process of the test piece to generate embedded defects.

7.4 Conclusions

It has been demonstrated through 2D FE simulations and experimental testing that the SR algorithms can be used to estimate the diameter of SDHs via direct imaging with a linear ultrasonic array.

It was observed that from the FE simulation data, the SR sizing results were most accurate when considering diameters equal to or smaller than the ultrasonic wavelength and that the sizing performance worsened as the diameter increased. The sizing results also appeared to plateau in the minimum sizeable volumetric at around $\lambda/3 - \lambda/2$.

The sizing performance of SDHs using the SR algorithms has been experimentally validated by accurately sizing three different SDH diameters: 1.5 mm, 3 mm and 4 mm, using a signal with a wavelength of 3 mm. The maximum percentage difference error in sizing was around 15%. The MF-TR-MUSIC algorithm also demonstrated a sizing capability when characterising a realistic 2 mm 3D embedded pore defect, which extended beyond the simplified 2D SDH case.

These results have highlighted that the SR algorithms may not be suitable to distinguish between planar and volumetric flaws due to the high similarity between the generated images for these defect types. It is recommended that a supplementary imaging algorithm, such as a series of angled array B-Scans, are carried out alongside the SR methods. Using B-Scans of different angles would easily allow a volumetric flaw to be distinguished from a planar flaw as a volumetric flaw would have similar image amplitude responses from a range of incident angles. This is unlike a planar flaw which would have a strong asymmetry in response with angle, centred along the specular reflection angle.

The results within this Chapter act as a positive step forward into investigating the applicability of the SR algorithms in directly sizing volumetric defects in practical NDE inspection scenarios, which until now has only been conventionally achievable through more costly radiographic techniques.

Chapter 8

SR Imaging Within Scattering Austenitic Stainless Steels

8.1 Introduction

Austenitic stainless steels are common manufacturing materials within the nuclear power industry because of their highly desirable material properties including high strength and toughness, as well as their superior corrosion and creep resistance at high temperatures compared to carbon steels [93, 94]. However, when austenitic stainless steels are welded they can exhibit a spatially varying anisotropic, heterogeneous and coarse grained structure that significantly impacts the capabilities of subsequent ultrasonic inspections. This is because these grain structures can be highly scattering and can exhibit complex beam bending effects [95, 96, 97, 98], both of which hinder defect detection and characterisation [99]. As a result, their ultrasonic NDE inspection poses a significant challenge to the nuclear sector.

The origin of the high scattering that can be exhibited by austenitic stainless steel welds is due to the large grain sizes formed when these welds are created because of the lack of grain refinement they exhibit during cooling. In typical NDE inspections, ultrasonic grain scattering lies within either the Rayleigh scattering regime, where the grain size R is much smaller than λ, or the stochastic scattering regime, where R is similar to λ [100]. Both of these scattering regimes exhibit a strong dependence on the grain size, as the attenuation coefficient due to Rayleigh scattering scales with R^3 [101] and the attenuation coefficient due to stochastic scattering scales linearly with R [102]. The grains in the parent material of components featuring austenitic stainless steel welds are generally very fine and therefore pose no challenge to ultrasonic propagation, whereas large grain boundary scattering within the welds act to significantly scatter and attenuate the ultrasonic beam energy.

As mentioned, complex beam deviation effects are another major challenge presented by austenitic stainless steel welds. This issue stems from the spatially-varying anisotropy that is commonly exhibited by these weld structures which occurs as the grains cool after weld deposition. As the grains cool, they can grow between consecutive weld runs due to re-melting of the previous weld bead to form long columnar grain structures that tend to direct themselves towards the parent material (which acts as a heat sink), leading to spatially-varying anisotropy across the weld structure. It is this spatially-varying anisotropy which leads to beam bending effects within

the weld material, not just the inherent anisotropy alone. Beam bending can also occur at the interfaces between isotropic parent material and anisotropic regions (such as welds or cladding layers) due to the sudden change in propagation properties. It is noted that several approaches have been developed that attempt to correct for beam bending effects by modelling the grain structures present within spatially-varying anisotropic weld materials, usually with information directly taken from macrographs or generic weld maps [99, 103, 104].

It is known that the magnitude of some of these undesirable material effects scale with ultrasonic inspection frequency [105]. Rayleigh scattering exhibits a strong frequency dependence as the magnitude of this type of scattering scales with ω^4 [101] whilst stochastic grain scattering scales with ω^2 [102]. Therefore ideally, one would reduce the inspection frequency as low as possible to minimise the impact of grain scattering on imaging. However, the inspection resolution is also proportional to frequency so there is an inevitable trade-off between achieving adequate ultrasonic inspectability (e.g. penetration depths, SNR) and defect resolution (i.e. sizing capability). In many cases, complex inspection procedures must be written using a large variety of specialised probes and scanning techniques to be able to demonstrate that an austenitic stainless steel welded component is sufficiently inspected.

The SR imaging algorithms that have been discussed within this thesis could potentially allow for a lower inspection frequency to be employed in order to reduce material scattering and beam bending effects, whilst retaining adequate inspection resolution. Tant *et al.* [35] considered the simulated 2D array inspection of an austenitic stainless steel weld section, including representative anisotropic microstructure measured experimentally [106], and experimental data collection on defect-free, ultrasonically noisy test pieces. In these cases, the FM and MF-FM imaging algorithms were applied to characterise a limited set of both planar and volumetric defects. It was found that in all cases, the MF-FM was able to generate image indications that were more representative of the defect morphologies, as compared to the single frequency FM. In both the simulated and experimental cases, the SR algorithms were able to size the variety of planar defects with a moderate degree of accuracy; typical estimations had a percentage error of between 20-50%. For the volumetric defects, a slightly improved sizing performance was achieved. It was also found that truncation of the eigenvalues to remove some of the effects of noise led to slight improvements in imaging performance of both the FM and MF-FM in some cases, however there were other cases where it worsened the defect orientation and sizing performance. It is noted that in this study, a 6 dB amplitude drop sizing technique was applied to the SR algorithm which is different from the approach applied in this thesis. The use of the 6 dB method when applied to the SR algorithms does not have the same theoretical basis for accurate amplitude based sizing as when used in conjunction with conventional probe methods [76]. It is therefore an arbitrary sizing technique until fully validated.

In this Chapter, the inspection performance of the SR and TFM algorithms

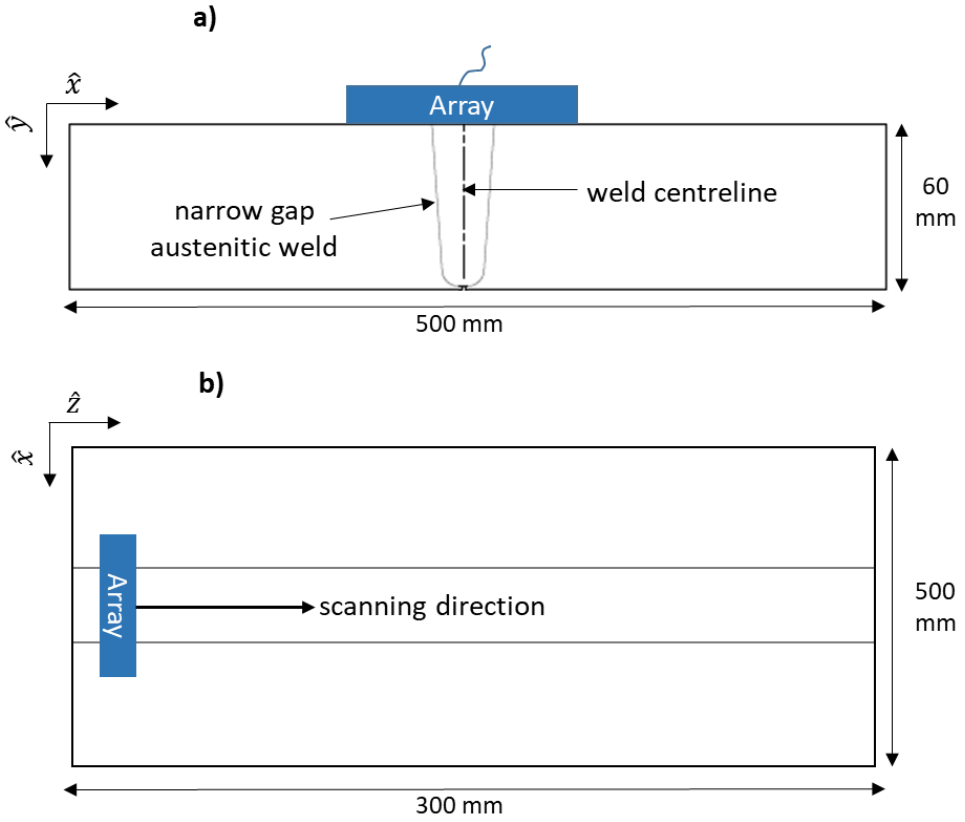


Figure 8.1: Schematic for the austenitic stainless steel welded test pieces containing various embedded defects. a) is the cross-sectional view of the test pieces and b) is a plan view of the test pieces. A 2 MHz 64-element linear array and a 1 MHz 32-element linear array were scanned along the weld centreline in the $\hat{z}$ direction. Figure not to scale.

were assessed when being used to detect and characterise embedded defects within narrow gap welded austenitic stainless steel test pieces. The conventional 0° array B-Scan algorithm was also considered as a representative NDE methodology currently used within industry.

8.2 Methodology

Three thick-wall narrow gap austenitic stainless steel welded plate test pieces were manufactured containing a variety of embedded manufacturing-style defects. The base plate material used for these test pieces was 304L stainless steel and the weld material used was 308L stainless steel. The narrow gap welds featured an included angle of 8°, with all defects embedded within the weld during the weld fill process. A schematic for the test pieces is shown in Fig. 8.1. This type of weld geometry is representative of welds within NSRP components which are known to exhibit significant grain scattering and anisotropy. The narrow gap geometry of the weld is designed to minimise the weld volume compared to traditional weld profiles meaning that ultrasonic beam paths are reduced to limit the magnitude of scattering and beam bending effects.

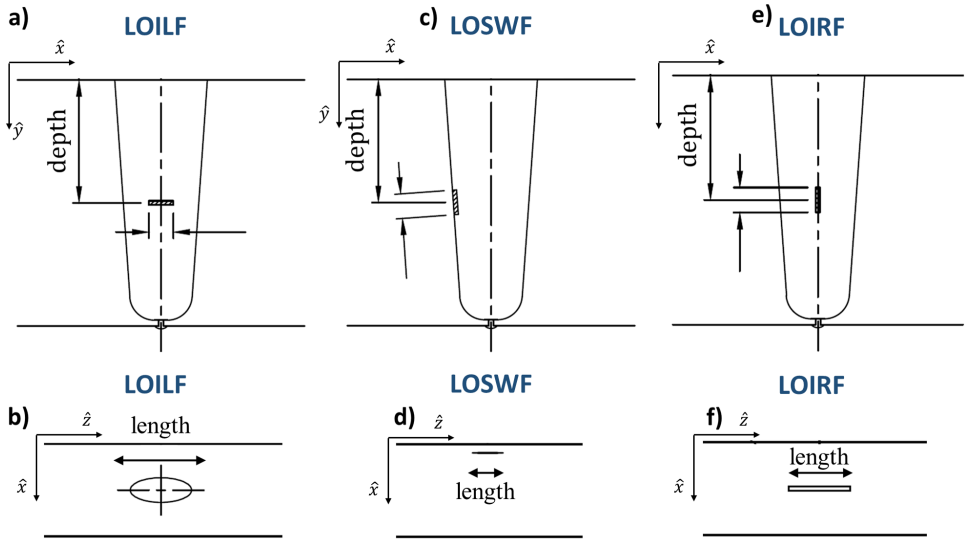


Figure 8.2: Schematic for the defects in the narrow gap austenitic stainless steel welded test pieces. The figures are a) cross-sectional view of the LOILF defects, b) plan view of the LOILF defects, c) cross-sectional view of the LOSWF defects, d) plan view of the LOSWF defects, e) cross-sectional view of the LOIRF defects, and f) plan view of the LOIRF defects. All defects were elliptical and planar.

The defects embedded within the test pieces were longitudinal Lack Of Inter Layer Fusion (LOILF) defects, Lack Of Inter Run Fusion (LOIRF) defects and Lack Of Side Wall Fusion (LOSWF) defects. Their geometries are illustrated in Fig. 8.2. The LOILF defects are elliptical planar defects which are longitudinally orientated in the $x - z$ plane, centrally positioned on the weld centreline and are defined by their width and length. The LOIRF defects are also elliptical planar defects but orientated in the $y - z$ plane, centrally positioned on the weld centreline and are defined by their TWH and length. The LOSWF defects are elliptical defects, with their width orientated in the $x - z$ plane, their length in the z-axis and are defined by their TWH and length. The LOSWF defects actually have a small component in the x-axis, however at 86° inclination they are also effectively completely through-wall orientated like the LOIRF defects. All these defects were located at different depths within the test pieces to investigate the impact of increased wave travel distance through the austenitic stainless steel weld material. Their morphological parameters are listed in Table 8.1. The defect tolerances listed in Table 8.1 were provided by the test piece manufacturer.

A 2 MHz 64-element linear phased array (IMASONIC, 96 mm active aperture size) and a 1 MHz 32-element linear phased array (IMASONIC, 96 mm active aperture size) were used in direct contact to collect FMC data from the test pieces with a MicroPulse FMC. The full array properties are detailed within Table 4.1. The arrays were placed centrally above each defect to maximise the array viewing angle in an effort to also maximise the SR imaging performance. The test pieces were scanned along the weld centreline. Centred on each defect position, a 30 mm scan region in the z-axis was used in conjunction with a 1 mm scan increment. The scan increment was the minimum value that was accurately achievable with the XY scanner and

Table 8.1: The embedded planar defect parameters within the narrow gap austenitic stainless steel welded test pieces.

Defect Number	Defect Type	Defect Size (mm)	Defect Tilt (°)	Depth (mm)
1	LOILF	(15 x 6) $\pm$ 0.5	0 $\pm$ 2	30
2	LOILF	(7.5 x 3) $\pm$ 0.5	0 $\pm$ 2	30
3	LOILF	(15 x 6) $\pm$ 0.5	0 $\pm$ 2	50
4	LOILF	(7.5 x 6) $\pm$ 0.5	0 $\pm$ 2	50
5	LOSWF	(15 x 6) $\pm$ 0.5	86 $\pm$ 2	30
6	LOSWF	(7.5 x 3) $\pm$ 0.5	86 $\pm$ 2	30
7	LOSWF	(15 x 6) $\pm$ 0.5	86 $\pm$ 2	50
8	LOSWF	(7.5 x 6) $\pm$ 0.5	86 $\pm$ 2	50
9	LOIRF	(15 x 6) $\pm$ 0.5	90 $\pm$ 2	30
10	LOIRF	(7.5 x 3) $\pm$ 0.5	90 $\pm$ 2	30
11	LOIRF	(15 x 6) $\pm$ 0.5	90 $\pm$ 2	50
12	LOIRF	(7.5 x 6) $\pm$ 0.5	90 $\pm$ 2	50

manipulator file. An illustration of the experimental set-up used to acquire FMC scan data is shown in Fig. 5.2. When using the 2 MHz array, a 25 MHz sampling frequency was used and for the 1 MHz array, a 50 MHz sampling frequency was used. The reason for selecting the sampling frequencies was to ensure that the file size of the scanned FMC data files remained around 300 MB to allow for practical data processing times.

The SR images were generated using the methodology described in Section 5.3 and a pixel size of 0.1 mm was used for all images. For all B-Scan images, the optimal aperture size was used on a case-by-case basis to achieve the most accurate sizing in an effort to demonstrate a measure of the maximum performance that could be achieved with the technique.

The MF-FM method was not able to produce representative images for any of the defects within the austenitic test pieces. This is another example within this thesis of the MF-FM having difficulty in generating images useable for defect characterisation, due to the significant noise levels present from the austenitic stainless steel welded test pieces. The MF-FM attempts to use the information from all the singular eigenvalues, including ones with small singular values which are significantly impacted by noise. This leads to the high sensitivity of the FM algorithms to noise. The MF-TR-MUSIC attempts to bypass the use of small valued eigenvalues by separating them into *noise* and *signal* subspaces. It is therefore less reliant on these small eigenvalues which are sensitive to noise and therefore tends to perform better in high noise scenarios.

To assess the approximate magnitude of the attenuation and beam deviation effects present within the austenitic stainless steel welds utilised within this Chapter, a simple test of measuring the backwall amplitude response across the weld profile (i.e. in the $\hat{x}$-axis of Fig. 8.2a)) was conducted.

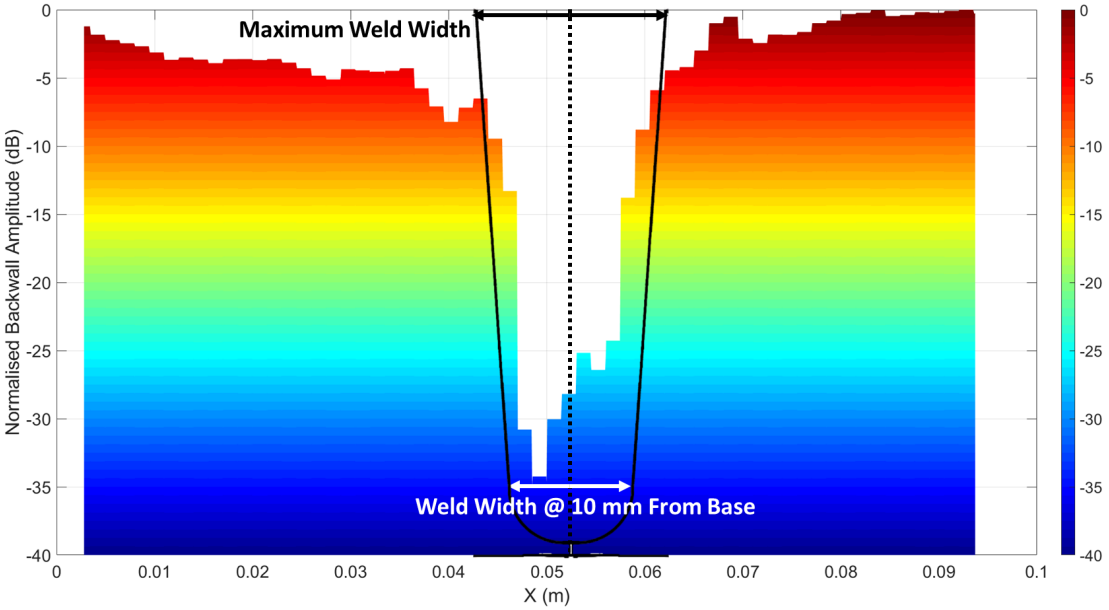


Figure 8.3: Variation of the backwall echo amplitude of one of the austenitic stainless steel test pieces used within this chapter. Each element of a 2 MHz 64-element array was used in isolation as a 0° pulse-echo compression wave transducer to measure the backwall response across the width of the austenitic stainless steel weld in a defect free region. Overlain on the plot is a scaled profile of the narrow gap weld profile showing that the region of significant signal attenuation occurs within the boundaries of the weld region.

This would allow a comparison of the total attenuative effects between the weld material and the expected low scattering parent plate material. This was achieved by centrally placing a 2 MHz 64-element array, listed in Table 4.1, across the weld and using each element of the array to collect a 0° pulse-echo A-scan. This data was taken on a section of the test piece away from known defect locations. These A-scans were then collated and the maximum amplitude response corresponding to the test piece backwall was measured and the cross-sectional variation of the echo was plotted in Fig. 8.3.

Fig. 8.3 shows that around the approximate location of the weld centreline, there is a significant drop-off in the amplitude of the backwall echo within a region corresponding to the known weld width of around 20 mm. The attenuation within the weld leads to between -25 dB to -35 dB drop in signal amplitude relative to the backwall responses from within the parent material. This therefore indicates that there are indeed significant attenuative effects occurring within the weld material due to the grain microstructure and the test pieces pose a realistic challenging case for ultrasonic inspections. It can also be seen that the left plate of the welded test piece shows around a 5 dB reduction in backwall response compared to the right plate of the test piece. Although they were made of the same material, there may be some small variation between them if they were manufactured from different batches or the variation could be related to coupling variations of the

array probe. It is noted that this effect is not significant and within typical experimental variations exhibited within industry.

8.3 SR Imaging Results & Discussion

8.3.1 Longitudinally Orientated Defects

The MF-TR-MUSIC, TFM and 0° B-Scan algorithms were used to image the defects listed in Table 8.1 using both the 2 MHz and 1 MHz linear ultrasonic arrays.

The array images for the longitudinal LOILF Defects #1-4 are shown in Fig. 8.4, Fig. 8.5, Fig. 8.6 and Fig. 8.7 and the sizing results are listed in Table 8.2, Table 8.3 and Table 8.4.

First considering the array images for Defect #1 (listed in Table 8.1) shown in Fig. 8.4, all of the algorithms produced images similar to the simulated and simple experimental test piece images shown in previous chapters of this thesis. The MF-TR-MUSIC algorithm generated the expected five indication and three indication patterns from the 2 MHz and 1 MHz array data respectively, as predicted by Fig 3.10. The TFM algorithm at 2 MHz produced a more detailed amplitude profile of the planar flaw than the corresponding 1 MHz TFM image, as expected with twice the theoretical resolution capability. The array 0° B-Scan images at either frequency appeared visually very similar in profile, with the 1 MHz image showing a broader defect indication.

From the corresponding defect width sizing results for Defect #1 listed in Tables 8.2-8.4, both the MF-TR-MUSIC and TFM algorithms estimated the defect width to be around 7 mm for either inspection frequency. These values were close to the manufacturer stated defect width of 6 mm and within the image sizing and manufacturing tolerances. Both methods also produced accurate tilt estimates of the defects of between 0°-10° indicating negligible TWH. The 2 MHz array 0° B-Scan technique estimated the defect width at 8 mm, which is within one error bar of the estimations produced by the TFM and SR algorithms suggesting a similar level of performance between all algorithms. The 1 MHz B-Scan image however significantly overestimated the defect width at 12 mm and had a much larger measurement error due to the inherent image resolution of 3 mm at that frequency. From the defect length sizing results for Defect #1, both the TFM and B-Scan algorithms estimated similar values around 16 mm which were close to the stated defect length of 15 mm. Accurate length sizing was expected due to the defect's large size (5λ at 2 MHz and 2.5λ at 1 MHz).

Considering the array images for Defect #2 (listed in Table 8.1) shown in Fig. 8.5, which was half the size of Defect #1, again all of the algorithms produced the expected typical image profiles. The MF-TR-MUSIC algorithms produced the expected three and two indication patterns from the 2 MHz and 1 MHz array data respectively, as predicted by Fig 3.10. However, there were some spurious indications present within the 2 MHz image above the defect indication, which were likely due to the high levels of material noise within the ultrasonic data. The cleaner 1 MHz MF-TR-MUSIC algorithm image is expected due to the predicted lower impact of grain

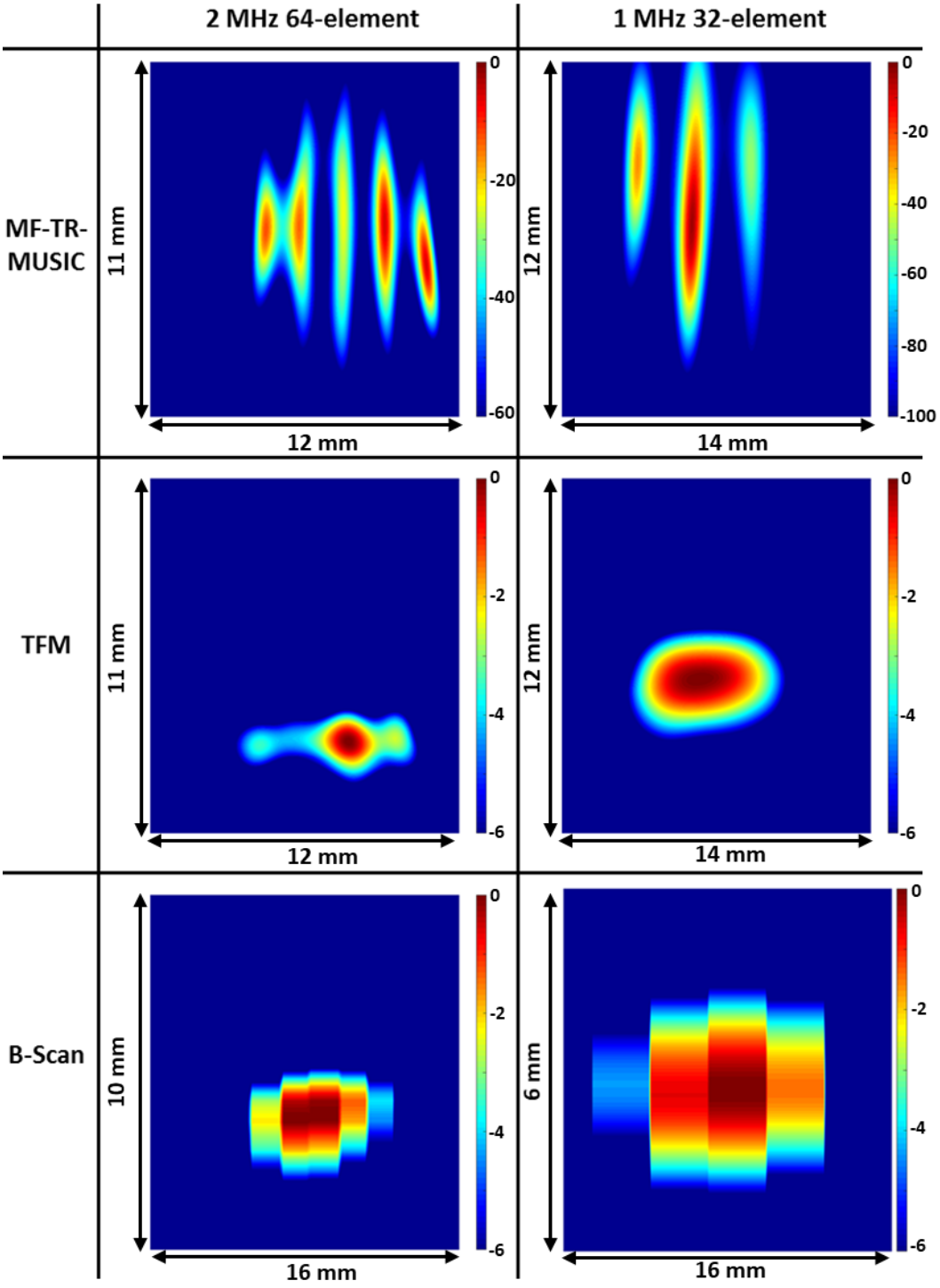


Figure 8.4: Defect #1 array images in the $x - y$ plane. All the images are plotted on a decibel scale normalised to the maximum image amplitude from the defect response. All TFM and B-Scan images are plotted between 0 and -6 dB. A 9 mm aperture was used to generate the 2 MHz B-Scan image and an 18 mm aperture was used to generate the 1 MHz B-Scan image. The array in each case was located above the defects.

scattering at this lower frequency. As for Defect #1, the 2 MHz TFM image of Defect #2 had a more detailed amplitude profile compared to the 1 MHz

Table 8.2: The MF-TR-MUSIC width sizing results for LOILF defects within austenitic stainless steel weld test pieces using the 2 MHz and 1 MHz arrays.

Defect Number	Frequency (MHz)	Width (mm)	Tilt (°)
1	2	7.0 ± 0.5	9.6 ± 0.8
1	1	7.2 ± 0.5	2.2 ± 0.8
2	2	4.5 ± 0.5	11.9 ± 1.3
2	1	4.5 ± 0.5	14.1 ± 1.3
3	2	5.7 ± 0.5	5.8 ± 1.0
3	1	6.0 ± 0.5	14.3 ± 1.0
4	2	3.3 ± 0.5	19.6 ± 1.7
4	1	4.0 ± 0.5	3.6 ± 1.4

image, which was operating at the theoretical diffraction limit.

From the Defect #2 width sizing results listed in Tables 8.2-8.4, both the MF-TR-MUSIC and TFM algorithms produced identical sizing results at each inspection frequency of 4.5 mm. This is an overestimation of the stated defect size by 50% and it is within three error bars of the manufacturing tolerance width. Both methods again generated reasonable orientation estimates of less than 15°, indicating correctly that the flaws were not oriented in the through-wall direction. The array B-Scan method overestimated the defect width by around 170% and 300% for the 2 MHz and 1 MHz cases respectively, indicating that the method is severely beam width limited and unable to resolve defect sizes at this scale. From the defect length sizing results for Defect #2, both of the TFM and array B-Scan algorithms produced results within measurement errors of each other. At 2 MHz, the array B-Scan algorithm produced the most accurate estimation of the length with a percentage error of 7% compared to the 30% TFM error, whereas at 1 MHz both algorithms overestimated the defect length by more than 60%.

Considering the array images for Defect #3 (listed in Table 8.1) shown in Fig. 8.6, which had the same dimensions as Defect #1 but 20 mm deeper, the images were largely similar to those of Defect #1 in Fig. 8.4 but with some notable differences. The 1 MHz MF-TR-MUSIC algorithm images featured the expected three indications for a defect of 1λ in width as shown in Fig 3.10, however the 2 MHz images did not follow this trend unlike Defect #1. The number of indications dropped from five in the 30 mm deep defect case to four indications for the 50 mm deep case. This was likely due to the reduction in SNR that was achieved for the deeper Defect #3 case due to the ultrasonic beam path lengths within the weld material being significantly larger and therefore a greater degree of scattering and beam deviation would have occurred. This may also be an experimental demonstration of a reduction in SNR leading to a reduction of indications within a SR imaging pattern that was found to occur in Section 3.6. The assumption of this statement is that the defect widths were exactly identical, which may not be the case due to manufacturing tolerances. Also, the 50 mm deep

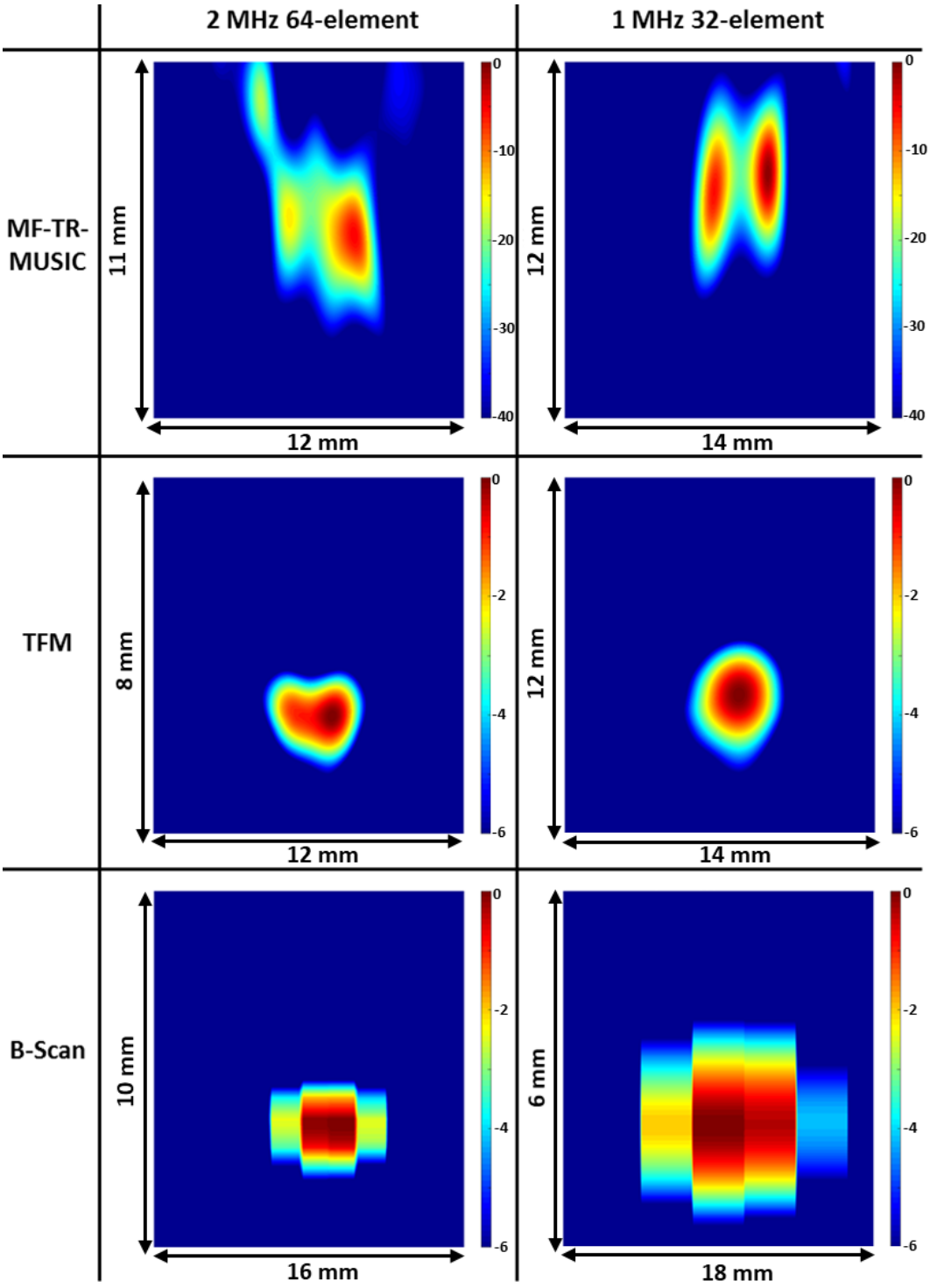


Figure 8.5: Defect #2 array images in the $x - y$ plane. All the images are plotted on a decibel scale normalised to the maximum image amplitude from the defect response. All TFM and B-Scan images are plotted between 0 and -6 dB. A 7.5 mm aperture was used to generate the 2 MHz B-Scan image and a 18 mm aperture was used to generate the 1 MHz B-Scan image. The array in each case was centred directly above the defects. The array in each case was located above the defects.

Table 8.3: The TFM sizing results for LOILF defects within austenitic stainless steel weld test pieces using the 2 MHz and 1 MHz arrays.

Defect Number	Frequency (MHz)	Length (mm)	Width (mm)	Tilt (°)
1	2	16 ± 1	7.0 ± 0.1	0.8 ± 0.8
1	1	18 ± 1	7.2 ± 0.1	4.0 ± 0.8
2	2	10 ± 1	4.5 ± 0.1	2.1 ± 1.3
2	1	12 ± 1	4.5 ± 0.1	7.8 ± 1.3
3	2	13 ± 1	5.7 ± 0.1	5.1 ± 1.0
3	1	16 ± 1	6.0 ± 0.1	5.8 ± 1.0
4	2	11 ± 1	3.3 ± 0.1	3.5 ± 1.7
4	1	14 ± 1	4.0 ± 0.1	7.3 ± 1.4

Table 8.4: The array B-Scan sizing results for LOILF defects within austenitic stainless steel weld test pieces using the 2 MHz and 1 MHz arrays. All defect inclinations were recorded as 0°.

Defect Number	Frequency (MHz)	Aperture Size (mm)	Length (mm)	Width (mm)
1	2	9	15 ± 1	8 ± 1
1	1	18	17 ± 1	12 ± 3
2	2	7.5	8 ± 1	8 ± 1
2	1	18	13 ± 1	12 ± 3
3	2	21	13 ± 1	12 ± 1
3	1	27	15 ± 1	12 ± 3
4	2	24	10 ± 1	8 ± 1
4	1	27	13 ± 1	9 ± 3

Defect #3 would have had a slightly reduced viewing angle compared to the 30 mm deep Defect #1 case (≈30° less) which also would have acted to hinder the SR imaging capability. Further studies would be required to determine the exact causes of this result in the SR images. Due to the reduction in SNR, the TFM images appeared significantly grainier than the images shown for Defect #1 at both inspection frequencies and the B-Scan indications were much larger than the shallower defect case.

From the defect width sizing results for Defect #3, again both the MF-TR-MUSIC and TFM algorithms estimated identical sizes for each inspection frequency and the widths estimated between frequencies were very similar. The results were also highly accurate for all cases, being within 5% error of the manufacturer stated defect width. This indicates that although in the 2 MHz case the number of expected indications dropped from five to four, accurate sizing was still achievable. The array B-Scan algorithm

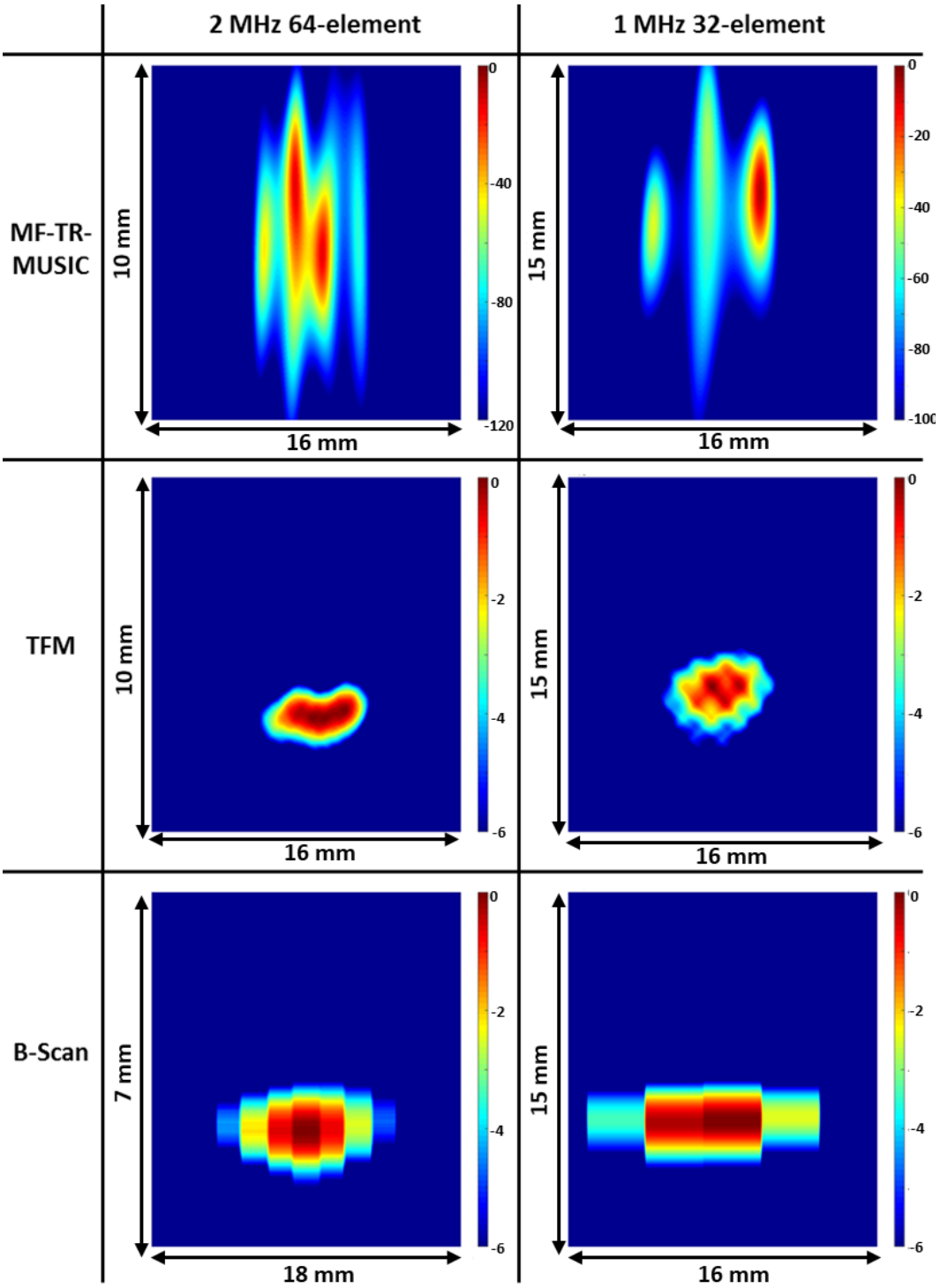


Figure 8.6: Defect #3 array images in the $x - y$ plane. All the images are plotted on a decibel scale normalised to the maximum image amplitude from the defect response. All TFM and B-Scan images are plotted between 0 and -6 dB. A 21 mm aperture was used to generate the 2 MHz B-Scan image and a 27 mm aperture was used to generate the 1 MHz B-Scan image. The array in each case was centred above the defects.

Table 8.5: The imaging SNR of the TFM and array B-Scan algorithms from the LOILF defects when using a 2 MHz 64-element array.

Defect Number	Defect Type	Size (mm)	SNR_{TMF} (dB)	SNR_{BScan} (dB)
1	LOILF	15 x 6	30.5	25.9
2	LOILF	7.5 x 3	27.5	18.9
3	LOILF	15 x 6	30.9	28.4
4	LOILF	7.5 x 3	26.1	19.5

significantly overestimated the defect width at each inspection frequency by 100%. From the defect length sizing results for Defect #3, as with the previous defect cases, both the TFM and B-Scan methods produced almost identical estimations which were close to the stated value of 15 mm. In terms of estimating the defect orientations, the MF-TR-MUSIC algorithm's performance slightly deteriorated compared to the Defect #1 case with the method overestimating the tilt by between 5°-15°. These tilts however would still estimate the TWH of the defect to be less than 20% of the width which is small. The TFM algorithm also slightly overestimated the defect tilt slightly by around 5° and it is therefore in agreement with SR technique.

Finally considering the array images for Defect #4 (listed in Table 8.1) shown in Fig. 8.7, which was 20 mm deeper than Defect #2, similar differences were observed. The MF-TR-MUSIC algorithm images had the same profiles as for the shallower Defect #2 case, the TFM images were grainier due to the decreased SRN and the array B-Scan images produced larger indications, again likely due to the decreased SNR.

From the Defect #4 width sizing results, once again the MF-TR-MUSIC and TFM algorithms produce identical estimations of this defect parameter for each frequency, with all results within 1 mm of the manufacturer stated value. The array B-Scan algorithm, as in the Defect #2 results, significantly overestimated the defect width alluding to the method being beam width limited. From the length sizing results of Defect #4, both the TFM and B-Scan algorithms produced similar estimations with the 2 MHz results slightly more accurate than the 1 MHz results.

Using the methodology described in Section 3.6, the imaging SNR of the TFM and array B-Scan algorithms was estimated from the LOILF defect's images. The imaging SNR results when using the 2 MHz and 1 MHz arrays are listed in Table 8.5 and Table 8.6. A representative example SNR case (Defect #1) is shown in Fig. 8.8.

The imaging SNR of both of the algorithms considered in Table 8.5 and Table 8.6 are relatively high considering the highly scattering nature of the component material. This is due to the favourable orientation of the LOILF defects which allowed a large specular component of the incoming ultrasound from the direct contact array to be reflected back on reception. The TFM algorithm achieved a higher imaging SNR compared to the array B-Scan algorithm, roughly around 5 dB better in each case. These SNR values

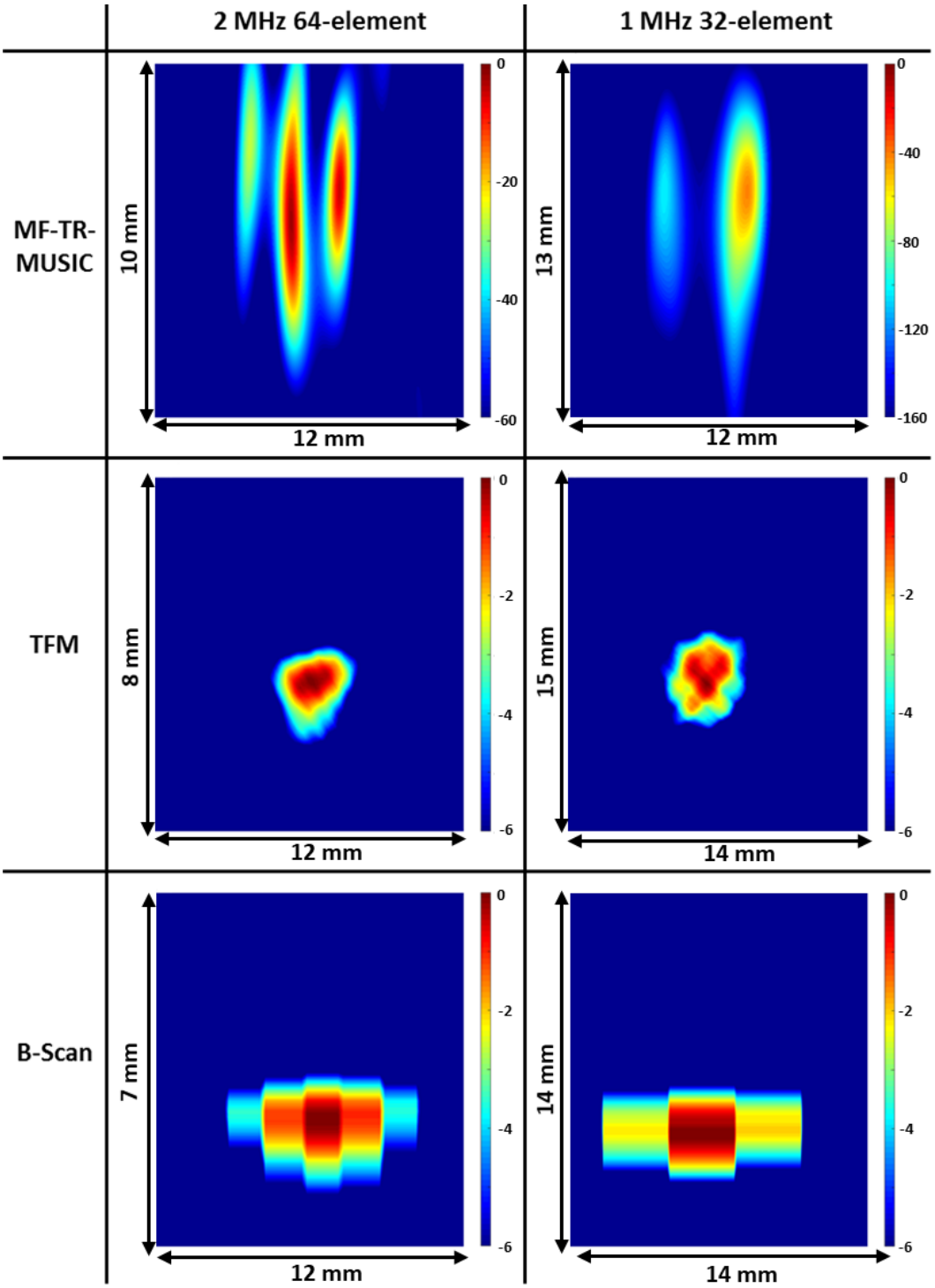


Figure 8.7: Defect #4 array images in the $x - y$ plane. All the images are plotted on a decibel scale normalised to the maximum image amplitude from the defect response. All TFM and B-Scan images are plotted between 0 and -6 dB. A 24 mm aperture was used to generate the 2 MHz B-Scan image and a 27 mm aperture was used to generate the 1 MHz B-Scan image. The array in each case was centred above the defects.

Table 8.6: The imaging SNR of the TFM and array B-Scan algorithms from the LOILF defects when using a 1 MHz 32-element array.

Defect Number	Defect Type	Size (mm)	SNR_{TMF} (dB)	SNR_{BScan} (dB)
1	LOILF	15 x 6	27.6	19.6
2	LOILF	7.5 x 3	23.2	12.9
3	LOILF	15 x 6	29.4	26.0
4	LOILF	7.5 x 3	25.2	17.5

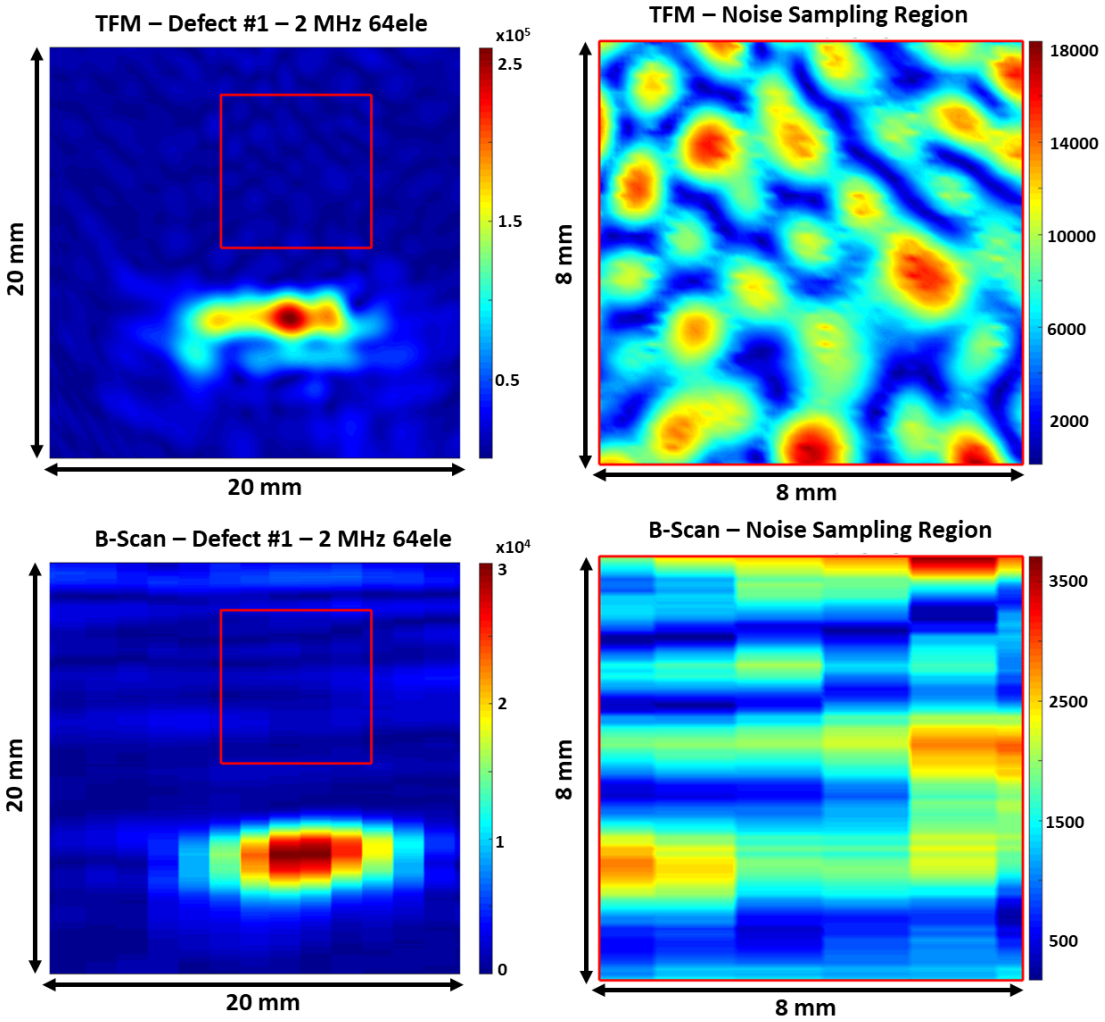


Figure 8.8: The imaging SNR methodology for Defect #1 within the austenitic stainless steel test pieces in the $x-y$ plane. Each image is plotted in an absolute amplitude scale with the array positioned directly above the defect indication.

within the austenitic stainless steel weld components were around 5-10 dB lower than for the SE defect images listed in Table 5.6, despite the SE defects having a specular area at least 7.5 times smaller than the LOILF defects, and between 10-20 dB smaller than the WE defect image SNR values listed in

Table 4.4. This big drop can be attributed to the scattering austenitic stainless steel weld material as the parent materials of the test pieces (304 and 304L stainless steels) were extremely similar. It is worth noting that during testing of the austenitic stainless steel welds, the 1 MHz array actually produced lower imaging SNR values compared to the 2 MHz array which is contrary to theoretical predictions of scattering scaling with frequency. The lack of increased SNR performance of the 1 MHz array in comparison to the 2 MHz array is likely due to the greater number of elements present within the 2 MHz array (64 elements compared to 32 elements), allowing the summation of a greater number of signals in the image processing, as well as the smaller size of the defect relative to the wavelength at 1 MHz compared to 2 MHz.

8.3.2 Through-Wall Orientated Defects

When applying the MF-FM or the MF-TR-MUSIC algorithms to the through-wall orientated defects (LOSWF & LOIRF flaws), very few suitable images for defect sizing were generated from either the 2 MHz or 1 MHz arrays. All of the SR images were extremely noisy with numerous artefacts present throughout the image meaning it was not possible to clearly distinguish any indications related to the embedded defects from the surrounded material. Example representative SR images for the through-wall defects are shown in Fig. 8.9. The significant impact of noise for the through-wall orientated defects in this image compared to the relatively low impact observed for the longitudinal LOILF defects discussed in Sec. 8.3.1 is due to the weak tip defect scattering responses obtained from the through-wall defects.

Although the array viewing angle was maximised for the direct contact array set-up used, it meant that only tip diffraction responses would have been obtained from the through-wall defects as opposed to the large amplitude specular reflections received from the LOILF defects. These tip diffraction responses were then subsequently swamped by the material grain noise leading to extremely low SNRs and poor quality SR images. The strong impact of noise is evident when examining the magnitude of the eigenvalues of the far-field operator F. Fig. 8.9c) shows the eigenvalues of F at 2 MHz for the LOIRF Defect #9. It can be seen that the magnitude of the eigenvalues drops almost instantly and there is no clear separation between the eigenvalues corresponding to the *signal* subspace and the *noise* subspace. This is in contrast to Fig. 8.9d) which shows the eigenvalues of F at 2 MHz for the LOILF Defect #1 which features several significant eigenvalues clearly separated from the remaining *noise* subspace. The geometry of Defect #1 allowed a high amplitude specular response to be received by the array resulting in this subspace separation between the first ten eigenvalues (corresponding to the *signal* subspace) and the remaining *noise* subspace eigenvalues by around 20 dB.

For the through-wall defects, it was found that only the TFM algorithm was able to generate some images which could be used to detect the defects. However, it was not possible to size or characterise any using the TFM algorithm again due to the large amount of noise and multiple indications located around the expected defect position. The 0° array B-Scan algorithm did not perform well in terms of either defect detection or sizing, which

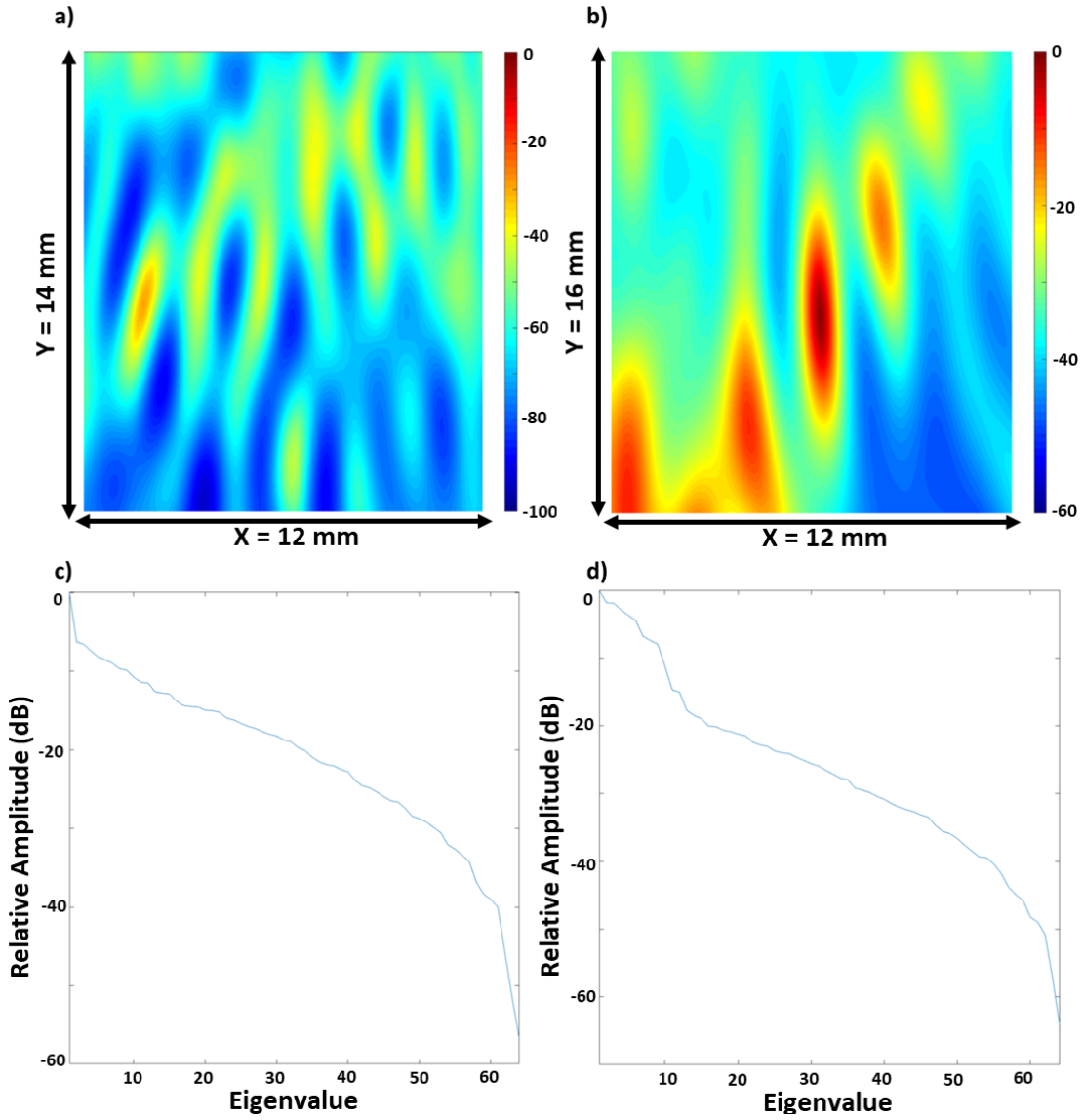


Figure 8.9: a) MF-TR-MUSIC image of Defect #9 (LOIRF), b) MF-TR-MUSIC image of Defect #7 (LOSWF), c) eigenvalues of F at 2 MHz when imaging Defect #9 with the MF-TR-MUSIC algorithm, d) eigenvalues of F at 2 MHz when imaging Defect #1 (LOILF) with the MF-TR-MUSIC algorithm. The array was positioned directly above the defect indication and all images were in the $x - y$ plane.

was expected due to the high misorientation angle between the defect and the incident beams. Examples of TFM images where the defects could be readily detected after FMC scanning are shown in Figs. 8.10 and 8.11. In both of these cases, an SNR_{TFM} of around 15 dB was achieved.

In the majority of cases reliable defect detection was not possible with the TFM algorithm, especially when operating at 2 MHz. Examples of cases where defect detection could not be reliably carried out are shown in Figs. 8.12 and 8.13.

Considering the Defect #11 TFM images in Fig. 8.12, the 2 MHz image only

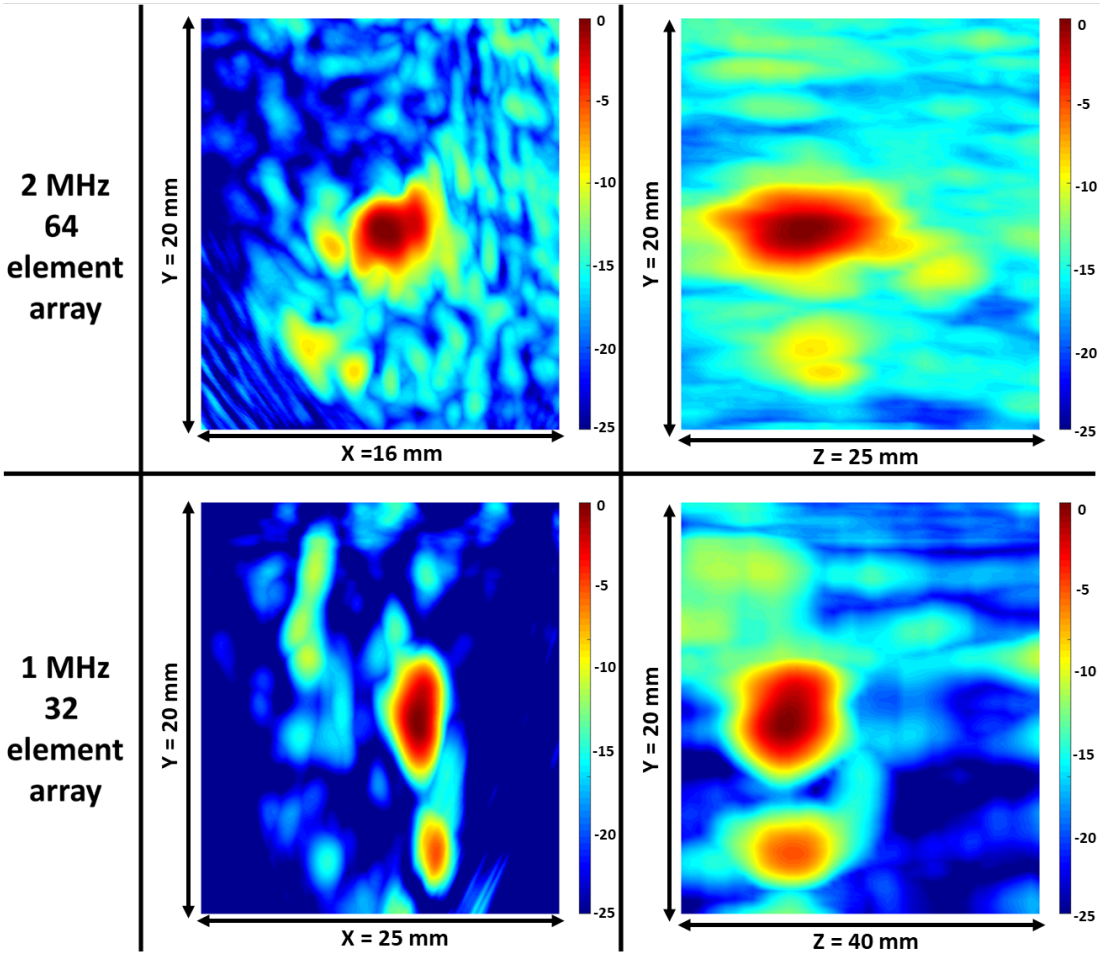


Figure 8.10: Defect #5 TFM array images; the first column corresponds to images in the $x - y$ plane and the second column corresponds to images in the $y - z$ plane. All the images are plotted on a decibel scale normalised to the maximum image amplitude from the defect response. The array was positioned directly above the defect indication.

resembled a noise map of the austenitic weld itself and the weak defect indication is lost within it. Any attribution of these indications to the known defect is highly dubious and is heavily reliant on prior knowledge of the test piece. It is therefore concluded that defect detection could not be achieved via TFM with the 2 MHz array. The 1 MHz results on the other hand are slightly better where defect tips could potentially be identified and an estimation of defect parameters could be inferred. The estimated parameters were 7.7 mm width and tilt angle of 72.6°. Defect length could not be estimated from defect tips and would require an angled beam inspection to use amplitude based sizing effectively.

Considering the 2 MHz TFM images of Defect #12 in Fig. 8.13, once again no defect indication could be detected and the TFM image only resembled a noise map of the austenitic weld. As with the case for Defect #11, the 1 MHz TFM image was able to potentially detect the defect and although

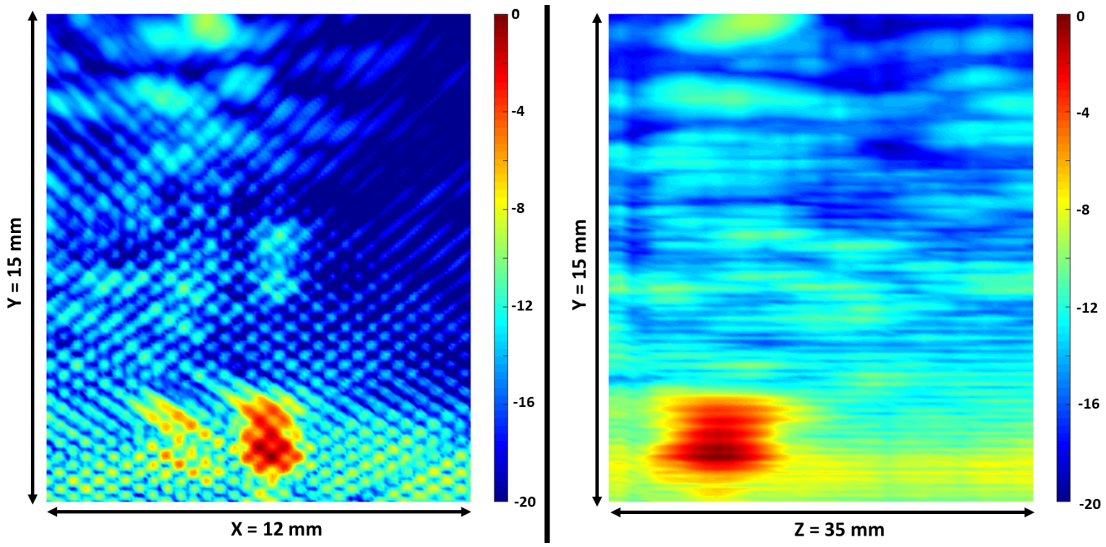


Figure 8.11: Defect #7 TFM array images using the 2 MHz 64-element array. The left image corresponds to images in the $x-y$ plane and the right image corresponds to images in the $y-z$ plane. All the images are plotted on a decibel scale normalised to the maximum image amplitude from the defect response. The array was positioned directly above the defect indication.

there was significant weld noise present, through-wall sizing could be carried out using the assumed tip diffraction indications. The defect was characterised to have a TWH of 3.3 mm and a tilt angle of 86.5° which is accurate compared to the defect specification listed in Table 8.1. In the through-wall defect TFM imaging cases, utilising a lower inspection frequency increased the detectability of misorientated defects through the austenitic stainless steel weld material.

The lack of performance of the TFM algorithm was as a result of the unfavourable array configuration used to inspect the through-wall orientated flaws (0° direct contact centrally located above the defects). A different array set-up using an angled wedge would increase the likelihood of a strong specular response being obtained instead of being reliant on detecting tip diffraction responses through the irregular coarse grain structure. Using an angled beam may also allow a shorter ray path through the austenitic weld material, reducing the impact of grain noise and beam bending effects. In addition, for the defects located in close proximity to the back-wall of the test pieces, an imaging method such as the Half Skip Total Focusing Method (HSTFM) would be more appropriate [107] to detect and size them. The HSTFM utilises reflections off the back-wall to enhance the imaging of surface breaking or near back-wall located defects and has been shown to exhibit improved performance over TFM in these cases [107, 108]. An alternative array set-up was not used in this work as they would act to reduce the viewing angle on the defects which would have a significant detrimental impact on the performance of the SR algorithms.

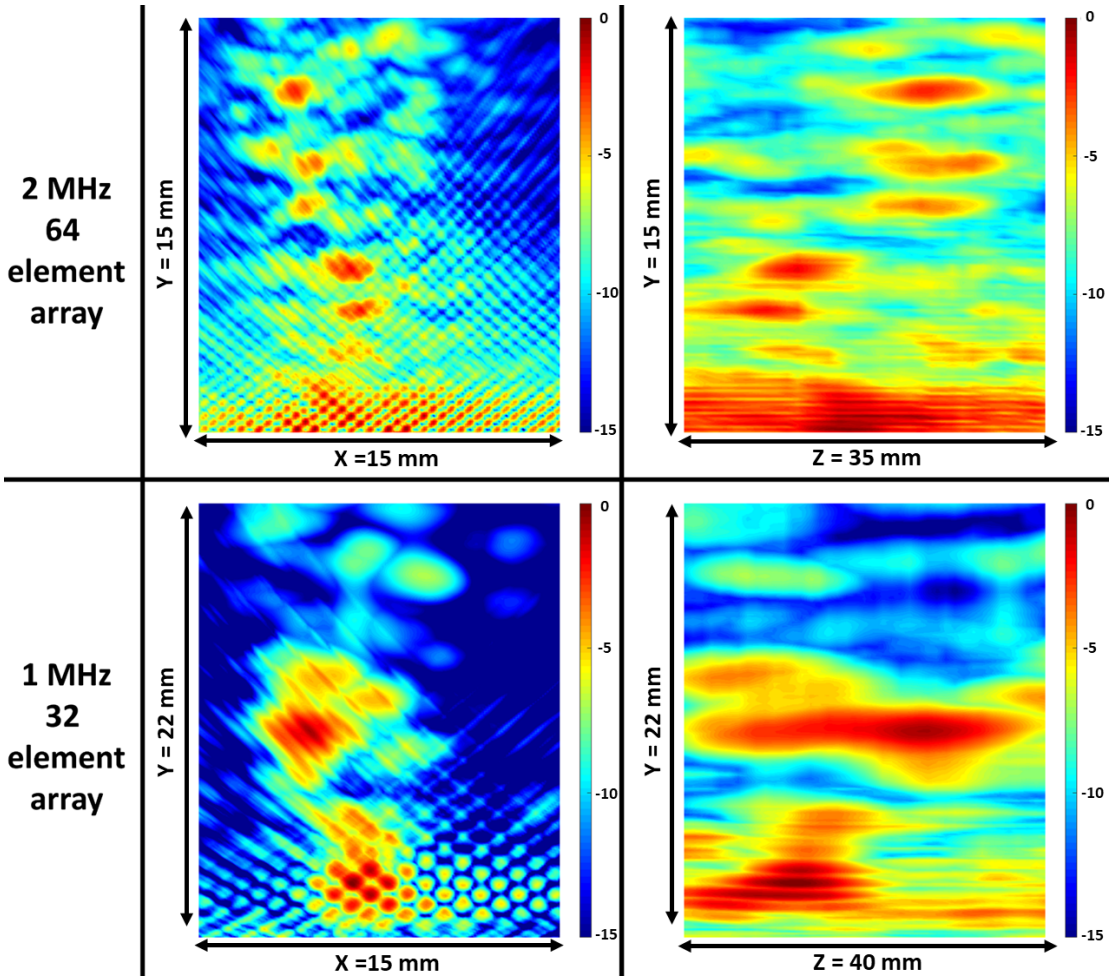


Figure 8.12: Defect #11 TFM array images; the first column corresponds to images in the $x-y$ plane and the second column corresponds to images in the $y-z$ plane. All the images are plotted on a decibel scale normalised to the maximum image amplitude from the defect response. The array was positioned directly above the defect indication.

8.4 Conclusions

In this Chapter, the experimental performance of the SR array algorithms when inspecting manufacturing-style defects within narrow gap austenitic stainless steel welded test pieces was investigated. These types of components are highly scattering and anisotropic making ultrasonic NDE extremely challenging.

Three main types of embedded defects were used: LOILF defects which were fully embedded longitudinally orientated defects, LOSWF defects which were located on the edge of the weld faces, and LOIRF defects which were through-wall orientated defects.

For the LOILF defects which were orientated parallel to the test piece inspection surface, it was found that the MF-TR-MUSIC, TFM, and 0° array B-Scan algorithms were able to effectively detect and characterise all of the defects. This level of performance was achieved in both the 2 MHz and

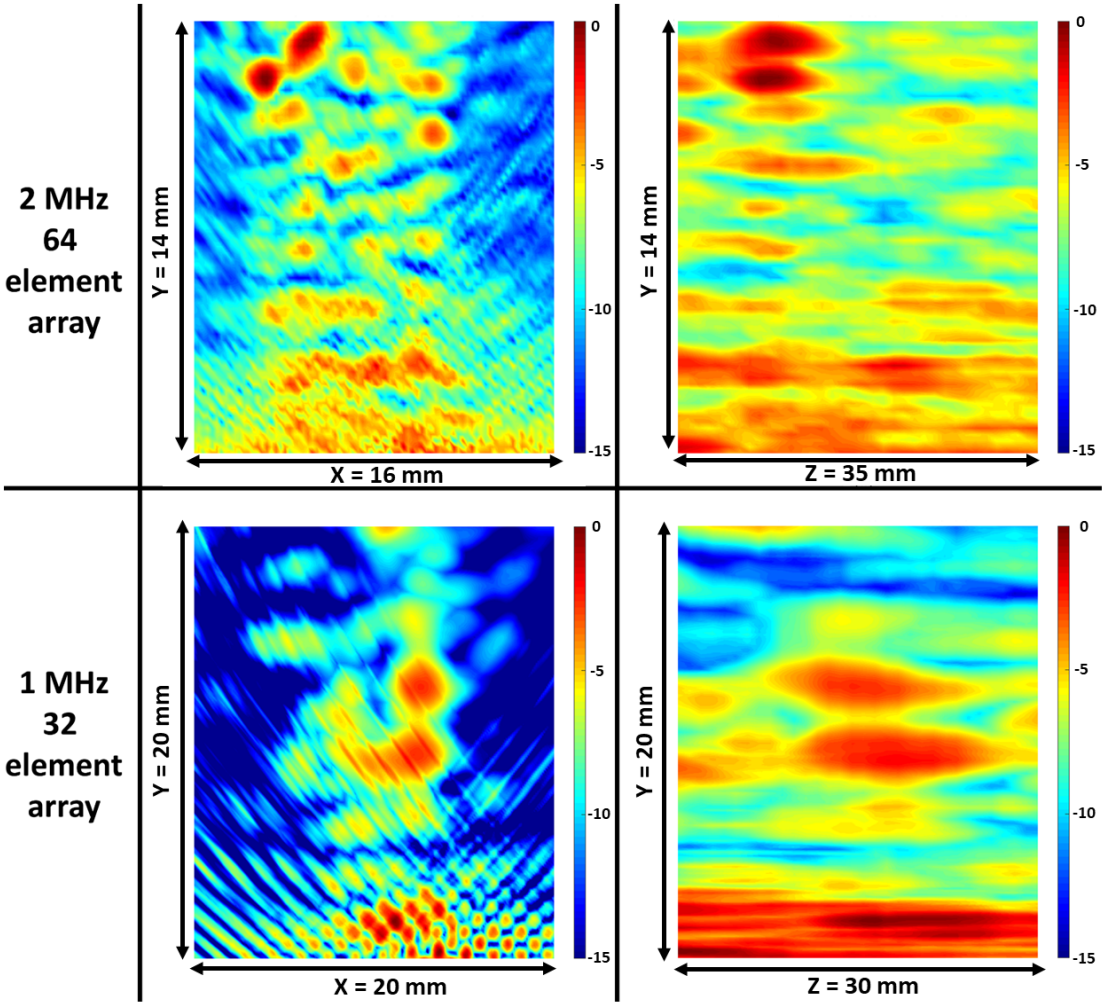


Figure 8.13: Defect #12 TFM array images; the first column corresponds to images in the $x-y$ plane and the second image corresponds to images in the $y-z$ plane. All the images are plotted on a decibel scale normalised to the maximum image amplitude from the defect response. The array was positioned directly above the defect indication.

1 MHz array configurations. This was the first time to the author's knowledge that the TR-MUSIC algorithm has been experimentally applied to inspect defects within austenitic welded components and demonstrates that the SR algorithms could be applied to these scattering and anisotropic materials.

For the through-wall LOSWF and LOIRF defects, the MF-TR-MUSIC algorithm was not able to detect or characterise any of the defects due to the lower SNR of these defects. This was as a result of only being able to receive tip diffraction responses through the weld due to the unfavourable inspection configuration. The TFM array algorithm was able to detect some of the defects however they struggled to accurately characterise them. It was found that a better defect detection performance was obtained when using the 1 MHz array compared to the 2 MHz array for the through-wall defects.

Chapter 9

Conclusions

9.1 Thesis Review & Main Achievements

The aim of this research was to investigate the applicability of the SR array imaging algorithms within NDE inspections of safety-critical components for the nuclear power industry in order to determine if they could potentially meet the increasing demand to accurately characterise and size embedded defects.

To do this, the performance of the recently developed FM and TR-MUSIC algorithms were applied to the ultrasonic array inspection of embedded flaws were assessed for an extensive range of defect parameters. These advanced techniques were compared to the TFM algorithm, which is widely considered to be the *'gold standard'* for array imaging within academia, in order to benchmark their performance. The performance was initially evaluated through 2D FE simulations followed by several stages of experimental validation. A particular focus was placed on investigating the sizing capability of the SR algorithms for sub-wavelength sized defects as a method to overcome the inherent resolution limitations of conventional array imaging methods, such as the TFM and array B-Scan algorithms. The studies within this thesis considered mainly 2D planar embedded flaws of varying size, orientation and surface roughness. This scope was also extended to consider realistic 3D defect morphologies and a post-processing methodology was developed to apply the SR algorithms to experimentally gathered scanned FMC datasets. Finally, the challenging inspection case of thick-walled austenitic stainless welds was considered and the applicability of the SR algorithms to these scattering and anisotropic materials was evaluated.

Within Chapter 2, the background theories of ultrasonic wave scattering were discussed. Descriptions of both the forward and inverse scattering problems were introduced, with approaches to overcoming the inverse scattering problem outlined. These approaches all attempt to determine the structure of scatterers with only knowledge of the incident and scattered wave fields. The Born approximation, which is a widely used method to simplify the problem, was introduced and it was shown to form the basis of the TFM. The TFM is an example of a beamforming algorithm, which by their very nature are explained to be restricted by the diffraction limit ($\lambda/2$) in their resolution. Mathematical formalisms to overcome this resolution limit were discussed, beginning with the LSM and followed by the FM and TR-MUSIC algorithms. These sampling methods, or commonly referred to

as SR methods, are theoretically capable of achieving unlimited resolutions if no effects such as noise are present and therefore have become attractive research interests for industry. It is noted however their derivation is based on imaging idealised point scatterers and assuming complete angular inspection coverage is obtained. Their capability to accurately image realistic extended defect morphologies with limited aperture linear arrays has not yet been fully established, therefore, it is key to understand their performance within these circumstances if they are to be used within practical NDE inspections.

In Chapter 3, the linear array inspection capability of the SR algorithms was assessed for a variety of planar embedded defects through 2D FE modelling. For the first time, the sizing and orientation estimation performance of the MF-FM and MF-TR-MUSIC algorithms were determined for a large range of defect parameters. It was found that within this limited view inspection scenario, the SR algorithms were not able to fully reconstruct the complete profile of the embedded planar flaws but instead generated clustered indication patterns across the defect extents. This imaging behaviour was expected as the SR algorithms are predicated on the assumption of complete angular coverage and therefore complete sampling of the far-field scattered wavefield, which cannot be practically achieved within realistic inspection cases. Importantly, it was found that indications were consistently generated from the tips of the planar defects which facilitated tip-sizing methodologies to be employed. Using these sizing techniques, it was found that the SR techniques showed far superior width sizing performance for sub-wavelength sized defects compared to the TFM and 0° array B-Scan algorithms, which was expected with the latter methods becoming beam-width limited at these small scales. This advantage in width sizing performance was also retained when imaging embedded planar defects with a range of misorientation angles and it was also shown the SR techniques could accurately estimate TWH. Significantly, a trend within the SR images of the planar defects was identified which linked the number of image indications generated to the defect size relative to the ultrasonic wavelength. This roughly linear trend could potentially enable defect sizing to be conducted by simply visually observing the images generated by the SR algorithms. The impact of incoherent noise on SR array imaging was also investigating and both the MF-FM and MF-TR-MUSIC algorithms demonstrated robustness to SNRs at or above 10 dB. However, for higher levels of incoherent noise there was an observable reduction in the number of F matrix eigenfunctions corresponding to the *signal* subspace, as the noise began to corrupt the eigenfunctions with lower eigenvalues corresponding to the higher spatial frequency information. This led to the SR algorithms producing indication patterns similar to those which would be expected of smaller defects in a noise-free scenario resulting in defect under-sizing, as well as distortion to the indications that were being generated.

Experimental validation of the simulated results presented in Chapter 3 was conducted using pseudo-2D WE planar defects in Chapter 4. It was found that the simulated sub-wavelength width and TWH sizing capabilities of the SR algorithms could be experimentally realised. The TFM algorithm was not able to match this level of performance at the smallest

length scale tested ($\lambda/2$), however it produced accurate characterisation results for the λ and 2λ sized defects that was matched by the SR techniques. The discontinuous clustered indication patterns observed in the simulated studies within Chapter 3 were also experimentally seen, again highlighting the impact of reduced viewing angle on the reconstructive abilities of the SR techniques. Importantly, the non-dimensional SR imaging trend for planar defects observed previously was experimentally validated over the $\lambda/2$-2λ defect size range considered, adding confidence that this trend could be used to visually estimate planar defect size using only knowledge of the ultrasonic wavelength.

The experimental scope was further extended to consider 3D embedded planar defects in Chapter 5, which are more representative of commonly encountered flaws. A methodology was established to process the scanned FMC datasets acquired in order to effectively apply the SR algorithms for defect width sizing. This method utilised information gained from the TFM algorithm to allow appropriate time-domain windowing of signals prior to SR image processing to enable accurate defect sizing. This step is vital for the methods to be used in practical NDE scenarios due to prior knowledge of the temporal location of defects not being readily available, making isolation of the defect scattered signal difficult. If this methodology was not applied, it was clear that even in defect-free regions the SR algorithms would generate erroneous high amplitude images emphasising the fact that the SR methods should only be used as a supplementary technique for defect sizing and not as a detection tool. During testing, it was found that the TR-MUSIC algorithm in particular allowed for excellent sizing for defects well below the diffraction limit, down to 1 mm ($\lambda/3$). This level of performance could not be achieved by either the MF-FM, TFM or the array 0° B-Scan algorithms.

A prominent challenge present within the nuclear industry is the inspection of rough defects. Due to the often extreme conditions components are exposed to within this sector, defect growth mechanisms such as thermal fatigue cracking and stress corrosion cracking can occur that are known to produce defects with significant surface roughness. Ultrasonically, this roughness often hinders defect detection and characterisation which can lead to a large degree of conservatism to be placed on their inspection. This inevitably is costly to industry due to the stringent component acceptance criteria that must be achieved. In Chapter 6, 2D FE Monte Carlo simulations was used to investigate the impact of roughness on the array imaging of rough planar embedded defects. The results presented showed that for sub-wavelength defects, both the FM and TR-MUSIC algorithms were able to size and estimate defect orientation accurately for low roughness cases of $\sigma = 10\ \mu m$ and for defects with up to $\sigma = 100\ \mu m$. The most accurate SR imaging performance was achieved for the $\lambda/2$ sized defects in either the 0° or 45° tilt orientation. This was in contrast to the poor performance of TFM in these cases which consistently oversized these defects and could not be used to estimate the defect orientation, thus making through-wall sizing with this method impossible. It was also found that when sizing the larger 3 mm (λ) flaws misorientated at 45°, the performance of the SR increased significantly as the roughness increased. It is postulated that this was because of a combination of the increased total scattered signal obtained from

the rougher misorientated flaws (due to an increase in diffractive scattered wave component) as well as a greater degree of multiple scattering occurring, leading to the SR algorithms being able to reconstruct the defects more accurately. The results presented within this Chapter highlight that the SR algorithms are able to tolerate a moderate degree of defect roughness that could be expected within realistic in-service flaws.

In Chapter 7, the challenge of sizing embedded volumetric flaws was considered. Conventionally, direct sizing of volumetric defects is only achievable using radiographic techniques and ultrasonic methods can only be used to infer an upper size limit based on the beam width. In this Chapter, 2D FE modelling was used to simulate the array inspection of smooth embedded volumetric defects to investigate the nature of the imaging responses generated by the SR algorithms. The practical equivalent of the 2D defects simulated within this Section are Side Drilled Holes (SDHs). Although SDH profiles do not relate to a type of defect found within real NDE inspection, they are common within ultrasonic NDE test pieces as calibration targets and act as a simplified case for 3D equivalent defects such as pores. It was demonstrated through 2D FE simulations that the SR algorithms can be used to estimate the diameter of SDHs via direct imaging with a linear ultrasonic array. The sizing performance of SDHs using the SR algorithms was then experimentally validated by accurately sizing three different SDH diameters, with the maximum percentage error of around 15%. The scope was extended to consider a 3D volumetric pore defect and using the scanning FMC methodology established within Chapter 5, the MF-TR-MUSIC algorithm was able to image and size a realistic 2 mm 3D embedded pore defect. These positive results highlight that the SR methods could be an accurate tool for sizing volumetric defects and could potentially facilitate a transition away from the radiographic techniques which are inherently more time consuming, costly and hazardous when compared to ultrasonic NDE. However, this Chapter demonstrated that the SR algorithms may not be suitable to distinguish between planar and volumetric flaws due to the high similarity between the images from these defect types. It is recommended that supplementary imaging algorithms, such as a series of angled array B-Scans, are carried out alongside the SR methods to help determine the true defect morphology.

In Chapter 8, the difficult inspection case of welded austenitic stainless steels was considered. These components which are common within the nuclear sector, can exhibit a spatially-varying anisotropy and coarse grained structure that significantly impacts upon the quality of an ultrasonic inspection. To investigate this problem, the experimental performance of the SR array algorithms when inspecting manufacturing-style defects within narrow gap austenitic stainless steel welded test pieces was considered. For defects which were orientated parallel to the test piece inspection surface, it was found that the MF-TR-MUSIC, TFM, and 0° array B-Scan algorithms were able to effectively detect and characterise them. This level of performance was achieved in both the 2 MHz and 1 MHz array configurations. It was found that the MF-FM algorithm could not be used to effectively size these flaws. This is due to the fact that the MF-FM algorithm utilised all eigenfunctions derived from the FMC datasets and the high coherent noise within the system would have corrupted the eigenfunctions

related to the higher frequency spatial information, thus deteriorating the imaging process. This is unlike the MF-TR-MUSIC algorithm which truncates some of the eigenfunctions and it is therefore less sensitive to these effects. It is therefore recommended that eigenfunction truncation is incorporated within the MF-FM to increase the robustness of the technique within inspection scenarios featuring significant noise. For the through-wall orientated defects, the MF-TR-MUSIC algorithm nor the conventional imaging techniques were able to size any of the defects due to the very low SNRs achieved. This was as a result of only being able to receive tip diffraction responses through the weld due to the unfavourable inspection configuration. Although not successful in all defect cases within the welded austenitic stainless steel test pieces, the MF-TR-MUSIC algorithm has shown robustness to significant levels of coherent noise experimentally, which compliment its demonstrated robustness to incoherent noise, defect misorientation and defect roughness through simulation. This research therefore presents evidence to suggest that the SR imaging technique could indeed have practical viability in offering an improved defect sizing capability within NDE inspections, particular for sub-wavelength sized flaws where conventional imaging techniques become limited.

9.2 Guidance for SR Algorithm Deployment & Future Work

The research conducted within this thesis has highlighted that the SR algorithms have the capability to outperform conventional array imaging techniques when characterising sub-wavelength sized planar defects as well as volumetric flaws. However, it is noted that the inspection set-up used throughout this thesis was optimised for SR imaging and that several challenges for their successful and stable deployment became clear.

This Section will therefore summarise the key factors which influence SR imaging performance and provide guidance for their usage within a linear array configuration. These factors would need to be considered as part of a process to validate the usage of the SR algorithms in industrial manufacturing and in-service NDE inspections, meaning that further work is required to understand the complex influence of these factors on imaging.

9.2.1 Multistatic Response Matrix Construction

One of the key steps in the implementation of the SR algorithms, as illustrated within Fig. 2.12, is the creation of the multistatic response matrix, $F(\omega)$, or matrices if using the multiple frequency variation of the algorithms (Eqs. (2.64) & (2.65)). Although only demonstrated briefly within Fig. 2.11, the SR algorithms are highly sensitive to the selection of frequency, particularly when using the single-frequency variations of the techniques. This is why only multiple-frequency variations of the FM and TR-MUSIC algorithms were implemented within this research in order to achieve a stable and accurate imaging capability.

Although the performance of the SR algorithms are improved when deployed in the multiple-frequency variation, there still exists a choice in

which frequencies are selected. As described within Section 2.8.3, the frequency selection range used to populate $F(\omega)$ throughout the thesis was set to be the full width at half maximum of the bandwidth profile of the ultrasonic tonebursts. For the commonly utilised 2 MHz waveforms generated, this corresponded to a half-spread of 0.4 MHz about the 2 MHz centre frequency. A total of nine equally spaced frequency values were sampled across this frequency range, with an odd number ensuring the centre frequency was considered. It is recommended that at least five frequency values are selected to generate accurate defect reconstructions. Testing by the author found that suitable images could be generated using a tighter frequency range than the full-width at half maximum (e.g. full-width at 70% maximum), therefore further work is required to fully understand the quantitative influence frequency range has on imaging performance in order to validate an appropriate range.

9.2.2 Noise

One of the prominent factors influencing the performance of the SR algorithms is that of signal noise. Within this thesis, it has been shown that the MF-FM and MF-TR-MUSIC algorithms have shown a reasonable degree of robustness to incoherent noise, with the MF-TR-MUSIC technique also showing robustness to coherent noise through testing within austenitic stainless steel welds.

However, it is noted that both SR methods are far more sensitive to noise than conventional TFM imaging. The difference in robustness originates from the lack of sensitivity of TFM to the low-eigenvalued eigenfunctions, which contain the higher spatial frequency scattered information. These eigenfunctions are more easily corrupted by signal noise but they also contain the information necessary to achieve super resolution. The SR methods are more reliant than TFM on these low-eigenvalued eigenfunctions, with the MF-FM using all eigenfunctions and MF-TR-MUSIC only using a selection corresponding to the *signal* subspace.

It is therefore recommended that when deploying the SR methods in practical NDE scenarios where there will inevitably exist a non-zero level of noise, that eigenvalue truncation is incorporated to a degree to ensure that imaging accuracy and stability is achieved. Throughout this research, an eigenvalue truncation threshold of -50 dB compared to the highest amplitude eigenvalue was used for FE simulated FMC datasets and this value was reduced to around -40 dB when imaging through low-noise materials as discussed in Chapters 4 & 5. When imaging through high noise materials, such as within Chapter 8, threshold values between -20 dB to -30 dB were used. These values were determined by observing the point at which a clear distinction between the *signal* and *noise* eigenfunction subspaces appeared, characterised by a steep drop in eigenvalue amplitude.

As currently these eigenvalue threshold values are manually selected based on observations, further work is required to provide a validated procedure to ensure that an appropriate threshold value can be selected easily by a

non-specialist or ideally automatically. This step is crucial if the SR techniques are to be used within an industrial scenario by NDE inspection engineers.

As discussed in Chapter 8, spatially-varying anisotropic coarse grained microstructures can lead to beam bending effects that can lead to defect indications appearing at incorrect positions and erroneous sizing. There may be opportunities to correct for these effects using prior knowledge of the weld grain structure to apply appropriate delay laws when imaging [93, 103]. This approach could also be investigated for the application of the SR algorithms to account for the anisotropy beam deviation phenomenon.

9.2.3 Viewing Angle

Although not extensively reported on within this thesis for a linear array configuration, a reduction in array viewing angle can lead to deterioration of the images generated by the SR algorithms which makes accurate defect sizing difficult. The studies conducted within this thesis as well as previous studies exclusively considered inspection cases where the viewing angle was optimised, i.e. with the array directly centred above/around the defect. This was done in order to establish the maximum performance that the SR techniques could achieve. The impact of reduced viewing angle was briefly considered within Chapter 3 where the performance of a simulated 2 MHz 64-element linear array was compared to that of a 2 MHz 32-element linear array. Although similar indication patterns were obtained in both array configurations, a reduction in planar defect width sizing accuracy as well as a reduction in the ability to estimate the inclination angle of highly misorientated defects was observed with the shorter 32-element array.

Within realistic NDE inspections, it can be common for it to be impossible to place an ultrasonic array directly over a potential defect location to maximise the viewing angle. Instances where this would occur are weld inspections where the welds caps have not been machined off, or geometric features such as nozzles that cannot allow the array to sit flush on component surfaces that exhibit high curvature. These cases would inevitably lead to defects being offset from the array centreline position and therefore act to reduce the viewing angle achieved.

Fig. 9.1 shows that for even relatively small defect offsets from the array centreline position, significant distortion to the SR images occurs. As the offset is increased from 5 mm to 25 mm, both the MF-FM and MF-TR-MUSIC algorithms generate indications which become increasingly skewed and progressively less representative of the true flat defect orientation. The TFM algorithm indications also become slightly tilted which is expected, however the magnitude of this is far less compared to the SR algorithms and it has minimal impact on defect sizing. This example illustrates that defect offset positions which are still within the footprint of the array can lead to significant SR image distortion due to the reduction in viewing angle. Other factors such as defect depth would also impact viewing angle and must also be considered when determining SR imaging performance. Further work is therefore required to quantify the practical limitations of

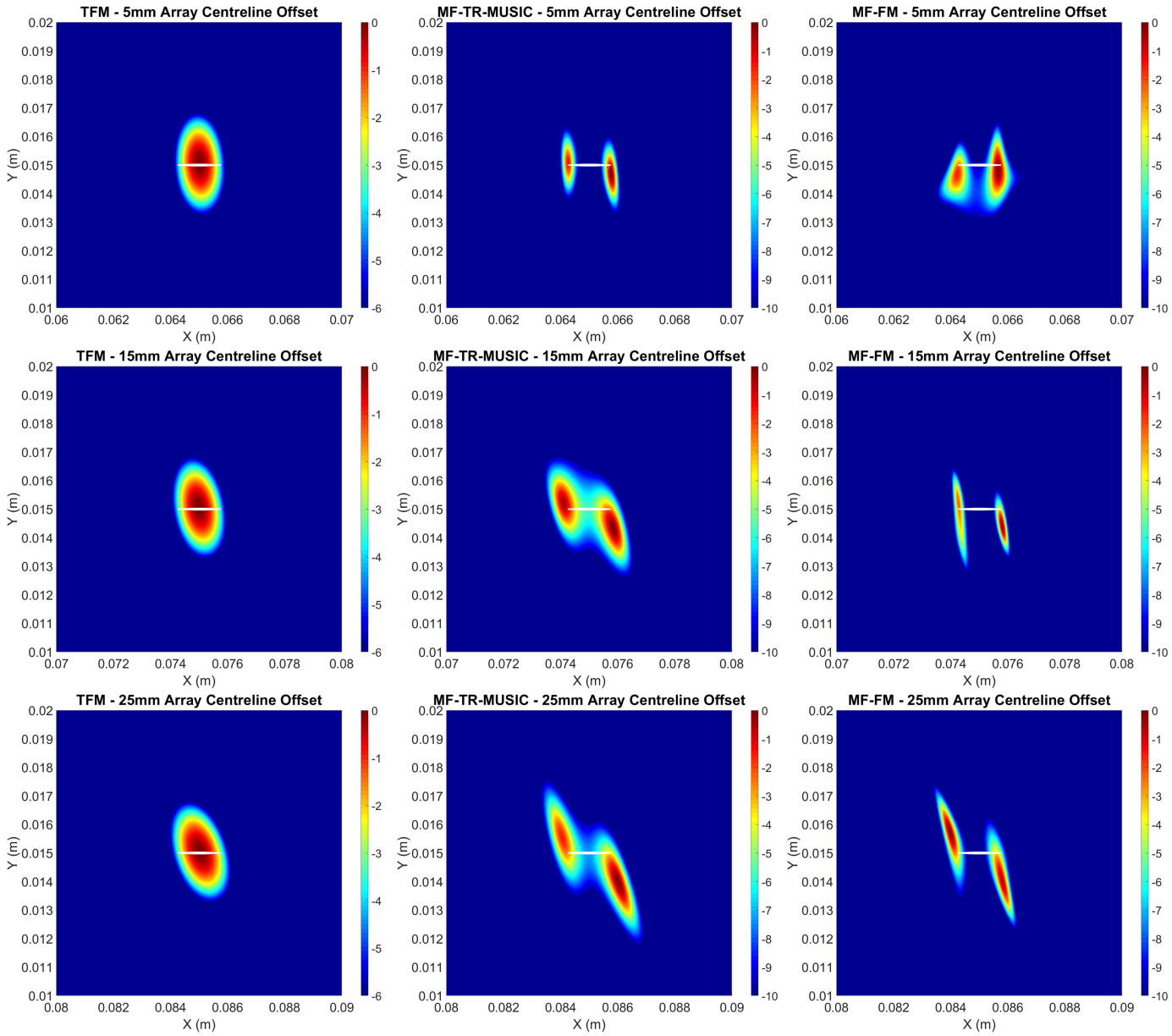


Figure 9.1: TFM, MF-TR-MUSIC and MF-FM images of a series of FE simulated 1.5 mm defects at a depth of 42 mm from a 64-element 2 MHz array located above the defects. The defects were offset from the array centreline by 5 mm (top row images), 15 mm (middle row images) and 25 mm (bottom row images). The same 2D FE modelling approach that was used in Section 3.2 was applied to these simulations.

linear array SR imaging to understand the complex factors which lead to image distortion and reduced characterisation accuracy.

One possible method to overcome the issue of offset defects and reduced array viewing angles could be through the usage of multiple arrays. For example by using two separate arrays to inspect an embedded weld defect, as shown in Fig. 9.2, the effective array viewing angle is doubled as both sides of the defect can be accessed through direct wave propagation. This dual

array imaging set-up is similar to TOFD and would be ideal for inspection under weld caps which do not allow central positioning of the array above the defect. A combined FMC dataset can be collected using both arrays in this set-up upon which the SR and the TFM algorithm can be applied. In this case, the usage of TFM has been termed Diffraction TFM (DTFM) within literature [109], and the method has several benefits over conventional TOFD including allowing for direct sizing of defects to be made from an image (whereas TOFD would require multiple separate scans and further interpretation of the data) and DTFM possessing a larger SNR compared to TOFD (due to the focussing nature of the TFM algorithm). To assess this set-up initially, a 2D FE simulation featuring the dual array inspection set-up illustrated in Fig. 9.2 was carried out. Fig. 9.2 shows the resultant TFM, MF-FM and MF-TR-MUSIC image algorithms for the embedded offset defect. It can be seen that a central, non-skewed indication for the defect is generated by the TFM algorithm and that both SR techniques produce tip indications that could be used for accurate through-wall sizing. The indications present on either size of the defect location are attributed to surface Rayleigh waves which propagate along the defect and are re-emitted from the tips as compression waves. Additional work is recommended to further validate the benefits of dual array imaging on SR imaging performance as preliminary results indicate that the improvements to the effective viewing angle can reduce the impact of image distortion for offset defects.

Additional methods of increasing the available array viewing angle that could be explored in future research are by using indirect wave propagation routes, such as those utilised by the HSTFM algorithm [107]. These additional propagation routes such as skipping off component's geometric features (i.e. backwalls) can be used to obtain additional defect scattering information beyond those obtained from direct reflections. This concept could be extended further by not only using indirect propagation routes of the same wave mode, but also considering multi-mode SR imaging. This approach has already begun to be researched for the TFM algorithm [110, 111], where information from multi-view TFM images corresponding to different wave modes and propagation routes have been combined to provide a more accurate defect characterisation procedure.

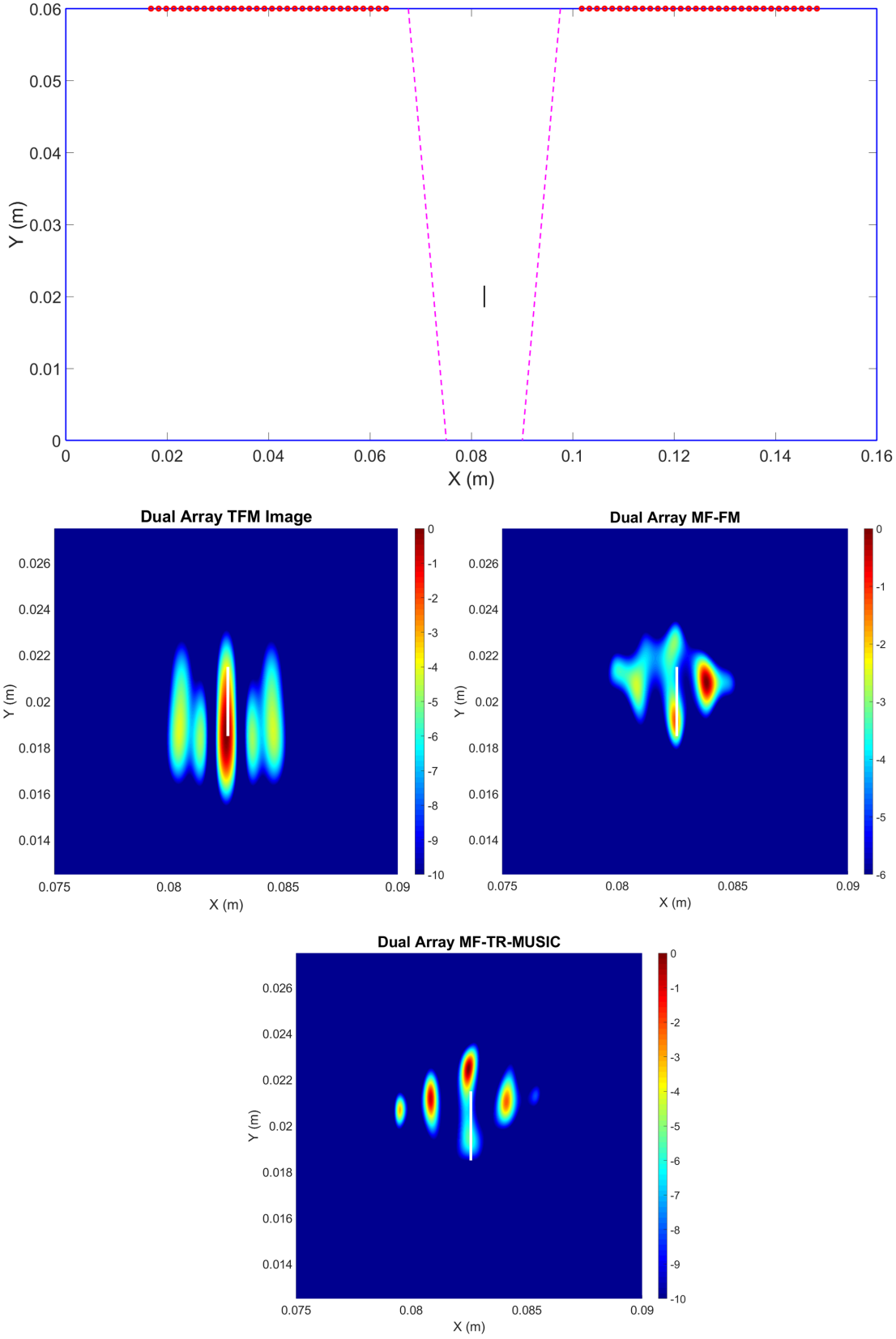


Figure 9.2: The schematic for the dual array inspection of an embedded planar defect (black) FE model. An example weld profile is shown by the magenta dashed lines, with the locations of the array elements denoted by the red circles. An FMC dataset would be collected from both the individual 32-element arrays to obtain 64x64 A-Scans. From this FMC dataset, the TFM, MF-FM and MF-TR-MUSIC algorithms were applied and the resultant images were obtained.

Bibliography

[1] R. Halmshaw, "Non-destructive testing." *Edward Arnold, Mill Rd, Dunton Green, Sevenoaks, Kent TN 13 2 YA, UK, 1991. 323*, 1991.

[2] P. N. Wells, "Ultrasonic imaging of the human body," *Reports on progress in physics*, vol. 62, no. 5, p. 671, 1999.

[3] J. Curie and P. Curie, "Development by compression of polar electricity in hemihedral crystals with inclined faces," *Mineralogy Bulletin*, vol. 3, no. 4, pp. 90–93, 1880.

[4] M. Fatemi and A. C. Kak, "Ultrasonic b-scan imaging: Theory of image formation and a technique for restoration," *Ultrasonic Imaging*, vol. 2, no. 1, pp. 1–47, 1980.

[5] T. Hasiotis, E. Badogiannis, and N. G. Tsouvalis, "Application of ultrasonic c-scan techniques for tracing defects in laminated composite materials," *Strojniški vestnik-Journal of Mechanical Engineering*, vol. 57, no. 3, pp. 192–203, 2011.

[6] S. Nath, K. Balasubramaniam, C. Krishnamurthy, and B. Narayana, "Sizing of surface-breaking cracks in complex geometry components by ultrasonic time-of-flight diffraction (tofd) technique," *Insight-Non-Destructive Testing and Condition Monitoring*, vol. 49, no. 4, pp. 200–206, 2007.

[7] J.-P. Ardouin and A. Venetsanopoulos, "Modelling and restoration of ultrasonic phased-array b-scan images," *Ultrasonic imaging*, vol. 7, no. 4, pp. 321–344, 1985.

[8] C. Holmes, B. W. Drinkwater, and P. D. Wilcox, "Post-processing of the full matrix of ultrasonic transmit–receive array data for non-destructive evaluation," *NDT & e International*, vol. 38, no. 8, pp. 701–711, 2005.

[9] M. Sutcliffe, M. Weston, B. Dutton, P. Charlton, and K. Donne, "Real-time full matrix capture for ultrasonic non-destructive testing with acceleration of post-processing through graphic hardware," *Ndt & E International*, vol. 51, pp. 16–23, 2012.

[10] R. Long, J. Russell, and P. Cawley, "Ultrasonic phased array inspection using full matrix capture," *Insight-Non-Destructive Testing and Condition Monitoring*, vol. 54, no. 7, pp. 380–385, 2012.

[11] P. B. Nagy, "Fatigue damage assessment by nonlinear ultrasonic materials characterization," *Ultrasonics*, vol. 36, no. 1-5, pp. 375–381, 1998.

[12] C. Brotherhood, B. Drinkwater, and S. Dixon, "The detectability of kissing bonds in adhesive joints using ultrasonic techniques," *Ultrasonics*, vol. 41, no. 7, pp. 521–529, 2003.

[13] J. Cheng, J. N. Potter, A. J. Croxford, and B. W. Drinkwater, "Monitoring fatigue crack growth using nonlinear ultrasonic phased array imaging," *Smart Materials and Structures*, vol. 26, no. 5, p. 055006, 2017.

[14] K. Langenberg, M. Berger, T. Kreutter, K. Mayer, and V. Schmitz, "Synthetic aperture focusing technique signal processing," *NDT international*, vol. 19, no. 3, pp. 177–189, 1986.

[15] B. W. Drinkwater and P. D. Wilcox, "Ultrasonic arrays for non-destructive evaluation: A review," *NDT & e International*, vol. 39, no. 7, pp. 525–541, 2006.

[16] C. Holmes, B. W. Drinkwater, and P. D. Wilcox, "Advanced post-processing for scanned ultrasonic arrays: Application to defect detection and classification in non-destructive evaluation," *Ultrasonics*, vol. 48, no. 6-7, pp. 636–642, 2008.

[17] E. Wolf, "Three-dimensional structure determination of semi-transparent objects from holographic data," *Optics Communications*, vol. 1, no. 4, pp. 153–156, 1969.

[18] E. Singe, "Suggested method for extending microscopic resolution into the ultramicroscopic regime," *Phil. Mag*, vol. 6, p. 356, 1928.

[19] E. Ash and G. Nicholls, "Super-resolution aperture scanning microscope," *Nature*, vol. 237, no. 5357, p. 510, 1972.

[20] E. Betzig, A. Lewis, A. Harootunian, M. Isaacson, and E. Kratschmer, "Near field scanning optical microscopy (nsom): development and biophysical applications," *Biophysical journal*, vol. 49, no. 1, pp. 269–279, 1986.

[21] E. Betzig, J. Trautman, T. Harris, J. Weiner, and R. Kostelak, "Breaking the diffraction barrier: optical microscopy on a nanometric scale," *Science*, vol. 251, no. 5000, pp. 1468–1470, 1991.

[22] H. Heinzelmann and D. Pohl, "Scanning near-field optical microscopy," *Applied Physics A*, vol. 59, no. 2, pp. 89–101, 1994.

[23] J.-J. Greffet and R. Carminati, "Image formation in near-field optics," *Progress in surface science*, vol. 56, no. 3, pp. 133–237, 1997.

[24] M. Born and E. Wolf, *Principles of optics: electromagnetic theory of propagation, interference and diffraction of light*. Elsevier, 2013.

[25] A. C. Kak and M. Slaney, "Principles of computerized tomographic reconstruction," *IEEE, New York*, 1998.

[26] D. Colton and A. Kirsch, "A simple method for solving inverse scattering problems in the resonance region," *Inverse problems*, vol. 12, no. 4, p. 383, 1996.

[27] D. Colton, M. Piana, and R. Potthast, "A simple method using morozov's discrepancy principle for solving inverse scattering problems," *Inverse Problems*, vol. 13, no. 6, p. 1477, 1997.

[28] A. Kirsch, "Characterization of the shape of a scattering obstacle using the spectral data of the far field operator," *Inverse problems*, vol. 14, no. 6, p. 1489, 1998.

[29] D. Colton, J. Coyle, and P. Monk, "Recent developments in inverse acoustic scattering theory," *Siam Review*, vol. 42, no. 3, pp. 369–414, 2000.

[30] F. Simonetti, "Multiple scattering: The key to unravel the subwavelength world from the far-field pattern of a scattered wave," *Physical Review E*, vol. 73, no. 3, p. 036619, 2006.

[31] Simonetti, "Localization of pointlike scatterers in solids with subwavelength resolution," *Applied Physics Letters*, vol. 89, no. 9, p. 094105, 2006.

[32] T. Hutt and F. Simonetti, "Super-resolution imaging in elastic media," in *AIP Conference Proceedings*, vol. 1335, no. 1. AIP, 2011, pp. 736–743.

[33] C. Fan, M. Pan, F. Luo, and B. W. Drinkwater, "Multi-frequency time-reversal-based imaging for ultrasonic nondestructive evaluation using full matrix capture," *IEEE transactions on ultrasonics, ferroelectrics, and frequency control*, vol. 61, no. 12, pp. 2067–2074, 2014.

[34] C. Fan, M. Caleap, M. Pan, and B. W. Drinkwater, "A comparison between ultrasonic array beamforming and super resolution imaging algorithms for non-destructive evaluation," *Ultrasonics*, vol. 54, no. 7, pp. 1842–1850, 2014.

[35] K. M. Tant, A. J. Mulholland, and A. Gachagan, "Application of the factorisation method to limited aperture ultrasonic phased array data," *Acta Acustica united with Acustica*, vol. 103, no. 6, pp. 954–966, 2017.

[36] C. Zhang, P. Huthwaite, and M. Lowe, "The application of the factorization method to the subsurface imaging of surface-breaking cracks," *IEEE transactions on ultrasonics, ferroelectrics, and frequency control*, vol. 65, no. 3, pp. 497–512, 2018.

[37] T. D. Hutt, "Towards next generation ultrasonic imaging," Ph.D. dissertation, Imperial College London, 2012.

[38] A. Kirsch and R. Kress, "Two methods for solving the inverse acoustic scattering problem," *Inverse problems*, vol. 4, no. 3, p. 749, 1988.

[39] D. L. Colton, R. Kress, and R. Kress, *Inverse acoustic and electromagnetic scattering theory*. Springer, 1998, vol. 93.

[40] J. Goodman, *Introduction to Fourier Optics*, ser. McGraw-Hill physical and quantum electronics series. Roberts & Company, 2005.

[41] L. E. Kinsler, A. R. Frey, A. B. Coppens, and J. V. Sanders, "Fundamentals of acoustics," *Fundamentals of Acoustics, 4th Edition, by Lawrence E.*

Kinsler, Austin R. Frey, Alan B. Coppens, James V. Sanders, pp. 560. ISBN 0-471-84789-5. Wiley-VCH, December 1999., p. 560, 1999.

[42] J. Rose, *Ultrasonic Waves in Solid Media*. Cambridge University Press, 2004.

[43] G. Giorgi, M. Brignone, R. Aramini, and M. Piana, "Application of the inhomogeneous lippmann–schwinger equation to inverse scattering problems," *SIAM Journal on Applied Mathematics*, vol. 73, no. 1, pp. 212–231, 2013.

[44] P. Hähner, "Scattering by media," in *Scattering*. Elsevier, 2002, pp. 74–94.

[45] A. Zinn, "On an optimisation method for the full-and the limited-aperture problem in inverse acoustic scattering for a sound-soft obstacle," *Inverse Problems*, vol. 5, no. 2, p. 239, 1989.

[46] A. Kirsch, "The music-algorithm and the factorization method in inverse scattering theory for inhomogeneous media," *Inverse problems*, vol. 18, no. 4, p. 1025, 2002.

[47] A. Abubakar, P. M. van den Berg, and S. Y. Semenov, "A robust iterative method for born inversion," *IEEE Transactions on Geoscience and Remote Sensing*, vol. 42, no. 2, pp. 342–354, 2004.

[48] M. Brandfass, A. D. Lanterman, and K. F. Warnick, "A comparison of the colton–kirsch inverse scattering methods with linearized tomographic inverse scattering," *Inverse Problems*, vol. 17, no. 6, p. 1797, 2001.

[49] J. Lambert, A. Pédron, G. Gens, F. Bimbard, L. Lacassagne, and E. Iakovleva, "Analysis of multicore cpu and gpu toward parallelization of total focusing method ultrasound reconstruction," in *DASIP 2012 IEEE-Conference on Design and Architectures for Signal and Image Processing*, 2012.

[50] S. L. Hahn, *Hilbert transforms in signal processing*. Artech House Boston, 1996, vol. 2.

[51] P. Waterman, "New formulation of acoustic scattering," *The journal of the acoustical society of America*, vol. 45, no. 6, pp. 1417–1429, 1969.

[52] A. Kirsch, *An Introduction to the Mathematical Theory of Inverse Problems*, ser. Applied Mathematical Sciences. Springer New York, 2011.

[53] F. Simonetti, M. Fleming, and E. A. Marengo, "Illustration of the role of multiple scattering in subwavelength imaging from far-field measurements," *JOSA A*, vol. 25, no. 2, pp. 292–303, 2008.

[54] D. Colton and A. Kirsch, "A simple method for solving inverse scattering problems in the resonance region," *Inverse Problems*, vol. 12, no. 4, p. 383, 1996.

[55] F. Cakoni and D. Colton, "The linear sampling method for cracks," *Inverse problems*, vol. 19, no. 2, p. 279, 2003.

[56] A. N. Tikhonov, A. Goncharsky, V. Stepanov, and A. G. Yagola, *Numerical methods for the solution of ill-posed problems*. Springer Science & Business Media, 2013, vol. 328.

[57] S. Gratton, P. L. Toint *et al.*, "Svd-tail: a new linear-sampling reconstruction method for inverse scattering problems," *Inverse Problems*, vol. 25, no. 9, p. 095013, 2009.

[58] A. Kirsch, "Characterization of the shape of a scattering obstacle using the spectral data of the far field operator," *Inverse Problems*, vol. 14, no. 6, p. 1489, 1998.

[59] C. Prada, S. Manneville, D. Spoliansky, and M. Fink, "Decomposition of the time reversal operator: Detection and selective focusing on two scatterers," *The Journal of the Acoustical Society of America*, vol. 99, no. 4, pp. 2067–2076, 1996.

[60] S. K. Lehman and A. J. Devaney, "Transmission mode time-reversal super-resolution imaging," *The Journal of the Acoustical Society of America*, vol. 113, no. 5, pp. 2742–2753, 2003.

[61] A. Kirsch and N. Grinberg, *The factorization method for inverse problems*. Oxford University Press, 2008, vol. 36.

[62] G. B. Arfken and H. J. Weber, "Mathematical methods for physicists," 1999.

[63] C. Prada and M. Fink, "Eigenmodes of the time reversal operator: A solution to selective focusing in multiple-target media," *Wave motion*, vol. 20, no. 2, pp. 151–163, 1994.

[64] Y. Labyed and L. Huang, "Ultrasound time-reversal music imaging of extended targets," *Ultrasound in medicine & biology*, vol. 38, no. 11, pp. 2018–2030, 2012.

[65] H. Lev-Ari and A. Devancy, "The time-reversal technique re-interpreted: Subspace-based signal processing for multi-static target location," in *Sensor Array and Multichannel Signal Processing Workshop. 2000. Proceedings of the 2000 IEEE*. IEEE, 2000, pp. 509–513.

[66] M. Cheney, "The linear sampling method and the music algorithm," *Inverse problems*, vol. 17, no. 4, p. 591, 2001.

[67] P. Huthwaite, "Accelerated finite element elastodynamic simulations using the gpu," *Journal of Computational Physics*, vol. 257, pp. 687–707, 2014.

[68] G. Miller and H. Pursey, "The field and radiation impedance of mechanical radiators on the free surface of a semi-infinite isotropic solid," *Proceedings of the Royal Society of London. Series A. Mathematical and Physical Sciences*, vol. 223, no. 1155, pp. 521–541, 1954.

[69] S.-C. Wooh and Y. Shi, "Three-dimensional beam directivity of phase-steered ultrasound," *The Journal of the Acoustical Society of America*, vol. 105, no. 6, pp. 3275–3282, 1999.

[70] M. Israeli and S. A. Orszag, "Approximation of radiation boundary conditions," *Journal of computational physics*, vol. 41, no. 1, pp. 115–135, 1981.

[71] P. Rajagopal, M. Drozdz, E. A. Skelton, M. J. Lowe, and R. V. Craster, "On the use of absorbing layers to simulate the propagation of elastic waves in unbounded isotropic media using commercially available finite element packages," *NDT & E International*, vol. 51, pp. 30–40, 2012.

[72] J. R. Pettit, A. E. Walker, and M. J. Lowe, "Improved detection of rough defects for ultrasonic nondestructive evaluation inspections based on finite element modeling of elastic wave scattering," *IEEE Transactions on ultrasonics, ferroelectrics, and frequency control*, vol. 62, no. 10, pp. 1797–1808, 2015.

[73] M. B. Drozdz, "Efficient finite element modelling of ultrasound waves in elastic media," Ph.D. dissertation, Imperial College London, 2008.

[74] SIMULIA, *Abaqus FEA version 6.13*. Dassault Systemes, France, 2013.

[75] *British Standards Institution, Non-destructive testing – Ultrasonic testing – Characterisation and sizing of discontinuities*. BS EN ISO 16827:2014, BSI, London, 2014.

[76] A. Birring, "Sizing discontinuities by ultrasonics," *Materials Evaluation*, vol. 68, no. 11, pp. 1208–1215, 2010.

[77] EXTENDE, *CIVA version 2016*. Massy, France, 2016.

[78] *Non-Destructive Testing – Ultrasonic testing – Time-of-flight diffraction technique as a method for detection and sizing of discontinuities*. ISO 16828:2012, Technical Report, International Organization for Standardization, Geneva, CH, 2012.

[79] J. Ogilvy and J. Temple, "Diffraction of elastic waves by cracks: application to time-of-flight inspection," *Ultrasonics*, vol. 21, no. 6, pp. 259–269, 1983.

[80] J. B. Keller, "Geometrical theory of diffraction," *Journal of the Optical Society of America*, vol. 52, no. 2, pp. 116–130, 1962.

[81] R. Y. Chiao and L. J. Thomas, "Analytic evaluation of sampled aperture ultrasonic imaging techniques for nde," *IEEE Transactions on Ultrasonics, Ferroelectrics, and frequency control*, vol. 41, no. 4, pp. 484–493, 1994.

[82] I. Virkkunen *et al.*, *Thermal fatigue of austenitic and duplex stainless steels*. Finnish Academy of Technology, 2001.

[83] J. Wåle and P. Ekstroem, "Crack characterization for in-service inspection planning," SAQ Inspection Ltd., Tech. Rep., 1995.

[84] J. Wåle, "Crack characterisation for in-service inspection planning-an update," Swedish Nuclear Power Inspectorate, Tech. Rep., 2006.

[85] J. Ogilvy, "Wave scattering from rough surfaces," *Reports on Progress in Physics*, vol. 50, no. 12, p. 1553, 1987.

[86] J. Zhang, B. W. Drinkwater, and P. D. Wilcox, "Effect of roughness on imaging and sizing rough crack-like defects using ultrasonic arrays," *IEEE transactions on ultrasonics, ferroelectrics, and frequency control*, vol. 59, no. 5, pp. 939–948, 2012.

[87] J. B. Elliott, M. J. Lowe, P. Huthwaite, R. Phillips, and D. J. Duxbury, "Sizing subwavelength defects with ultrasonic imagery: An assessment of super-resolution imaging on simulated rough defects," *IEEE transactions on ultrasonics, ferroelectrics, and frequency control*, vol. 66, no. 10, pp. 1634–1648, 2019.

[88] J. Greenwood, "A unified theory of surface roughness," *Proceedings of the Royal Society of London. A. Mathematical and Physical Sciences*, vol. 393, no. 1804, pp. 133–157, 1984.

[89] J. A. Ogilvy and H. M. Merklinger, "Theory of wave scattering from random rough surfaces," 1991.

[90] J. Ogilvy, "Computer simulation of acoustic wave scattering from rough surfaces," *Journal of Physics D: Applied Physics*, vol. 21, no. 2, p. 260, 1988.

[91] L. Bai, A. Velichko, and B. W. Drinkwater, "Characterization of defects using ultrasonic arrays: a dynamic classifier approach," *IEEE transactions on ultrasonics, ferroelectrics, and frequency control*, vol. 62, no. 12, pp. 2146–2160, 2015.

[92] A. Velichko, L. Bai, and B. Drinkwater, "Ultrasonic defect characterization using parametric-manifold mapping," *Proceedings of the royal society a: mathematical, physical and engineering Sciences*, vol. 473, no. 2202, p. 20170056, 2017.

[93] G. Connolly, M. Lowe, J. Temple, and S. Rokhlin, "Correction of ultrasonic array images to improve reflector sizing and location in inhomogeneous materials using a ray-tracing model," *The Journal of the Acoustical Society of America*, vol. 127, no. 5, pp. 2802–2812, 2010.

[94] Y. Cui and C. D. Lundin, "Austenite-preferential corrosion attack in 316 austenitic stainless steel weld metals," *Materials & design*, vol. 28, no. 1, pp. 324–328, 2007.

[95] R. Hudgell and B. Gray, *The Ultrasonic Inspection of Austenitic Materials: State of the Art Report*. United Kingdom Atomic Energy Authority, Northern Division, 1985.

[96] X. Edelmann, "Application of ultrasonic testing techniques on austenitic welds for fabrication and in-service inspection," *NDT International*, vol. 14, no. 3, pp. 125–133, 1981.

[97] A. Lhémery, P. Calmon, I. Lecœur-Taıbi, R. Raillon, and L. Paradis, "Modeling tools for ultrasonic inspection of welds," *NDT & E International*, vol. 33, no. 7, pp. 499–513, 2000.

[98] J. Tomlinson, A. Wagg, and M. Whittle, "Ultrasonic inspection of austenitic welds," Tech. Rep., 1980.

[99] J. Moysan, A. Apfel, G. Corneloup, and B. Chassignole, "Modelling the grain orientation of austenitic stainless steel multipass welds to improve ultrasonic assessment of structural integrity," *International Journal of Pressure Vessels and Piping*, vol. 80, no. 2, pp. 77–85, 2003.

[100] L. W. Schmerr, *Fundamentals of ultrasonic nondestructive evaluation*. Springer, 2016.

[101] W. P. Mason and H. McSkimin, "Attenuation and scattering of high frequency sound waves in metals and glasses," *The Journal of the Acoustical Society of America*, vol. 19, no. 3, pp. 464–473, 1947.

[102] H. Huntington, "On ultrasonic scattering by polycrystals," *The Journal of the Acoustical Society of America*, vol. 22, no. 3, pp. 362–364, 1950.

[103] G. D. Connolly, M. J. Lowe, J. A. G. Temple, and S. I. Rokhlin, "The application of fermat's principle for imaging anisotropic and inhomogeneous media with application to austenitic steel weld inspection," *Proceedings of the Royal Society A: Mathematical, Physical and Engineering Sciences*, vol. 465, no. 2111, pp. 3401–3423, 2009.

[104] O. Nowers, D. J. Duxbury, J. Zhang, and B. W. Drinkwater, "Novel ray-tracing algorithms in nde: Application of dijkstra and a$*$ algorithms to the inspection of an anisotropic weld," *NDT & E International*, vol. 61, pp. 58–66, 2014.

[105] D. S. Kupperman and K. J. Reimann, "Ultrasonic wave propagation and anisotropy in austenitic stainless steel weld metal," Argonne National Lab., IL, Tech. Rep., 1980.

[106] G. Harvey, A. Tweedie, C. Carpentier, and P. Reynolds, "Finite element analysis of ultrasonic phased array inspections on anisotropic welds," in *AIP Conference Proceedings*, vol. 1335, no. 1. AIP, 2011, pp. 827–834.

[107] M. V. Felice, A. Velichko, and P. D. Wilcox, "Accurate depth measurement of small surface-breaking cracks using an ultrasonic array post-processing technique," *Ndt & E International*, vol. 68, pp. 105–112, 2014.

[108] M. V. Felice, A. Velichko, P. D. Wilcox, and C. J. Lane, "Depth measurement of small surface-breaking cracks using the half-skip total focusing method," in *AIP Conference Proceedings*, vol. 1650, no. 1. AIP, 2015, pp. 994–1000.

[109] P. D. Wilcox, C. Holmes, B. W. Drinkwater *et al.*, "Enhanced defect detection and characterisation by signal processing of ultrasonic array data," *Proc. 9th ECNDT*, 2006.

[110] N. Budyn, R. Bevan, A. J. Croxford, J. Zhang, P. D. Wilcox, A. Kashubin, and P. Cawley, "Sensitivity images for multi-view ultrasonic array inspection," in *AIP Conference Proceedings*, vol. 1949, no. 1. AIP Publishing LLC, 2018, p. 080001.

[111] N. Budyn, R. L. Bevan, J. Zhang, A. J. Croxford, and P. D. Wilcox, "A model for multiview ultrasonic array inspection of small two-dimensional defects," *IEEE Transactions on Ultrasonics, Ferroelectrics, and Frequency Control*, vol. 66, no. 6, pp. 1129–1139, 2019.